A THEORETICAL STUDY OF ROTOR FORCES AND TORQUES IN HELICAL TWIN SCREW COMPRESSORS

CHENG XIANG YOU, B.Sc, M.Sc

Thesis submitted to the

University of Strathclyde

for the degree of

Doctor of Philosophy

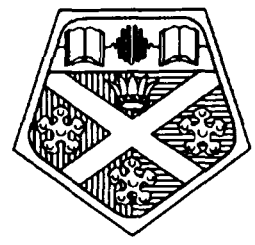

Division of Dynamics and Control

Department of Mechanical Engineering

University of Strathclyde

Glasgow, UK

December 1994

To my wife, Ping

my parents, Lin Feng and Xin Cheng

and my auntie, Hui Ying

Abstract

Helical twin screw compressors are being increasingly used in the oil and gas process industry and for refrigeration and air conditioning duties. This machine is capable of high reliability. To achieve it both thermodynamic efficiency and rotor forces must be taken into consideration at the design stage.

In this study, a computer program for analysing the forces in a twin screw compressor has been developed. It takes into account all significant factors and includes a rotor profile generation program and a geometrical characteristics calculation program. The programs developed have been integrated with an existing performance simulation program and used to investigate several design aspects of a refrigeration twin screw compressor and an unusual refrigeration system design.

A comprehensive examination of lobe tip designs suggests that lobe tip design parameters must be optimised if minimum power consumption is to be achieved and the use of a sealing strip gives an advantage.

A parameter study for optimum rotor geometrical parameter combinations has shown that the 4+5 and 5+6 combinations have in general high efficiencies, but less rigidity, while the 5+7 and 4+6 combinations give the opposite results. The highest wrap angle and length/diameter ratio do not always lead to the highest compressor performance.

A comprehensive examination of the influence of the slide valve on compressor performance and bearing forces has been conducted. Procedures for determining the optimum slide stop and volume ratios are presented.

The detrimental effect of the non-return valve in a refrigeration system driven by a twin screw compressor has been examined. A non-reversing clutch fitted to the prime mover is an alternative, but must be designed according to the shut down torque which is higher than the normal running torque. This is demonstrated.

An analytical model for axial-torsional coupled vibration in an oil-injected twin screw compressor has been created. A frequency analysis of all the excitations has been conducted by using an FFT technique. It is found that the fundamental harmonic dominates the gas torque, while the first two harmonics dominate the axial forces.

Acknowledgements

I would like to take this opportunity to formally express my sincere gratitude and appreciation to following people and organisations whose help throughout my study and research work, I truly treasure.

- to my supervisor **Dr. J.S. FLEMING**, head of Division of Dynamics and Control, special thanks for his invaluable guidance, supervision, encouragement, constructive criticism throughout this project. His assistance during the thesis writing up has much enhanced the qualities of this thesis and will benefit my future research;

- to Professor **J. SPENCE,** former head of Department of Mechanical Engineering, for giving me the opportunity to study in the department and for recommending me for the university postgraduate studentship;

- to the academic staff in the Department of Mechanical Engineering in particular **Dr. A.B. Tramschek**, for his valuable discussion and kind help in permitting the use of his literature; **Dr. M.R. THOMAS,** for his kind help with the FFT analysis and solving computer related problems; **Dr. R. BARRON, Dr. I.A. CRAIGHEAD**, for their concern, encouragement and kind help in permitting my attendance at their courses; **Professor S.M. FRASER** and **Dr. D. MACKENZIE** for their kind help in permitting my attendance at the *CFD* and *FE* M.Sc courses respectively.

- to the secretarial and technical staff in the Department of Mechanical Engineering, especially **Ms. J. HARBIDGE, Mrs. M. TROUBE, Mrs. C.J. HOUSTON, Mrs. M. STEWART, Mr. A. CAIRNEY, Mr. J. KEMP, Mr. W. MASON, Mr. B. MUIRHEAD** for their hospitality and endless help during my study;

- to my colleague **Mr Y. TANG** for many valuable discussions and pleasant cooperation throughout this project;

- to **HOWDEN COMPRESSORS Ltd, Glasgow.** for supplying experimental data and technical reports. In particular, special thanks to **Mr. B. YOUNG** and **Mr. H. ANDERSON** for their kind help;

- to **the Committee of Vice-Chancellors and Principals of the Universities of the United Kingdom** for the Overseas Research Student Award and **Strathclyde University** for the David Livingstone Bursary given to me to cope with my tuition fees;

- to **Ms. C. MORELLI** (Registry-General), for her kind help in solving the administrative problems which occurred during my study;

- to **Professor K. ROCH**, former research director of South Bank Polytechnic, and his wife **Mrs. R. ROCH** for their concern, encouragement and friendship during my stay;

- to my fellow students and research staff, **Dr. S.B. LI, Ms. L. LI, Mr. H.M. MAHGOUB, Mr. L. MA, Dr. Z.W. XING, Mr A. BWALYA** for their friendship and for creating a pleasant working atmosphere during my study;

- to my wife **PING**, my parents, **LIN FENG** and **XIN CHENG**, my mother-in-law, **SHUN LING**, my father-in-law, **QING YUN**, my auntie **HUI YING** and all my **family members** for their understanding, full support and love in all ways during my study.

Contents

---

[1] Appendix 3 is attached to this written volume in a separate container inside the rear cover.

List of Figures

List of Tables

Symbols and Abbreviations

This list covers symbols used throught the main text, but due to an insufficient number of symbols being available from the English and Greek alphabets on occasions the same symbol is used for different things. On those occasions the definition is given locally.

Symbols

A	Addendum of the female rotor, mm
C	Centre distance between the male and female rotors, mm
d	Outer diameter of rotors, mm
f	Frequency, Hz
F	Force components (e.g. gas/contact forces, bearing reactions, etc), N
h	Pitch length of rotors, mm
H	Oil film thickness, mm
i	Transmission rate, defined as $i = \omega_2 / \omega_1$
I	2nd moment of area, mm^4
k	Stiffness coefficient, N/m or Nm/rad, or for constant $k = 1 + i$
l	Distance between two points (with subscripts from 3), mm
L	Length of rotors, mm
M	Moment, Nm
p	Gas or oil pressure, N/m^2 or bar
P	Viscous friction power loss, kw
r	Radius of circles, mm
s	Length of arc, mm
S	Area (e.g. blow hole area, inter-lobe area, etc), mm^2
t	Parameter in the parameter equations of curves

T	Torques applied to the rotors, Nm
u	Speed of shear of the oil film, m/s
U	Rotor tip speed, m/s
V	Cavity volume, mm^3
x,y,z	Coordinates in rotating coordinate systems, mm
X,Y,Z	Coordinates in fixed coordinate systems, mm
W	Rotor tip width, mm
$\bar{z}$	Lobe number of rotors

Greek

α	Male rotor angle of rotation, rad
β	angle for defining rotor profile, degree
δ	Helix angle, rad
ε	Pressure angle, rad
η	Coefficient of viscosity of oil, $N \cdot s/m^2$
ϑ	Torsional displacement or orientation angle of lines, rad
σ	Stress, N/m^2
τ	Shear stress, N/m^2
φ	Male rotor angle, rad
ψ	Female rotor angle, rad
ω	Angular velocity of rotors, rad/s

Subscripts (various combinations of the subscripts are used)

1,2	male and female rotor, respectively
3 .. 13	index for variables
a,r,t	axial, radial and tangential direction, respectively
b	bearing loads
c	centre of circular arc or cavity volume
d	at the beginning of the discharge process
e	end point
h	housing or housing cusp

i	inner radius or inlet side
j	an arbitrary point
n,	normal direction of the profile at contact point in rotor transverse plane
n3	normal direction of the profile at contact point in 3-dimension
o	outer radius or outlet side or oil
p	pitch circle
s	start point or at the end of the suction process
w	wrap angle of the rotors

Abbreviations

COP	Coefficient of performance
DFT	Discrete Fourier transform
FFT	Fast Fourier transform
IMechE	Institution of Mechanical Engineers
RHS	Right hand side
rpm	revolution per minute
SRM	Svenska Rotor Maskiner AB.
VDI	Verein Deutscher Ingenieure
VLCR	Volumetric load capacity ratio, i.e. the ratio of the effective suction volume V_s over the maximum suction volume at full load, $V_s/V_{s,max}$
VR	Volume ratios for the discharge ports
Z_{stop}	Slide stop length of a slide valve (mm)

Chapter 1

Introduction

1.1 Background

Helical twin screw compressors are becoming more and more important to industry. Though first introduced half a century ago, the twin screw compressor had to await the development of the last ten to 15 years in manufacturing technology to compete effectively with other types. Their utilization now dominates air compression requirements for the entire construction industry (Hodge, 1970; Shaw, 1990). The fundamental reason for this dominance is the innate reliability potential of two rugged rotors as opposed to the lower reliability of a machine containing all the moving parts required in reciprocating and rotary vane compressors types that dominated prior to the introduction of the modern twin screw machines.

The application of twin screws to process refrigeration has also been especially successful (Villadsen and Fleming, 1980; Wu, 1985; Svenningson and Sjölin, 1992). The twin screw compressor is now used throughout the world in plants for process refrigeration, cold storage and heat pump schemes etc. It is anticipated that twin screw compressors will come to dominate in the industrial refrigeration world, where reliability is of prime importance (Shaw, 1990).

What comes next? Where does the twin screw of the future fit, especially in the large and growing world of air conditioning and commercial refrigeration applications. Centrifugal compressors have proven best at handling large volumes of vapour. This fact has allowed them to dominate the large tonnage air conditioning market while the low pressure CFC *R11* refrigerant was available. However, from the 1st of January 1995 *R11* will not be available. R-22 is currently regarded as the only refrigerant acceptable in the short term for general air conditioning purposes but it is a relatively high pressure refrigerant and therefore is not well suited to centrifugal compressors. Reciprocating compressors are used in parallel for a portion of this range yet there is an upper limit as to how many reciprocating compressors are desirable on a given unit. Volumetric space, first cost, reliability and maintenance considerations are against parallel reciprocating compressors. High tonnage individual reciprocating compressors are neither practical nor cost effective in today's market and thus there is a rapidly growing belief that twin screw compressors are likely to be used increasingly (Shaw, 1990).

The demand at present for the twin screw compressors is certainly real. However, can the twin screw meet the demands of the future?

First, it is obvious that the demands for high efficiency will remain and may increase if energy prices increase. It used to be the case that inaccurately machined rotors could be sealed by injecting huge quantities of oil but that resulted in efficiency levels that are unacceptable today in air conditioning and refrigeration. Highly efficient twin screw compression calls for good rotor profiles and accurate and well positioned rotors, which in turn rely on the development of high efficiency rotor profiles and fast and accurate machining methods.

Second, there exists an increasing demand for low noise and vibration. Pure rotation of balanced rigid components does not result in vibration. Thus a twin screw compressor has no intrinsic problems in this regard. However, manufacturing inaccuracies influence meshing and contribute to vibration and

noise. In addition, proper volume ratio matching has a major impact on twin screw noise.

Plant reliability is very highly prized by plant users at the present time. It is considered to be of great economic value. Compared to a reciprocating compressor which has pressure-actuated valves and an inherent inability to deal with the ingestion of liquid refrigerant, the reliability potential of the twin screw is obvious. Balanced rigid body rotation, good rotor meshing geometry combined with oil injection, rolling element bearings, absence of valves, an inherent ability to pass liquid refrigerant: all of these factors contribute to the high reliability potential of the twin screw compressor.

Other demands are apparent and look certain to increase; e.g. for a reduction in equipment size and weight, and for control by the continuous variation of speed. Twin screw compressors are ideally suited to capacity control by speed variation since the minimum and maximum rotor tip speeds at which they operate successfully are widely separated and the compressor efficiency is reasonably high over most of the speed range. Furthermore, for a given volumetric delivery, a twin screw compressor will be physically smaller than its main rival, the reciprocator, due to the relatively lower speeds to which the reciprocator is limited by its self-acting valves. Existing twin screws already have capacity control by a slide which effectively alters the volume ratio, usually at a constant speed, 3000 rpm in Europe and 3600 rpm in North America.

Finally, the demand for minimum first cost and running costs will always be with us. Both of these costs have been falling for some time for twin screw compressors and look like continuing to fall due to the steady improvements in manufacturing technology which are occurring. Improved manufacturing technology is also contributing to producing machines of greater reliability.

And last but by no means least, the twin screw compressor is a positive displacement machine and as such physically adapts to compressing a variety

of refrigerants having unusual characteristics far more successfully than any dynamic (centrifugal) machine and of course does not suffer from surge, which is a major disadvantage of centrifugal machines. Virtually all the new refrigerants currently replacing the soon-to-be-banned CFCs are mixtures ("blends") of two, three and occasionally four separate substances, each of which is environmentally benign. The efficiency of a centrifugal compressor is likely to be poor when compressing some of these blends. As a consequence, part of the centrifugal market opens up to the larger twin screw compressors (or multiple twin screws) to match the higher throughput which is a characteristic of centrifugal compressors.

Quite clearly, the future of the twin screw compressor is exceptionally bright. This explains the increased activity in research and development in countries in which it is manufactured. The greater demands soon to be made of this compressor type will only be met if its characteristics are better understood and if accurate, flexible and user-friendly design techniques are placed at the disposal of designers and research and development engineers working on its development and applications. The purpose of the work reported here is to develop analytical means of determining the driving torque and the bearing reaction forces for all possible running conditions of a twin screw compressor.

1.2 Objectives

Despite the great efforts applied to improving the performance and reliability of twin screw compressors, there is still comparatively little published information on many topics of interest. The reason for this is the need for commercial confidentiality. Almost anything of detailed substance that can be said about twin screw compressors is likely to be of commercial value, therefore it remains unsaid.

Great secrecy, for example, surrounds the geometric detail of rotor profiles because profiles govern to a great extent reliability and performance. The

emphasis of the profile development work has been put on the reduction of leakage and the increase in compressor thermodynamic efficiency, while little attention has been given (in the published work) to its influence on the time variation of rotor torque and bearing forces in magnitude and direction. Furthermore, there does not appear to have been any attempt to calculate the loss which occurs in a oil injected machine due to the injection of oil.

Similarly, previous works on rotor geometrical parameters such as lobe combination, length / diameter ratio and helix angles have been mainly concentrated on their impact on compressor thermodynamic performance. Few publications are available with respect to their influence on rotor torques, bearing forces and rotor deflections.

The capacity control of the helical screw compressor in refrigeration applications is often realized by making use of a slide valve device which, when designed well gives good part load efficiency. However, a search of the literature shows a lack of a comprehensive assessment of its influence on compressor performance, especially on the unexpected and dangerous occurrence of the maximum bearing forces at part load.

Refrigeration systems with a helical twin screw compressor are usually fitted with a non-return valve (sometimes in the suction line of the compressor) to prevent the reverse flow of gas from the high pressure side driving the machine to a dangerously high speed following system shutdown. Since the non-return valve reduces the COP of the refrigeration system, it is worthwhile investigating systems from which the non-return valve has been removed. A non-reversing clutch is an adequate alternative to a non-return valve, providing that it is designed properly.

In addition, periodic loads exerted on the rotors due to gas compression and lobe interaction cause coupled axial and torsional vibration in oil-injected twin screw compressors. The natural frequencies of such coupled vibration modes in a large machine may be relatively low and therefore require to be examined

at the design stage. To avoid any possible excitation of resonance, the frequencies of the forces and torques applied to the rotors must be different from the natural frequencies of the system. Thus, a frequency analysis of all the excitations is also worthwhile.

The work reported here aims to provide a better understanding of all the above mentioned aspects of the helical twin screw compressor by making use of analytical techniques. Carrying out parameter studies experimentally is in any case impractical due to the high costs of tests, e.g. different rotor tip designs or length / diameter ratios would require the manufacture of a large number of different rotors, requiring different cutter blades and would be very expensive, hence the author's decision to tackle this problem analytically.

To facilitate the parameter study, a suite of computer programs have been developed. These include the programs for rotor profile generation, geometrical parameter calculation, rotor torques and bearing forces calculation as well as vibration analysis. Although a number of programs with similar functions have been reported by some researchers, only a simple description can usually be found in their publications (e.g. Singh and Onuschak, 1984; Stošić, et al, 1988; Bennewitz, 1992; Xing, et al, 1992). Some did describe the methods used, but they either utilize assumptions to simply the complex rotor profile geometry, which affects accuracy of predictions, or use fairly crude methods in the calculation of some important factors (e.g. Rinder, 1979; Zhou, et al, 1990; Adams and Soedel, 1992). Because of this, novel methods and techniques are demanded in the development of these programs, and due to the complexity of rotor geometry, these tasks are challenging.

The bearing force and torque programs developed by the author combined with the University of Strathclyde's modelling program (Tang and Fleming, 1992) form a complete computer program package for the design and the analysis of the behaviour of helical twin screw compressor. Thanks are due to Howden Compressors Ltd. of Glasgow, Scotland, for the measurement data needed for the verification of the programs.

The objectives of this project may be summarized as follows:

- The development of a program for the generation of rotor profiles;
- The development of a program for the calculation and analysis of rotor profile geometrical characteristics;
- The development of a generalized program for the calculation of rotor torques, bearing forces and rotor deflections;
- To examine the effect of rotor tip designs on compressor efficiency, rotor torques and bearing forces, as well as viscous friction loss in an oil injected machine;
- To optimize rotor geometrical parameters (lobe combination, length / diameter ratio and wrap angle) with respect to compressor efficiency, bearing forces and rotor deflection;
- To examine the effects of slide valve parameter variation on compressor efficiency and on the optimal design technique, taking both compressor efficiency and bearing forces into consideration;
- To evaluate the influence of the non-return valve on the COP of the refrigeration system and to examine an alternative designs which does not make use of a non-return valve.
- To create a model for the analysis of the axial and torsional coupled vibration of the oil injected twin screw compressor system, and to evaluate the frequency composition of all the excitations.

1.3 A Review of the Twin Screw Compressor

1.3.1 History of Screw Compressor Development

In the early 1930s Svenska Rotor Maskiner AB (SRM, Sweden), in view of the difficulties with surging in the centrifugal and axial-flow type compressors at that time, intended to develop a new type compressor, incapable of surge,

which should meet the requirement of a high average efficiency under varied conditions of pressure and speed, a high maximum efficiency - preferably above 85% - with small bulk, low weight and also be suitable for direct drive from a turbine.

Their pioneer study led to the development of the positive-displacement rotary compressor, having two cooperating rotors directly coupled via timing gears with helical lobes and grooves, running dry with small clearances between the rotating parts and between each rotor and the housing and achieving a pressure ratio of more than 2:1 in one stage (Lysholm, 1943).

In 1938 Howden Compressors became the first company in the world to commercially produce screw compressors under the SRM patent. In order to obtain high efficiency, the female rotor grooves were given an asymmetric shape with the leading flank circular and the trailing flank generated by the tip of the male rotor. Though some pilot installations worked very well, it proved difficult in practice to achieve sufficient manufacturing accuracy to ensure trouble free operation.

In 1946 SRM introduced the circular symmetric rotor profile which had less risk of damaging the sealing edges due to thermal distortion or errors in timing of the rotors. In the following seven years a large amount of work was carried out with respect to compressor designs, rotor machining techniques and product standardization. During the years 1953-1958 some 600 dry screw compressors for stationary use, with symmetric profile and diameters 65 to 630 mm, were produced by SRM licensees. Light-weight designs for airborne applications were introduced in 1956, and by 1958, 425 units were produced in total (Svenningson and Sjölin, 1992).

The technological breakthrough which enormously increased the attractiveness of the screw compressor came in the late 1950s, when the oil injection machine was introduced by Howden Compressors Ltd. Compared with the 'dry' versions the oil injected type has several major advantages. It permits

the rotors to be run together like a pair of gears thus eliminating the need for timing gears and the metal-to-metal contact of the rotor surfaces is prevented by the presence of an hydrodynamic oil film. Of course, greater care has to be taken with rotor profile design since the rotors now act also as a pair of gears. Since in this case it is not necessary to use timing gears, which must be used when the rotors are run dry, considerable savings in complexity and cost are achieved.

Next, because of the sealing and cooling effects of the oil injected into the compression cavities, very much higher stage pressure ratios became possible and lower rotor tip speeds could be used —— both whilst maintaining acceptable efficiencies. In the dry machine high tip speeds are needed to limit the leakage, by reducing the time available for leakage. The achievable higher pressure ratios of the oil injected machine permitted the application of screw compressors to the fields of portable air compression and process refrigeration in the early 60's (both require efficient operation and large pressure differentials). The allowable lower rotor tip speeds make the rotors simpler and more robust, and greatly reduce the noise produced by meshing.

In the latter part of 60's, research and development efforts were made to improve the efficiency of the screw compressor. This resulted in what has become known as the SRM-asymmetrical profile (which did not have the drawbacks of the Lysholm asymmetrical profile). A 5 to 10 percent gain in adiabatic efficiency resulted.

Although several profile patents came into existence, the industry generally adopted SRM asymmetric profiles popularly known as SRM A and SRM C during the 70's (Singh and Onuschak, 1984).

In the late 70's, with increasing market penetration of the compressor market by twin screws and increasing numbers of compressors (especially small diameters of 63 to 127 mm) being produced, new manufacturing methods became of particular interest. This resulted in a modification of the profile

form, leading to easier manufacture of the rotors. Several new profiles have appeared on the scene, e.g. the Sigma profile (Karsser, Germany), X profile (Atlas Copco, Sweden) and G.H.H profile (G.H.H, Germany), and even SRM has come out with a new profile called SRM D since 1982 (Singh and Onuschak, 1984; Wu, 1985; Svenningson and Sjölin, 1992). In addition, it is known that many other manufacturers like Hitach (Japan) and Ingersoll-Rand (USA) and Energoinvest (Yugoslavia) have also developed their own rotor profiles.

The SRM D in fact is not a specific profile, but a versatile system for determining the best profile for any chosen application, taking into account performance-related data, aspects of reliability and life, and economy-related factors such as rotor materials and manufacturing methods. The D-profile concept has proved its ability in several applications from very small oil injected compressor to the largest screw compressor ever built, with a rotor diameter of 845 mm.

The SRM D profile is covered by patents until the beginning of next century. It represents a considerable progress and a technological trend. It is likely that in the future the industry will preferably use a 'flexible' profile like SRM D for different applications, in which small changes in a basic profile are made to suit the application.

1.3.2 Main Components and Compression Principle

The essential features of a twin screw compressor are as follows: a pair of meshing rotors, a housing, bearings, an oil management system, a drive system, and capacity control devices. The oil and drive systems are not the subject of study here and the capacity control devices will be discussed in Chapter 6. Only the rotor characteristics and the compression principle are presented here.

Rotor Pairs

Fig. 1.1 shows a typical rotor pair (i.e. twin screws). One rotor is called the male, the other the female, each having a special end shape usually referred to as rotor profile or rotor end profile. As mentioned earlier, the currently preferred profile design is asymmetric, a feature of which is reduced leakage which improves the efficiency of the compressor. The helical movement of the end profile of a rotor along its axis forms the helical lobes, with the male rotor usually having 3,4 or 5 lobes, paired with the female rotors having 5,6 or 7 lobes. Fewer lobes decrease the pressure ratio and increase the volumetric flow, whereas more lobes produce the opposite effects.

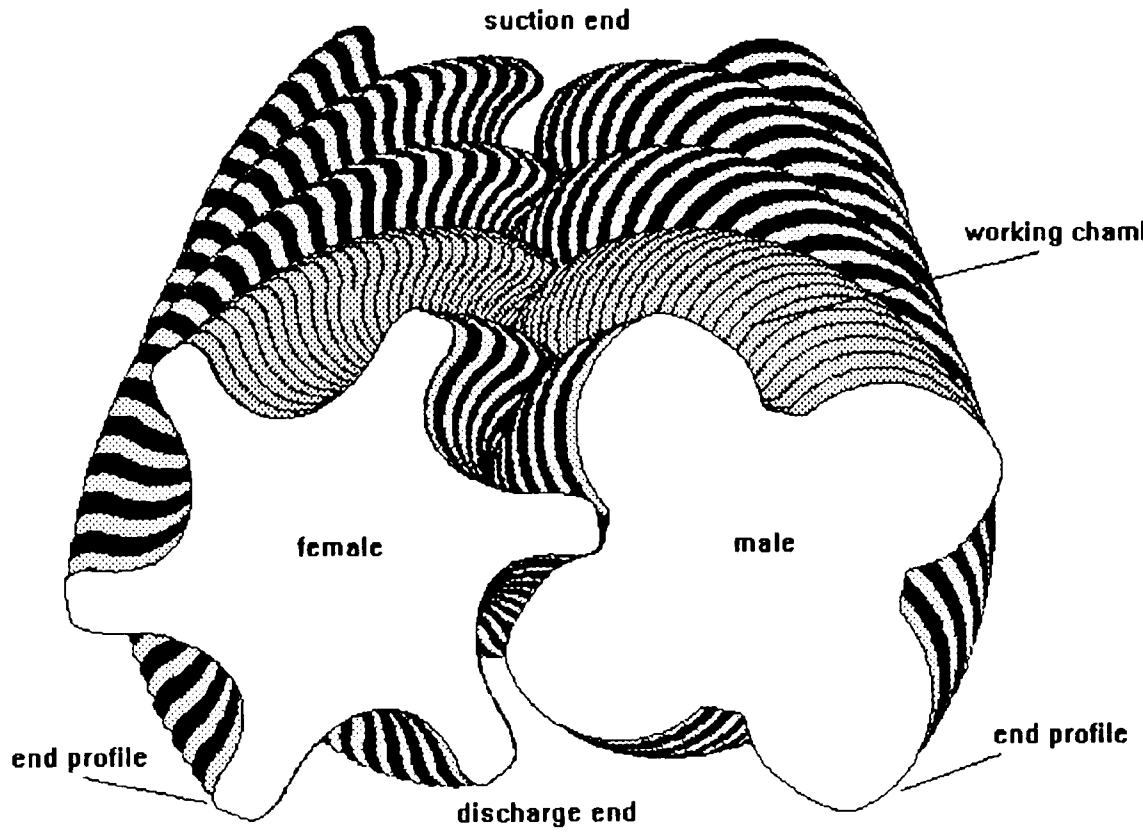

Fig 1.1 Typical rotor pair of twin screw compressors

Compression Principle

The screw compression principle involves a highly skewed three-dimensional mechanism having a series of adjacent spaces which are confined by the

meshed crests and roots of the rotors and the compression chamber walls. Fig. 1.2 depicts this mechanism as a series of two-dimensional S-shaped projections moving diagonally from left to right on a plane along the periphery of the female rotor. To understand this analogy, it is essential to assume that the casing seals the gas/vapour paths all around, even though the meshing of the rotors plays a large part in this respect. On this simplified basis, the screw compression principle's sequence can be described as follows:

• As the screws unmesh, a cavity is created and its size (A) increases until its maximum size (B) is exposed to suction. During this interval, suction gas/vapour is drawn continuously into the expanding cavity. One pair of male and female rotor inter-lobe cavities forms a working chamber, as shown in Fig. 1.1.

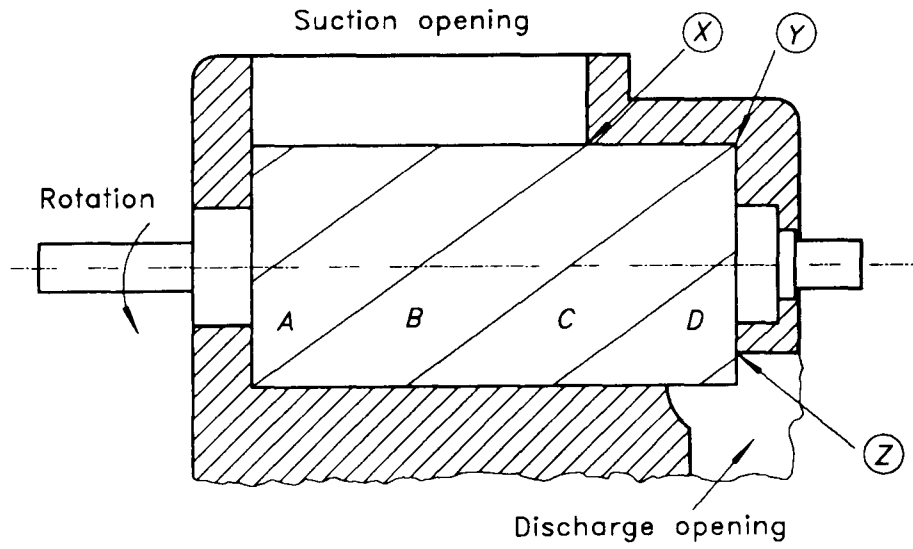

Fig. 1.2 Screw compressor principle

• When the crest between cavities *A* and *B* reaches point *X*, the volume of cavity *B* is cut off from both the suction and the discharge openings of the compression chamber. This volume represents the ideal maximum suction volume generally called the "Theoretical Displacement".

• When the crest between cavities *B* and *C* passes point Y, the volume of the cavity *B* begins to decrease and continues to decrease until this crest

reaches point *Z* which sets the minimum compression volume *D*. During this interval, the pressure of the gas/vapour is increased due to the decrease in volume from *B* to *D*.

- When the leading crest of cavity *D* passes point *Z*, the cavity opens to the compressor discharge and the gas/vapour is expelled due to the continuing rotation of the rotors. The cavities discharge at a frequency equal to the male rotor speed multiplied by the number of lobes (threads) on the male rotor. In the discharge line, flow is continuous but with a pressure pulsation at this frequency.

1.4 Thesis Preview

The written work presented here though presented in eight chapters is seen as consisting of four parts.

The first part is this introductory chapter which delineates the history and present importance of helical twin screw compressors and outlines the objectives of the project.

The second part consists of three chapters which contribute to the development of the several computer programs. Rotor profile generation is the most fundamental work for the study of twin screw compressors and therefore the analytical method and corresponding program development is given in Chapter 2, with SRM A- and SRM D-profiles as numerical examples. Seal line length, blow hole area and cavity volume, etc. are the most important geometrical characteristics of the twin screws and are determined in Chapter 3. Compression gas induced rotor torques, bearing forces and rotor deflection are discussed in Chapter 4, taking rotor contact and the tilting effect of axial forces into account.

The third part of the written presentation also has three chapters, dealing with several aspects of the twin screw compressor and system designs. The

influence of various rotor tip designs and rotor geometrical parameter combinations on compressor efficiency, rotor torques, rotor deflection and viscous friction loss are examined in Chapter 5. Chapter 6 demonstrates how the work developed here is used for the design of certain components of refrigeration twin screw compressors, in particular the slide valve and its optimisation. Refrigeration system development is dealt with by demonstrating the criteria for the removal of the non-return valve from the system. An analysis of the axial-torsional vibration of twin screw compressor systems is presented in Chapter 7, together with a Fourier analysis of the calculated gas torques and bearing forces.

In the last part, Chapter 8, conclusions are drawn and suggestions for further research are made.

Chapter 2

Rotor Profile Generation

2.1 Introduction

The objective of this chapter is to develop a computer program for the generation of rotor profiles of helical twin screw compressors.

The end profile shapes of a twin screw compressor's rotors have a great effect on the compressor's efficiency and reliability. Their importance was clearly demonstrated when the industry switched from symmetric profiles to the current asymmetric profiles about twenty five years ago. The asymmetric profile greatly reduced one primary source of leakage, the blow hole area, resulting in a 5 to 10 percent gain in adiabatic efficiency. Although such large gains in performance with further profile modifications may not be likely, many new profiles claim better performance through shorter rotor-to-rotor seal line, near-zero or zero blow hole area, etc. Profiles also strongly influence the manner in which the rotor torques and bearing forces vary with time, machine capacity, suction and discharge port shapes and sizes and male to female driving characteristics.

Profile generation in the past was a laborious task, the work having to be performed graphically. This situation as evidenced by the published literature

did not change until a computerized method was introduced by Rinder in 1979 (Rinder, 1979). Since then, many researchers/manufacturers have reported similar approaches for the generation of twin-screw rotor profiles (e.g. Singh and Onuschak, 1984; Stošić, et al, 1988; Xing, et al, 1992). Descriptions of the methods used and the programs developed can be found in these and other publications.

In this chapter, a computer program for rotor profile generation is presented. The underlying mathematical method is described in detail. The development of the program is based on the analysis of the very successful SRM A and D profiles, which are also taken as numerical examples for demonstrating the capability of the developed program.

2.2 Method

Profile generation consists in essence of determining, for a given curve on one rotor, the conjugate curve, for this forms the necessary shape of the other rotor. In this study, the analytical envelope method has been adopted for rotor profile generation (Deng and Shu, 1988).

Principle

The analytical envelope method may be understood by considering Fig. 2.1, in which a curve *2* is known on the female rotor (rotor 2) and its conjugate curve *1* on the male rotor (rotor 1) is to be determined. When two conjugated curves are in contact, the two pitch circles of the rotors rotate like a pair of purely rolling friction wheels with circular speeds of ω_1 and ω_2. If a circular speed of $-\omega_1$ is supposedly applied to both of the rotors, the relative movement relationship between the two rotors remains unchanged. While the male rotor of speed of ω_1 becomes static, the female rotor performs two movements: one is that the centre of the female rotor O_2 rotates around the

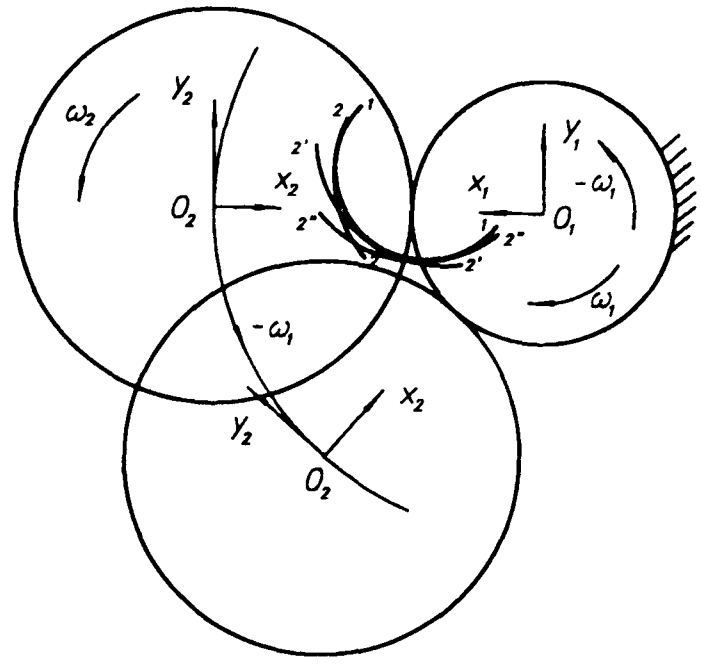

Fig. 2.1 Envelope method

centre of the male rotor O_1 with a circular speed of ω_1, the other is that the female rotor rotates around the centre of itself with a circular speed of ω_2. When the female rotor executes such a combined movement, the tracks of the known curve *2* constitute a set of curves on the static plane (e.g. *2'*, *2"* in Fig. 2.1). Since the curve *1* on the male rotor is conjugate with the curve *2*, at any moment, the curve *1* will have a common tangent with one of the curves in this curve set *2* at the contact point. Obviously, only the envelope of the curve set *2* meets this condition. Therefore, the envelope of the curve set *2* is the curve *1* being sought on the male rotor, which is in conjugation with the known curve *2* on the female rotor. Expressing the above relationship mathematically describes the analytical envelope method.

Coordinate Systems and Transfer Equations

The coordinate systems used throughout this study are shown in Fig. 2.2. Each rotor has a motionless Cartesian coordinate system (*X,Y,Z*) and a rotating one (*x,y,z*), with *Z*-axes and *z*-axes coinciding with the axes of the rotors.

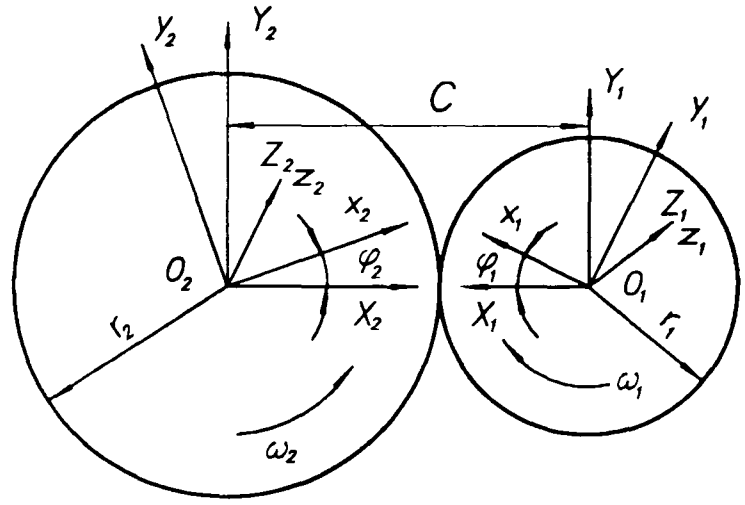

Fig. 2.2 Coordinate systems

The following relationships between the two rotating coordinate systems exist:

$$\begin{aligned} x_1 &= -x_2 \cdot \cos(k \cdot \varphi_1) + y_2 \cdot \sin(k \cdot \varphi_1) + C \cdot \cos(\varphi_1) \\ y_1 &= x_2 \cdot \sin(k \cdot \varphi_1) + y_2 \cdot \cos(k \cdot \varphi_1) - C \cdot \sin(\varphi_1) \end{aligned} \tag{2.1}$$

and

$$\begin{aligned} x_2 &= -x_1 \cdot \cos(k \cdot \varphi_1) + y_1 \cdot \sin(k \cdot \varphi_1) + C \cdot \cos(i \cdot \varphi_1) \\ y_2 &= x_1 \cdot \sin(k \cdot \varphi_1) + y_1 \cdot \cos(k \cdot \varphi_1) - C \cdot \sin(i \cdot \varphi_1) \end{aligned} \tag{2.2}$$

where k - Coefficient, $k = 1 + i = 1 + \omega_2 / \omega_1$;

φ_1 - Angle between the rotating and the fixed coordinate systems of the male rotor.

Equations (2.1) and (2.2) correspond to coordinate transfer from female rotor to male rotor and from male rotor to female rotor, respectively.

Analytical Envelope Method

Assume that a profile curve on one rotor, e.g., on the female rotor, is known, like the curve *2* in Fig. 2.1. It may be expressed as

$$\begin{aligned} x_2 &= x_2(t) \\ y_2 &= y_2(t) \end{aligned} \tag{2.3}$$

where t is the parameter of the curve. According to the above described envelope principle, the conjugate curve *1* on the male rotor can thus be determined as follows:

(a) Seek the equation for the curve set *2*, produced by the curve *2* when rotating relative to the "fixed" male rotor. This equation can be obtained by using the coordinate transfer equation (2.1) which takes the form of

$$\begin{aligned} x_1 &= x_1(t, \varphi_1) \\ y_1 &= y_1(t, \varphi_1) \end{aligned} \tag{2.4}$$

The two parameters in the above equation have different meanings. t is the parameter of the curve *2*, usually called the curve parameter; while φ_1 stands for the position of a curve in the curve set, generally called position parameter.

(b) Seek the envelope condition for the curve set *2*. According to the concept of envelope, at least one point of any curve in the curve set must be on the envelope. The envelope condition defines which point on the curve *2* is on the envelope when the rotor is in a particular position, i.e. providing a relationship between the parameters t and φ_1.

Suppose that the envelope condition may be expressed as $\varphi_1 = \varphi_1(t)$, the equation of the envelope then takes the form of

$$\begin{aligned} x_1 &= x_1(t, \varphi_1(t)) \\ y_1 &= y_1(t, \varphi_1(t)) \end{aligned} \tag{2.5}$$

The slope of any point $N(x_1, y_1)$ on the envelope is obtained by differentiating the above equation:

$$\frac{dy_1}{dx_1} = \frac{\left(\dfrac{\partial y_1}{\partial t} + \dfrac{\partial y_1}{\partial \varphi_1}\dfrac{\partial \varphi_1}{\partial t}\right)dt}{\left(\dfrac{\partial x_1}{\partial t} + \dfrac{\partial x_1}{\partial \varphi_1}\dfrac{\partial \varphi_1}{\partial t}\right)dt} \tag{2.6}$$

While the slope of the curve in the curve set that is in contact with the envelope at point $N(x_1, y_1)$ is (Note, for a particular curve in the curve set, φ_1 is constant).

$$\frac{dy_1}{dx_1} = \frac{\left(\frac{\partial y_1}{\partial t}\right)}{\left(\frac{\partial x_1}{\partial t}\right)} \tag{2.7}$$

Obviously, the tangent at the contacting point $N(x_1, y_1)$ is common for both the envelope and the curve. Thus, the RHS of the Eq. (2.6) equals the RHS of the Eq. (2.7), resulting in

$$\frac{\partial x_1}{\partial t}\frac{\partial y_1}{\partial \varphi_1} - \frac{\partial x_1}{\partial \varphi_1}\frac{\partial y_1}{\partial t} = 0 \tag{2.8}$$

Eq. (2.8) is the implicit expression of the envelope condition $\varphi_1 = \varphi_1(t)$, which correlates the curve parameter t with the position parameter φ_1. In other words, the position of contact points has been defined, i.e. the point on the curve with parameter t will be in contact at the angle φ_1.

(c) Seek the equation of the conjugate curve on the male rotor. According to the envelope principle, the envelope is the required conjugate curve. Thus the equation of the conjugate curve takes the form of Eq. (2.5), or in a implicit form:

$$\begin{cases} x_1 = x_1(t, \varphi_1) \\ y_1 = y_1(t, \varphi_1) \\ \dfrac{\partial x_1}{\partial t}\dfrac{\partial y_1}{\partial \varphi_1} - \dfrac{\partial x_1}{\partial \varphi_1}\dfrac{\partial y_1}{\partial t} = 0 \end{cases} \tag{2.9}$$

Similarly, for a given curve on the male rotor

$$\begin{aligned} x_1 &= x_1(t) \\ y_1 &= y_1(t) \end{aligned} \tag{2.10}$$

the equation for the conjugate curve on the female rotor takes the form of

$$\begin{cases} x_2 = x_2(t, \varphi_1) \\ y_2 = y_2(t, \varphi_1) \\ \dfrac{\partial x_2}{\partial t}\dfrac{\partial y_2}{\partial \varphi_1} - \dfrac{\partial x_2}{\partial \varphi_1}\dfrac{\partial y_2}{\partial t} = 0 \end{cases} \tag{2.11}$$

2.3 The Commonly Used Profile Curve Types

As discussed in Chapter 1, many profiles have been proposed but only a very limited number of them have been in practical use. In order to develop a generalized computer program for twin screw rotor profile generation, it is of interest to evaluate existing rotor profiles first. For this purpose, the very successful SRM A and D profiles have been chosen as representatives in this study.

SRM-A Profile

SRM-A profile was invented by L.B. Schibbye in 1966 and can be designed either for oil-free or oil-flooded compressors (Schibbye, 1966). The profile for the latter is a modification of that for the former and includes more curve types and, therefore, has been taken as an example here, as shown in Fig. 2.3.

As can be seen, the female rotor is provided with six helical grooves, while the male rotor with four helical lands. The two rotors are designed to connect to each other through direct flank contact without any synchronizing gears. The force is transmitted from the male rotor to the female rotor through the upper flank A - K with reference to the rotating direction in Fig. 2.3.

The profile sketch on the female rotor is made up of many segments and is constructed in the following way (N.B., for simplicity, all descriptions hereafter are with reference to the shown "zero-position" in Fig. 2.3 in which the line connecting two rotor centres goes through the innermost point of the bottom

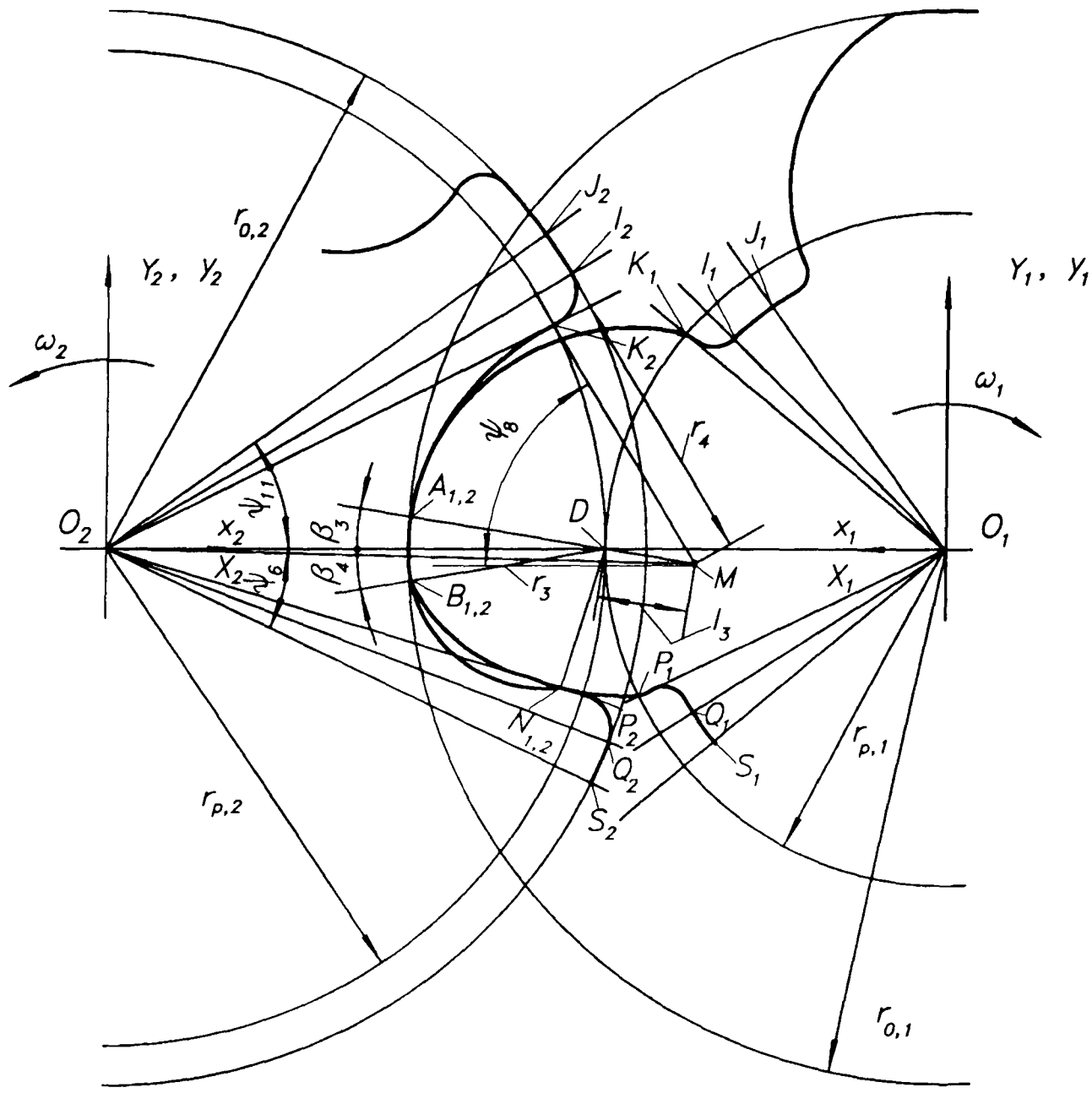

Fig. 2.3 SRM A-profile

portion $A_2 B_2$ of the female rotor profile):

(1) The minor bottom segment $A_2 B_2$ extending between the two given angles β_3 and β_4 is shaped as a circular arc of radius r_3 having its centre at the intersecting point D of the pitch circles.

(2) The segment $A_2 K_2$ is similarly a circular arc extending from the point A_2 where it has a tangent common to that of the segment $A_2 B_2$ to the point K_2 on the pitch circle of the female rotor. Its centre point M must, therefore, be located on the connecting line $A_2 D$ and the distance l_3 determines that

the two radius vectors $K_2 M$ and $K_2 O_2$ should form a right angle.

(3) The segment $B_2 N_2$ is a general epicycloid curve generated by the point B_1 on the male rotor. The end point N_2 is to be determined according to such a condition that two connecting lines $N_2 O_2$ and $N_2 D$ should form a right angle.

(4) The segment $N_2 P_2$ is a straight line which goes through the centre point O_2 of the female rotor and ends on the pitch circle of the female rotor.

(5) Both the segments $K_2 I_2$ and $P_2 Q_2$ are circular arcs with their centres on the pitch circle of the female rotor for smooth connection of the adjacent two segments.

(6) Similarly, both the segments $I_2 J_2$ and $Q_2 S_2$ are circular arcs with their centres coinciding with the centre of the female rotor O_2 and with the same diameter as the outside diameter of the female rotor.

The profile segments on the male rotor can then be generated by the corresponding segments on the female rotor according to the mesh condition.

(a) The segment $A_1 B_1$ is a circular arc and coincides with its generating curve $A_2 B_2$ in the " zero position " shown in Fig. 2.3.

(b) The segment $A_1 K_1$ is the envelope of the curve set generated by the circular arc $A_2 K_2$ when the female rotor relatively rotates around the male rotor.

(c) The segment $B_1 N_1$ is a point-generated epicycloid curve by the point N_2 on the female rotor.

(d) The segment $N_1 P_1$ is similarly generated by the straight line $N_2 P_2$ on the female rotor.

(e) Both the segments $K_1 I_1$ and $P_1 Q_1$ are the same circular arcs as their generating curves $K_2 I_2$ and $P_2 Q_2$, respectively.

(f) Finally, both the segments $I_1 J_1$ and $Q_1 S_1$ are circular arcs and are generated by the circular arcs $I_2 J_2$ and $Q_2 S_2$ on the female rotor, respectively.

SRM D Profile

SRM D-profile was invented by Ake Astberg, an engineer working for SRM in the early 1980s (Astberg, 1984). It is shown in Fig. 2.4. Compared with SRM A-profile, the geometrical relationship between the segments of the D profile is much more sophisticated as explained below. It is in fact intended to be a design technique for producing a range of profiles, rather than one profile.

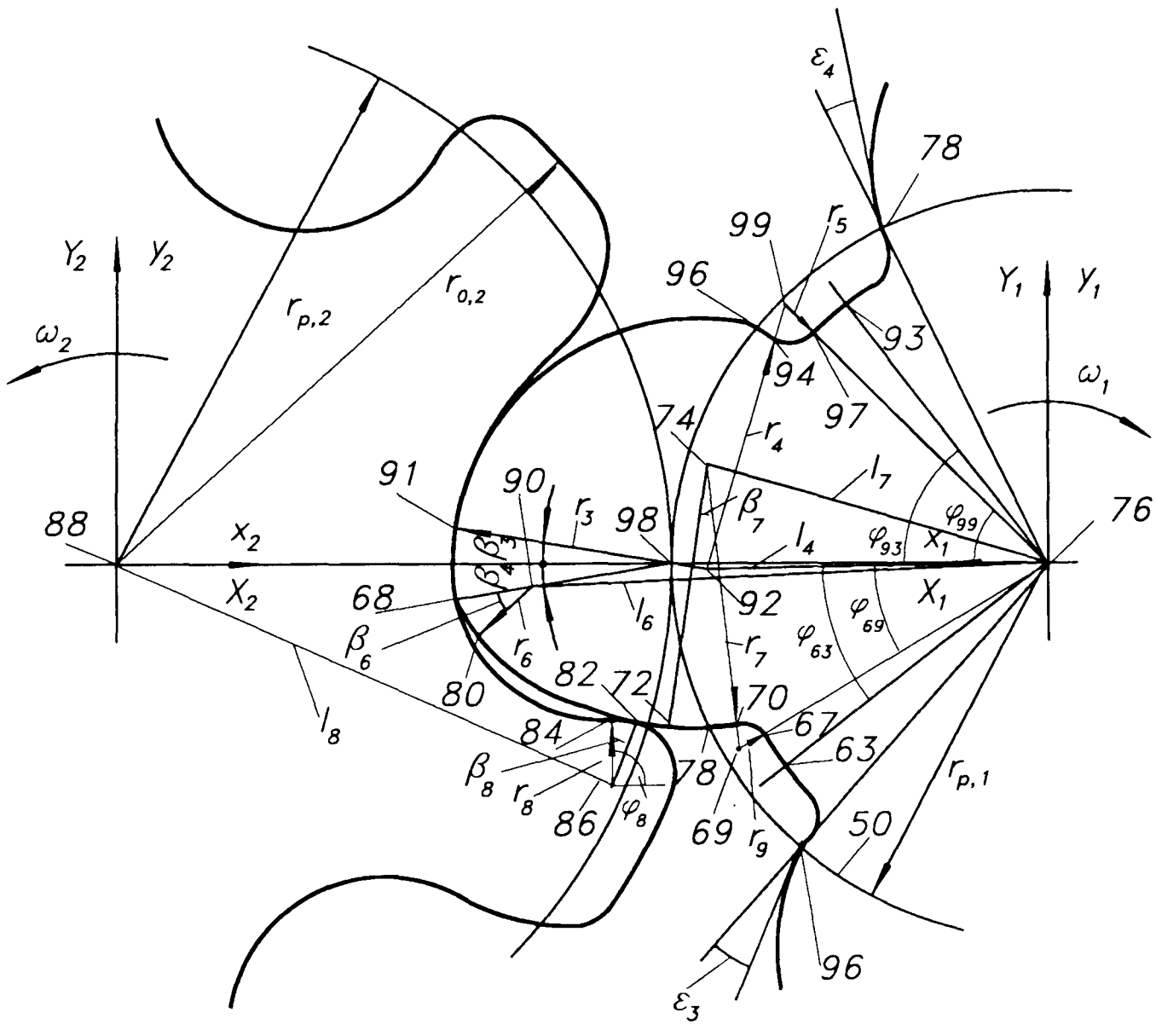

Fig. 2.4 SRM D-profile

First, the profile segment *70-72* of the male rotor follows a circular arc having a radius r_7 and its centre *74* disposed on a distance l_7 from the centre *76* of the male rotor. The start point *70* is located inside the pitch circle *50*, with a radial distance from the centre *76* of the male rotor of about 95 % of the pitch radius $r_{p,1}$ of the rotor. The end point *72* is disposed outside the pitch circle *50*, having a radial distance from the rotor centre *76* of about 110 % of the pitch radius $r_{p,1}$. The portion *70-72* intersects with the pitch circle *50* at a point *78* and has at this point a tangent which forms an angle ε_4 with a radial line *76-78*. The angle ε_4 is about 20°. The length of the radius r_7 is about 1.6 times the product of the pitch radius $r_{p,1}$ and $sin(\varepsilon_4)$. The distance l_7 is somewhat larger than the product of the pitch radius $r_{p,1}$ and $cos(\varepsilon_4)$.

Second, the segment *72-80* of the male rotor follows a generally epitrochoidal curve, generated by a section *82-84* of the female rotor. At the start point *72,* it has a tangent common with that of the segment *70-72*. The end point *80* of the segment is disposed close to the crest portion of the male rotor. The segment *82-84* follows a circular arc having a radius r_8 and its centre *86* disposed on a distance l_8 from the centre *88* of the female rotor. The length of the radius r_8 is about 5% of the distance between the centres *76, 88* of the rotors. The distance l_8 is about equal to the product of the pitch radius $r_{p,2}$ of the female rotor and $\sqrt{\cos(\varepsilon_4)}$.

Third, the segment *80-68* of the male rotor follows a circular arc having a radius r_6 and its centre *90* disposed on a distance l_6 from the centre *76* of the male rotor. Similarly, at the start point *80* it has a tangent common with that of the segment *72-80*. The length of the radius r_6 is about 5% of the distance between the centres *76, 88* of the rotors. The distance l_6 is about equal to the difference between the outer radius of the male rotor $r_{0,1}$ and the radius r_6.

Fourth, the crest segment of the male rotor *68-91* is the same as that of the SRM A-profile, which follows a circular arc having a radius r_3 and its centre *98* is disposed on the intersecting point of the pitch circles with reference to the shown "zero position" in Fig. 2.4. It extends from angle β_4 to angle β_3 and has a tangent common with that of its adjacent segments in the two end points *68* and *91*, respectively.

Fifth, the segment *91-94* of the male rotor follows a circular arc having a radius r_4 and its centre *92* disposed on a distance l_4 from the centre *76* of the male rotor. Its start point *94* is located inside the pitch radius *50*, having a distance from the centre *76* of the rotor of about 95% of the pitch radius $r_{p,1}$. The flank intersects with the pitch circle *50* at a point *96* and has at this point a tangent which forms an angle ε_3 with a radial line *76-96*. The angle ε_3 is about 30°. The length of the radius r_4 is about 1.4 times the product of the pitch radius $r_{p,1}$ and $\sin(\varepsilon_3)$. The distance l_4 is somewhat larger than the product of the pitch radius $r_{p,1}$ and $\cos(\varepsilon_3)$.

Sixth, the segments *67-70* and *94-97* follow a circular arc and have a tangent common with that of the adjacent segments at the two end points, respectively.

Finally, the segments *63-67* and *93-97* of the male rotor are the same as those of the SRM A-profile.

Implications

From the definition of the SRM A and D profiles the following implications may be obtained.

- These profiles are composed of nine segments. The "original" segments, i.e. "known" segments, are of three curve types only. While the A-profile includes a circular arc, a point and a straight line, the D-profile consists of only circular arcs.

• The rotor profiles have a very complicated geometry, especially the modern profile of SRM D. Before being able to generate the conjugate curves, the exact geometry (e.g. the start and end points and the radius and centre position of a circular arc) of the "known" segments of the profiles must be determined first.

These implications must be clearly understood if a computer program for the generation of rotor profiles is to be successfully developed.

2.4 Development of the Computer Program

2.4.1 General Considerations

In order to develop a computer program for the generation of rotor profiles, following have been taken into consideration:

- According to the implications of the previous section, the commonly adopted "known" profile segments are circular arcs, points and straight lines. It is thus essential that the program can generate conjugate curves of these three curve types at this stage.

- Since different profiles have different definitions, it is essential that the program has a standard input file. For the existing SRM A and D profiles each may have a sub-program to calculate the geometry of its segments. Other profiles consisting of curve types of circular arc, point and straight line may also use the program to generate rotor profiles as far as their segments' geometry are given in a file of the format of the standard input file.

- The program should have a standard output file to facilitate the further use of the profile data, e.g. for calculating the geometrical characteristics of the rotor profile and also of compressor geometry; i.e. for a range of length / diameter ratios, wrap angles, port geometries, etc. Also it should facilitate

the examination of the generated profile by displaying the profiles on the screen. Hard copies of the generated profile may be obtained either by making use of screen-saver while viewing on the screen, or of commercial software taking the generated data as the input file.

- Finally, the program should be as user friendly as possible, e.g. in a menu driven way that is convenient to the user.

2.4.2 Envelope Conditions of Three Typical Profile Segments

This section discusses the envelope conditions of three typical profile segments, i.e. circular arc, point and straight line. These segment curves are either on the male or female rotor and, to give the designer a variety choices, may occur in a range of positions. As shown in Eqs. (2.9) and (2.11), the conjugate curves of the known curves can be determined if the envelope condition is known.

In addition, for a smooth connection between the segments of a profile, the first differentials of the curves are required to be equal at the connecting points. Accordingly, the expressions of the first derivative are also derived.

Circular Arc

For a given circular arc on the female rotor, as shown in Fig. 2.5, the equation of the arc can be expressed as

$$\begin{aligned} x_2 &= x_{2c} + r\cdot\cos(t) \\ y_2 &= y_{2c} + r\cdot\sin(t) \end{aligned} \qquad t_s \le t \le t_e \qquad (2.12)$$

where x_{2c}, y_{2c} are the coordinates of the arc centre, r is the radius of the arc, and t is the parameter which calculates from the positive X-axis in the direction of the positive Y-axis and extends from 0 to 2π.

By using Eqs. (2.1) and (2.8), the envelope condition becomes

$$x_{2c}\cdot\sin(t) - y_{2c}\cdot\cos(t) - r_{p,2}\cdot\sin(t+i\cdot\varphi_1) = 0 \tag{2.13}$$

where $r_{p,2}$ is the radius of the pitch circle of the female rotor, i stands for the transmission ratio, $i = \omega_2/\omega_1$.

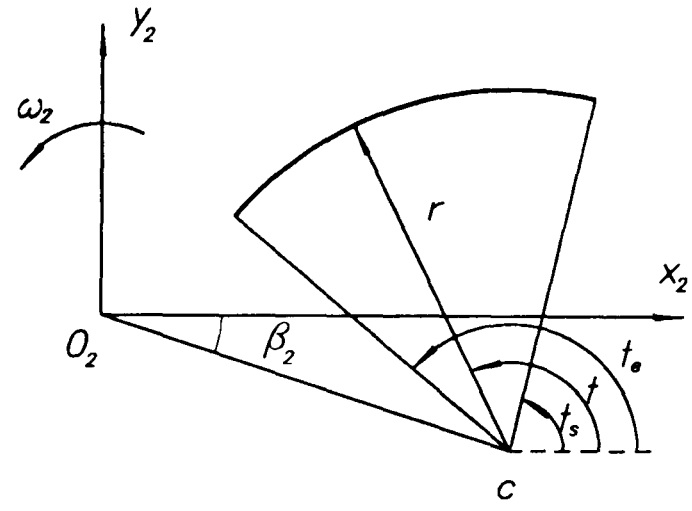

Fig. 2.5 Circular arc on female rotor

The first derivative can be written as

$$\frac{dy_2}{dx_2} = -\frac{1}{\tan(t)} \tag{2.14}$$

and for its generated curve, i.e., an epicycloid type curve, the first derivative takes the form of

$$\frac{dy_1}{dx_1} = \frac{dy_1/dt}{dx_1/dt} \tag{2.15}$$

where

$$dy_1/dt = r\cdot\cos(t+k\cdot\varphi_1) + \left[k\cdot x_{2c}\cdot\cos(k\cdot\varphi_1) - k\cdot y_{2c}\cdot\sin(k\cdot\varphi_1) + k\cdot r\cdot\cos(t+k\cdot\varphi_1) - C\cdot\cos(\varphi_1)\right]\cdot(d\varphi_1/dt)$$

$$dx_1/dt = r\cdot\sin(t+k\cdot\varphi_1) + \left[k\cdot x_{2c}\cdot\sin(k\cdot\varphi_1) + k\cdot y_{2c}\cdot\cos(k\cdot\varphi_1) + k\cdot r\cdot\sin(t+k\cdot\varphi_1) - C\cdot\sin(\varphi_1)\right]\cdot(d\varphi_1/dt)$$

$$d\varphi_1/dt = \frac{\left[\dfrac{x_{2c}\cdot\cos(t) + y_{2c}\sin(t)}{r_{p,2}\cdot\cos(t+i\cdot\varphi_1)} - 1\right]}{i}$$

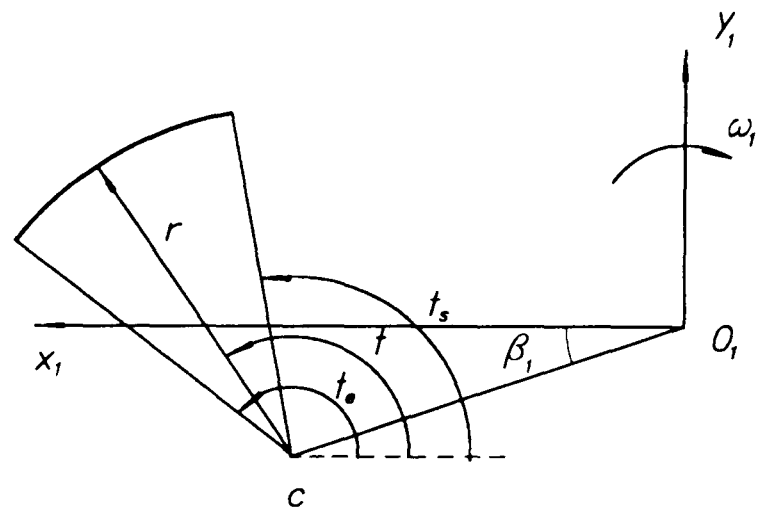

Fig. 2.6 Circular arc on male rotor

Similarly, for a given arc on the male rotor as shown in Fig. 2.6,

$$\begin{aligned} x_1 &= x_{1c} - r\cdot\cos(t) \\ y_1 &= y_{1c} + r\cdot\sin(t) \end{aligned} \qquad t_s \le t \le t_e \tag{2.16}$$

where x_{1c}, y_{1c} and r have the same meanings as those used in Eq. (2.12), while t is defined as shown in Fig. 2.6.

The corresponding results can be derived with the envelope condition of the form of

$$x_{1c}\cdot\sin(t) - y_{1c}\cdot\cos(t) - r_{p,1}\cdot\sin(t-\varphi_1) = 0 \tag{2.17}$$

where $r_{p,1}$ is the radius of the pitch circle of the male rotor, and the first derivative of the original arc is

$$\frac{dy_1}{dx_1} = \frac{1}{\tan(t)} \tag{2.18}$$

and the first derivative of the generated curve is

$$\frac{dy_2}{dx_2} = \frac{dy_2/dt}{dx_2/dt} \tag{2.19}$$

where

$$\begin{aligned} dy_2/dt = {} & r\cdot\cos(t-k\cdot\varphi_1) + \left[k\cdot x_{1c}\cdot\cos(k\cdot\varphi_1) - k\cdot y_{1c}\cdot\sin(k\cdot\varphi_1)\right. \\ & \left. -k\cdot r\cdot\cos(t-k\cdot\varphi_1) - C\cdot i\cdot\cos(i\cdot\varphi_1)\right]\cdot(d\varphi_1/dt) \end{aligned}$$

$$dx_2/dt = -r\cdot\sin(t-k\cdot\varphi_1) + \left[k\cdot x_{1c}\cdot\sin(k\cdot\varphi_1) + k\cdot y_{1c}\cdot\cos(k\cdot\varphi_1) + k\cdot r\cdot\sin(t-k\cdot\varphi_1) - C\cdot i\cdot\sin(i\cdot\varphi_1)\right]\cdot(d\varphi_1/dt)$$

$$d\varphi_1/dt = 1 - \frac{x_{1c}\cdot\cos(t) - y_{1c}\sin(t)}{r_{p,1}\cdot\cos(t-\varphi_1)}$$

Point

For a given point on the female rotor, i.e. $x_2 = x_{2j}$, $y_2 = y_{2j}$, the envelope condition (2.8) is always satisfied. Its first derivative takes the form of

$$\frac{dy_1}{dx_1} = \frac{k\cdot x_{2j}\cdot\cos(k\cdot\varphi_1) - k\cdot y_{2j}\cdot\sin(k\cdot\varphi_1) - C\cdot\cos(\varphi_1)}{k\cdot x_{2j}\cdot\sin(k\cdot\varphi_1) + k\cdot y_{2j}\cdot\cos(k\cdot\varphi_1) - C\cdot\sin(\varphi_1)} \tag{2.20}$$

Similarly, for a point on the male rotor, i.e. $x_1 = x_{1j}$, $y_1 = y_{1j}$, the corresponding result is

$$\frac{dy_2}{dx_2} = \frac{k\cdot x_{1j}\cdot\cos(k\cdot\varphi_1) - k\cdot y_{1j}\cdot\sin(k\cdot\varphi_1) - C\cdot i\cdot\cos(i\cdot\varphi_1)}{k\cdot x_{1j}\cdot\sin(k\cdot\varphi_1) + k\cdot y_{1j}\cdot\cos(k\cdot\varphi_1) - C\cdot i\cdot\sin(i\cdot\varphi_1)} \tag{2.21}$$

Straight Line

A given straight line on the female rotor can be expressed as follows (see Fig. 2.7):

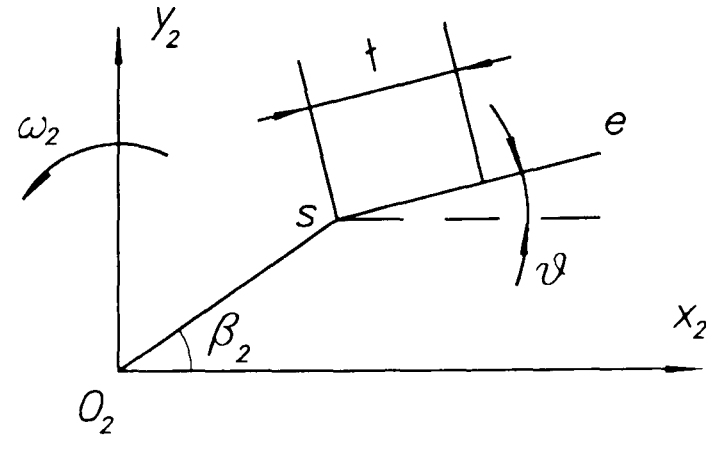

Fig. 2.7 Line on female rotor

$$\begin{aligned} x_2 &= x_{2c} + t\cdot\cos(\vartheta) \\ y_2 &= y_{2c} + t\cdot\sin(\vartheta) \end{aligned} \qquad t_s \le t \le t_e \tag{2.22}$$

where ϑ is the angle measured from the positive x-axis in the direction of the positive y-axis.

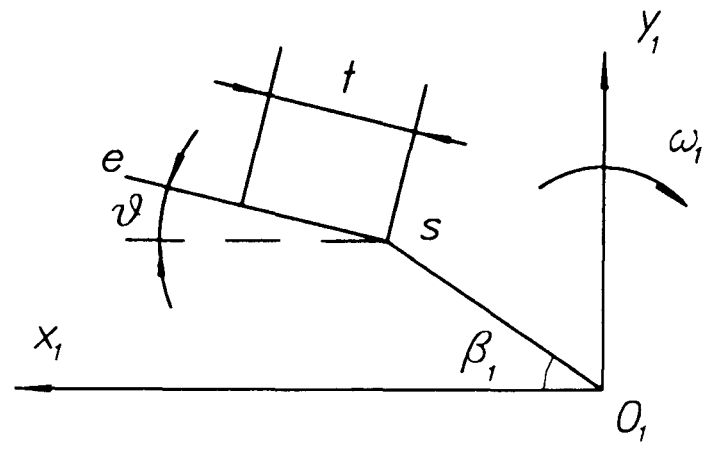

Fig. 2.8 Line on male rotor

By using Eqs. (2-1) and (2.8), the envelope condition becomes

$$x_{2c}\cdot\cos(\vartheta) + y_{2c}\cdot\sin(\vartheta) - r_{p,2}\cdot\cos(\vartheta + i\cdot\varphi_1) + t = 0 \tag{2.23}$$

and the first derivative of the generated curve takes the form of

$$\frac{dy_1}{dx_1} = \frac{dy_1/dt}{dx_1/dt} = \frac{\partial y_1/\partial t + (\partial y_1/\partial\varphi_1)\cdot(d\varphi_1/dt)}{\partial x_1/\partial t + (\partial x_1/\partial\varphi_1)\cdot(d\varphi_1/dt)} \tag{2.24}$$

where

$$\frac{\partial x_1}{\partial t} = -\cos(\vartheta + k\cdot\varphi_1)$$

$$\frac{\partial y_1}{\partial t} = \sin(\vartheta + k\cdot\varphi_1)$$

$$\frac{\partial x_1}{\partial\varphi_1} = k\cdot x_{2c}\cdot\sin(k\cdot\varphi_1) + k\cdot y_{2c}\cdot\cos(k\cdot\varphi_1) + k\cdot t\cdot\sin(\vartheta + k\cdot\varphi_1) - C\cdot\sin(\varphi_1)$$

$$\frac{\partial y_1}{\partial\varphi_1} = k\cdot x_{2c}\cdot\cos(k\cdot\varphi_1) - k\cdot y_{2c}\cdot\sin(k\cdot\varphi_1) + k\cdot t\cdot\cos(\vartheta + k\cdot\varphi_1) - C\cdot\cos(\varphi_1)$$

$$\frac{d\varphi_1}{dt} = -\frac{1}{r_{p2}\cdot i\cdot\sin(\vartheta + i\cdot\varphi_1)}$$

Similarly, for a given straight line on the male rotor, as shown in Fig. 2.8, the equation has the form of

$$\begin{aligned} x_1 &= x_{1c} + t\cdot\cos(\vartheta) \\ y_1 &= y_{1c} + t\cdot\sin(\vartheta) \end{aligned} \qquad t_s \le t \le t_e \tag{2.25}$$

Since the above equation has the same form as Eq. (2.22), it can be predicted that all the results are also of similar form as listed below:

The envelope condition:

$$x_{1c}\cdot\cos(\vartheta) + y_{1c}\cdot\sin(\vartheta) - r_{p,1}\cdot\cos(\vartheta+\varphi_1) + t = 0 \tag{2.26}$$

and the first derivative of the generated curve:

$$\frac{dy_2}{dx_2} = \frac{dy_2/dt}{dx_2/dt} = \frac{\partial y_2/\partial t + (\partial y_2/\partial\varphi_1)\cdot(d\varphi_1/dt)}{\partial x_2/\partial t + (\partial x_2/\partial\varphi_1)\cdot(d\varphi_1/dt)} \tag{2.27}$$

where

$$\frac{\partial x_2}{\partial t} = -\cos(\vartheta+k\cdot\varphi_1)$$

$$\frac{\partial y_2}{\partial t} = \sin(\vartheta+k\cdot\varphi_1)$$

$$\frac{\partial x_2}{\partial\varphi_1} = k\cdot x_{1c}\cdot\sin(k\cdot\varphi_1) + k\cdot y_{1c}\cdot\cos(k\cdot\varphi_1) + k\cdot t\cdot\sin(\vartheta+k\cdot\varphi_1) - C\cdot i\cdot\sin(i\cdot\varphi_1)$$

$$\frac{\partial y_2}{\partial\varphi_1} = k\cdot x_{1c}\cdot\cos(k\cdot\varphi_1) - k\cdot y_{1c}\cdot\sin(k\cdot\varphi_1) + k\cdot t\cdot\cos(\vartheta+k\cdot\varphi_1) - C\cdot i\cdot\cos(i\cdot\varphi_1)$$

$$\frac{d\varphi_1}{dt} = -\frac{1}{r_{p1}\cdot\sin(\vartheta+\varphi_1)}$$

2.4.3 Description of the Program

Program Overview

Utilizing the method and expressions derived in the previous sections a computer program for rotor profile generation is developed. The program is written in Turbo-Pascal language and runs on IBM compatible personal

computers. The use of the program is fairly easy because the program is designed in a menu-driven way.

The program starts with a welcome picture (University logo) and then puts out the main menu which looks like:

- Pre-Generation
- Profile Generation
- View Generated Profile
- Save Generated Data
- End

The user can either input profile sketch parameters on-line or read a parameter data file from disk. After that, all the user needs to do is just follow the menu until finally obtaining the desired profile. The generated data is then stored in a data file and is ready for further uses. The generated profile can be viewed on the screen with adjustable scaling. The saved data files can be used for obtaining hard copy by using many commercially available software packages.

Pre-Generation

The purpose of the pre-generation is to prepare a standard input file for the use of the "Generation" subroutine. As mentioned above, a typical profile is made up of many segments, mostly circular arcs, points and straight lines. Before the profile generation can begin, these segments need to be defined adequately. For a circular arc, e.g., centre point coordinates, radius and the start and end angles with respect to a given coordinate system need to be known. This subroutine is designed to acquire all this necessary information either by calculation for the already included profile types or directly input or read for other profile types.

For existing profile types, the program at present includes SRM A and D

profiles. According to the definitions of these profiles, all the segment position parameters can be determined, provided some basic parameters are chosen by the designer. Since these involve many mathematical expressions, the derivatives are given in Appendix 1 of this volume. For these two types of profile, the user can choose a basic parameter data file which includes centre distance of the rotors, outer diameters of the rotors, the number of lobes, etc (the details are given in Appendix 1). These parameters can be viewed on screen, changed at will, and saved for later use. Then, the program will calculate all segment parameters according to the definition of the profile and output a standard data file.

For profiles other than SRM A and D, additional work outside this program is inevitable. This is because each type of profile has its special geometrical relationship between the segments and thus the profile sketch can not be drawn arbitrarily. However, after the determination of profile segment parameters, usually by an individual profile oriented program, the profile segment parameters can either be input on-line or be saved into a disk file and then be read into the program under the option of 'Input a Parameter Data File' or 'Read a Parameter Data File' in the 'Pre-Generation' of the profiles.

Profile Generation and View Generated Profile

This program can virtually generate any profile made up of the following type:

- Circular arc
- Straight line
- Point

That is to say, the segments on any one of the rotors could be of these types, then the program generates the corresponding segments on the other rotor.

After completion, the user can view both the generating and generated segments with adjustable scaling for verification. While viewing, the scale of the picture can be enlarged/reduced by simply pressing *PageUp/PageDown*,

and the position of it can be moved around by pressing *Arrow Keys.* The percentage of the variation for both scaling and moving is, as default, *10%*, but the user can choose *1%, 5% or 25%* at any stage of viewing by pressing the *Insert* key. Repeatedly using these features enables expanding any part of the picture to any magnification.

The program also provides facilities for viewing the generated data and making a hard copy of it for further use as can be seen from the main menu. The user may also load a previously generated profile from the disk and have following options when viewing on the screen:

- Male Rotor Only
- Female Rotor Only
- Meshed Rotors at Any Rotating Position

A instruction for running the program is given in Appendix 2 of this volume.

Numerical Examples

As numerical examples, SRM A- and D profiles are generated by using the program developed here, and are shown in Figs. 2.9 and 2.10. The outer diameter of the rotors is 204 mm and the centre distance is 160 mm.

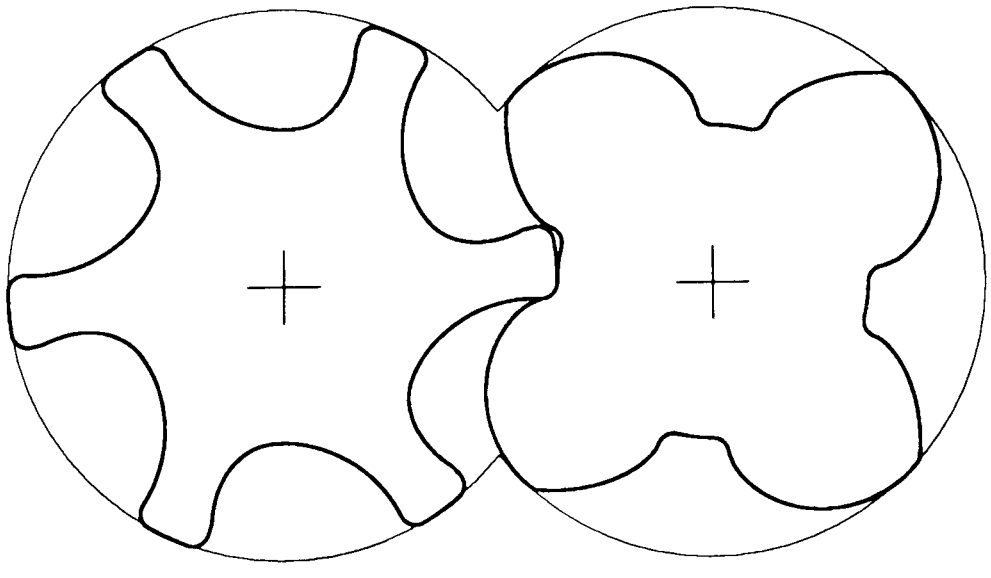

Fig. 2.9 Generated profile (SRM A)

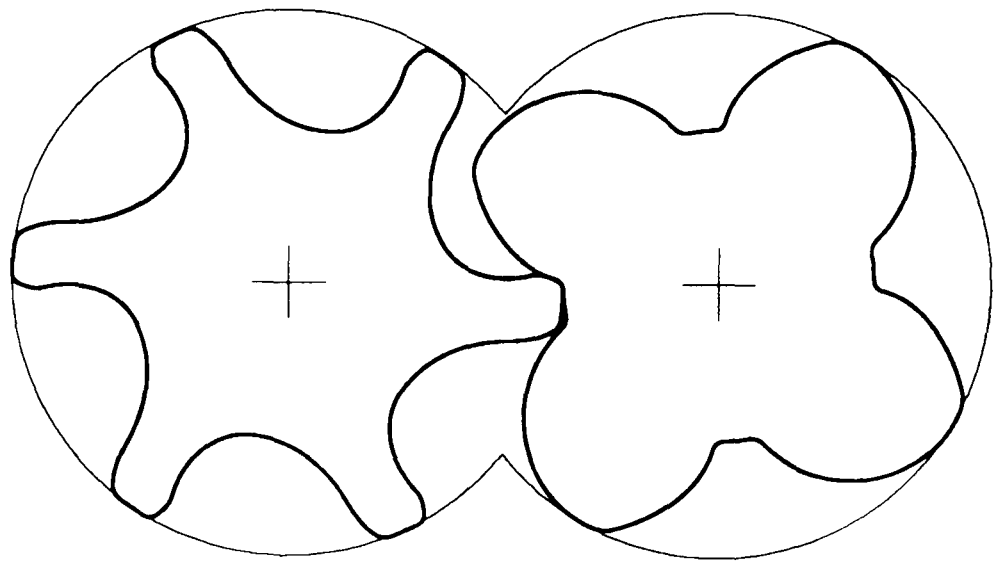

Fig. 2.10 Generated profile (SRM D)

2.5 Conclusions

Utilizing the analytical envelope method, a computer program for the generation of twin screw compressor rotor profiles has been developed. The program has been used successfully for the generation of SRM A- and D-profiles. The program is also applicable to most other existing profiles or any new profile types, if the "known" segments of these profiles are circular arcs or straight lines or points. The program is reasonably user friendly being menu driven. Input parameters can be viewed and changed easily, and any part of generated profiles can be examined in great detail. The output data file of the program can then be used as the input file for rotor geometrical characteristics analysis which is discussed in the next chapter.

Chapter 3

Geometrical Characteristics

3.1 Introduction

Screw compressor performance to a great extent, depends on the geometry of the rotor profile and on various operating clearances. Previous research has quantified the influence of these variables on compressor performance and has shown that the effects are significant (e.g. Singh and Patel, 1984, 1986; Tang and Fleming, 1992). A major share of the performance losses can be attributed to various leakage paths within the compressor (mechanical and viscous losses are the other culprits). Leakage losses are directly proportional to the effective leakage areas.

Screw compressors, due to their complex geometry, have many leakage paths which influence performance in different ways. For example, leakage across the inter-rotor contact line takes place from the cavity in compression directly to the compressor inlet. The result is a substantial power increase and a capacity loss. On the other hand, the blow holes and the rotor tips permit leakage both into and out of the cavity. While such leakage has very little influence on machine capacity, continous recompression of the leaked flow does cause a power loss and an increase in the discharge gas temperature.

When generating a new profile or modifying an old one the influence on the geometrical parameters of the compressor as a unit must be considered carefully. The earlier approach through hand calculation, plotting and planimetry has been replaced by computerized methods, which not only eases the analysis of specific properties but saves much time (e.g. Rinder, 1979; Singh and Onushak, 1984).

This chapter presents methods for the determination of the most important geometrical characteristics of a helical twin screw compressor as functions of the male rotor angle of rotation:

- sealing line length between the rotors
- sealing line length between rotor tip and housing bore
- blow hole area
- inter lobe area
- cavity volume

The first three characteristics relate to the leakage loss which should be minimized, while the remaining two characteristics are parameters indicating the effective use of the rotor geometry and the capacity, and therefore should be maximized in the design of compressors. The computer program developed is also described, the capability of which is demonstrated with SRM A- and D-profiles as numerical examples.

3.2 Sealing Line Length between the Rotors

The sealing line between the rotors is the name used for the line describing the meshing along the rotors (Fig. 3.1). This line forms the boundary between the high pressure and the low pressure side of the compressor. As the rotors rotate, the sealing line moves along the rotor axis, sealing the compression chamber and delivering the compression gas/vapour from the suction side to the discharge side. Since leakage may occur across the sealing line, both the length and continuity of the sealing line are of importantance.

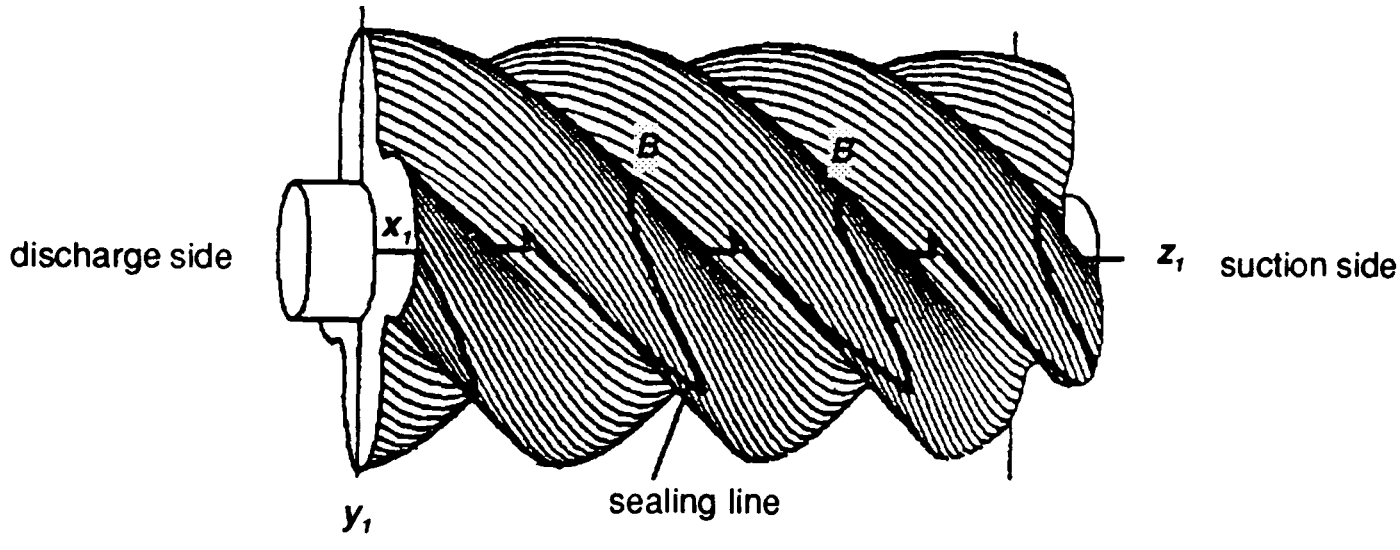

Fig. 3.1 Male rotor with sealing line

3.2.1 Sealing Line Equation

For simplicity, first consider the projection of the sealing line on the end plane, i.e. *x-y* plane with respect to the coordinate systems defined in the previous chapter (see Fig. 2.2).

It should be noted that the sealing line equation is relative to the static coordinate system because sealing line does not rotate with the rotors. According to the envelope condition (Eq. 2.8) a point on the rotor flank, e.g. (x_2, y_2) will be the contact point (i.e. on the sealing line) at the angle φ_1. Therefore, the sealing line equation can be obtained by transferring the contact point from the rotating coordinate system into static coordinate system:

$$\begin{aligned} X_2 &= x_2 \cdot \cos(i \cdot \varphi_1) - y_2 \cdot \sin(i \cdot \varphi_1) \\ Y_2 &= x_2 \cdot \sin(i \cdot \varphi_1) + y_2 \cdot \cos(i \cdot \varphi_1) \end{aligned} \tag{3.1}$$

if expressed in the female rotor coordinate system, or

$$\begin{aligned} X_1 &= x_1 \cdot \cos(\varphi_1) - y_1 \cdot \sin(\varphi_1) \\ Y_1 &= x_1 \cdot \sin(\varphi_1) + y_1 \cdot \cos(\varphi_1) \end{aligned} \tag{3.2}$$

if defined in the male rotor coordinate system. x_1, y_1, x_2, y_2 are rotor flank point coordinates, while φ_1 is the male rotor angle by which the corresponding point is in contact. From the point of view of numerical computation all these are known after the rotor profile is generated by using the profile generation

program as described in Chapter 2.

Then, the *z* value of the point on the sealing line can be calculated according to the following expression:

$$Z_1 = \mp \frac{h_1}{2\pi}(\alpha - \varphi_1) \tag{3.3}$$

where the negative sign on the RHS represents a right-hand screw male rotor and the positive sign represents the left-hand one, respectively. α is the male rotor angle of rotation. In this study the zero position for α occurs when in the discharge side end plane the male rotor tip point lies on the line connecting the centres of the rotors (see Fig. 2.3 in section 2.3).

3.2.2 Sealing Lines of Some Typical Profile Curves

Although the sealing line can easily be obtained numerically as described above, an examination of the sealing lines of some typical profile curves, especially those which are located in some special positions, such as a circular arc with its centre on the pitch circle or a straight line going through the centre of the rotor, may help in understanding the sealing lines of various rotor profiles.

Circular Arc

For a circular arc on the female rotor, as shown in Fig. 2.5 (section 2.4), substituting its coordinates (Eq. 2.12, section 2.4) into the sealing line equation (3.1) leads to

$$\begin{aligned} X_2 &= x_{2c}\cdot\cos(i\cdot\varphi_1) - y_{2c}\cdot\sin(i\cdot\varphi_1) + r\cdot\cos(i\cdot\varphi_1 + t) \\ Y_2 &= x_{2c}\cdot\sin(i\cdot\varphi_1) + y_{2c}\cdot\cos(i\cdot\varphi_1) + r\cdot\sin(i\cdot\varphi_1 + t) \end{aligned} \tag{3.4}$$

If the centre of the arc is on the pitch circle of the female rotor, i.e.

$$\begin{aligned} x_{2c} &= r_{p,2}\cdot\cos(\beta_2) \\ y_{2c} &= r_{p,2}\cdot\sin(\beta_2) \end{aligned}$$

where β_2 is the angle between the radial line of the arc centre c and the X_2 axis (see Fig. 2.5, section 2.4). Then, according to the envelope condition (Eq. 2.13, section 2.4) there exists

$$\varphi_1 = -\beta_2 / i$$

and the Eq. (3.4) becomes

$$X_2 = r_{p,2} + r\cdot\cos(t-\beta_2)$$
$$Y_2 = r\cdot\sin(t-\beta_2)$$

i.e.

$$(X_2 - r_{p,2})^2 + Y_2^2 = r^2 \qquad (3.5)$$

This means that for a circular arc with its centre located on the pitch circle of the female rotor, the projection of the sealing line in the X-Y plane is also a circular arc with same radius and its centre is always on the pitch point (the contact point of the two pitch circles of the rotors).

It can be verified that the same result can be obtained for the circular arc with its centre located on the pitch circle of the male rotor.

Point

For a point on the female rotor, e.g. (x_{2j}, y_{2j}) which may be expressed as

$$x_2 = x_{2j} = r\cdot\cos(\beta_2)$$
$$y_2 = y_{2j} = r\cdot\sin(\beta_2) \qquad (3.6)$$

where r is the radial distance of the point from the centre of the rotor, while β_2 is the angle between the radial line and the x-axis.

Substituting of the above equation into sealing line equation (3.1) leads to

$$X_2 = r\cdot\cos(\beta_2 + i\cdot\varphi_1)$$
$$Y_2 = r\cdot\sin(\beta_2 + i\cdot\varphi_1)$$

i.e.

$$X_2^2 + Y_2^2 = r^2 \qquad (3.7)$$

It is obvious that the sealing line of a point on the female rotor is a circle arc in the *X-Y* plane with its center coincident with the center of the rotor and its radius being equal to the radial distance of the point from the center of the rotor. This conclusion holds for the points on the male rotor as well.

Straight Line

Similarly, for a straight line on the female rotor as shown in Fig. 2.7 (section 2.4), substituting of its coordinates (Eq. 2.22, section 2.4) and envelope condition (Eq. 2.23, section 2.4) into the sealing line equation (3.1) leads to

$$\left(X_2 - \frac{r_{p,2}}{2}\right)^2 + Y_2^2 = \left(\frac{r_{p,2}}{2}\right)^2 + r^2 \cdot \sin^2(\beta_2 - \vartheta) + r \cdot r_{p,2} \cdot \sin(\beta_2 - \vartheta) \cdot \sin(\vartheta + i \cdot \varphi_1) \qquad (3.8)$$

If $\beta_2 = \vartheta$, i.e. a radial line, then the above equation becomes

$$\left(X_2 - \frac{r_{p,2}}{2}\right)^2 + Y_2^2 = \left(\frac{r_{p,2}}{2}\right)^2 \qquad (3.9)$$

which is a circular arc with its center located at point $(r_{p,2} / 2, 0)$ and its radius being equal to the half of that of the female pitch circle.

It can be expected that a similar result will be obtained for a straight line on the male rotor.

3.2.3 Sealing Line Length

As shown in Fig. 3.1, a working chamber is sealed by part of the sealing line from top point *B* on the lobe of suction side to the top point *B* on the lobe of discharge side. In order to calculate the leakage loss from the working chamber, the length of this part of the sealing line has to be determined, which varies with male rotor angle of rotation. Utilizing the sealing line equation (3.1) or (3.2), the coordinates of a series of points on the sealing line, e.g. $X_1(j)$, $Y_1(j)$, $Z_1(j)$, can be calculated for a male rotor angle of rotation. Assuming that

two adjacent points are close enough to be taken to be connected by a straight line (e.g. the distance between two adjacent points is limited here to about 0.3 mm for a compressor of outer diameter 204 mm), then the sealing line length is

$$l_{r\text{-}r}(\alpha) = \sum_{j} \Delta l_{r\text{-}r}(\alpha, j) \tag{3.10}$$

where

$$\Delta l_{r\text{-}r}(\alpha, j) = \sqrt{[X_1(j) - X_1(j\text{-}1)]^2 + [Y_1(j) - Y_1(j\text{-}1)]^2 + [Z_1(j) - Z_1(j\text{-}1)]^2} \quad \text{if} \quad 0 \le Z_1(j) \le L_r \tag{3.11}$$

It should be noted that the coordinates of rotor flank points are produced for one rotor lobe by the rotor profile generation program, while the sealing line of a working chamber involves two adjacent rotor lobes (see Fig. 3.1). Therefore, for an angle of rotation α associated with a part of the sealing line on the suction side lobe, an angle of rotation $\alpha + 2\pi/\bar{z}_1$ would be associated with a corresponding part on the discharge side lobe.

In addition, the sealing line may not always be continuous, which is true for SRM A profile for example. An approximate approach is to use a straight line to span the discontinuity.

3.3 Sealing Line Length between Rotor Tip and Housing Bore

In addition to the clearance between the rotors discussed in the previous section, the clearance between rotor tips and housing bore is another major source of leakage. As shown in Fig. 3.2, a working volume has four rotor tip curves which form the cavity leakage boundaries at the housing surface. If the two that are located on the suction side are identified by male rotor rotating angle α, the other two situated on the discharge side can then be expressed by male rotor rotating angle $\alpha + 2\pi/\bar{z}_1$. From the principle of the formation of

screw rotors, it is known that these rotor tip curves are general cylindrical spirals. After creating the parameter equation of a curve, the length of the curve can be obtained by integrating the equation along the curve. Since the length of the sealing line varies with the rotation of the rotors, the integration limits have to be determined accordingly.

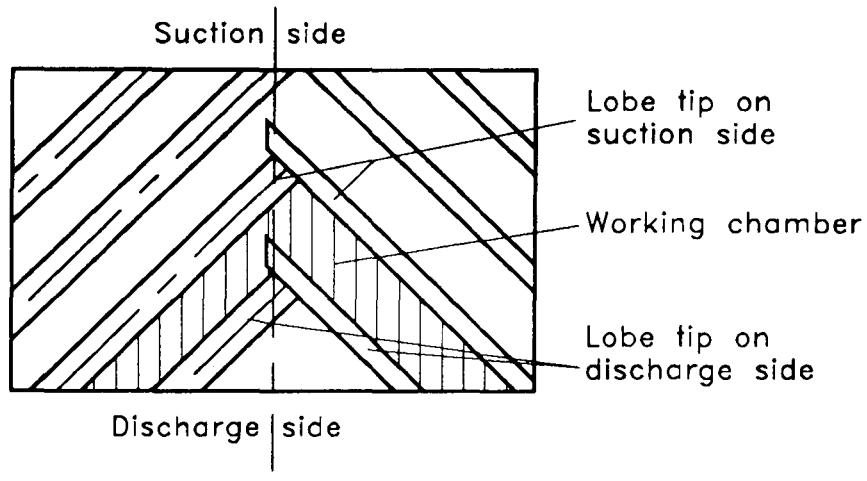

Fig. 3.2 Sealing line length between rotor tips and housing

3.3.1 Male Rotor Tip Curve on the Suction Side

The male rotor tip curve is formed by the outermost point of the profile which, referring to the coordinate systems defined in Fig. 2.2 (section 2.2), has the coordinates $X_1 = r_{o1}$, $Y_1 = 0$, $Z_1 = 0$ in the zero position. For an arbitary male rotor angle of rotation α, the male rotor tip curve can be expressed as

$$\begin{aligned} X_1 &= r_{o,1} \cos(t+\alpha) \\ Y_1 &= r_{o,1} \sin(t+\alpha) \\ Z_1 &= h_1/(2\pi) \cdot t \end{aligned} \tag{3.12}$$

where α is the male rotor angle of rotation, while t is the angular parameter of the rotor tip curve.

The length of the curve is then obtained by integrating the above equation:

$$\begin{aligned} l'_{r\text{-}h}(\alpha) &= \int_{t_s}^{t_e} \sqrt{[\dot{X}_1(t)]^2 + [\dot{Y}_1(t)]^2 + [\dot{Z}_1(t)]^2}\, dt \\ &= (t_e - t_s) \cdot \sqrt{r_{o1}^2 + [h_1/(2\pi)]^2} \end{aligned} \tag{3.13}$$

where t_e and t_s are start- and end-point values of integration, which are a function of male rotor angle of rotation α.

Consider the rotors to be rotated *backwards* from the end of the discharge process to the end of the compression process. In the first range of rotation the rotor tip has not reached the intersect point of the two housing bores (see Fig. 3.3), thus no sealing edge exists, resulting in

$$L'_{r-h}(\alpha) = 0 \qquad \text{for} \quad -\alpha \le \varphi_h \tag{3.14}$$

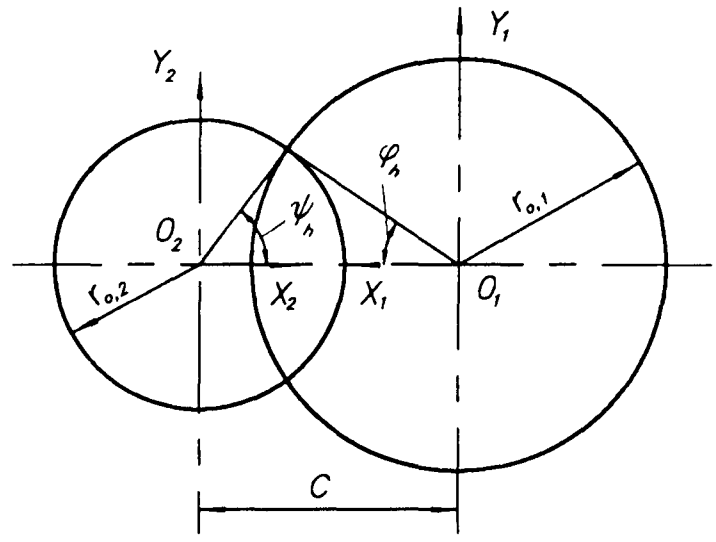

Fig. 3.3 Intersection of the housing bores

If the rotors keep rotating backwards, a rotor tip forms a sealing edge against its housing bore, with the effective sealing line starting from the angle φ_h to the rotating angle α. Thus,

$$L'_{r-h}(\alpha) = (-\alpha - \varphi_h)\sqrt{r_{o,1}^2 + [h_1/(2\pi)]^2} \tag{3.15}$$

which is valid for

$$0 \le (-\alpha - \varphi_h) \le \varphi_w \quad \text{and} \quad -\alpha \le 2\pi - \varphi_h$$

where φ_w is the wrap angle of the male rotor. This condition is easy to understand because the screw angle for calculating the length of the rotor tip curve will never exceed its wrap angle, while at the same time the start point of the tip curve should still form a sealing edge against housing.

However, for a small wrap angle, the whole rotor tip curve may be in contact with the housing over a certain range of rotating angle. In such a case, the

length of the sealing tip curve remains unchanged at its maximum value over a range of rotor rotation:

$$L'_{r\text{-}h}(\alpha) = \varphi_w \sqrt{r_{o,1}^2 + [h_1/(2\pi)]^2} \tag{3.16}$$

for

$$(-\alpha - \varphi_h) \geq \varphi_w \quad \text{and} \quad -\alpha \leq 2\pi - \varphi_h$$

In the last range of rotation in which part of the rotor tip curve at the discharge side projects beyond the intersection point of the two housing bores, the sealing edge no longer exists. As a result of this, the length of this part of the sealing tip, which equals

$$[-\alpha - (2\pi - \varphi_h)] \sqrt{r_{o1}^2 + [h_1/(2\pi)]^2}$$

must be subtracted from the results calculated by Eqns. (3.15) and (3.16). Thus:

$$L'_{r\text{-}h}(\alpha) = (2\pi - 2\varphi_h) \sqrt{r_{o,1}^2 + [h_1/(2\pi)]^2} \tag{3.17}$$

for

$$0 \leq (-\alpha - \varphi_h) \leq \varphi_w \quad \text{and} \quad -\alpha \leq 2\pi - \varphi_h$$

and

$$L'_{r\text{-}h}(\alpha) = (\varphi_w + \alpha + 2\pi - \varphi_h) \sqrt{r_{o,1}^2 + [h_1/(2\pi)]^2} \tag{3.18}$$

for

$$(-\alpha - \varphi_h) \geq \varphi_w \quad \text{and} \quad -\alpha \geq 2\pi - \varphi_h \ .$$

3.3.2 Female Rotor Tip Curve on the Suction Side

The tip curve of the female rotor is also formed by the outermost point of the profile crest portion, as can be seen in Figs. 2.3 and 2.4 in section 2.3. The coordinates of this point in the zero-position may be expressed as

$$X_2 = r_{o,2} \cdot \cos(t_0), \quad Y_2 = r_{o,2} \cdot \sin(t_0), \quad Z_2 = 0$$

where t_0 is the angle of the point relative to the X_2 - axis. Thus, the equation

of the rotor tip for an arbitary male rotor rotating angle α takes the form of

$$\begin{aligned} X_2 &= r_{o,2} \cdot \cos\left(t_0 + i \cdot (t + \alpha)\right) \\ Y_2 &= r_{o,2} \cdot \sin\left(t_0 + i \cdot (t + \alpha)\right) \\ Z_2 &= h_1 / (2\pi) \cdot t \end{aligned} \tag{3.19}$$

where t is the angular parameter of the tip curve.

The length of the effective tip curve can then be obtained in the same way as for the male rotor tip sealing line. The results are listed below:

- for $-\alpha \le (\psi_h - t_0)/i$ there exists

$$L''_{r\text{-}h}(\alpha) = 0 \tag{3.20}$$

- for $0 \le \left[-\alpha - (\psi_h - t_0)/i\right] \le \varphi_w$ and $-\alpha \le (2\pi - t_0 - \psi_h)/i$:

$$L''_{r\text{-}h}(\alpha) = \left[-\alpha - (\psi_h - t_0)/i\right] \cdot \sqrt{r_{o,2}^2 i^2 + [h_1/(2\pi)]^2} \tag{3.21}$$

- for $0 \le \left[-\alpha - (\psi_h - t_0)/i\right] \ge \varphi_w$ and $-\alpha \le (2\pi - t_0 - \psi_h)/i$:

$$L''_{r\text{-}h}(\alpha) = \varphi_w \cdot \sqrt{r_{o,2}^2 \cdot i^2 + [h_1/(2\pi)]^2} \tag{3.22}$$

- for $0 \le \left[-\alpha - (\psi_h - t_0)/i\right] \le \varphi_w$ and $-\alpha \ge (2\pi - t_0 - \psi_h)/i$:

$$L''_{r\text{-}h}(\alpha) = (2\pi - 2\psi_h)/i \cdot \sqrt{r_{o,2}^2 \cdot i^2 + [h_1/(2\pi)]^2} \tag{3.23}$$

- for $\left[-\alpha - (\psi_h - t_0)/i\right] \ge \varphi_w$ and $-\alpha \ge (2\pi - t_0 - \psi_h)/i$:

$$L''_{r\text{-}h}(\alpha) = \varphi_w - \left[-\alpha - (2\pi - t_0 - \psi_h)/i\right] \cdot \sqrt{r_{o,2}^2 \cdot i^2 + [h_1/(2\pi)]^2} \tag{3.24}$$

3.3.3 Rotor Tip Curves on the Discharge Side

As mentioned earlier, rotor tip curves on the discharge side are the same as those on the suction side, except that they are identified by male rotor rotating angle $\alpha + 2\pi/\bar{z}_1$ instead of α. Therefore, all the above discussed equations are also applied to rotor tip curves on the discharge side, provided that the angle α is substituted by $\alpha + 2\pi/\bar{z}_1$ in these equations. The total length of

rotor tip curves on the suction side or the discharge side is then obtained by adding the corresponding results of the male and the female rotors together.

3.4 Blow Hole Area

The blow hole is the term used to describe leakage triangles in helical twin screw compressors, as shown in Fig. 3.4.

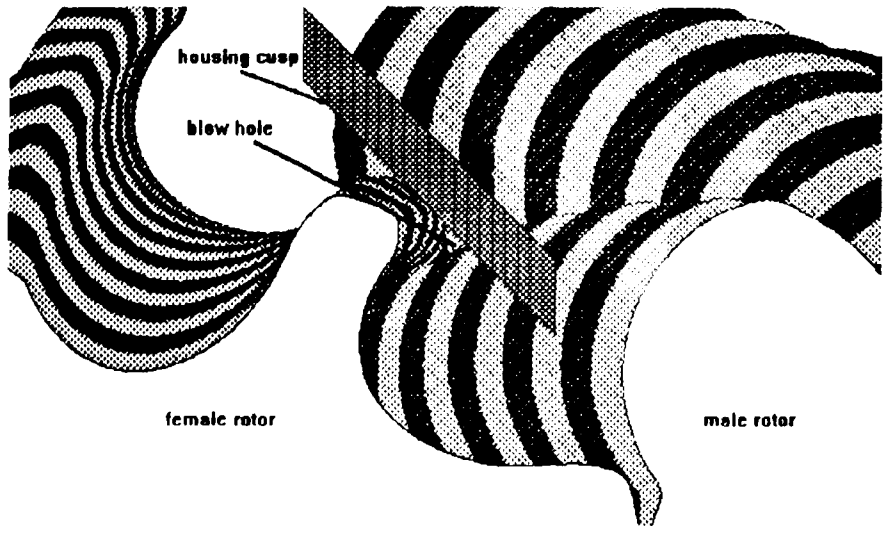

Fig. 3.4 Blow hole (pressure side)

The presence of blow holes is an inevitable consequence of the rotor profile geometrics. The contact line of male and female rotors does not reach the housing cusps (the intersecting line of two housing cylinders), as can be seen from Fig. 3.5. As a result of this, leakage triangles are formed both in the pressure and suction sides. The blow hole in the suction side is much greater than that in the pressure side. It is, however, of minor significance for the efficiency and the leakage in screw compressors, because the suction side blow hole only exists at the beginning of the compression process and at that stage only a very small pressure difference exists between adjacent cavities in the suction side.

On the pressure side, however, the size of the blow hole plays an important role in the usability of rotor profiles. Leakage, from one closed cavity to another through the leakage triangle, affects the performance by raising the

specific power and the discharge gas temperature. The area of the blow hole on the pressure side is therefore an important geometrical parameter of rotor profiles and the knowledge of it is critical to the accurate prediction of performance when using computer models.

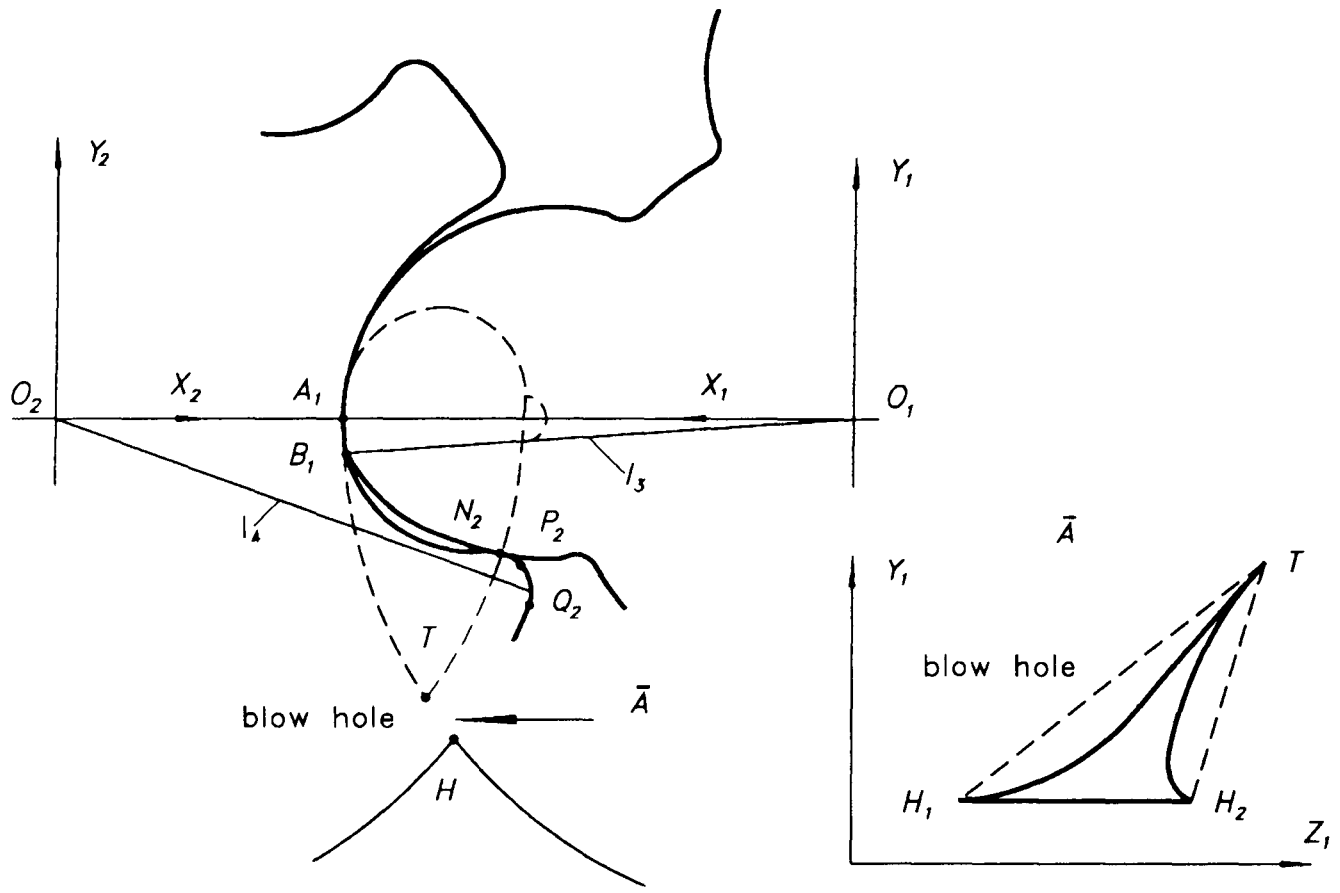

Fig. 3.5 Position of the blow hole

Strictly speaking, the blow hole is a three-dimensional curvilinear triangle, with two vertices being the points where adjacent male and female rotor crest lines meet the rotor housing cusp, and the third vertex being the nearest rotor-to-rotor contact point. As shown in Fig. 3.5, H_1 and H_2 are two housing cusp vertices, and T is the contact point vertex of the blow hole triangle. Lines T-H_1 and T-H_2 follow the contact paths as the rotors are rotated and do not lie in the same plane. Therefore, the determination of blow hole area requires a integration of a curvilinear surface, which is a large amount of work for a very small gain of accuracy of around 1.5 - 2.0% (Singh and Bowman, 1990). Accordingly, an approximate method "three vertex plane approach" (Singh and Bowman, 1990) was modified in the study for the determination of blow hole area from a knowledge of rotor and housing geometry.

The so called three vertex plane approach is to use the three vertices of the blow hole to define a plane and the intersection of this plane with the rotors and housing cusp are taken as the leakage triangle. Thus, the coordinates of the three vertices must be determined first, from which a plane is defined. Then the boundary of the blow hole must be set by the intersection of the plane with the rotors and the housing cusp. Since the blow hole area is in a *3D* plane, it is easier to determine the area of its projection to a coordinate plane, e.g. *Y-Z* plane, by numerical integration. The desired blow hole area for leakage flow calculation should be in the plane normal to the middle flow line through the blow hole and this can be obtained through geometric projection.

In addition, the variation of blow hole area with male rotor angle of rotation is required in the form of an input file for the performance simulation program.

3.4.1 Coordinates of Three Vertices of Blow Hole

The coordinates of the three vertices in the coordinate system X_1, Y_1, Z_1 can be determined by using the rotor flank point parameters (X_1, Y_1, φ_1) at the zero-position, which are part of the output of the rotor profile generation program and thus may be treated as known parameters.

Point *T* (rotor-to-rotor contact point):

$$\begin{aligned} X_{1,T} &= X_{1,B_1} \cos(\varphi_{1,B_1}) - Y_{1,B_1} \sin(\varphi_{1,B_1}) \\ Y_{1,T} &= X_{1,B_1} \sin(\varphi_{1,B_1}) + Y_{1,B_1} \cos(\varphi_{1,B_1}) \\ Z_{1,T} &= h_1 / (2\pi) \cdot (\varphi_{1,B_1} - \alpha) \end{aligned} \tag{3.25}$$

where α is the male rotor angle of rotation and $X_{1,B1}$, $Y_{1,B1}$, $\varphi_{1,B1}$ are the parameters of point B_1, which is the first contact point on the male rotor flank.

Point H_1 (male rotor tip - housing cusp intersecting point):

$$
\begin{aligned}
X_{1,H_1} &= r_{o1}\cos(\varphi_h) \\
Y_{1,H_1} &= r_{o1}\sin(\varphi_h) \\
Z_{1,H_1} &= Z_{1,T} + \frac{h_1}{2\pi}\left(\varphi_h - \arctan(\frac{Y_{1,T}}{X_{1,T}}) + \arctan(\frac{Y_{1,B_1}}{X_{1,B_1}})\right)
\end{aligned}
\tag{3.26}
$$

where φ_h is the angle of housing cusp relative to the X_1 - axis (Fig. 3.3).

Point H_2 (female rotor tip - housing cusp intersecting point):

$$
\begin{aligned}
X_{1,H_2} &= X_{1,H_1} \\
Y_{1,H_2} &= Y_{1,H_1} \\
Z_{1,H_2} &= Z_{1,T} + \frac{h_2}{2\pi}\left(\psi_h - \arctan(\frac{Y_{1,T}}{a - X_{1,T}}) - \arctan(\frac{Y_{2,Q_2}}{X_{2,Q_2}}) + \arctan(\frac{Y_{2,N_2}}{X_{2,N_2}})\right)
\end{aligned}
\tag{3.27}
$$

where Q_2, N_2 are points on the female rotor flank as shown in Fig. 3.5.

3.4.2 Equation of the Plane

The above points in space may be used to define a plane. The equation of the plane can be obtained by expanding the determinant

$$
\begin{vmatrix}
X_1 - X_{1,H_2} & Y_1 - Y_{1,H_2} & Z_1 - Z_{1,H_2} \\
X_{1,T} - X_{1,H_2} & Y_{1,T} - Y_{1,H_2} & Z_{1,T} - Z_{1,H_2} \\
X_{1,H_1} - X_{1,H_2} & Y_{1,H_1} - Y_{1,H_2} & Z_{1,H_1} - Z_{1,H_2}
\end{vmatrix} = 0
\tag{3.28}
$$

The expansion of the determinant can be written as

$$
A_p \cdot X_1 + B_p \cdot Y_1 + C_p \cdot Z_1 + D_p = 0
\tag{3.29}
$$

where A_p, B_p, C_p, D_p are coefficients of the plane equations.

The results of the coefficients are listed below:

$$
\begin{aligned}
A_p &= (Y_{1,T} - Y_{1,H_2}) * (Z_{1,H_1} - Z_{1,H_2}) \\
B_p &= -(X_{1,T} - X_{1,H_2}) * (Z_{1,H_1} - Z_{1,H_2}) \\
C_p &= 0 \\
D_p &= -X_{1,H_2} * (Y_{1,T} - Y_{1,H_2}) * (Z_{1,H_1} - Z_{1,H_2}) + Y_{1,H_2} * (X_{1,T} - X_{1,H_2}) * (Z_{1,H_1} - Z_{1,H_2})
\end{aligned}
\tag{3.30}
$$

3.4.3 The Boundary Lines of the Blow Hole

As mentioned before, the boundary lines of the blow hole are the intersecting lines of the above defined plane with the rotors and with the housing cusp (see Fig. 3.5).

Boundary Line T-H_1

It is the intersecting line of the plane with the male rotor flank ranging from B_1 to A_1. For an arbitrary point j on the rotor flank within this range there exists:

$$\begin{aligned} A_p \cdot X_{1,j} + B_p \cdot Y_{1,j} + D_p &= 0 \\ X_{1,j}^2 + Y_{1,j}^2 &= l_{3,j}^2 \end{aligned} \tag{3.31}$$

from which the $X_{1,j}$, $Y_{1,j}$ can be obtained:

$$X_{1,j} = \frac{-2A_p \cdot D_p - B_p \cdot \sqrt{(A_p^2 + B_p^2) * l_{3,j}^2 - D_p^2}}{A_p^2 + B_p^2}$$

$$Y_{1,j} = -\frac{A_p X_{1,j} + D_p}{B_p}$$

where $l_{3,j}$ is the distance of the point j from the centre of the male rotor.

The $Z_{1,j}$ is obtained like $Z_{1,T}$:

$$\begin{aligned} Z_{1,j} = Z_{1,T} + \frac{h_1}{2\pi} [&\arctan(\frac{Y_{1,j}}{X_{1,j}}) - \arctan(\frac{Y_{1,T}}{X_{1,T}}) \\ &+ \arctan(\frac{Y_{1,B_1}}{X_{1,B_1}}) - \arctan(\frac{Y_{1,j,0}}{X_{1,j,0}})] \end{aligned} \tag{3.32}$$

where $X_{1,j,0}$, $Y_{1,j,0}$ are the coordinates of the point j at the zero-position.

Boundary line T-H_2

It is the intersecting line of the plane with the female rotor flank points ranging from N_2 to Q_2 (Fig. 3.5). Similarly, for an arbitary flank point j within this range there exists:

$$\begin{aligned} A_p \cdot X_{1,j} + B_p \cdot Y_{1,j} + D_p &= 0 \\ (C - X_{1,j})^2 + Y_{1,j}^2 &= l_{4,j}^2 \end{aligned} \tag{3.33}$$

Thus

$$X_{1,j} = \frac{-tem2 - \sqrt{tem2^2 - 4 \cdot tem1 \cdot tem3}}{2 \cdot tem1}$$
$$Y_{1,j} = -\frac{A_p \cdot X_{1,j} + D_p}{B_p} \qquad (3.34)$$

where

$$tem1 = A_p^2 + B_p^2$$
$$tem2 = 2 \cdot A_p \cdot D_p - 2 \cdot C \cdot B_p^2$$
$$tem3 = D_p^2 - I_{4,j}^2 \cdot B_p^2 + C^2 \cdot B_p^2$$

And the $Z_{1,j}$ value is

$$Z_{1,j} = Z_{1,T} + \frac{h_2}{2\pi}\left[\arctan\left(\frac{Y_{1,j}}{C - X_{1,j}}\right) - \arctan\left(\frac{Y_{1,T}}{C - X_{1,T}}\right)\right.$$
$$\left. - \arctan\left(\frac{Y_{2,j,0}}{X_{2,j,0}}\right) + \arctan\left(\frac{Y_{2,N_2,0}}{X_{2,N_2,0}}\right)\right] \qquad (3.35)$$

where $(X_{2,j,0}, Y_{2,j,0})$ and $(X_{2,N_2,0}, Y_{2,N_2,0})$ are the coordinates at the zero position of the points j and point N_2 of the female rotor flank, respectively.

Boundary line H_1-H_2

It is the intersecting line of the plane with the housing cusp. This is a straight line, the end points of which have known coordinates. Thus, all the blow hole boundary lines have been defined.

3.4.4 Blow Hole Area and the Variation with Rotating Angle

As mentioned before, to simplify the integration process the area of the blow hole's projection in the Y-Z plane is determined first. This can be done by using the following trapezium integration equation (see Fig. 3.6):

$$S_4 = \int_{Y_{1,min}}^{Y_{1,max}} \left[Z_{1,T-H_2}(Y_1) - Z_{1,T-H_1}(Y_1)\right] dY_1$$
$$= \sum_j \left(\frac{Z_{1,T-H_2}(j) + Z_{1,T-H_2}(j+1)}{2} - \frac{Z_{1,T-H_1}(j) + Z_{1,T-H_1}(j+1)}{2}\right) \cdot \left|Y_1(j+1) - Y_1(j)\right| \qquad (3.36)$$

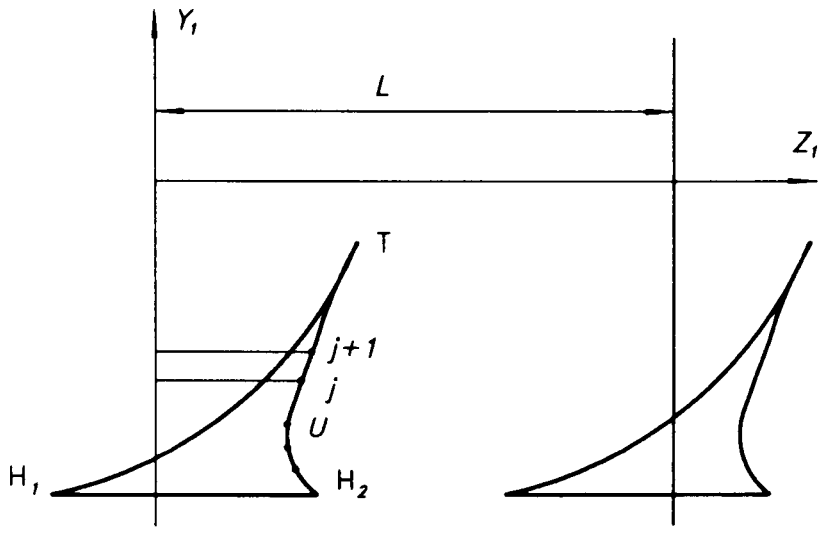

Fig. 3.6 Blow hole in *Y-Z* plane

After obtaining S_4, i.e. the blow hole area in the *Y-Z* plane, it can be seen from Fig. 3.7 that some transfer is needed to get the desired blow hole area S_3 which is in the plane normal to the middle flow line through the blow hole.

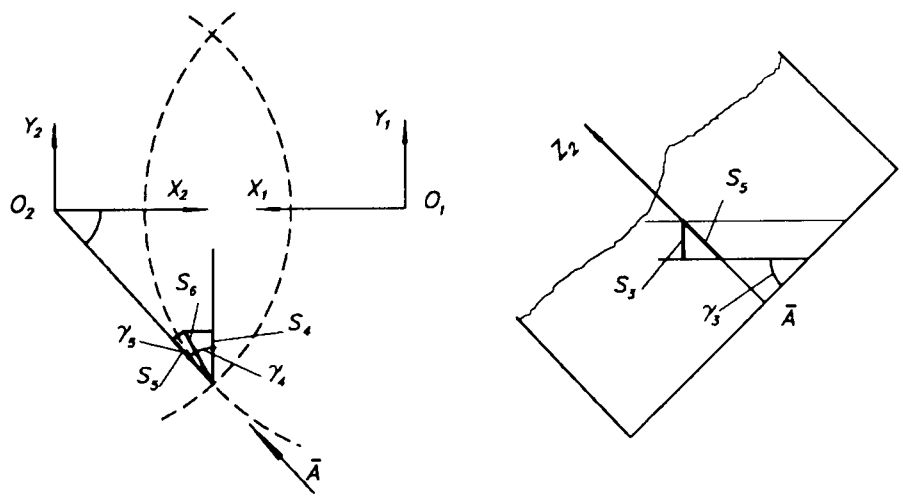

Fig. 3.7 Blow hole area in different planes

The blow hole area in the actual three vertex plane is

$$S_6 = S_4 / \cos(\gamma_4) \tag{3.37}$$

where $\gamma_4 = \arctan\left[(X_{1,T} - X_{1,H_1}) / (Y_{1,T} - Y_{1,H_1})\right]$.

The blow hole area in the radial plane is

$$S_5 = S_6 \cdot \cos(\gamma_5) \tag{3.38}$$

where $\gamma_5 = \pi / 2 + \psi_h - \gamma_4$.

Finally, the desired blow hole area S_3 is

$$S_3 = S_5 \cdot \cos(\gamma_3) \tag{3.39}$$

where γ_3 is the helix angle of the middle flow line throungh the blow hole.

Fig. 3.6 schematically shows the variation of blow hole area with the rotation of the rotors. The blow hole contour will remain unchanged but will move along the axis from the suction side to the discharge side. The effective blow hole area is the part within the rotor length L. It should be noted that the calculation may be carried out in one side only, either in the suction or discharge side of the rotor. The results for the other side can then be derived from the fixed rotating angle difference $2\pi L / h_1$.

3.5 Inter Lobe Area and Cavity Volume

Both the inter-lobe area and the cavity volume of the working chamber are important geometrical characteristics of a helical twin screw compressor. For a given rotor diameter, the larger the inter-lobe area, the more effective the usage of the rotor geometry. As rotors rotate, the cavity volume varies periodically from zero to its maximum value then back to zero. The knowledge of its variation with rotating angle is essential to the design and performance simulation of the twin screw compressor.

Although a so called exact method has been introduced by Singh and Schwartz (1990), the traditional slice method (Rinder, 1979) has been used in this study for its ease understanding and programming.

3.5.1 Method Overview

The principle of the slice method, as implied by its name, is to divide the rotors into slices of small thickness along their axes, as shown in Fig. 1.1 (section 1.3). The cavity volume of a working chamber is thus composed of a series

of small volumes, each of them being equal to the product of the cross-sectional inter-lobe area and the thickness of the slice. Because of the engagement of rotor lobes, the inter-lobe areas of the slices are different. To calculate the inter-lobe areas of all the slices, let us consider the discharge side end plane (the front piece of the slices in Fig. 1.1) of the rotors, becuase all the slices can be expressed by the end plane with different rotating angle. The problem of calculating the cavity volume is, therefore, transformed into the following two tasks:

- to calculate the variation of the inter-lobe area with the male rotor angle of rotation in the discharge side end plane;
- to integrate the above areas along the rotor axes with reference to the contact point and wrap angle of the rotors.

The two sections that follow are designed to discuss the above tasks in detail. Although the geometry of the SRM-asymmetric profile types have been adopted in the study, the method and thus the program should be applicable to other rotor profiles.

3.5.2 Inter-Lobe Area

General Consideration

Figs. 3.8 to 3.14 show the variation of the inter-lobe area with male rotor angle of rotation α (on the discharge end plane $z = 0$). According to the different contact situation of the rotors the whole range of rotation may be divided into following stages.

At the beginning, the rotors are at the position for which the male rotor angle of rotation α is zero (Fig. 3.8). This position stands for the end of the compression process of the working chamber being considered. That is, the top section of the male rotor flank is coincident with the bottom section of the female rotor flank. The inter-lobe area is thus equal to zero, i.e. $S(\alpha) = 0$.

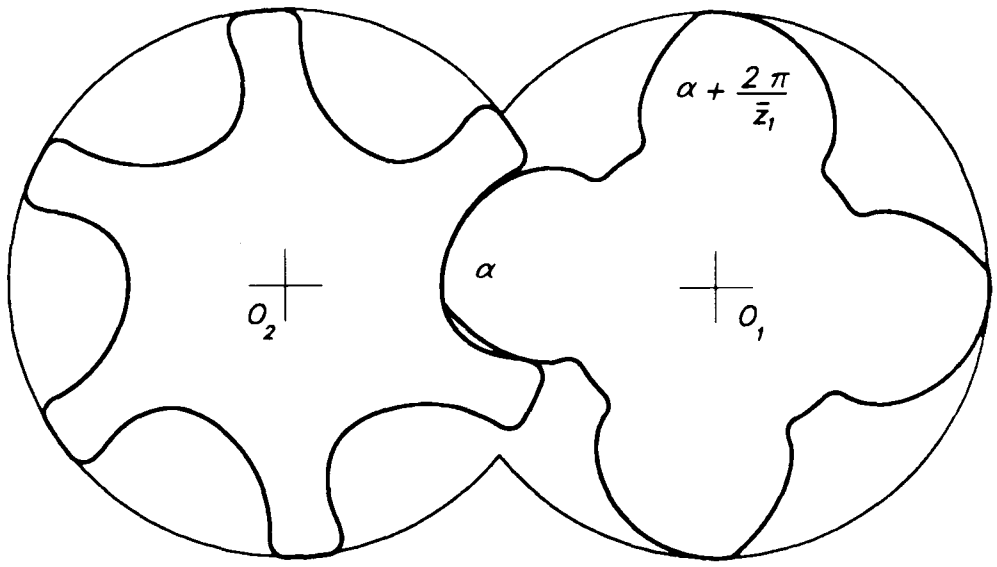

Fig. 3.8 Inter-lobe area at the zero-position

Supposing that the rotors are rotated backwards from the end of the discharge to the beginning of the suction. After a small rotating angle, a gap appears between the engaged rotor lobes (Fig. 3.9). There are two contact points in this first stage of rotation, and an inter-lobe area exists between the male and female rotor flanks.

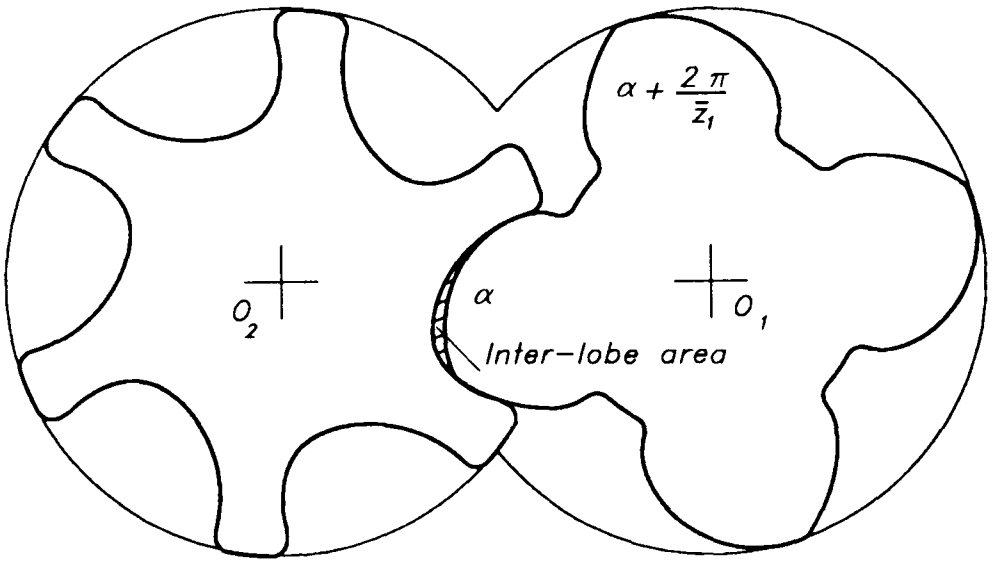

Fig. 3.9 Inter-lobe area at the first stage of rotation

With the continued rotation of the rotors, the contact point of the trailing flank of the rotors will pass its nearest position to the housing cusp point (point *T* in Fig. 3.5 of section 3.4). Consequently, only one contact point between the rotors exists in this second stage of rotation (Fig. 3.10). The inter-lobe area

is accordingly bounded by the male rotor flank, the female rotor flank, the female rotor housing bore and the male rotor housing bore.

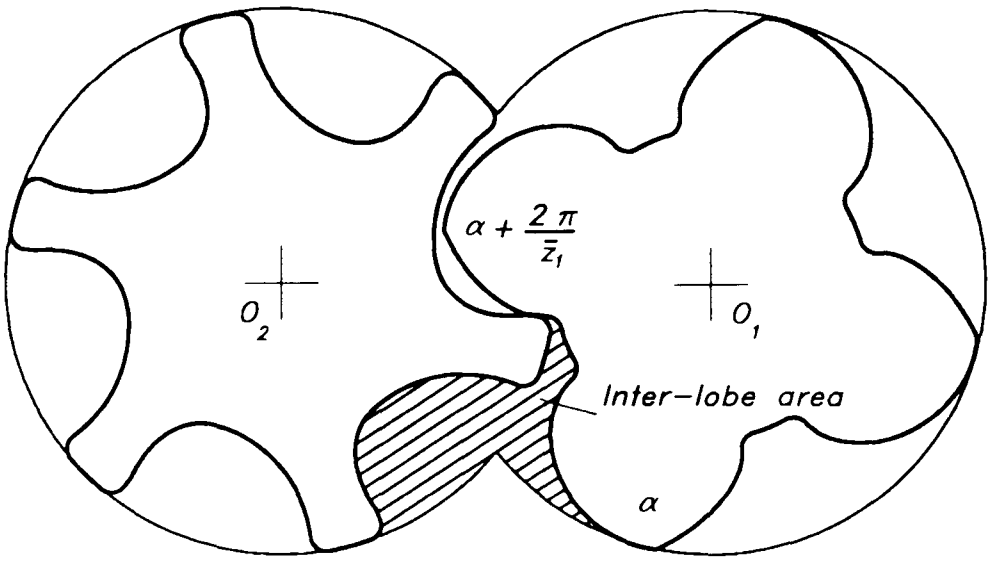

Fig. 3.10 Inter-lobe area at the second stage of rotation

If the rotors rotate continuously, the observed inter-lobe area is eventually separated into two separate parts, one for the male and the other for the female (Fig. 3.11). The maximum value of the inter-lobe area is obtained. This equals the sum of the areas of these two parts. The inter-lobe area remains unchanged for most of this third stage of rotation.

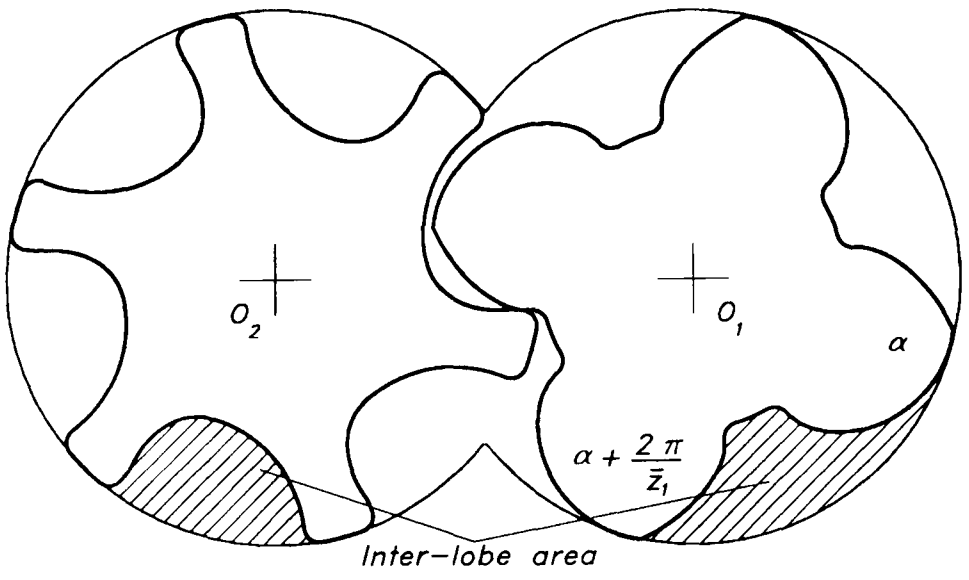

Fig. 3.11 Inter-lobe area at the third stage of rotation

However, with the further rotation of the rotors, the female rotor flank gradually intrudes into the range of the male rotor outer diameter (see Fig. 3.12). The inter-lobe area thus starts to reduce at the end of the third stage of rotation.

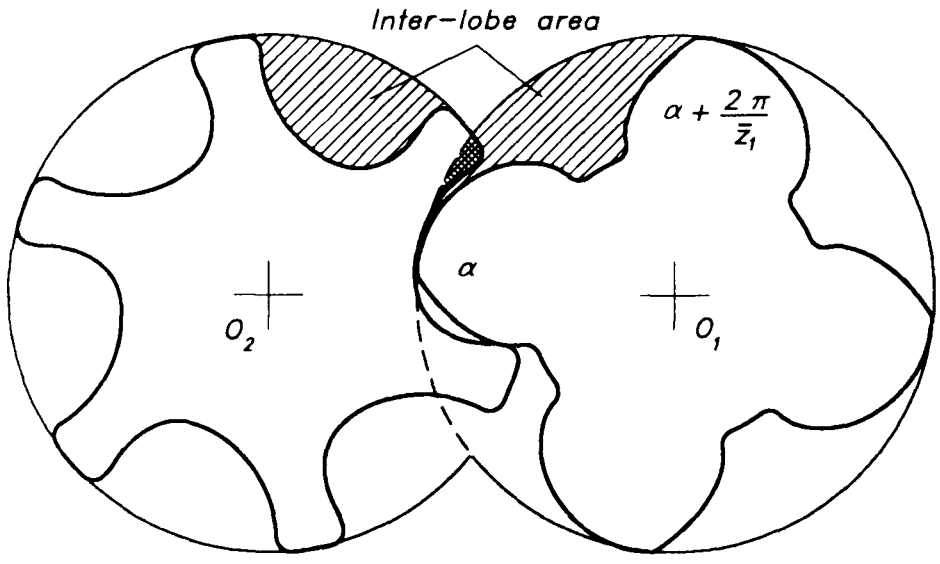

Fig. 3.12 Inter-lobe area at the end of the third rotation stage

The fourth stage of rotation begins when the male rotor lobe comes into contact again with the female rotor. Only one contact point exists as can be seen from Fig. 3.13. The inter-lobe area is again bounded by the male rotor flank, the female rotor flank, male rotor housing bore and the female rotor housing bore.

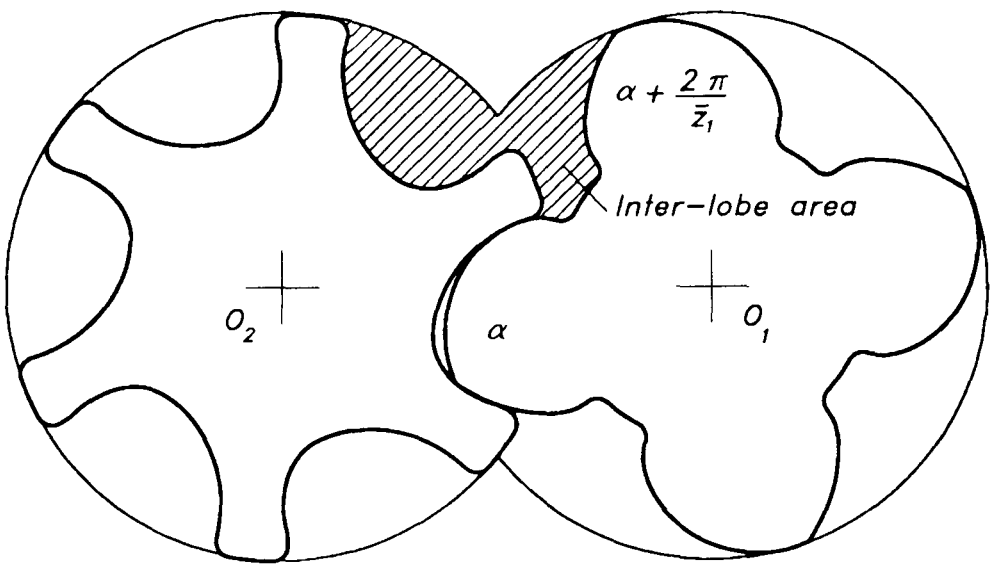

Fig. 3.13 Inter-lobe area at the fourth stage of rotation

The final stage of rotation is reached when the male rotor lobe of rotating angle $\alpha + 2\pi / \bar{Z}_1$ comes in contact with the female rotor (Fig. 3.14). The inter-lobe area bounded by the male rotor flank and the female rotor flank between the two contact points is gradually reduced to zero.

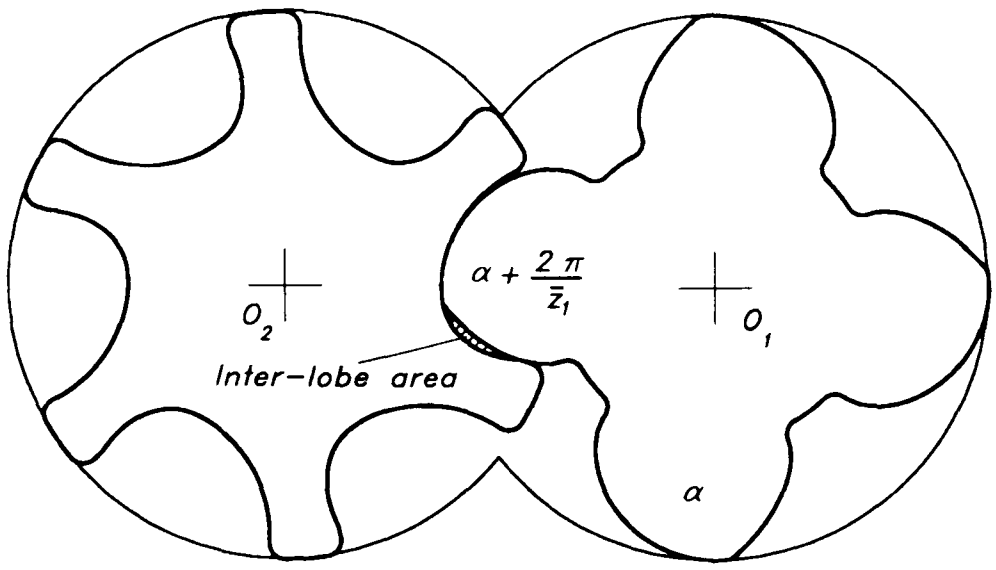

Fig. 3.14 Inter-lobe area at the fifth stage of rotation

Numerical Calculation

From the above analysis, the inter-lobe area at an arbitrary male rotor angle of rotation can generally be expressed as an area bounded by the curves of the combination of the male rotor flank, the female rotor flank, the male rotor housing bore and the female rotor housing bore. If the ranges of these boundary curves are known, the inter-lobe area can then be determined through the boundary integration:

$$S(\alpha) = (1/2) \oint x dy - y dx \tag{3.40}$$

Obviously, the ranges of the boundary curves depend both on the male rotor angle of rotation and on the rotor profile geometry, and have to be considered individually for the different stages of rotation.

For an arbitary male rotor angle of rotation, the corresponding contact point(s) must be determined first. This would best be done numerically. For this purpose the angle φ_{1j} belonging to the individual flank point, with which the flank point becomes the contact point, plays an important role.

For all flank points, which form the boundary of the inter-lobe area, the following relation exists:

$$\varphi_{1j} > \alpha$$

while for all flank points which are located outside the range of the inter-lobe area, there exists:

$$\varphi_{1j} < \alpha$$

Therefore, the angle φ_{1j} serves as an indicator, whether a flank point lies within the inter-lobe area range or not. The practical evaluation of the boundary integration for the calculation of the area $S(\alpha)$ can then be carried out in the following way:

Consider two adjacent flank points of the male rotor, i.e., $n_1\ (j)$ and $n_1\ (j+1)$. By checking the corresponding angle $\varphi_1(j)$ and $\varphi_1(j+1)$, it can be determined wether both the points belong to the boundary of the inter-lobe area. If that is the case, the integration of the area for this element can be obtained by using the trapezium equation

$$\Delta S(j) = (1/2)\left[\frac{X_1(j)+X_1(j+1)}{2}\left(Y_1(j+1)-Y_1(j)\right) - \frac{Y_1(j)+Y_1(j+1)}{2}\left(X_1(j+1)-X_1(j)\right)\right] \tag{3.41}$$

where j is the index of the male rotor flank points. The integration along the boundary of the female rotor flank can be performed in the same way, and the sum of the integrations of these elements is the inter-lobe area at that angle of rotation.

For the start and end point of the integration, where either $n_1\ (j)$ or $n_1\ (n+1)$ is located outside the calculation range of the inter-lobe area, linear interpolation may be adopted for improving the accuracy of the result.

3.5.3 Cavity Volume

As described before, the cavity volume can be obtained by integrating the inter-lobe area along the rotor axis, that is

$$V(\alpha) = \int_0^{z_{1,e}} S(\alpha+\gamma)\, dz_1 \tag{3.42}$$

where α is the male rotor angle of rotation with reference to the end plane ($z=0$), while γ is the angular variable of the cavity volume range, which is related to the z_1 coordinate by the equation

$$dz_1 = (h_1/2\pi)\, d\gamma \tag{3.43}$$

Thus, the cavity volume becomes

$$V(\alpha) = (h_1/2\pi) \int_0^{\gamma_e} S(\alpha+\gamma)\, d\gamma \tag{3.44}$$

For the case that $-\alpha$ is less than the wrap angle of the male rotor, i.e. $-\alpha < \varphi_w$, the cavity volume is sealed by the rotor flanks in the suction side, so the upper limit of the above integration γ_e simply equals

$$\gamma_e = -\alpha$$

However, for the case where $-\alpha$ is larger than the male rotor wrap angle, i.e., $-\alpha > \varphi_w$, the cavity volume is *not* sealed by the rotor flanks on the suction side but by the end plane of the housing. As the result of this, the upper limit of the above integration γ_e should be equal to the wrap angle, i.e.,

$$\gamma_e = \varphi_w$$

Again, the integration of the Eq. (3.44) can numerically be performed by using the trapezium equation:

$$V(\alpha) = \frac{h_1}{2\pi} \sum_j \frac{S(\alpha+\gamma(j)) + S(\alpha+\gamma(j+1))}{2} \left(\gamma(j+1) - \gamma(j)\right) \tag{3.45}$$

where

$$0 \le \gamma(j) \le -\alpha \qquad \text{for} \quad -\alpha < \varphi_w$$
$$0 \le \gamma(j) \le \varphi_w \qquad \text{for} \quad -\alpha \ge \varphi_w$$

By altering the angle α, the variation of the cavity volume with the male rotor angle of rotation can finally be obtained.

3.6 Development of the Computer Program

Based on the methods described in sections 3.2 - 3.5, a computer program was developed for the calculation of the geometrical characteristics of helical screw compressors. The program was designed in a menu driven way, with its main menu looking like this:

- Read in a Rotor End Profile Data File
- Read/Input Rotor Length and Wrap Angle
- Sealing Line Length between the Rotors
- Sealing Line Length between the Rotors and Housing Bores
- Blow Hole Area
- Inter-Lobe Area and Cavity Volume
- Results Report Output
- End

The user starts with choosing a rotor end profile data file created by the rotor profile generation program, and then is required to read or input rotor structure parameters (length and male rotor wrap angle).

After defining the above parameters, the user can enter one of the sub-menus to calculate the corresponding characteristics. The sub-menus provide the user with facilities for calculation, viewing on the screen and data saving. The menu for sealing line length between rotors, for instance, looks like:

- Start Calculation
- View on Screen
- Save Results
- Back to Main Menu

For viewing on the screen, the user can either use just calculated results or read a data file saved before. And in general several options are available for viewing results in a number of ways, e.g. for sealing line length between the rotors there exist

- Viewing Sealing Line in *X-Y* Plane with Rotor Profiles
- Viewing Sealing Line in *X-Y* Plane
- Viewing Sealing Line in *Y-Z* Plane
- Viewing Sealing Line in *X-Z* Plane
- Viewing Sealing Line in *3D*
- Viewing Variation of Sealing Line Length with Rotating Angle
- End

While viewing, the scale of the picture can be enlarged/reduced and the position of it can be moved around very easily as described in Chapter 2, section 2.4. Thus any part of the picture can be examined in great detail.

The calculated parameters and their variation with male rotor angle of rotation can be saved to disk files for further use and the overall results can be displayed on screen and output to the connected printer by pressing *p* when viewing.

A instruction for running the program is given in Appendix 2 of this volume.

3.7 Numerical Examples

To demonstrate the capability of the developed computer program, a numerical example is presented in this section with SRM A-profile. The main parameters used are shown below and the calculated results are presented in Figs. 3.15-3.22.

• Rotor profile	SRM A	• Centre distance	80 mm
• Rotor outer diameter	102 mm	• Lobe combination	4+6
• Male rotor wrap angle	300 °	• Rotor length	150 mm

Fig. 3.15 shows sealing line between the rotors in the *x-y* plane together with the rotor profile, while a *3D* schematic view is given in Fig. 3.16. It can be seen that the sealing line between the rotors is not continuous between *1*

and *2*, and between *3* and *4*. As mentioned before, this may increase the leakage loss and should be avoided in the design of rotor profiles.

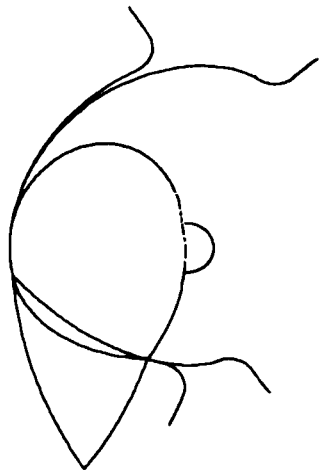

Fig. 3.15 Sealing line per lobe (*x-y*)

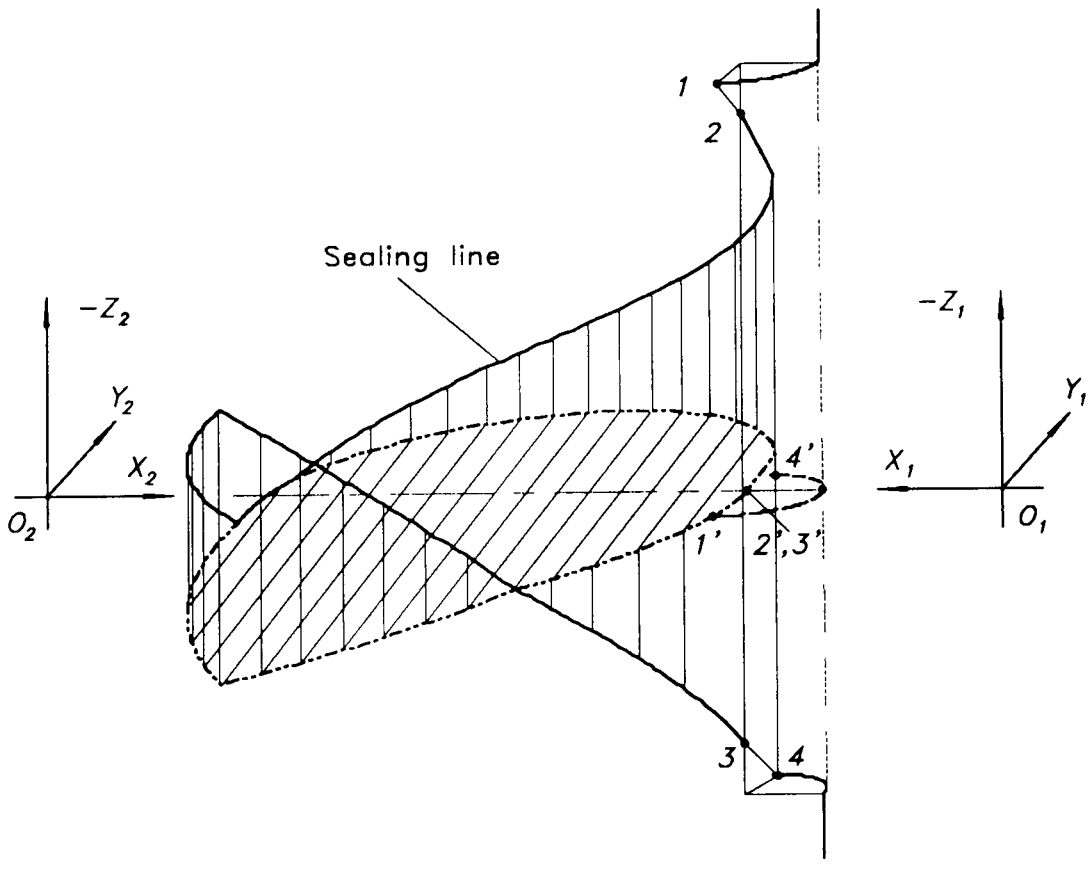

Fig. 3.16 Sealing line per lobe in *3D*

The variation of the sealing line length between the rotors with male rotor angle of rotation is shown in Fig. 3.17. As the rotors rotate, sealing line moves along the rotor axis from the suction side to the discharge side. The length of the sealing line thus increases/decreases rapidly as the corresponding working chamber enters/leaves the effective rotor length, while it remains constant

being its maximum value over a large rotation angle range as the working chamber lies within the rotor length.

Fig. 3.18 shows the variation of the sealing line length between the rotors and the housing bores with male rotor angle of rotation. The two curves are identical except that the sealing line on the suction side is delayed by an angle of $2\pi / \bar{z}_1$.

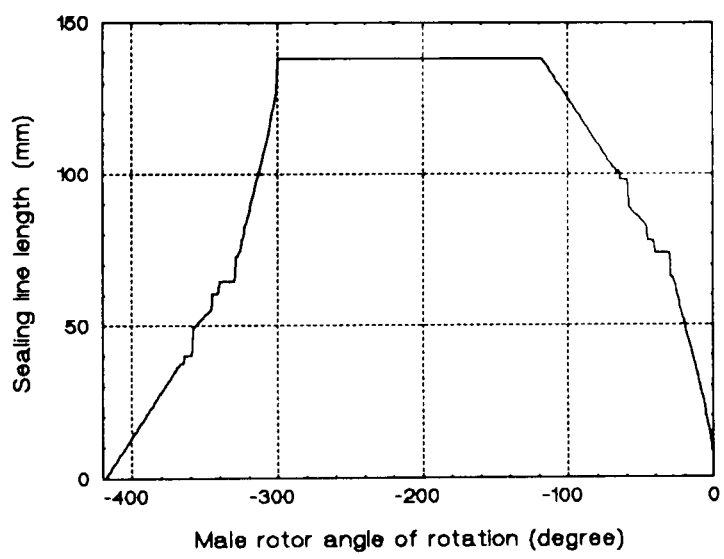

Fig. 3.17 Variation of sealing line length between the rotors with male rotor angle of rotation

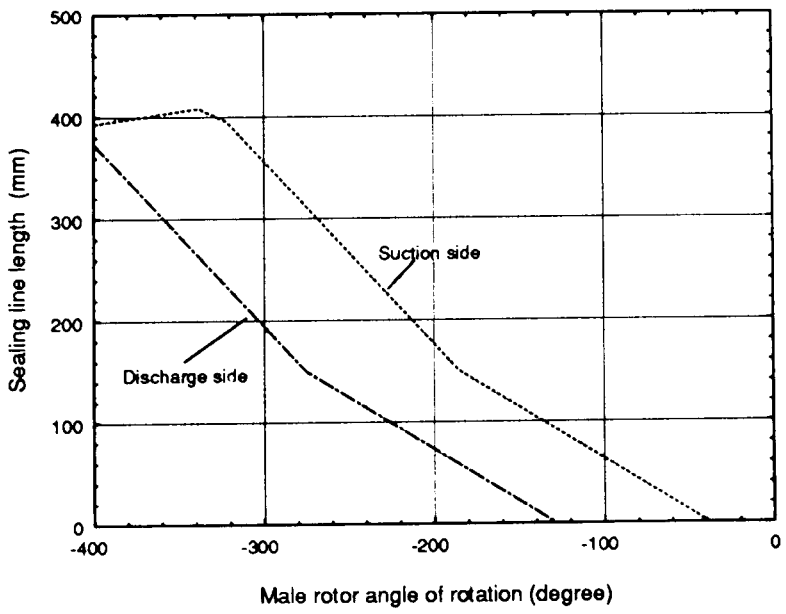

Fig. 3.18 Variation of sealing line length between the rotors and the housing bores with male rotor angle of rotation

The projection of the blow hole contour in *Y-Z* plane is shown in Fig. 3.19, together with the sealing line between the rotors. As described before, the bottom line of the blow hole triangle coincides with the housing cusp, while the top point coincides with the nearest rotor contacting point. This figure in fact implies the ways of reducing the blow hole area: either let the nearest rotor contacting point move closer to the housing cusp, or use modifying rotor tip designs, which determine the remaining two boundaries of the blow hole triangle.

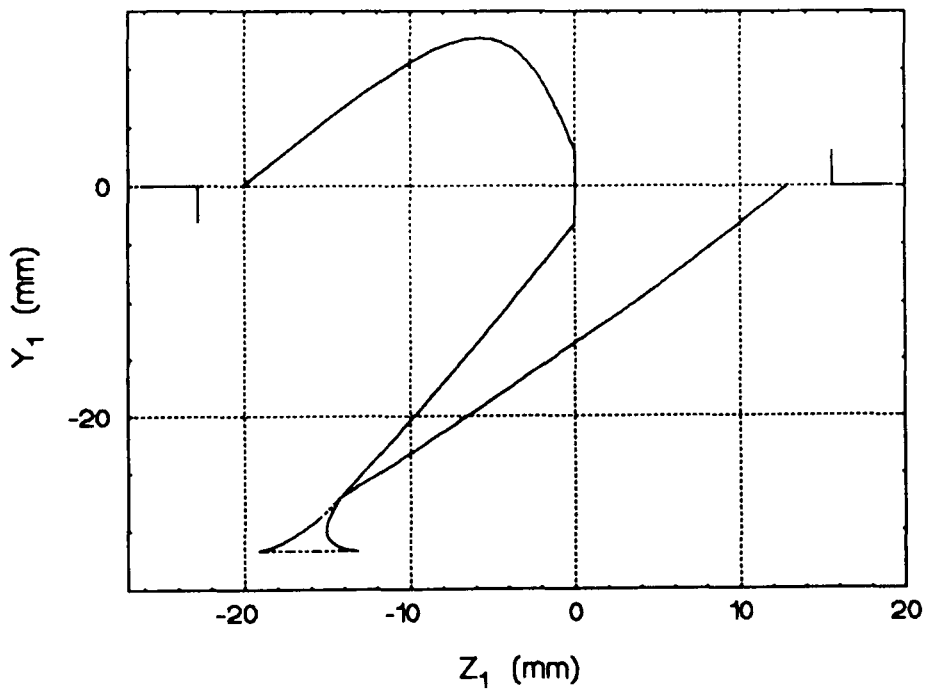

Fig. 3.19 Blow hole contour in *Y-Z* plane and its position

The variation of the blow hole area with the male rotor angle of rotation is shown in Fig. 3.20. Similar to the sealing line between the rotors, the blow hole area remains constant of its maximum value over most of the male rotor rotational angle and only varies as it enters / leaves the rotor length range.

Figs. 3.21 and 3.22 show the relationship of the inter-lobe area and the cavity volume with the male rotor angle of rotation. The point at which maximum cavity volume occurs is usually set to be the compression start point of the working chamber.

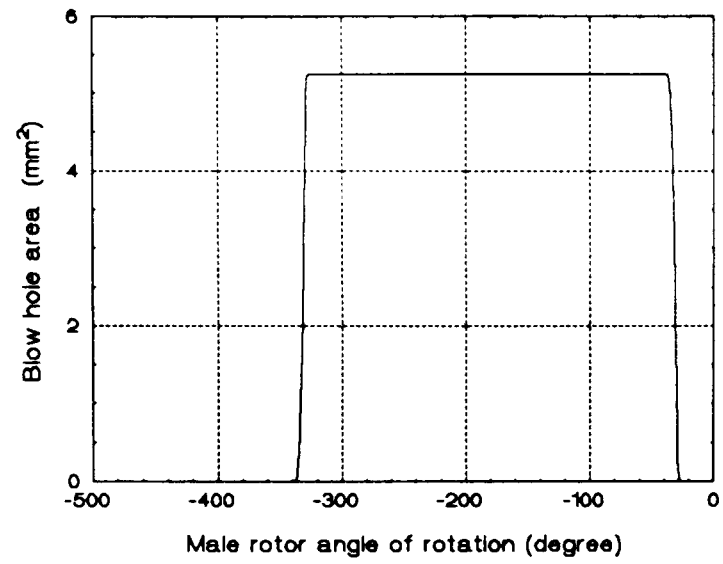

Fig. 3.20 Blow hole area vs male rotor angle of rotation

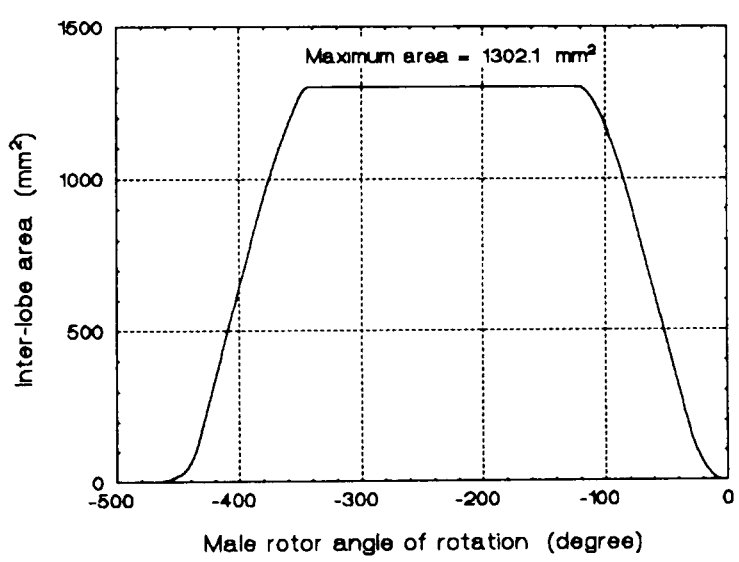

Fig. 3.21 Inter-lobe area vs male rotor angle of rotation

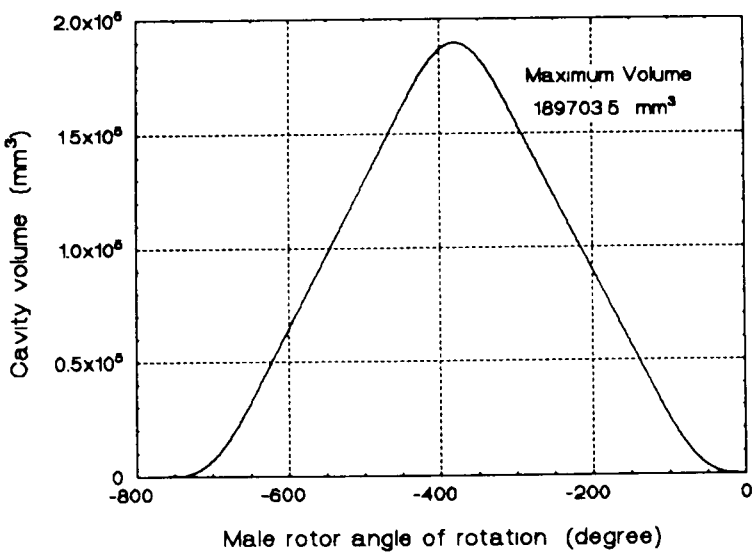

Fig. 3.22 Cavity volume vs male rotor angle of rotation

3.8 Conclusions

A computerized method for analyzing the main geometrical characteristics of twin-screw compressors has been developed and used to demonstrate its capabilities through an example. The program can be used in many ways:

- It can be instrumental in inventing and analyzing entirely new profiles or modifying the existing profiles from the point of view of geometrical characteristics.
- It can be used in optimizing a machine's geometrical parameters such as number of lobes, wrap angle, length/diameter ratio, etc.
- It can be an aid to better design of the machine through providing an understanding of the importance of different leakage areas.
- It can be used to generate input data for the performance simulation program, such as the variation of sealing line length, blow hole area and cavity volume as functions of the male rotor angle of rotation.

The program has been applied successfully to SRM A- and D-profiles constructed to a wide range of geometrical parameters. It should be applicable to other types of rotor profiles, although some minor modifications may be needed if profile shapes differ significantly from the SRM-asymmetrical type.

Chapter 4

Rotor Force and Deflection

4.1 Introduction

In a helical screw compressor the gas in the compression cavities applies forces to the rotors which vary with time periodically, but in a relatively complex manner. In addition, for oil injected twin screws the contact between the rotors also imposes dynamic loads on the rotors. These forces together cause the deformation of the rotors and impose oscillating loads on bearings of a magnitude so great as to warrant designers devoting considerable resources to achieving their determination at the design stage.

The methods available in the literature for calculating these rotor loads either utilize assumptions which greatly simplify the complex rotor profile geometry, which affects the magnitudes of the computed loads (Adams and Soedel, 1992), or use fairly crude methods to calculate axial forces (Rinder, 1979; Zhou, et al, 1990).

In this study a method having finer discrimination than that obtained by other authors is used which enables the axial and radial components and the moments of forces applied to the rotors together with the bearing loads and rotor deflection to be computed. All the factors which influence bearing loads

have been taken into account, including rotor contact and off centre axial gas and contact force components. Forces and torques are expressed as functions of the male rotor angle of rotation.

This Chapter presents the method used and the corresponding computer program developed. The predictions of radial bearing forces are compared with measurement data and the results for a numerical example are presented to demonstrate the capability of the program.

4.2 Forces and Torques due to Compression

Compression gas acts on the helical screw surfaces. It also acts on the rotor end faces due to gas leakage across the end faces and also to the exposure of lobe ends to the suction and discharge pressures when lobes pass across the suction and discharge ports. Gas forces applied to the helical screw surfaces may be resolved into axial, radial and tangential components (from which torque is derived); while forces imposed on the rotor end faces do not influence gas torque.

Since the axial forces both on the rotor helical screw surfaces and on the rotor end faces are not imposed along the rotor axis, bending of the rotor occurs which influences the radial loads on the bearings. In this study, these axial forces inducing bending moments have been taken into account.

4.2.1 Forces and Torques Applied to Helical Surfaces

Gas forces applied to the rotor helical surfaces may be determined by integrating axial, radial and tangential components over the whole acting range of the rotor helical surfaces.

For the integration, the slice method (see also section 3.5) is used. The rotors are assumed to be comprised of a set of thin slices taken normal to the rotor axis. From the geometry of the helical screw rotor, it is known that these thin

slices are all identical except that they are in different positions in space (expressed by male rotor angle of rotation). The integration can be carried out first for one slice for a chosen male rotor angle of rotation and then the contributions of all the other slice elements along the rotor axis are summed to give the overall gas pressure loads. Since the relative angular positions of the different cavities are known the integration need be performed for one cavity only. The effects of different cavities can then be superposed to obtain the net gas effects on the rotors.

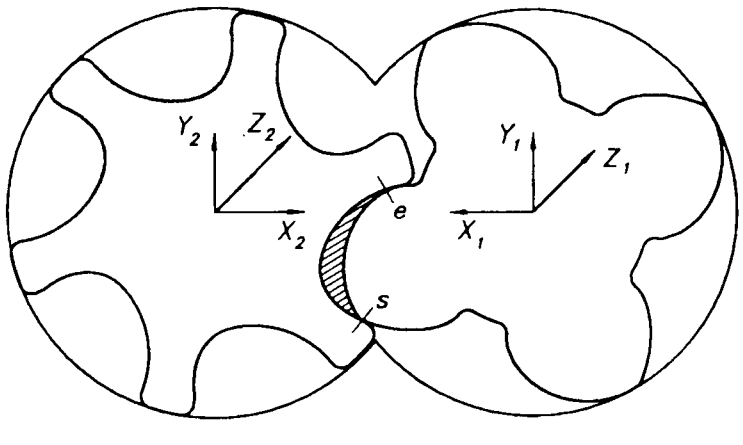

Fig. 4.1 Acting range of compression gas

In this study the slice at $Z_1 = Z_2 = 0$ (discharge side) has been chosen as the integration slice with a thickness of ΔZ. The ΔZ is so small that the contact point(s) of the two rotors is/are treated unchanged over the thickness of the slice and thus the contact point(s) of the rotors at $Z_1 = Z_2 = 0$ plane can be used to stand for the contact point(s) of the slice. Corresponding to a male rotor angle of rotation α, the contact point(s) of the two rotors can be determined which set the acting range of compression gas (the shaded area in Fig. 4.1 [1]).

As shown in Fig. 4.2 (a,b), for a element ds of the rotor profile (either male or female rotor) with a thickness ΔZ the differential force components are

$$\begin{aligned} -dF_X &= p \cdot ds \cdot \sin(\vartheta) \cdot \Delta Z = p \cdot ds \cdot (dY/ds) \cdot \Delta Z = p \cdot dY \cdot \Delta Z \\ dF_Y &= p \cdot ds \cdot \cos(\vartheta) \cdot \Delta Z = p \cdot ds \cdot (dX/ds) \cdot \Delta Z = p \cdot dX \cdot \Delta Z \end{aligned} \tag{4.1}$$

[1] The coordinate system used for the female rotor here is for the convenience of expressing twin screw rotors, while in a regular Cartesian coordinate system like the one used for the male rotor here, a rotation from positive X to positive Y causes an advance in the positive Z direction.

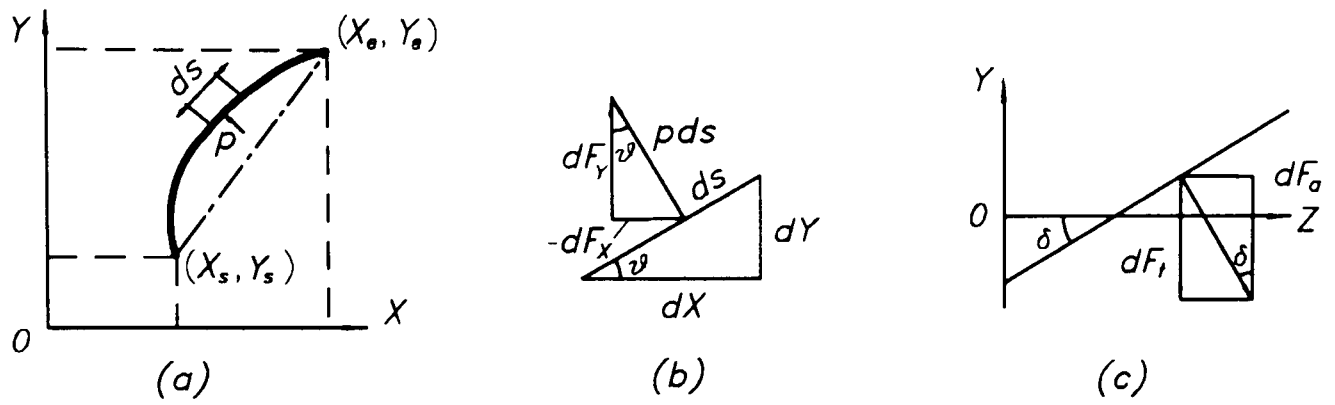

Fig. 4.2 Compression gas force on a slice

and the torque around z-axis is

$$dT = dF_Y \cdot X - dF_X \cdot Y = p \cdot (Y \cdot dY + X \cdot dX) \cdot \Delta Z \tag{4.2}$$

The axial component can be deduced from the relation between axial and tangential components as shown in Fig. 4.2 (c).

$$dF_a = dF_t \cdot \tan(\delta) \tag{4.3}$$

where δ is the helix angle of the rotor at radius r and can be expressed as

$$\tan(\delta) = \frac{2\pi r}{h} \tag{4.4}$$

where h is axial pitch length of helical lobes.

Recalling that the tangential component is

$$dF_t = \frac{dT}{r} \tag{4.5}$$

$$\text{thus,} \quad dF_a = \frac{2\pi}{h_1} \cdot dT \tag{4.6}$$

For any known integration limits which are functions of male rotor angle of rotation, integrating the above equations results in the following force components and torque:

$$F_X(\alpha) = -p \cdot \int_{Y_s(\alpha)}^{Y_e(\alpha)} dY \cdot \Delta Z = -p \cdot \left[Y_e(\alpha) - Y_s(\alpha) \right] \cdot \Delta Z \tag{4.7}$$

$$F_Y(\alpha) = +p \cdot \int_{X_s(\alpha)}^{X_e(\alpha)} dX \cdot \Delta Z = +p \left[X_e(\alpha) - X_s(\alpha) \right] \cdot \Delta Z \tag{4.8}$$

$$T(\alpha) = p\cdot\left[\int_{Y_s(\alpha)}^{Y_e(\alpha)} Y\cdot dY + \int_{X_s(\alpha)}^{X_e(\alpha)} X\cdot dX\right]\cdot\Delta Z$$
$$= p\cdot\left[\frac{Y_e(\alpha)^2 - Y_s(\alpha)^2}{2} + \frac{X_e(\alpha)^2 - X_s(\alpha)^2}{2}\right]\cdot\Delta Z \qquad (4.9)$$

$$F_a(\alpha) = \frac{2\pi}{h}\cdot T(\alpha) \qquad (4.10)$$

Utilizing the above equations, and assuming that the rotors rotate from the end of discharge (i.e. $\alpha = 0$) backwards to the beginning of compression, the force components as functions of α can be determined.

Then, forces and torques for one cavity volume were obtained by the sum of the effects of all the slices within the cavity. The torque corresponding to a male rotor angle of rotation α (at the discharge end face), for instance, is

$$T_c(\alpha) = \sum_{\varphi_s}^{\varphi_e} T(\varphi) \qquad (4.11)$$

where φ_s and φ_e stand for the lower and upper limit of the cavity volume, which must be determined according to the male rotor angle of rotation α (referred to the discharge end face).

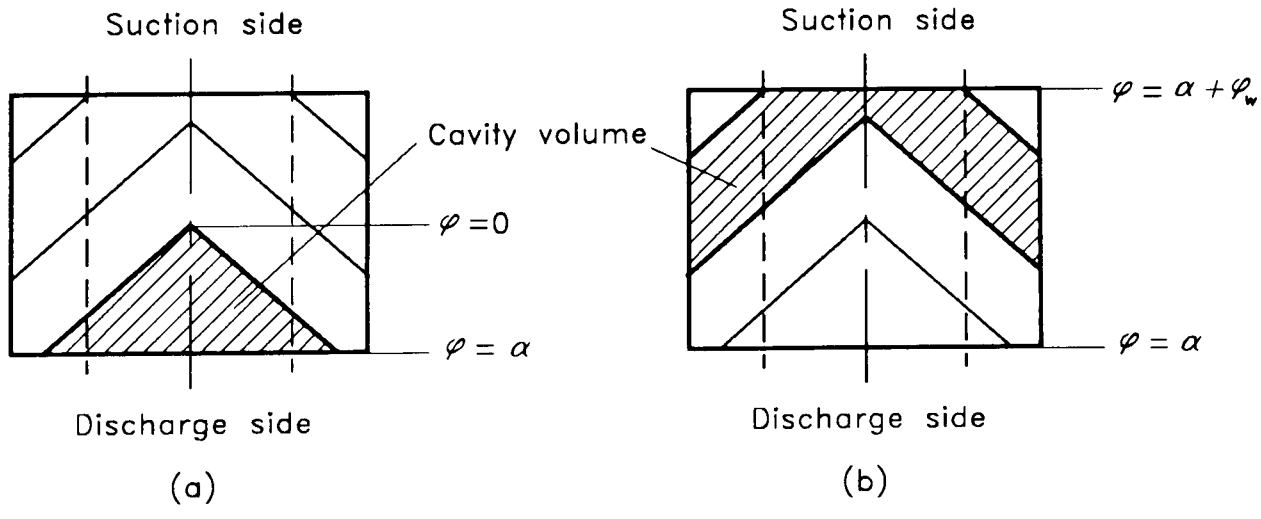

Fig. 4.3 Cavity volume integration limits

As shown in Fig. 4.3 (a), for the cavity volume concerned (shaded part) the absolute value of the rotational angle α is less than the male rotor wrap

angle. The cavity is closed at the other side (suction side) by the engaged lobes, which corresponds to the $\varphi = 0$. Thus,

$$\varphi_s = 0, \quad \varphi_e = \alpha, \qquad \text{for} \quad |\alpha| < \varphi_w \tag{4.12a}$$

However, if the absolute value of the rotational angle α becomes larger than the male rotor wrap angle (as shown in case (b) of Fig. 4.3), the cavity volume is opened to the suction side and ranges whole the length of the rotor. Thus,

$$\varphi_s = \alpha + \varphi_w, \quad \varphi_e = \alpha, \qquad \text{for} \quad |\alpha| > \varphi_w \tag{4.12b}$$

The value of ΔZ is obtained from the geometry:

$$Z = \frac{h}{2\pi}\varphi, \qquad \text{thus,} \quad \Delta Z = \frac{h}{2\pi}\Delta\varphi \tag{4.13}$$

Finally, the torques applied to the rotors are obtained from the summation for all the cavities:

$$T_{1,2}(\alpha) = \sum_{j=0}^{j=\bar{z}_1-1} T_c\left(\alpha - \frac{2\pi}{\bar{z}_1}\cdot j\right) \tag{4.14}$$

In the above derivation no specific male or female rotor is referred, thus the above equations hold for both male and female rotors (the coordinates defined in Fig. 4.2).

In addition, the bending moments induced by off centre axial forces are determined at the same time as the X and Y components of force are computed. Similarly, these transverse moments of force can be resolved into X and Y planes, i.e. M_X, M_Y, and integrated in the integration slice for each male rotor angle of rotation. However, attention must be payed to the directions of axial forces which are either towards suction or discharge. A simple way to solve this problem is to add a condition statement in the computer program to judge if the location is beyond the top point (for male rotor) or bottom point (for female rotor), at which the direction of the axial gas force component reverses.

4.2.2 Forces Applied to Rotor End Planes

The axial force on the rotor end planes is computed as the summation of the loads on each of the rotor lobes. Since the pressure variation across a lobe between two adjacent cavities is almost linear (Rinder, 1979), a simple method for the calculation of the axial force applied to a single lobe is to use the mean of the two pressures in the cavities it connects. In other words, the axial force applied to the shaded part A in Fig. 4.4 could be determined by using the pressure in the cavity multiplied by the shaded area. An approximation, but one which saves much analytical work.

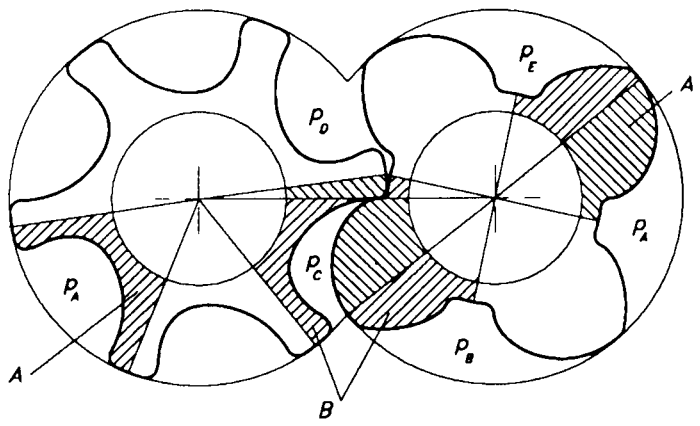

Fig. 4.4 Compression gas forces on the rotor end planes

Similarly, let the rotors rotate from the discharge end (i.e. $\alpha = 0$) backwards to the beginning of compression. Only one pair of lobes needs to be considered, and the overall axial force and bending moment can be obtained by superposing the effects of all the lobes. For a male rotor angle of rotation α, the contact status of the lobes under consideration should be determined first. If the lobes are in contact like the shaded part B in Fig. 4.4, the contact point(s) may divide the lobe area into two or three or even four parts. It can be seen from Fig. 4.4 that each part of the lobe area corresponds to a cavity volume pressure, which should be used when calculating the axial force and bending moments.

In addition to setting the cavity volume pressure, the area of each part of the lobe and its geometrical centre have to be determined for different male rotor

angles of rotation. For simplicity, Green's formula was used to transfer the area integration into curve integration along the boundary of the shaded area. This is explained below.

The area and the moments of the area may be expressed as

$$S = \iint dX dY, \quad M_X = \iint Y \cdot dX dY, \quad M_Y = \iint X \cdot dX dY \tag{4.15}$$

Recalling Green's equation:

$$\iint \left(\frac{\partial V}{\partial X} - \frac{\partial U}{\partial Y} \right) \cdot dX dY = \oint U(X,Y)\, dX + V(X,Y)\, DY \tag{4.16}$$

and the condition $U = -\frac{Y}{2}$, $V = \frac{X}{2}$ leads to

$$S = \frac{1}{2} \oint (-Y \cdot dX + X \cdot dY) \tag{4.17}$$

Similarly, $U = -Y^2$, $V = -X \cdot Y$ leads to

$$M_X = \oint (-Y^2 \cdot dX - X \cdot Y \cdot dY) \tag{4.18}$$

and $U = X \cdot Y$, $V = X^2$ leads to

$$M_Y = \oint (X \cdot Y \cdot dX + X^2 \cdot dY) \tag{4.19}$$

Since the boundary curves are known for any chosen male rotor angle of rotation, which consist of a rotor profile, circular arcs and radial lines, the curve integration was then carried out numerically.

In addition, it should be noted that though the rotor end plane at the suction side does not coincide with that at the discharge side, the calculation can be carried out just for one of them. The results of the other may be derived since the fixed angle difference is known (i.e. wrap angle).

4.3 Contact Forces between the Rotors

The contact between the rotors in helical twin screw compressors has been modelled using the theory of involute helical gears (e.g. Adams and Soedel,

1992). The common normal between the rotors at the point of contact was assumed to be constant. Obviously, this is not true due to the actual complex profile geometry. The rotor contact forces are in fact distributed along the power transmission sections of the sealing line between the rotors, and the direction of the contact forces also varies along the sealing line.

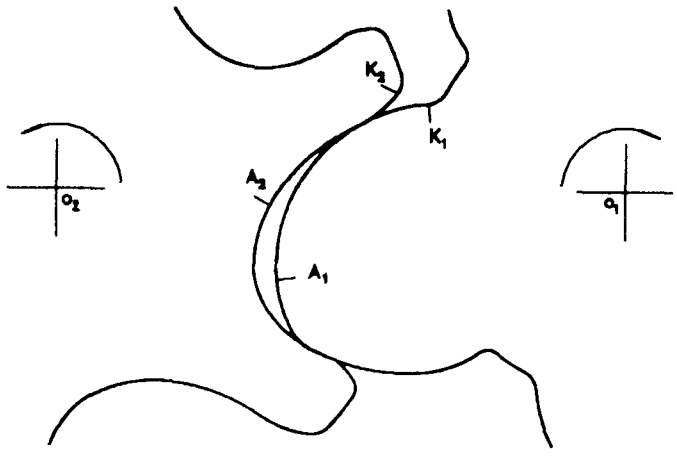

Fig. 4.5 Power transmission section of the rotor profile concerned

In this study, a method considering these factors was used to calculate the rotor contact forces. The method is based on the following simplifications which the author believes do not result in serious error.

(a) The rotor profile considered and shown in Fig. 4.1 (i.e. SRM asymmetric type), is suitable for male rotor drive. Power is transmitted from the male to the female rotor through the transmission section of the profile (*A* to *K* in Fig. 4.5) to overcome the compression gas-induced resistance torque. Since the compression is carried out in a cavity formed by a pair of rotor lobes, the resistance torque arising from cavity pressure is balanced by the torque due to lobe contact forces in the case of the female rotor which performs the function of an idler in a male rotor drive arrangement.

(b) The magnitude of the inter-rotor contact force will in reality vary along the contact line but in the model it is taken to be constant to make a solution achievable. The orientation of this force does however vary along the contact line. In reality, both the magnitude and orientation of this force vary with time as the rotor angle and cavity pressure vary.

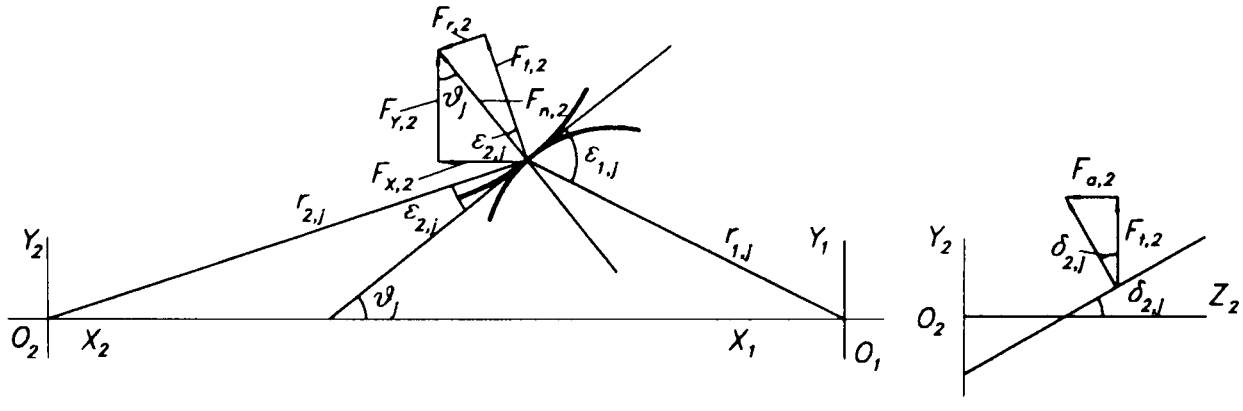

Fig. 4.6 Relations between components of the rotor contact forces

Fig. 4.6 shows the relationship between the components of the contact forces, from which the following expressions may be obtained:

$$F_{n3,2,j}^2 = F_{n,2,j}^2 + F_{a,2,j}^2 \tag{4.20}$$

$$F_{n,2,j} = F_{t,2,j} / \cos(\varepsilon_{2,j}) \tag{4.21}$$

$$F_{a,2,j} = F_{t,2,j} \cdot \tan(\delta_{2,j}) \tag{4.22}$$

Substituting Eqs. (4.21) and (4.22) into Eq. (4.20) leads to

$$F_{t,2,j} = \frac{F_{n3,2,j}}{\sqrt{1/\cos^2(\varepsilon_{2,j}) + \tan^2(\delta_{2,j})}} \tag{4.23}$$

According to assumption (a), the compression gas torque of the cavity equals

$$T_2(\alpha) = \int_s^e F_{t,2,j} \cdot r_{2,j} \cong F_{n3,2,j} \cdot \sum_s^e \frac{r_{2,j}}{\sqrt{1/\cos^2(\varepsilon_{2,j}) + \tan^2(\delta_{2,j})}} \tag{4.24}$$

where the magnitude of the contact forces $F_{n3,2,j}$ is constant along the contact line according to the assumption (b). Obviously, the integration limits *s* and *e* vary with male rotor angle of rotation α and should be determined first, together with the compression gas induced female rotor torque $T_2(\alpha)$. Then the magnitude of the contact forces $F_{n3,2,j}$ can be determined from the above equation for a male rotor angle of rotation α.

The components of the contact force and its bending moments are then

obtained as follows:

$$F_{n,2,j} = F_{n3,2,j} / \sqrt{1 + \cos^2(\varepsilon_{2,j}) \cdot \tan^2(\delta_{2,j})} \tag{4.25}$$

$$F_{X,2,j} = -F_{n,2,j} \cdot \sin(\vartheta_i) \tag{4.26}$$

$$F_{Y,2,j} = +F_{n,2,j} \cdot \cos(\vartheta_i) \tag{4.27}$$

$$F_{a,2,j} = +F_{n,2,j} \cdot \tan(\delta_{2,j}) \cdot \cos(\varepsilon_{2,j}) \tag{4.28}$$

$$M_{X,2,j} = -F_{a,2,j} \cdot Y_{2,j} \tag{4.29}$$

$$M_{Y,2,j} = +F_{a,2,j} \cdot X_{2,j} \tag{4.30}$$

Since $F_{n3,2,j} = F_{n3,1,j}$, similar expressions can be derived for the male rotor.

4.4 Bearing Loads

Compression gas induced bearing radial loads can be determined by using the free body diagram of the rotor as shown in Fig. 4.7.

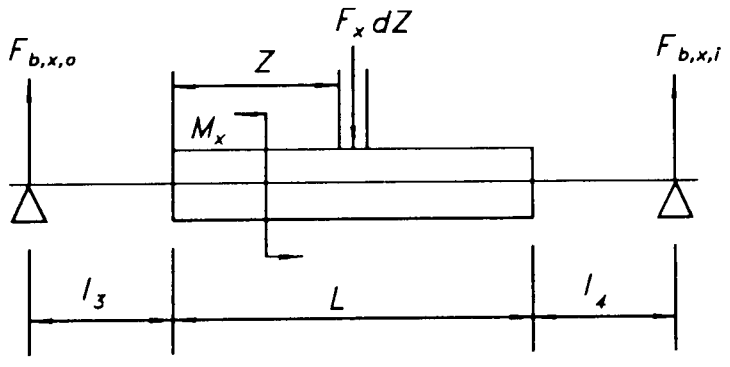

Figure 4.7 Free body diagram of the rotor

For a male rotor angle of rotation α the corresponding cavity volume ranges from $Z = 0$ to $Z = Z_c$, thus the radial forces in the X direction are given by:

$$F_{b,X,o,c} = -\int_0^{Z_c} F_x(Z) \cdot \frac{(l_4 + L - Z)}{(l_3 + L + l_4)} \cdot dZ$$

$$F_{b,X,i,c} = -\int_0^{Z_c} F_x(Z) \cdot \frac{(l_3 + Z)}{(l_3 + L + l_4)} \cdot dZ$$

Utilizing Eq. (4.13), and recalling $L = (h_1/2\pi)\cdot\varphi_w$, and adding the effects of the additional bending moments due to axial gas force, the above equations become

$$F_{b,X,o,c}(\alpha) = -\frac{h_1}{2\pi}p(\alpha)\int_0^{\bar{\varphi}} F_x(\alpha+\varphi)\frac{(\varphi_4+\varphi_w-\varphi)}{(\varphi_3+\varphi_4+\varphi_w)}d\varphi + \frac{M_X(\alpha)}{(\varphi_3+\varphi_4+\varphi_w)} \quad (4.31)$$

$$F_{b,X,i,c}(\alpha) = -\frac{h_1}{2\pi}p(\alpha)\int_0^{\bar{\varphi}} F_x(\alpha+\varphi)\frac{(\varphi_3+\varphi)}{(\varphi_3+\varphi_4+\varphi_w)}d\varphi - \frac{M_x(\alpha)}{(\varphi_3+\varphi_4+\varphi_w)} \quad (4.32)$$

where

$\varphi_3 = (2\pi/h_1)\cdot l_3$

$\varphi_4 = (2\pi/h_1)\cdot l_4$

The integration limits are the same as those used in the calculation of the torques, see Eq. (4.12a) and (4.12b).

And the overall bearing loads due to compression gas are

$$F_{b,X,o} = \sum_{j=0}^{\bar{z}_1-1} F_{b,X,o,c}\left(\alpha - \frac{2\pi}{\bar{z}_1}\cdot j\right) \quad (4.33)$$

$$F_{b,X,i} = \sum_{j=0}^{\bar{z}_1-1} F_{b,X,i,c}\left(\alpha - \frac{2\pi}{\bar{z}_1}\cdot j\right) \quad (4.34)$$

Obviously, the above procedure holds for male and female rotors and for the y direction as well.

Finally, the effects of the rotor contact forces were added to the above results. The method used is similar. For a male rotor angle of rotation α, the contribution of one cavity was obtained by integrating from the start point s to the end point e of the contact line. The overall effects of all the cavities were acquired by superposing the effects of all individual cavities.

4.5 Rotor Deflection

In general, the female rotor is less rigid but under larger loads than the male rotor in helical twin screw compressors. Accordingly, only the deflection of the female rotor is considered in this study, though the discussion here is applicable to the male rotor equally.

The rotor-shafts over the bearing span are divided into a set of small sections, each being of length ΔZ, as shown in Fig. 4.8. The deflection of each section may be assumed as a second order curve of the form

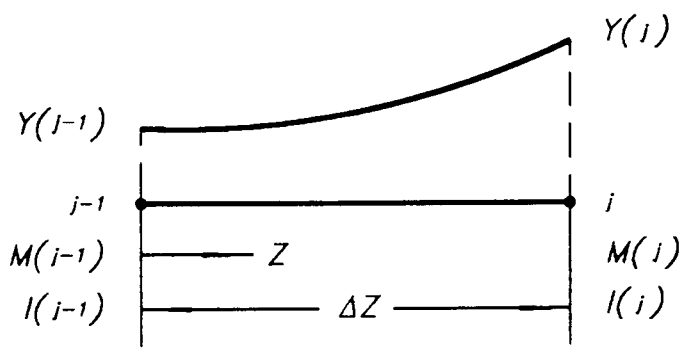

Fig. 4.8 Female rotor deflection

$$Y(Z) = A\cdot\left(\frac{Z}{\Delta Z}\right)^2 + B\cdot\left(\frac{Z}{\Delta Z}\right) + C \tag{4.35}$$

And its slope takes the form of

$$Y'(Z) = 2\cdot A\cdot\left(\frac{Z}{(\Delta Z)^2}\right) + \frac{B}{\Delta Z} \tag{4.36}$$

where Z is a coordinate originated from point *j-1*, while A,B,C are coefficients of the curve and can be determined using the boundary conditions at $Z = 0$ and $Z = \Delta Z$.

At $Z = 0$, there exist

$$Y(0) = C = Y(j-1)\ , \qquad Y'(0) = \frac{B}{\Delta Z} = Y'(j-1)$$

and at $Z = \Delta Z$ there exists

$$Y'(\Delta Z) = \frac{2\cdot A + B}{\Delta Z} = Y'(j)$$

After obtaining the coefficients A,B,C, the deflection at point j can be expressed as

$$Y(j) = A + B + C = Y(j-1) + \frac{[Y'(j-1) + Y'(j)]}{2} \cdot \Delta Z \tag{4.37}$$

In addition, the slope at point *j* may be correlated to slope at point *j-1* using the relation between the bending moment and the deflection:

$$Y''(Z) = \frac{M(Z)}{E \cdot I} \tag{4.38}$$

The above equation may be approximated as

$$Y'(j) = Y'(j-1) + \left(\frac{M(j-1)}{I(j-1)} + \frac{M(j)}{I(j)} \right) \frac{\Delta Z}{2 \cdot E} \tag{4.39}$$

Then, the deflection of the shaft can be determined according to the following procedure (point *0* and *N* denotes two bearing positions respectively):

- use known condition $Y(0) = Y(N) = 0$.
- assign an initial value to *Y'(0)*, e.g. *-0.0004*.
- calculate *Y'(1)*, then *Y(1)*, step by step until *Y(N)*.
- check if *Y(N) < 1E-10*, if not, change *Y'(0)*, and repeat calculation.

In this study the *Middle Point* method (Li, et al, 1981) was used for seeking the correct *Y'(0)* value and the speed of convergence was satisfactory. The number of the shaft sections is about 100.

However, the difficulties in calculating the rotor deflection of a helical screw compressor lie in the determination of the bending moment *M(j)* and the 2nd moment of area *I(j)*.

To calculate the bending moments, the maximum bearing loads corresponded male rotor angle of rotation α must be determined first, which defines the position of the rotor for calculating the deflection. It is noticed that the resultant bearing loads at the suction side usually do not have the same orientation as that at the discharge side. Accordingly, the calculation of the deflection has to been carried out in *X-Z* and *Y-Z* coordinate planes, respectively. Using the components of the maximum bearing loads and the

corresponding gas and contact forces applied to the rotors, the bending moments M_X, M_Y can then be determined.

Due to the helical lobes of the rotor, the 2nd moments of area I_X, I_Y vary along the rotor length. To obtain the relationship of I_X, I_Y with male rotor angle of rotation α, a method similar to the one described in section 4.2.2 was used, which utilizes Green's Equation to transfer the area integration of the 2nd moments of area into a curve integration around the boundary of the rotor cross-sectional area:

$$I_X = \iint Y^2 \cdot DXDY = \oint (-Y^3 \cdot DX - 2X \cdot Y^2 \cdot dY) \tag{4.40}$$

$$I_Y = \iint X^2 \cdot DXDY = \oint (2 \cdot X^2 \cdot Y \cdot DX + X^3 \cdot dY) \tag{4.41}$$

For a male rotor angle of rotation α, the coordinates of the boundary of the rotor cross-sectional area are known. Then the above integrations can be carried out numerically.

In addition to the deflection, the maximum tension stresses were also determined in this study, though the maximum values were low and not a problem for this kind of compressor.

4.6 Development of the Computer Program

The traditional method for calculating the bearing loads was to use the ideal gas equation to provide gas pressure data. However, the bearing loads and rotor deflection in the twin screw compressors are influenced by many factors. In a refrigeration compressor, for instance, the real compression process is complex, involving different refrigerants, oil injection, liquid and gaseous refrigerant injection, internal and external leakages, different port designs as well as different slide valve settings, etc. In order to take all these effects into account in a user friendly manner, a bearing load computation must link the

geometrical characteristics with an accurate simulation of the thermodynamic processes which take place.

Therefore, the bearing load program was integrated with the rotor profile generation program, geometrical characteristics program and a thermodynamic simulation program (for a *p-v* diagram, Tang and Fleming, 1992). The program was written in Turbo-Pascal and developed to be menu-driven. After reading rotor profile data, gas pressure data and rotor structural data, the rotor radial and axial forces and torques together with bearing loads and female rotor deflection can be computed. The results are automatically saved to disk files with the name specified. An overall results report (including the maximum bearing loads and their orientation and the maximum rotor deflection and its position) can be displayed on the screen and printed out by pressing the *p* while viewing. The program also facilitates displaying the following results on the screen:

- the variation of the rotor torques with α
- the variation of the axial forces with α
- the variation of the bearing radial loads with α
- the distribution of the gas radial loads along the rotor length
- the distribution of the female rotor stresses along rotor-shaft length
- the deflection of the female rotor-shaft

4.7 Verification of the Computer Program

The computer program was verified by comparing the predictions with the measurement data (Howden Compressors Ltd., 1991a) for the machine and working conditions specified below.

Compressor Specification

Compressor:	K200 (SRM)
Profile:	Standard asymmetric (A profile used)
	Addendum: 0.0294 D_1

	Radius of male rotor tip curve: 0.1863 D_1
	Range angles of male rotor tip curve: 9° and 10°
Outer Diameter:	$D_1 = D_2 = 204$ mm
Length/diameter ratio:	1.05
Male rotor wrap angle:	300°
Lobe combination:	4 + 6
Capacity control:	Slide valve
Discharge ports:	Axial and radial ports with same volume ratio of 4.3

Running Conditions

Compression Medium:	Air
Male rotor speed:	3000 rpm
Suction temperature:	20°
Oil injection:	Rate: 150-300 kg/min, Density: 920 kg/m^3,
	Temp.: 40°, Pressure: less than discharge pressure
Suction pressure:	1 bar
Discharge pressure:	2 to 8 bar
Discharge port:	Downwards

In Tables 4.1 and 4.2 the predictions of the program are compared with measured data. For a clearer view, the magnitude of the bearing forces are also shown in Figs. 4.9 and 4.10. It is to be noted that the bearing forces are represented by the bearing reactions, the direction of which are defined according to the coordinates system defined in Fig. 4.1. The zero degree of resultant force of the male rotor is thus towards the centre of the female rotor, and *vice versa*.

It can be seen that the calculated results are in general higher than the measurements at the inlet side, while lower at the outlet side. This may be partly caused by representing both bearing supports as point loads at the bearing centres when in reality their actual behaviour may be significantly different from this.

Table 4.1 Male rotor maximum bearing loads and their orientations

Discharge pressure (bar)	Inlet resultant N (direction of resultant deg)			Outlet resultant N (direction of resultant deg)		
	calculated	measured	± %	calculated	measured	± %
2	1586 (-37)	1505 (-45)	+5.4	1216 (-40)	1165 (-44)	+4.4
3	1773 (-35)	1685 (-42)	+5.2	1259 (-36)	1350 (-37)	-6.8
4	1921 (-33)	1875 (-41)	+2.5	1272 (-33)	1525 (-32)	-16.6
5	2204 (-31)	2075 (-39)	+6.2	1359 (-29)	1760 (-27)	-22.8
6	2647 (-31)	2285 (-38)	+15.8	1596 (-24)	1935 (-24)	-17.5
7	3076 (-30)	2545 (-37)	+20.9	1823 (-20)	2145 (-22)	-15.0
8	3495 (-29)	2755 (-37)	+26.9	2072 (-17)	2380 (-19)	-13.0

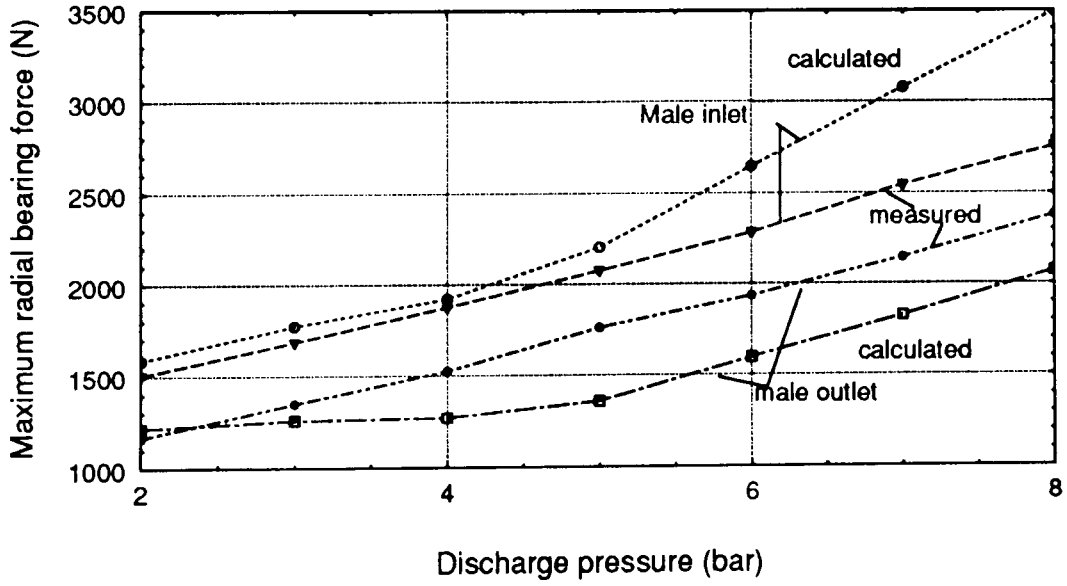

Fig. 4.9 Comparison between calculated and measured radial bearing loads (male rotor)

Of total 28 data sets compared, over 82 percent of the predictions reasonably matches the measured data with their difference in magnitude lower than 20 percent. The predictions of the direction of resultant forces are in a good agreement with the measured values, especially for the female rotor (see Table 4.2).

Table 4.2 Female rotor maximum bearing loads and their orientations

Discharge pressure (bar)	Inlet resultant N (direction of resultant deg)			Outlet resultant N (direction of resultant deg)		
	calculated	measured	± %	calculated	measured	± %
2	1765 (-60)	1520 (-56)	+16.1	2404 (-38)	2730 (-48)	-12.0
3	1897 (-59)	1700 (-55)	+11.5	2588 (-36)	2985 (-42)	-13.3
4	1991 (-58)	1850 (-54)	+7.6	2718 (-35)	3435 (-40)	-20.9
5	2188 (-56)	2075 (-53)	+5.4	2989 (-33)	3605 (-40)	-17.1
6	2543 (-55)	2255 (-52)	+12.8	3526 (-32)	3905 (-39)	-9.7
7	2859 (-54)	2450 (-53)	+16.7	4013 (-31)	4280 (-37)	-6.2
8	3182 (-54)	2590 (-53)	+22.9	4508 (-30)	4730 (-35)	-4.7

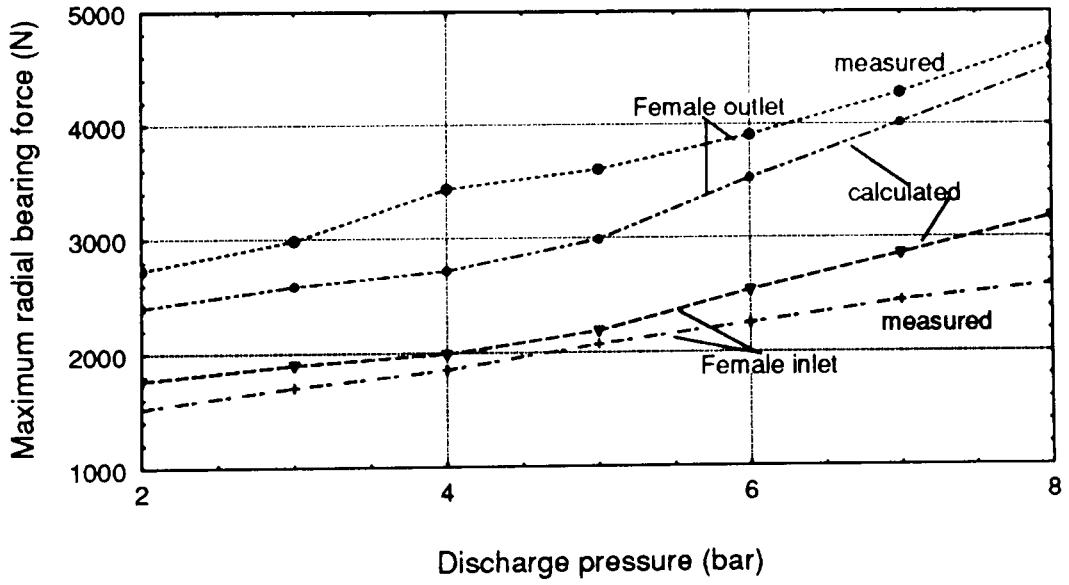

Fig. 4.10 Comparison between calculated and measured radial bearing loads (female rotor)

In general, it can be concluded that the calculated results give an encouraging level of agreement with the measured data, given the simple bearing support model and the seemingly crude assumption of an inter-rotor contact force of constant magnitude along the contact line for a male rotor angle of rotation α.

4.8 Working Model

To demonstrate the capability of this integrated program a numerical example relating to an oil injected refrigeration compressor model is now presented. Its main geometrical and running conditions are as follows:

Profile type:	SRM D	Lobe combination:	4+6
Centre distance:	160 mm	Outer Diameter of rotors:	204 mm
Working medium:	R22	Length/diameter ratio:	1.65
Male rotor speed:	3000 rpm	Suction pressure:	4.21 bar
Suction superheat:	30 °C	Discharge pressure:	15.34 bar
Discharge port:	Downwards	Slide valve:	Closed

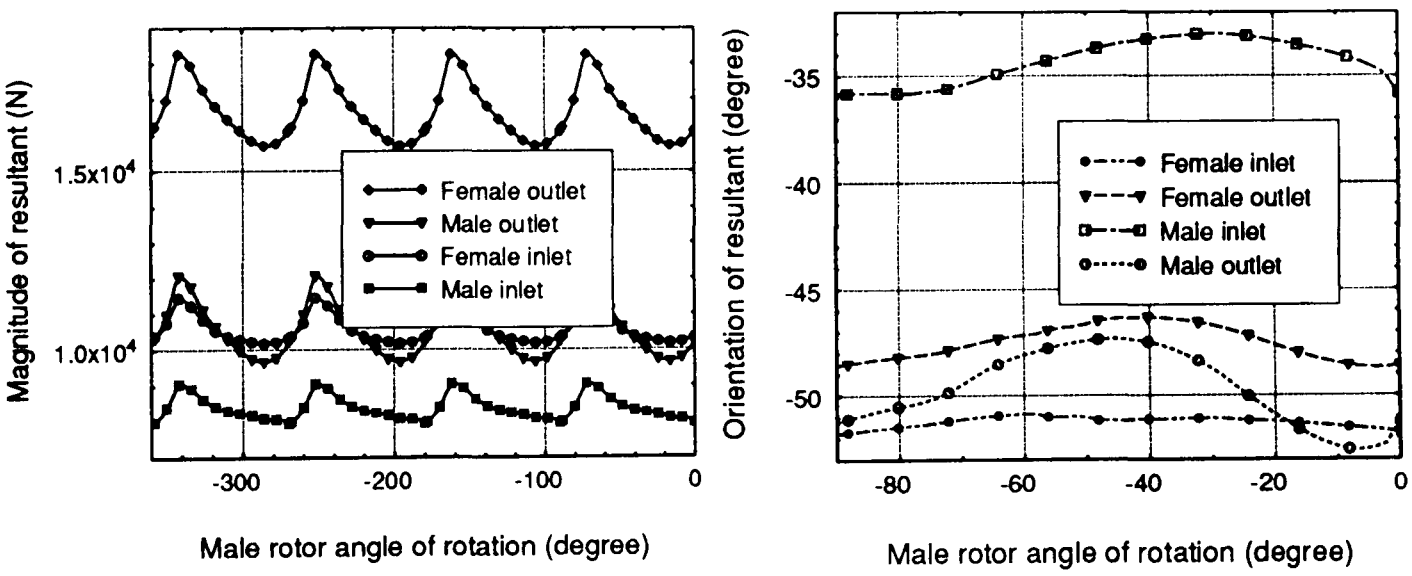

Fig. 4.11 Variation of bearing radial loads with male rotor angle of rotation[1]

At full volumetric capacity (slide valve closed) the variation of bearing radial and axial loads with male rotor angle of rotation is shown in Figs. 4.11 and 4.12. As expected, the bearing loads vary with time periodically, with a frequency equivalent to the male rotor rotating speed multiplied by the number of male rotor lobes. It can be seen that the axial load on the male rotor is the largest one among all of the components and is about 3 times of that on female rotor. In contrast, the radial loads on the female rotor are higher than

[1] One period only shown for the orientation of resultant

those on the male rotor, and the loads on the discharge end bearings are larger than those on the suction end bearings.

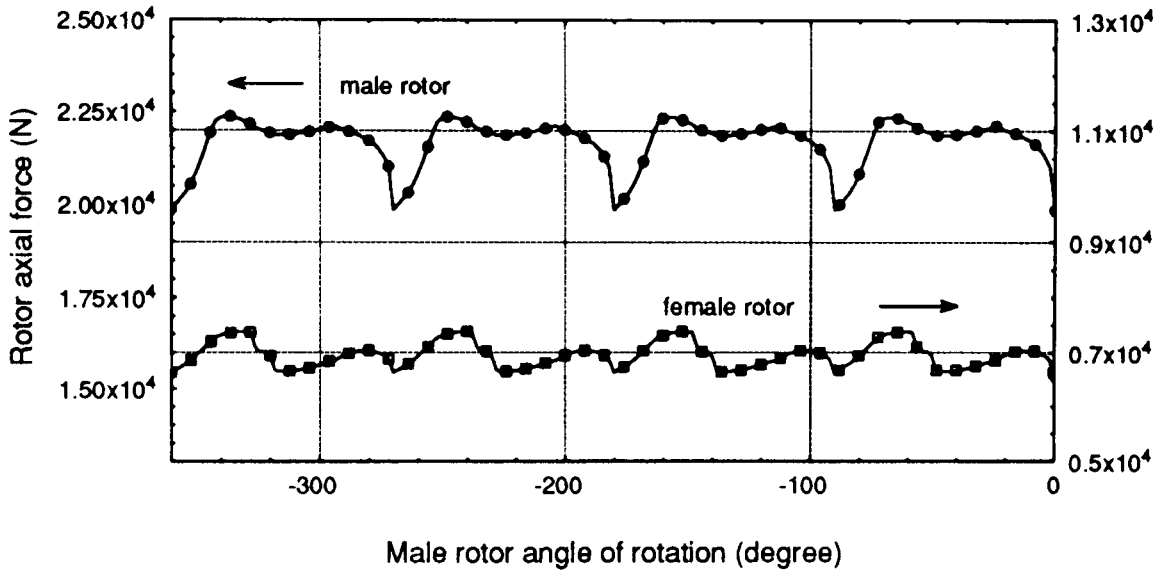

Fig. 4.12 Variation of bearing axial loads with male rotor angle of rotation

The variation of the gas torques with the male rotor angle of rotation is shown in Fig. 4.13. It can be seen that the female rotor resisting torque is very small compared with that of the male rotor. It implies that only a small part of input power needs to be transferred to the female rotor. The negative sign of the torques means that the torques are opposite in sign to that of the rotation of the rotors.

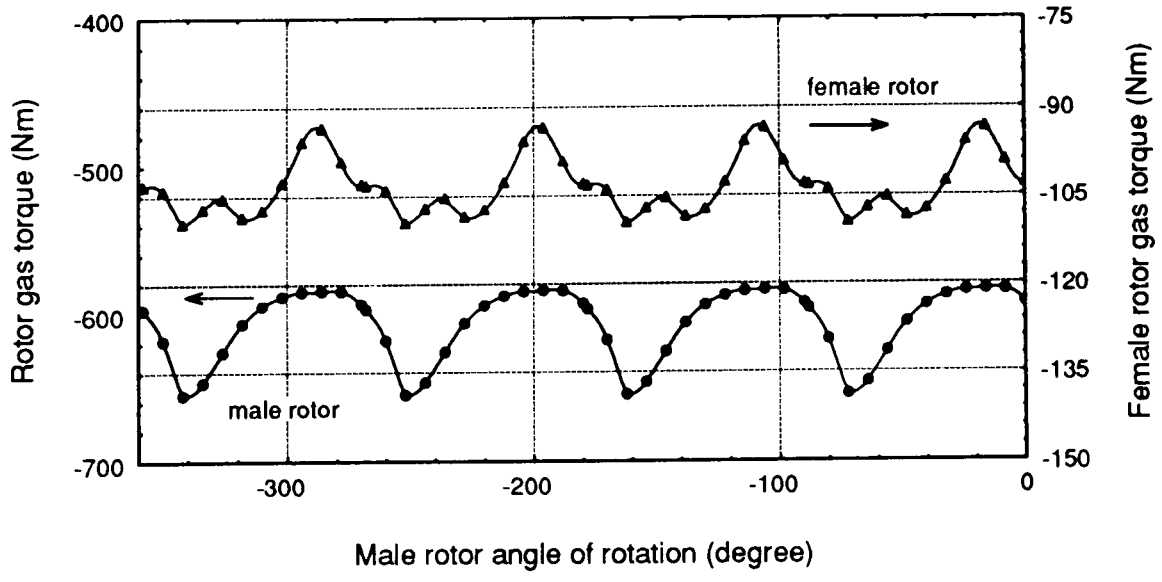

Fig. 4.13 Variation of gas torques with male rotor angle of rotation

Fig. 4.14 shows the deflection of the female rotor-shaft. As expected, the maximum deflection occurs at the position relatively close to the discharge side end of the rotor. Its value is about 0.0123 mm.

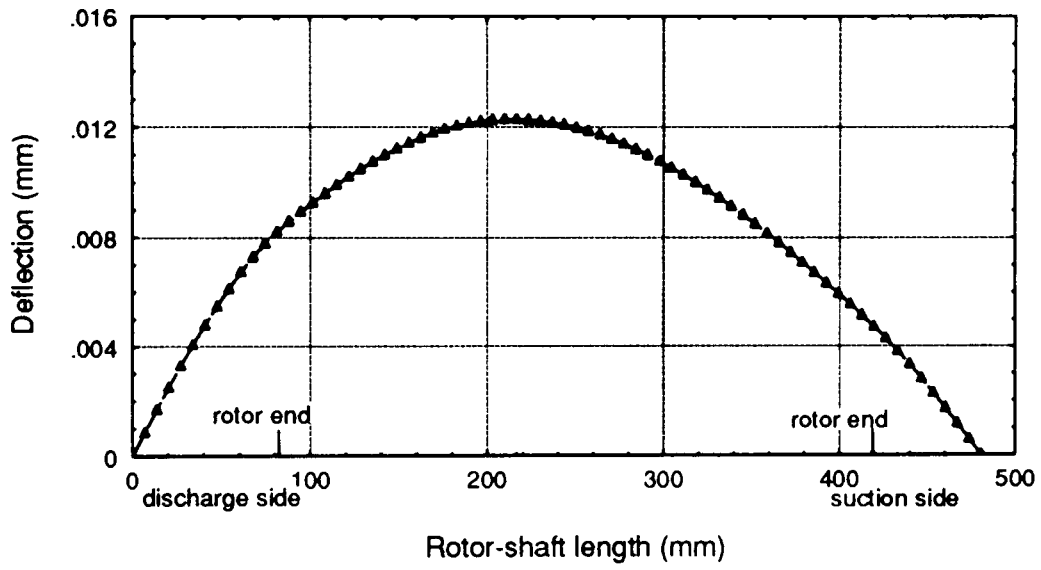

Fig. 4.14 Deflection of the female rotor-shaft

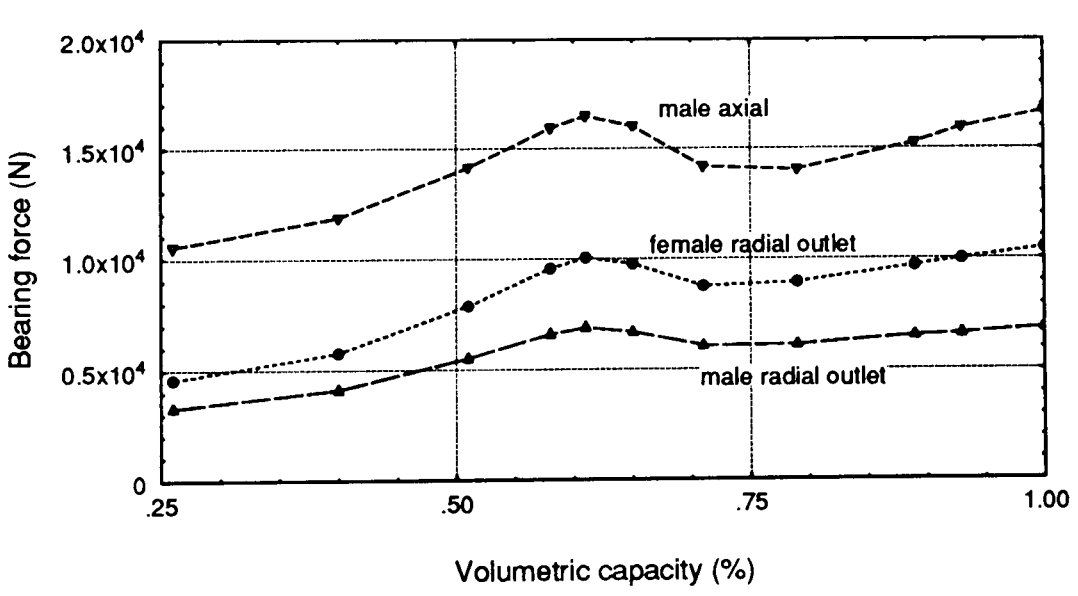

Fig. 4.15 Variation of maximum bearing forces vs volumetric capacity

With the integrated program, the bearing forces at different running conditions, e.g. different suction and discharge pressures, different slide valve settings, etc. can be easily obtained. A example is given in Fig. 4.15, with evaporating and condensing temperature being -5 °C and 40 °C respectively and volumetric capacity ranging from 18% to 100%. It can be seen that the second highest peak value appears at a volumetric capacity of about 60%. As

will be discussed later in Chapter 6, this value may become larger than that at full capacity in a compressor containing a slide stop of an unwisely chosen length.

4.9 Conclusions+

A bearing load program has been integrated with a geometrical calculation program and a performance simulation program. The result is a calculation facility which is capable of computing the torques and bearing forces of a helical twin screw compressor for various settings of geometrical parameters and running conditions. Sophisticated techniques were used in the bearing force program to calculate the contributions of all influencing factors such as rotor contact, axial components of gas forces on screw surfaces and on the rotor end planes. The program was verified by comparing the predictions with the measured radial bearing forces. The capability of such an integrated program has been demonstrated by applying it to a compressor for a range of slide valve settings.

+ The first part of this chapter, *Computerized analysis of gas compression induced rotor forces and torques*, has been presented at the International Compressor Engineering Conference, Xian, China, July 1993 (You, et al, 1993).

The second part of the chapter, *Rotor contact forces and the integrated bearing force analysis program,* has been presented at the International Compressor Engineering Conference at Purdue, USA, July 1994 (You, et al, 1994a).

Chapter 5

Optimum Lobe Tip Designs and Rotor Geometrical Parameter Combinations

5.1 Introduction

Modern rotor profiles have made possible the design and manufacture of high efficiency twin screw compressors. However, making the right choice of rotor profile is not on its own enough to ensure a high performance screw compressor. One of the major characteristics of the design process of a modern rotor profile, like the SRM D-profile, is its flexibility. The profiles can be applied to various applications with the potential of obtaining high performance. However, the potential achieved depends to a great extent on the choice of profile parameters and rotor geometrical parameters.

The definition of a profile, e.g. SRM D-profile, requires many parameters, as can be seen in Fig. 2.4 of section 2.3. Each parameter may influence the compressor performance in one or more aspects. The pressure angles at the pitch circle of the male rotor, for instance, govern whether the rotors are easy to machine, while the width of the female rotor lobes affects the rigidity of the rotor. In this study not all of these profile parameters are discussed. The discussion in this chapter concentrates on some of the parameters which

influence the design of lobe tips. Although much work has been done in this area associated with the development of the modern rotor profiles (e.g. Astberg, 1984; Edström, 1985), few publications have been found on the following two topics: (i) oil viscous friction loss at the lobe tips, and (ii) the effects of the lobe tips on the compressor efficiency, capacity and rotor contact force. An investigation of these two topics with respect to the optimum lobe tip designs has been conducted and the results are presented in sections 5.2 and 5.3, respectively.

Rotor geometrical parameters are as follows: rotor lobe combination, length / diameter ratio and wrap angle. Virtually any practical profile can be combined with any practical rotor geometry. The skill of the designer lies in choosing the best combination for his/her application. Much work has been carried out on the optimization of these parameters (Edström, 1985; Singh, 1986; Peveling, 1987; Pamlin, 1992; Fleming, et al, 1994). However, previous work has been mainly concentrated on their influence on the volumetric and indicated efficiencies of the compressor. A very good paper written by Pamlin (1992) described the importance of taking the female rotor deflection into account when making the choice of lobe combination. However, since in his simulation a relatively high pressure level was used, some of the conclusions are in doubt if running conditions are changed. In addition, influencing factors such as bearing forces and rotor contact force were not taken into account, which, in fact, are very important and sometimes are critical, e.g. when deciding the length / diameter ratio. For an optimum rotor physical parameter combination, all these and many other practical factors such as ease of manufacture and installation, must also be taken into account. In this study, a comprehensive parameter study with four commonly used lobe combinations together with five different length / diameter ratios and five different wrap angles has been conducted and the results are presented in section 5.4.

The chapter is summarised in section 5.5 with many conclusions and practical recommendations.

5.2 Lobe Tip Designs with Respect to Oil Viscous Friction Loss

The injection of oil directly into the compression cavities of the helical twin screw compressor was an innovation which enormously increased the range of applications of the machine. Its application to process refrigeration has been particularly successful (Sjöholm, 1986; Shaw, 1990).

The influence of oil injection upon the screw compressor performance has been studied by a number of researchers (e.g. Kauder and Piatkowski, 1987; Stošić, et al, 1988, 1990). In general, the injection of oil has the following results: the rotors do not have to be manufactured to as high an order of accuracy as is needed in a dry machine because the oil acts as a sealant between the rotors and the housing and between each other; the accurate timing gears of the dry machine can be eliminated so that one rotor drives the other directly; and the oil cools the gas being compressed bringing the compression closer to isothermal with a gain in thermodynamic efficiency.

However, the injection of oil has the disadvantage of requiring a greater power input to the driven rotor to overcome the viscous friction of the oil film, an effect which is greatest at the greatest rotor radius i.e. between the tips and the bores. This section presents a method for the calculation of this viscous friction loss and examines the effects of different lobe tip designs on both the viscous friction loss and cusp blow hole area, the geometry of which depends critically on tip shape.

5.2.1 Viscous Friction Calculation

This study was based on the SRM-asymmetric type profiles shown in Figs. 2.9 and 2.10 (section 2.4), in which lobe tips are designed with or without sealing strips, as shown in Fig. 5.1. For designs without sealing strips, the male lobe

tip appearance (case *A*) is mainly determined by two tip angles β_3 and β_4, while the female lobe tip shape (case *C*) is similarly described by tip angle β_7 and the radius of two minor circular arcs r_5 and r_9. For designs with sealing strips, cases *B* and *D* in Fig. 5.1, more parameters were included such as the widths of the sealing strips W_1, W_2, the range angles of concave sections of male rotor β_5 and β_6, and the height of sealing strip of female rotor H_3. These parameters not only influence the lobe tip appearance but also the viscous friction loss of lobe tips.

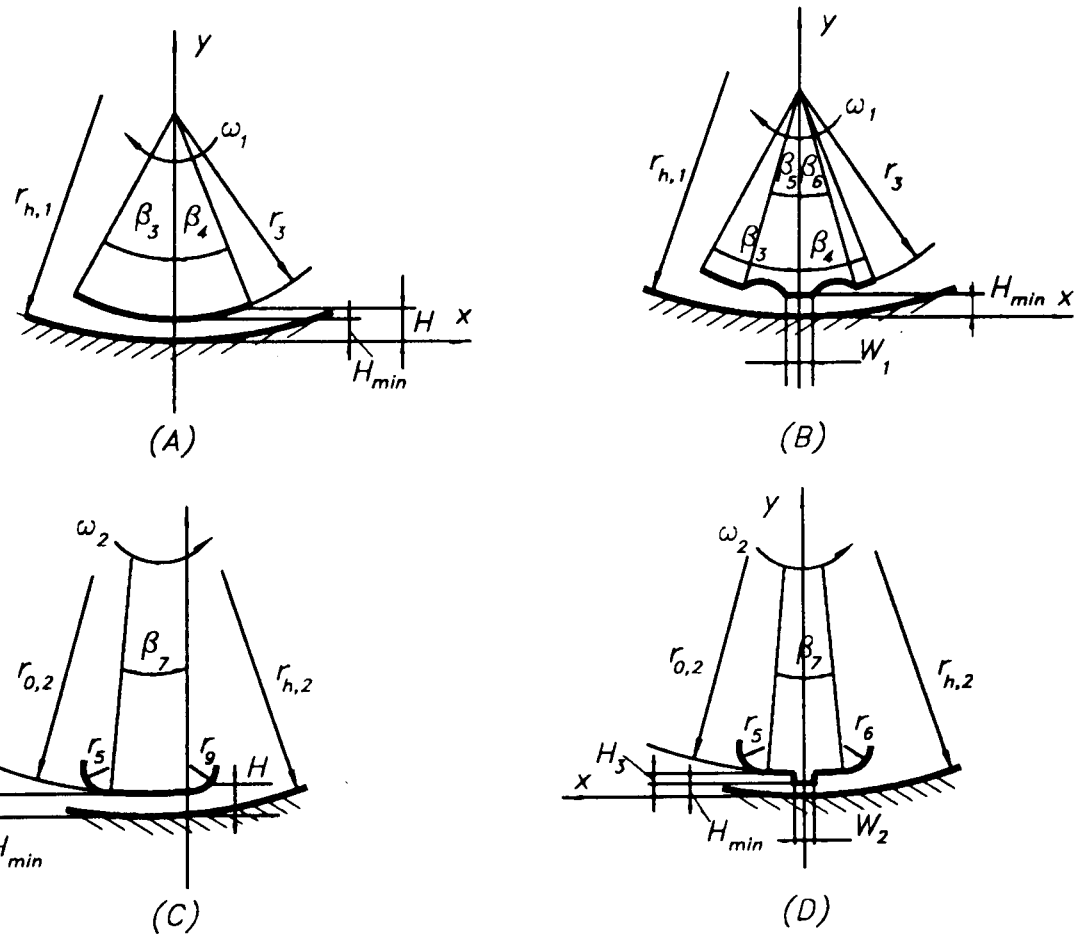

(A) male rotor without sealing strip (B) male rotor with sealing strip

(C) female rotor without sealing strip (D) female rotor with sealing strip

Fig. 5.1 Lobe tip designs

Following assumptions were utilized in the calculation of viscous friction loss at the lobe tips:

- The viscosity and density of the oil were uniform everywhere in the machine and did not vary with time. This assumption was held to be valid for

small quantities of injected oil having a small thermal mass which is quickly mixed with existing oil and spread around the cavity. The effect of pressure variation on oil viscosity was also considered to be negligible in such circumstances.

- The one-dimensional Reynolds equation was assumed applicable. The pressure is constant through the thickness of the film.
- The lubricant oil was taken to be a newtonian fluid and thus Newton's viscous law could be used.
- There is no slip at the boundaries. The velocity of the oil layer adjacent to the boundary is the same as that of the boundary.

According to Newton's viscous law, the shear stress on a surface is

$$\tau = \eta \frac{\partial u}{\partial y} \tag{5.1}$$

then the total frictional force F is

$$F(\alpha) = l(\alpha) \cdot \int_0^B \tau \, dx = l(\alpha) \cdot \eta \cdot \int_0^B \frac{\partial u}{\partial y} dx \tag{5.2}$$

where $l(\alpha)$ is the tip sealing line length of rotor which varies with male rotor angle of rotation α, and B stands for the effective acting range of oil on the surface.

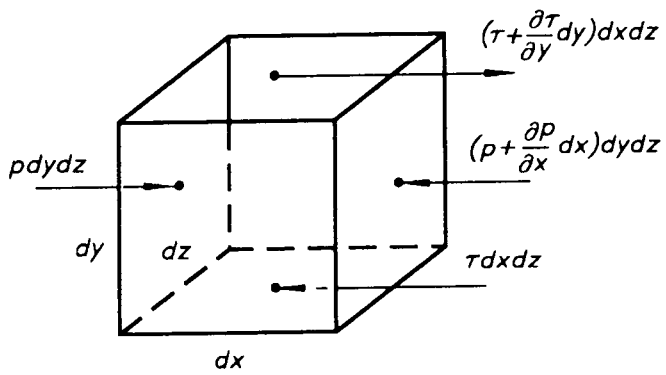

Fig. 5.2 Equilibrium of an element

From the equilibrium of an element, Fig. 5.2, there exists

$$\frac{\partial \tau}{\partial y} = \frac{\partial p}{\partial x} \tag{5.3}$$

Substituting Eq. (5.1) into the above equation leads to

$$\frac{\partial}{\partial y}\left(\eta \frac{\partial u}{\partial y}\right) = \frac{\partial p}{\partial x}$$

which can be integrated since p is not a function of y, thus

$$\frac{\partial u}{\partial y} = \frac{1}{\eta}\frac{dp}{dx}\left(y - \frac{H}{2}\right) + \frac{(U_1 - U_2)}{H} \tag{5.4}$$

where H is the oil film thickness, and U_1, U_2 are the speeds of the fluid at the surfaces $y = 0$ and $y = H$ respectively, which, according to the assumption, are the speeds of the boundary surfaces.

Recalling Reynolds equation in one dimension

$$\frac{dp}{dx} = 6\,(U_1 + U_2)\cdot\eta\cdot\frac{H - \bar{H}}{H^3} \tag{5.5}$$

where $\bar{H}$ is the oil film thickness when $dp/dx = 0$ and substituting Eqs. (5.4) and (5.5) into Eq. (5.2) results in

$$F = l(\alpha)\cdot\eta\cdot\int_0^B \left[3(U_1+U_2)\frac{H-\bar{H}}{H^2} + \frac{(U_1 - U_2)}{H}\right]dx \tag{5.6}$$

Two terms are to be integrated on the RHS of the above equation. The first is due to the distortion of the velocity distribution which gives rise to the pressure generation. The second term is the simple viscous frictional shear with a linear velocity gradient. Both terms exist when considering the lobe tip viscous friction loss in a helical screw compressor.

To make the above integration solvable the function $\bar{H}$ must be defined. This depends on the pressure distribution in the oil film. Due to the difficulty in obtaining the real pressure profile, it is assumed, as in many other applications (Cameron, 1981), that the Reynolds or Sommerfeld condition can be used, depending on different lobe tip designs.

For case (A) in Fig. 5.1 $\bar{H}$ derived from the Reynolds condition is

$\bar{H} = 1.22575\, H_{min}$ (Cameron, 1981). Since only the lobe tip is of interest, the integration limits for the first term in Eq. (5.6) were taken as x_s to $\bar{x}$, and for the second term as x_s to x_e, where

$$x_s = -r_3 \sin(\beta_3)$$

$$\bar{x} = \sqrt{2 \cdot H_{min} \cdot \left(\frac{\bar{H}}{H_{min}} - 1 \right) \cdot \left(\frac{1}{1/r_3 - 1/r_{h,1}} \right)}$$

$$x_e = r_3 \sin(\beta_4)$$

Then the integration can be carried out numerically.

For case (B), a male rotor with sealing strips, it was assumed that the concave sections simply reduce the effective surface range, and therefore the same integration method used for case (A) was used except that the integration limits were changed appropriately.

Similarly, the above method was applied to the minor circular arc of radius r_9 of case (C) in Fig. 5.1. However, instead of Reynolds' condition, the half-Sommerfeld condition was used since the arc extends only to the minimum oil film thickness H_{min}. $\bar{H}$ was obtained as $\bar{H} = 1.7778\, H_{min}$. As the tip width corresponding to β_7 is concentric with the rotor bore, only the second term of the integration in Eq. (5.6) exists with H being constant. The effect of another minor arc r_5 was negligible due to oil rupture phenomena at the trailing part.

Finally, case (D) in Fig. 5.1 differs from case (C) due to the introduction of a sealing strip which in effect forms a converging shape at the lobe tip. This part was approximately simulated as a Rayleigh step (Cameron, 1981): the pressure gradients were linear in two steps of oil film thickness H_{min} and $H_{min} + H_3$, of length B_3 and B_4, respectively, i.e.

$$\left(\frac{dp}{dx}\right)_3 = \frac{p_{max}}{B_3}, \quad \left(\frac{dp}{dx}\right)_4 = \frac{p_{max}}{B_4}$$

where the maximum pressure equals

$$p_{max} = \frac{6(U_1+U_2)\cdot\eta\cdot(H^*-1)}{H_{min}^2\cdot\left(\frac{(H^*)^3}{B_3}+\frac{1}{B_4}\right)} \quad \text{with} \quad H^* = \frac{H_{min}+H_3}{H_{min}}.$$

After calculating the viscous friction the power loss was then obtained

$$P = F\cdot U \tag{5.7}$$

where U is the lobe tip speed.

5.2.2 Working Model

A compressor model was used in this study with its main parameters shown below:

- Outer diameter of rotors: 204 mm
- Centre distance: 160 mm
- Male rotor wrap angle: 300 °
- Lobe Combination: 4+6
- Length / diameter ratio: 1.65
- Rotor profile: SRM-D

The lobe tip design parameters are shown in Table 5.1. The male and female lobe tip clearances are 0.063 and 0.058 mm, respectively.

Table 5.1 Lobe tip design parameters

β_3 (deg)	β_4 (deg)	β_5 (deg)	β_6 (deg)	β_7 (deg)	H_3 (mm)	$\frac{r_9}{C}$	$\frac{W_1}{C}$	$\frac{W_2}{C}$
15	8	7	7	6.15	0.32	0.01	0.01	0.01

The thermodynamic performance was computed by using the University of Strathclyde's simulation program (Tang and Fleming, 1992) for the following case:

- Working fluid: *R* 22
- Evaporating / condensing temperature: -5.0 / 25.0 °C
- Suction / discharge pressure: 4.21 / 10.44 bar
- Suction superheat: 30.0 °
- Male rotor speed: 3000 rpm
- Capacity control: slide valve closed

- Volume ratios for radial / axial discharges: 2.6 / 5.0
- Rate and temperature of oil: 150 kg/min, 40 °C
- Viscosity of oil: 0.05106 N.s/m^2

This working model and the running conditions were derived from a test compressor, with its lobe tips having sealing strips (Howden Compressors Ltd, 1991b). The calculation of the viscous friction loss as described here could thus be compared with the experimental results. The simulation of the compression process gave a calculated value for the indicated power of 154.20 kw. The viscous friction power loss at the rotor tips was calculated here to be 5.17 kw, giving a combined power consumption of about 160 kw, 14 kw less than the total measured power input of 174 kw. This is as expected since the viscous friction power losses also exist in the other "contact" regions, namely the rotor flanks and rotor end faces. In addition, power is also needed to increase the kinetic energy of the injected oil (150-300 kg/min). A calculation for this based on the assumption that all the oil mass flow rate of 150 kg/min has its velocity increased from zero in the circumferential direction up to the rotor circumferential velocity at the outer radius of the rotor of 102 mm, gives a power consumption of about 2.5 kw. This leaves about 12.2 kw for dissipation in viscous effects at the meshing region and the end faces and all other mechanical losses, which seems not unreasonable.

Accurate calculations of oil momentum change loss, meshing loss, end face loss and other friction losses are outside the scope of this present work and are suggested as suitable topics for future work.

5.2.3 Discussion

The effects of lobe tip design parameters on both the blow hole leakage loss and viscous friction loss were investigated. The study was carried out in mono-parameter way, i.e. only one parameter was changed at a time. The initial values of the lobe tip design parameters are given in Table 5.1.

Lobe tip designs with and without sealing strips

The computational results for lobe tip designs with and without sealing strips (using the above parameters) are tabulated in Table 5.2. As the sealing strips are of a very small height, their use results in a small increase in blow hole area, which did not cause a significant increase in the leakage loss through the blow hole. Accordingly, the volumetric efficiency remained almost unchanged. In contrast, the introduction of sealing strips significantly decreased the lobe tip viscous power loss by about 78% compared with the design without sealing strips. Although this figure was obtained with the above mentioned parameter combination, a similar tendency can be expected in general since the increase in the blow hole area will be small in general.

Table 5.2 Comparison between lobe tip designs with or without sealing strips

Parameters		Without sealing strips	With sealing strips
Blow hole area (mm^2)		26.52	28.24
Leakage through blow hole (kg/min)	out	15.916	16.927
	in	14.576	15.507
	net	1.340	1.420
Volumetric efficiency		93.86	93.85
Indicated power (kw)		154.20	154.42
Lobe tip viscous friction power loss * (kw)	male rotor	14.26	2.32
	female rotor	9.20	2.85
	total	23.46	5.17
Power loss ratio (%)		15.21	3.35

* The mean values are used due to their small variation with male rotor angle of rotation.

However, the use of sealing strips will make the manufacture of rotors more complicated. It is, therefore, most likely that two types of lobe tip design will continue being used in practice. Thus, it is meaningful to examine both arrangements.

Effects of tip parameters on designs **without** sealing strips

For lobe tip designs without sealing strips the main parameters include tip angles β_3, β_4 and β_7 and the radius of the leading circular arc r_9 (Fig. 5.1). The computation results for different tip angles are tabulated in Table 5.3. It can been seen that none of the changes in tip angles caused a significant change in blow hole leakage loss, which is of course only a fraction of the total cavity leakage. However, with the decrease of the leading tip angle β_3 from 15 to 8 degrees the viscous friction loss is reduced by about 20%.

Table 5.3 Effects of tip design angles β_3, β_4 and β_7 (without sealing strips)

Parameters		Case 1	Case 2	Case 3	Case 4
Male lobe tip angle β_3 (deg)		15.0	13.0	11.0	8.0
Male lobe tip angle β_4 (deg)		8.0	6.0	4.0	8.0
Female lobe tip angle β_7 (deg)		6.15	6.34	6.55	5.60
Blow hole area (mm^2)		26.52	25.93	25.53	26.52
Theoretical capacity (m^3/min)		20.31	20.31	20.31	20.31
Leakage through blow hole (kg/min)	out	15.916	15.601	15.372	15.983
	in	14.576	14.276	14.097	14.638
	net	1.340	1.325	1.275	1.345
Volumetric efficiency		93.86	94.19	93.97	94.21
Indicated power (kw)		154.20	153.93	154.19	154.08
Lobe tip viscous friction power loss * (kw)	male	14.26	13.01	11.51	11.05
	female	9.20	8.82	9.31	7.93
	total	23.46	21.83	20.82	18.98
Power loss ratio (%)		15.21	14.18	13.50	12.32

* The mean values are used due to their small variation with male rotor angle of rotation.

Similar results were obtained with the variation of r_9 as shown in Table 5.4. Increasing the ratio r_9 / C from 1.0 to 5.5% increased the blow hole area by about 20%, but the volumetric efficiency remains almost unchanged. The reason for this is the reduction in leakages through the tip/bore clearances due

to the increase in tip width. Changing the value of r_g / C from 1.0 to 5.5% reduced the viscous friction power loss by about 12%.

Table 5.4 Effects of r_g of female rotor (without sealing strips)

Parameters		Case 1	Case 2	Case 3	Case 4
r_g / C		0.010	0.025	0.040	0.055
Blow hole area (mm^2)		25.89	26.52	27.98	30.96
Theoretical capacity (m^3/min)		20.31	20.31	20.31	20.31
Leakage through blow hole (kg/min)	out	15.542	15.916	16.862	18.56
	in	14.234	14.576	15.453	17.01
	net	1.308	1.340	1.409	1.55
Volumetric efficiency		93.82	93.86	94.31	93.88
Indicated power (kw)		154.09	154.20	153.72	154.81
Lobe tip viscous friction power loss * (kw)	male rotor	14.23	14.23	14.23	14.23
	female rotor	9.30	9.20	7.64	6.47
	total	23.53	23.46	21.87	20.69
Power loss ratio (%)		15.27	15.21	14.23	13.36

* The mean values are used due to their small variation with male rotor angle of rotation.

Effects of tip parameters on designs **with** sealing strips

The effects of the main parameters of lobe tip designs with sealing strips are tabulated in Table 5.5. It can be seen that the width of the sealing strips has the most significant influence of all the parameters considered, with a decrease of W_1 / C from 4.0% to 1.0% resulting in a decrease of viscous friction loss by about 63%. Thus, from the point of view of viscous friction loss the sealing strip should be designed to be as narrow as possible.

It can be seen that the increase of the concave range angles β_5 and β_6 of the male lobe tip results in a very limited decrease in viscous friction power loss. Similar results were obtained with the variation of the sealing strip height of the female lobe tip, H_3.

Table 5.5 Effects of W_1, W_2, β_5, β_6 and H_3

Parameters		Lobe tip viscous friction power loss * (kw)		
		Male rotor	Female rotor	Total
$\frac{W_1}{L} = \frac{W_2}{L}$	0.01	2.32	2.85	5.17
	0.02	4.37	3.73	8.10
	0.03	6.53	4.60	11.13
	0.04	8.54	5.46	14.00
β_5 , β_6 (deg)	$\beta_5 = \beta_6 = 4$	4.70	2.85	7.55
	$\beta_5 = \beta_6 = 7$	2.32	2.85	5.17
	$\beta_5 = 9$, $\beta_6 = 7$	1.87	2.85	4.72
	$\beta_5 = 13$, $\beta_6 = 7$	1.32	2.85	4.17
H_3 (mm)	0.2	2.32	3.37	5.69
	0.4	2.32	2.59	4.91
	0.6	2.32	2.19	4.51

* The mean values are used due to their small variation with male rotor angle of rotation.

5.2.4 Conclusions

The following conclusions can be drawn from this study:

- The method used to compute the viscous friction loss of lobe tips in a oil injected helical screw compressor appears to have promising accuracy given the unknowns which still exist, e.g. friction on rotor flanks and rotor ends, and the speeding up of the injected oil.

- The introduction of sealing strips could greatly reduce the viscous friction loss, without at the same time causing a significant increase in blow hole leakage loss;

- For a lobe tip design without sealing strips a relatively small leading tip angle of the male rotor β_3 and a relatively big radius of leading circular arc

r_g could also reduce the viscous friction loss to some extent, without at the same time causing an increase in blow hole leakage loss;

- For a lobe tip design with sealing strips a further reduction of viscous friction can be achieved by making the sealing strip as narrow as possible.

5.3 Lobe Tip Designs with Respect to Efficiency, Capacity and Contact Force

The demands for compressor high efficiency, high capacity / power ratio and low contact force (hence long rotor life) are always present. Compared with certain other performance influencing parameters, the effect of lobe tip design parameters are relatively small and therefore have received comparatively little attention.

The contact force between the rotors is related to the torque transmitted directly from one to the other. Most helical twin screw compressors utilize male rotor drive. The advantage of this arrangement is that only a small part of the input torque is transmitted to the female rotor. A simulation carried out by the author has shown that the torque transmitted ratio, the ratio of transmitted torque over the input torque, is to a great extent influenced by the male lobe tip segment designs.

In general, the requirements for high efficiency, large capacity and low contact force do not always lead to the use of same lobe tip design parameters. Indeed, a compromise is often needed and the tip design parameters must be optimised accordingly.

Taking SRM D-profile as an example and utilizing the University of Strathclyde's performance simulation program (Tang and Fleming, 1992) and the force analysis program described in Chapter 4, a parameter study has been carried out and the results are presented in this section.

As shown in Fig. 5.3, the main parameters defining the tips of the SRM D-profile include the radius of the male rotor crest r_3, its corresponding range angles β_3, β_4, the radius of the minor circular arc r_6 and the female rotor addendum A. For obtaining an optimum lobe tip design, the effects of these parameters are examined in such a way that each time only one parameter is changed. Unless otherwise specified, the parameters and running conditions used in the computation are given below.

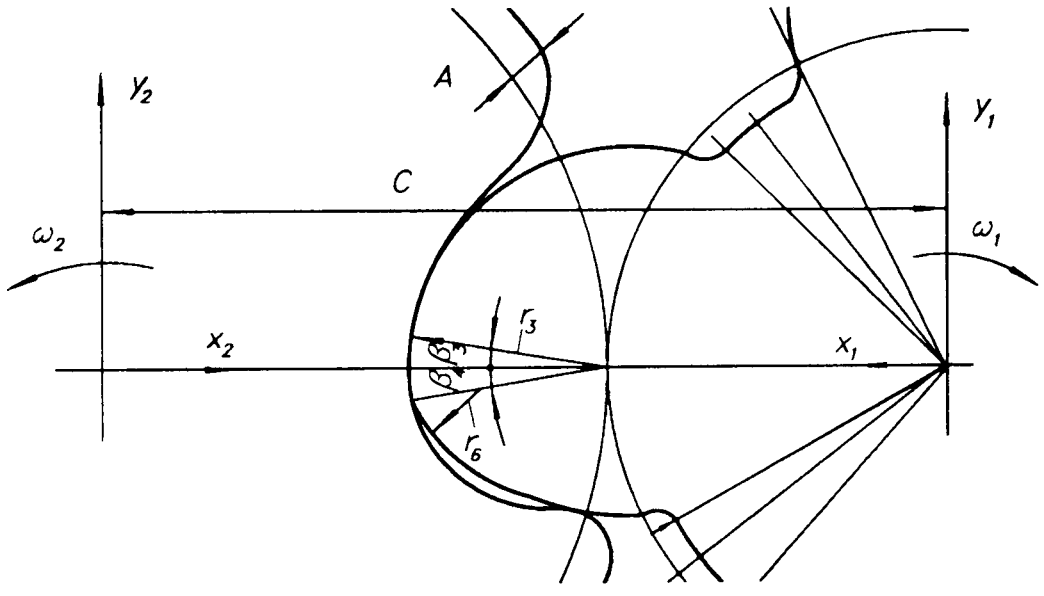

Fig. 5.3 Rotor tip of SRM D-profile

- Rotor profile and lobe combination: SRM-D, 4/6
- Outer diameter and centre distance of the rotors: 204, 160 mm
- Length / diameter ratio and male rotor wrap angle: 1.65, 300 °
- Driving rotor and rotating speed: Male, 3000 rpm
- Medium, evaporating and condensing temperature: *R22*, -5, 40 °C
- Suction / discharge pressure: 4.21 / 15.34 bar
- Oil injection rate and temperature: 150 kg/min, 40 °C
- Volume ratios for radial and axial discharge: 2.6 and 5.0
- Radius of the male rotor crest r_3 over C : 23.725 %
- Range angles of the male rotor crest β_3, β_4: 8.0 and 15.0 degrees
- Radius of the minor circular arc r_6 over C: 7.50 %
- Addendum of the female rotor A over C: 3.725 %

In addition, the following definitions are used:

$$\text{Input torque} = \text{Male rotor torque} + \frac{\bar{z}_1}{\bar{z}_2}\cdot(\text{Female rotor torque})$$

$$\text{Transmitted Torque Ratio (TTR)} = \frac{\text{Female rotor torque}}{\text{Input torque}}$$

5.3.1 Effects of the Radius of the Male Rotor Crest r_3

From the geometry of the rotors, the radius of the male rotor crest r_3 can be expressed as

$$r_3 = C\cdot\left(\frac{\bar{z}_2-\bar{z}_1}{\bar{z}_1+\bar{z}_2} + \frac{A}{C}\right) \tag{5.8}$$

where C is the centre distance of the rotors, while A the addendum of the female rotor. It can be seen that the centre distance C, the addendum A and the lobe combination may all influence the value of r_3. The former two factors are discussed in this section, while the later one is presented in section 5.4 of this chapter.

Table 5.6 shows the results of changing the centre distance C. It can be seen that the female rotor torques and the input torques increase with the increase in centre distance, the transmitted torque ratios, however, remain almost unchanged. In this example, although the values of r_3 and r_6 increase with the increase in centre distance, their ratios over centre distance are kept constant. This implies that the transmitted torque ratio mainly depends upon the shape of the lobe tips, the centre distance of the rotor has little influence on it.

However, since the capacity of the compressor increases with increasing centre distance, the input torque and hence the female rotor torque are increased, resulting in an increased contact force (Table 5.6), which is expressed as the force per unit length of the power transmission section of the contact line (see section 4.3 of Chapter 4).

Table 5.6 Effects of the centre distance C *

Items	Centre distance C (mm)				
	120	140	160	180	200
Female rotor torque (Nm)	43.8	69.3	103.4	147.2	201.9
Input torque (Nm)	285.7	452.2	675.8	963.6	1323.9
Transmitted torque ratio	10.23	10.21	10.20	10.18	10.17
Max contact force (N/mm)	11.7	13.8	15.9	18.0	20.3

* $r_3 / C = 23.75\ \%$, $r_6 / C = 7.5\ \%$

The effects of the female rotor addendum are shown in Table 5.7. As can be seen, the smaller the A / C, the lower the transmitted torque ratio and hence the lower the contact force between the rotors. The isentropic indicated efficiency also increases with decreasing A / C. However, this tendency is offset by the decrease in actual capacity with the decrease in A / C. Therefore, a balanced view must be taken when designing a helical twin screw compressor. In this example, an A / C of 3.725 percent would be an appropriate choice, which gives a relatively high capacity of 275.0 kg/min with the highest volumetric efficiency of 92.29 percent and an acceptably high indicated efficiency of 82.41 percent.

Table 5.7 Effects of the female rotor addendum A

Items	A / C (%)				
	1.0	2.0	3.0	3.725	5.0
Female rotor torque (Nm)	27.7	51.2	78.7	103.4	143.8
Transmitted torque ratio	3.58	5.97	8.32	10.20	13.48
Maximum contact force (N/mm)	7.3	10.7	13.6	15.9	19.5
Real capacity (kg/min)	212.0	233.8	257.2	275.0	285.8
Volumetric efficiency (%)	92.10	92.12	92.16	92.29	91.97
Isentropic indicated efficiency (%)	83.33	83.02	82.71	82.41	81.57

5.3.2 Effects of the Range Angles β_3, β_4

Table 5.8 shows the effects of the range angle β_3. With the increase in β_3, the transmitted torque ratio and hence the rotor contact force are reduced. The real capacity of the compressor increases somewhat with increasing β_3. Therefore, from this point of view a larger β_3 would be an advantage. However, the highest volumetric and indicated efficiency do not appear at the largest β_3. Taking rotor contact force, real capacity, volumetric and indicated efficiencies all into account, a β_3 of 30° would be the best choice in this example.

Table 5.8 Effects of the range angle β_3

Items	Range angle β_3 (degree)				
	2.0	10.0	20.0	30.0	40.0
Female rotor torque (Nm)	119.5	109.7	96.6	85.6	73.2
Transmitted torque ratio (Nm)	11.83	10.82	9.52	8.41	7.19
Maximum contact force (N/mm)	17.9	16.6	15.2	14.3	13.3
Real capacity (kg/min)	273.5	274.7	275.5	276.6	277.0
Volumetric efficiency (%)	92.25	92.37	92.31	92.43	92.34
Isentropic indicated efficiency (%)	82.38	82.50	82.45	82.57	82.48

In contrast, an increase in the range angle β_4 causes an increase in the transmitted torque ratio and hence the contact force. Also, the compressor real capacity decreases slightly with increasing β_4 (Table 5.9). From this point of view, a small β_4 is preferable. It is interesting to notice that both the volumetric efficiency and isentropic indicated efficiency obtain their highest value at the smallest β_4. Therefore, choosing β_4 becomes straight forward, the smaller the better.

To examine the overall effects of β_3 and β_4 together, five different combinations were studied and the results are presented in Table 5.10.

Table 5.9 Effects of the range angle β_4

Items	Range angle β_4 (degree)				
	0.0	4.0	8.0	12.0	16.0
Female rotor torque (Nm)	79.5	90.2	103.4	115.4	127.7
Transmitted torque ratio	7.79	8.87	10.20	11.38	12.60
Maximum contact force (N/mm)	13.5	14.6	15.9	16.9	18.1
Real capacity (kg/min)	277.4	275.8	275.0	273.8	272.7
Volumetric efficiency (%)	92.44	92.26	92.29	92.24	92.19
Isentropic indicated efficiency (%)	82.77	82.58	82.41	82.28	82.08

The importance of choosing right combination of β_3 and β_4 is obvious when observing the above table. The real capacity for $\beta_3 / \beta_4 = 40 / 2$ is increased by 6.7 percent compared with that for $\beta_3 / \beta_4 = 2 / 16$, the transmitted torque and the contact force are reduced by about 60 percent and 46 percent, respectively. As can be seen, this is accompanied with a 0.47 % higher volumetric efficiency and a 0.81 % higher isentropic indicted efficiency.

Table 5.10 Effects of different combinations of β_3 and β_4

Items	Angle combinations β_3 / β_4				
	2 / 16	8 / 12	15 / 8	20 / 6	40 / 2
Female rotor torque (Nm)	142.1	124.5	103.4	88.1	51.9
Transmitted torque ratio	14.61	12.31	10.20	8.66	5.07
Maximum contact force (N/mm)	20.4	18.0	15.9	14.3	11.1
Real capacity (kg/min)	261.1	272.9	275.0	275.9	278.6
Volumetric efficiency (%)	91.89	92.16	92.29	92.28	92.36
Isentropic indicated efficiency (%)	81.83	82.20	82.41	82.49	82.64

5.3.3 Effects of the Radius of the Circular Arc r_6

Similar to the tip range angle β_4, the effects of the radius of the circular arc

r_6 are straight forward (Table 5.11). With the decrease in r_6, the transmitted torque and the contact force are reduced, while the compressor capacity, volumetric and isentropic indicated efficiency are increased. Accordingly, from the point of view of the contact force, capacity and efficiencies, the r_6 should be kept as small as possible.

Table 5.11 Effects of the radius of the circular arc r_6

Items	r_6 / C				
	1.5	4.5	7.5	10.5	13.5
Female rotor torque (Nm)	72.4	86.6	103.4	120.9	141.6
Transmitted torque ratio	7.13	8.53	10.20	11.90	13.92
Maximum contact force (N/mm)	13.0	14.4	15.9	17.3	19.0
Real capacity (kg/min)	277.1	276.3	275.0	273.6	272.8
Volumetric efficiency (%)	92.33	92.38	92.29	92.23	92.16
Isentropic indicated efficiency (%)	82.68	82.65	82.41	82.25	82.00

5.3.4 Conclusions

The following conclusions can be drawn from this simulation:

- The influence of the lobe tip design parameters on compressor efficiencies, real capacity and rotor contact forces are significant, and must not be underestimated.

- The transmitted torque ratio is to a great extent determined by the male lobe tip segment designs, while the influence of the centre distance is relatively small.

- From the point of view of obtaining high efficiency, large capacity and low contact force, the lobe tip parameters should be chosen as follows:

  - β_3 should be relatively large, while β_4 should be as small as possible;
  - r_6 should be as small as possible;
  - A should be relatively large, with an A / C ratio of about 3.7 percent.

It is worth mentioning that the above conclusions are obtained without taking the lobe tip viscous loss into consideration. In fact, some of these conclusions are in contradiction with those obtained in section 5.2.4. A balanced view is given at the end of this chapter.

5.4 Optimum Rotor Parameter Combinations

Helical twin screw compressors are used in many different applications. For a certain application, one must make the right choice of rotor lobe combination, length / diameter ratio, wrap angle, etc. so as to enable the compressor to work at a performance level that is made possible by the profile used.

At present, the most commonly used rotor lobe combinations are 4+5, 4+6, 5+6, 5+7, although 3+4, 3+5, 3+6 and 6+7 have also been used. For each combination a rather wide range of length / diameter ratios, normally from 1.0 to 2.0, can be used. Also, a very wide range of male rotor wrap angles, usually from 250 to 350 degrees, can be used.

In this study, the four most commonly used rotor lobe combinations, together with five different length / diameter ratios and five different wrap angles, are compared with respect to the factors such as the compressor's efficiency, the rotor deflection, the contact force and the bearing forces.

As a base for comparison, the following running conditions are used:

- Medium: *R22*
- Evaporating temp.: -5 °C
- Suction pressure: 4.21 bar
- Oil injection rate: 150 kg/min
- Male rotor speed: 3000 rpm
- Condensing temp.: 40 °C
- Discharge pressure: 15.34 bar
- Oil temperature: 40 °C

To compare the stiffness of the rotors, a common method has to be used to calculate the diameter of rotor shaft and the position of the bearings. To limit rotor deflection the bearings should be positioned as close to the rotor body as possible. A reasonable value is to position the bearings on the suction side about 0.3 $D_{o,1}$ from the nearest rotor end plane and 0.4 $D_{o,1}$ on the

discharge side (Fig. 5.4). These values are well suited for a slide valve capacity-regulated refrigeration compressor (Pamlin, 1992). It is common to make the shaft diameter outside the rotor body 13-17 mm smaller than the rotor root diameter. For the calculated size of compressor, a 17 mm reduction can be suitable. In this study, only female rotor deflection is calculated since it is always the female that gives the highest deflection value.

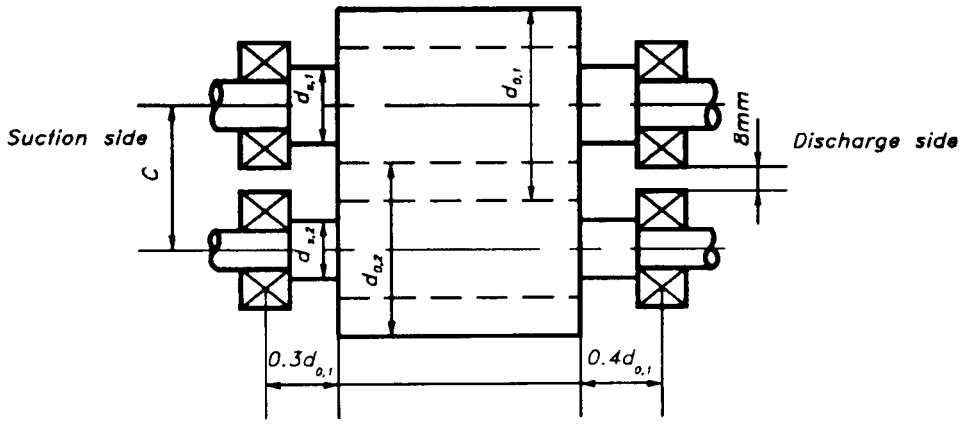

Fig. 5.4 Rotor-bearing arrangement

5.4.1 Lobe Combination

Four different rotor combinations have been calculated with the following common parameters:

- Compressor real capacity: 275 kg/min
- Length / male rotor diameter and male rotor wrap angle: 1.65, 300°
- Volume ratios for radial and axial discharge: 2.6, 5.0

and the results are shown in Table 5.12.

To obtain the same capacity the dimension of the compressor has to be changed accordingly for different lobe combinations. Generally, a compressor should have a dimension as small as possible, a weight as low as possible. From this point of view the 4+5 combination seems to be an excellent choice.

For both the volumetric efficiency and isentropic indicated efficiency it can be shown that the differences between these lobe combinations are very small in

this particular case. Naturally a different set of conditions could change the picture.

The transmitted torque ratios for both the 4+5 and 4+6 combinations are relatively small. However, as can be seen from the Table, the difference between the contact forces for all the lobe combinations is small due to the variation of the compressor dimensions.

Table 5.12 Different lobe combinations

Parameters	Lobe combination $\bar{z}_1 + \bar{z}_2$			
	4 + 5	5 + 6	4 + 6	5 + 7
Centre distance C (mm)	151.3	159.0	160.0	173.4
Male rotor outer diameter (mm)	206.3	210.0	203.9	209.2
Female rotor outer diameter (mm)	179.4	185.3	203.9	215.2
Rotor length (mm)	340.4	346.5	336.4	345.2
Total rotor weight (kg)	96.7	108.6	104.7	127.2
Volumetric efficiency (%)	92.62	92.91	92.29	92.76
Isentropic indicated efficiency (%)	82.76	82.78	82.41	82.68
Female rotor torque (Nm)	86.8	116.1	103.4	141.0
Transmitted torque ratio (%)	10.34	14.31	10.20	14.89
Maximum contact force (N/mm)	16.3	18.0	15.9	18.8
Max. female rotor deflection (mm)	0.0207	0.0178	0.0123	0.0087
$0.002\ C^{0.5}$ (mm)	0.0246	0.0252	0.0253	0.0263

Good performance and mechanical reliability require for a deflection not greater than $0.002\ C^{0.5}$ mm (Pamlin, 1992). According to this criterion the deflection limit values for the different lobe combinations are also given in Table 5.12. It can be seen that the 4+5 and 5+6 combinations have relatively larger deflections than the 4+6 and 5+7 combinations. Although there is no problem for 4+5 and 5+6 combinations for this particular case, a change in discharge pressure or suction pressure may change the picture.

Effects of the discharge pressure

Table 5.13 shows the results for a higher discharge pressure of 24.27 bar (condensing temperature 60°). The suction pressure remains unchanged, i.e. 4.21 bar (evaporating temperature -5°). Optimum volumetric ratios for both radial and axial discharges were used which took the values of 3.6 and 5.0, respectively.

Table 5.13 Different lobe combinations with higher discharge pressure

Parameters	Lobe combination $\bar{z}_1 + \bar{z}_2$			
	4 + 5	5 + 6	4 + 6	5 + 7
Real capacity (kg/min)	274.3	274.4	274.5	274.2
Volumetric efficiency (%)	92.46	92.72	92.14	92.60
Isentropic indicated efficiency (%)	80.02	80.39	79.17	80.19
Female rotor torque (Nm)	118.8	160.6	140.5	195.3
Transmitted torque ratio (%)	9.87	13.88	9.60	14.42
Maximum contact force (N/mm)	31.6	33.4	31.9	35.0
Max. female rotor deflection (mm)	0.0295	0.0247	0.0174	0.0119
$0.002\ C^{0.5}$ (mm)	0.0246	0.0252	0.0253	0.0263

The increase in discharge pressure increases the leakage, resulting in a slim reduction of the compressor capacity and hence volumetric efficiency. The isentropic indicated efficiency for the 4+6 combination is slightly lower comparing with the remaining combinations. However, for this condition the 4+5 combination may be troubled due to excessive female rotor deflection. It can also be envisaged that for a higher discharge pressure the 5+6 combination will also cause trouble with the female rotor deflection.

High female rotor deflection is mainly a result of the small female rotor shaft diameter, large length / diameter ratio and the necessary distance between the rotor body and the radial bearing centre. The female rotor shaft diameter is up to the lobe combination and also influenced by the length / diameter ratio. A

small length / diameter ratio calls for a larger rotor diameter to keep the displacement volume constant, which may reduce the female rotor deflection significantly. The necessary distance between the rotor and the bearing has to be decided according to compressor applications. If the compressor is to be designed for a refrigeration duty but without a slide valve, or for air compression, the distance between the rotor body and bearing can then be reduced. It is thus possible that the female rotor deflection is limited to a level which enables the compressor to run up to very high discharge pressures.

Effects of the suction pressure

Table 5.14 shows the results for a lower suction pressure of 1.05 bar (evaporating temperature -40°). The discharge pressure remains unchanged, i.e. 15.34 bar (condensing temperature 40°). Similarly, volumetric ratios for both radial and axial discharges were optimized, with the values being 4.5 and 5.0, respectively.

Table 5.14 Different lobe combinations with lower suction pressure

Parameters	Lobe combination $\bar{z}_1 + \bar{z}_2$			
	4 + 5	5 + 6	4 + 6	5 + 7
Real capacity (kg/min)	67.8	67.7	67.9	67.7
Volumetric efficiency (%)	91.58	91.67	91.35	91.67
Isentropic indicated efficiency (%)	78.82	77.13	78.93	77.07
Female rotor torque (Nm)	44.1	65.0	48.5	78.7
Transmitted torque ratio (%)	8.44	12.63	7.70	13.06
Maximum contact force (N/mm)	17.1	23.1	15.7	24.5
Max. female rotor deflection (mm)	0.0136	0.0111	0.0075	0.0054
$0.002\ C^{0.5}$ (mm)	0.0246	0.0252	0.0253	0.0263

In contrast, the 4+5 and 4+6 combinations have a relatively higher isentropic indicated efficiency and a lower level of the contact force compared with the 5+6 and 5+7 combinations at these conditions. This implies that the right

choice of lobe combination should be made according to the running conditions the compressor is to work with.

Comparing Table 5.14 with Table 5.12, it is interesting to note that the decrease in the suction pressure, although also causing an increase in pressure ratio, reduces the female rotor deflection in this example. This is due to the fact that the helical twin screw compressor has a fixed volume ratio. The lower the suction pressure, the lower the pressure at the end of the compression process, and hence the lower the compression gas forces applied to the rotors.

5.4.2 Length / Diameter Ratio

Five different length / male rotor diameter ratios ranging from 1.0 to 2.2 have been calculated for the four lobe combinations with the following common parameters:

- Compressor real capacity: 275 kg/min
- Male rotor wrap angle: 300^{o}
- Volume ratios for radial and axial discharge: 2.6, 5.0

and the results are shown in Figs. 5.5 - 5.10.

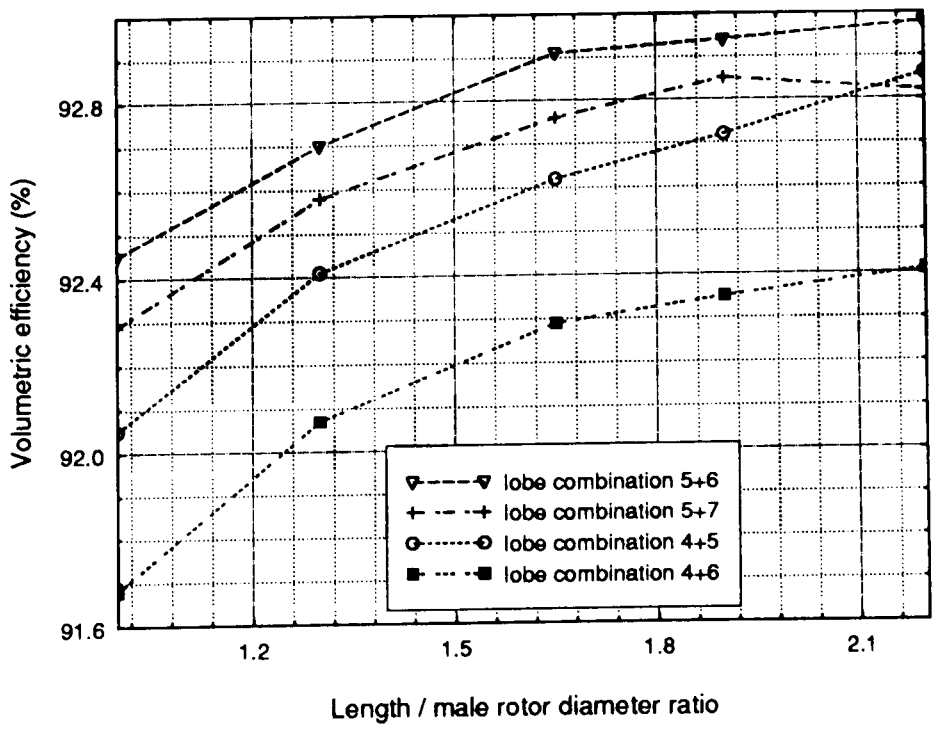

Fig. 5.5 Volumetric efficiency vs length / diameter ratio

From Fig. 5.5 it can be seen that for the 4+5, 4+6 and 5+6 combinations the volumetric efficiency increases with the increase in length / male rotor diameter ratio. This is a result of the reduction in both the leakages and theoretical capacity. The exception is the 5+7 combination which shows a peak efficiency at the length / male rotor diameter ratio of 1.9. For a certain length / diameter ratio the 5+6 combination has the highest volumetric efficiency among all the lobe combinations considered.

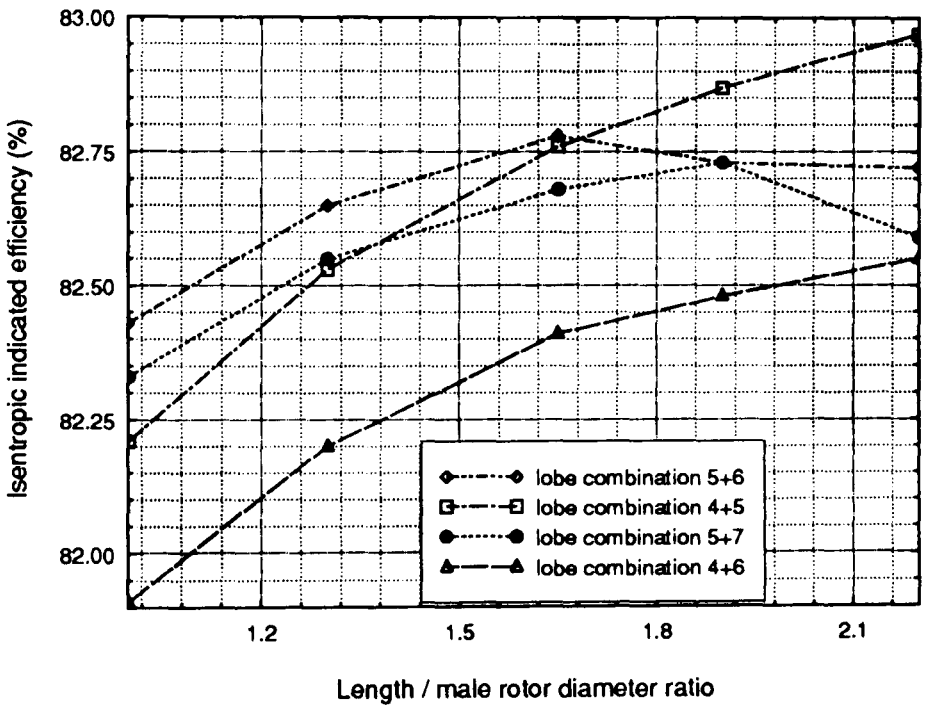

Fig. 5.6 Isentropic indicated efficiency vs length / diameter ratio

The 5+6 combination also shows a relatively higher isentropic indicated efficiency for length / diameter ratios up to 1.7 (Fig. 5.6). For higher length / diameter ratios, the 4+5 combination seems to have better performance but cannot, unfortunately, be used above $L/D_{o,1} = 1.7$ at these conditions due to excessive female rotor deflection. The 5+6 combination shows the next best results in this example. However, as discussed in the previous section, for higher pressure levels the 5+6 combination will most likely be troubled by excessive female rotor deflection. Whilst the 5+7 combination shows a performance very close to the 5+6 combination for $L/D_{o,1}$ above 1.7, it's deflections are much smaller as can be seen from Fig. 5.7. Thus, the 5+7 combination would be more appropriate for $L/D_{o,1}$ above 1.7.

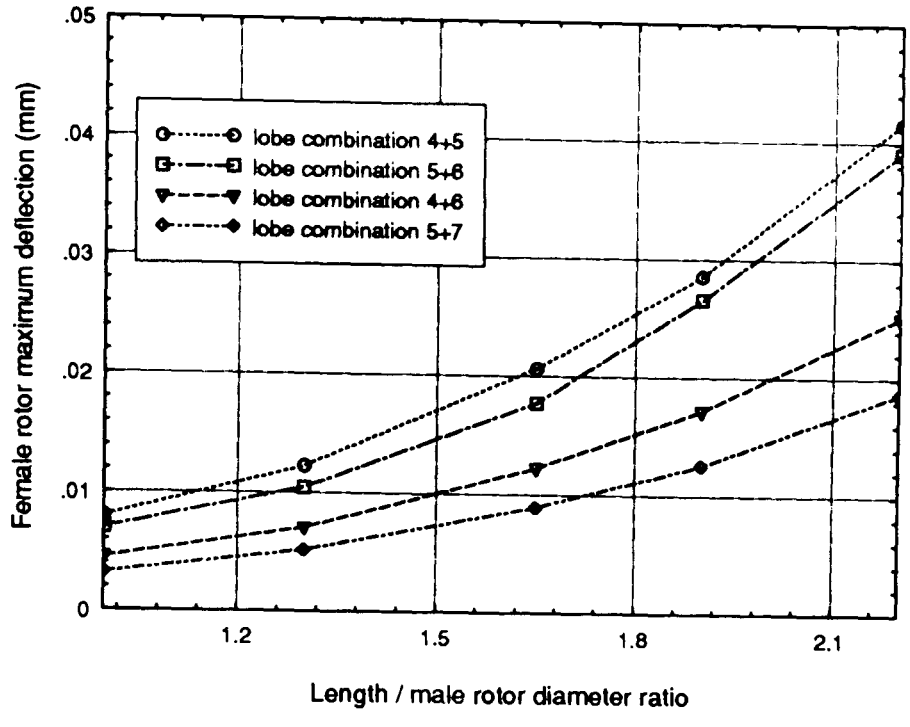

Fig. 5.7 Female rotor deflection vs length / diameter ratio

A previous study conducted by Pamlin (1992) suggested that for all the lobe combinations the highest length / diameter ratio should always be used, considering at the same time the acceptable female rotor deflection. However, Fig. 5.6 indicates that the isentropic indicated efficiency does not always increase with the increase in length / male rotor diameter ratio for the 5+6 and 5+7 combinations. The possible reason for the different results is that the running conditions he used are at a higher pressure level (discharge pressure 20 bar, suction pressure 6 bar). This important information implies that for the 5+6 and 5+7 combinations the length / diameter ratio still needs to be optimised for the conditions at which the compressor is to work.

In addition, the bearing forces are another important factor one must take into consideration when choosing the length / diameter ratio. Figs. 5.8 and 5.9 show the variation of the bearing forces of the male and female rotor with the length / diameter ratio, respectively. Since the rotors are relatively exposed more to the compression gas and the discharge port moves away from the inlet side with increasing length / diameter, the bearing forces on the outlet side increase significantly, while decrease slightly on the inlet side. By comparing the bearing forces on the outlet side for $L/D_{o,1} = 1.0$ and 2.2, there

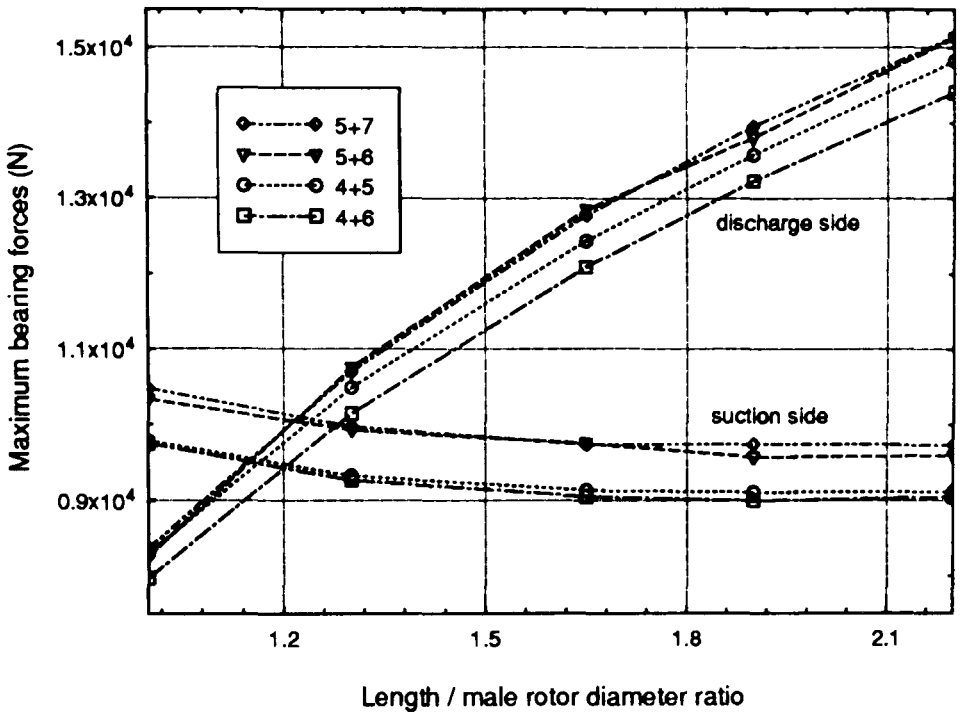

Fig. 5.8 Maximum bearing forces vs length / diameter ratio (male rotor)

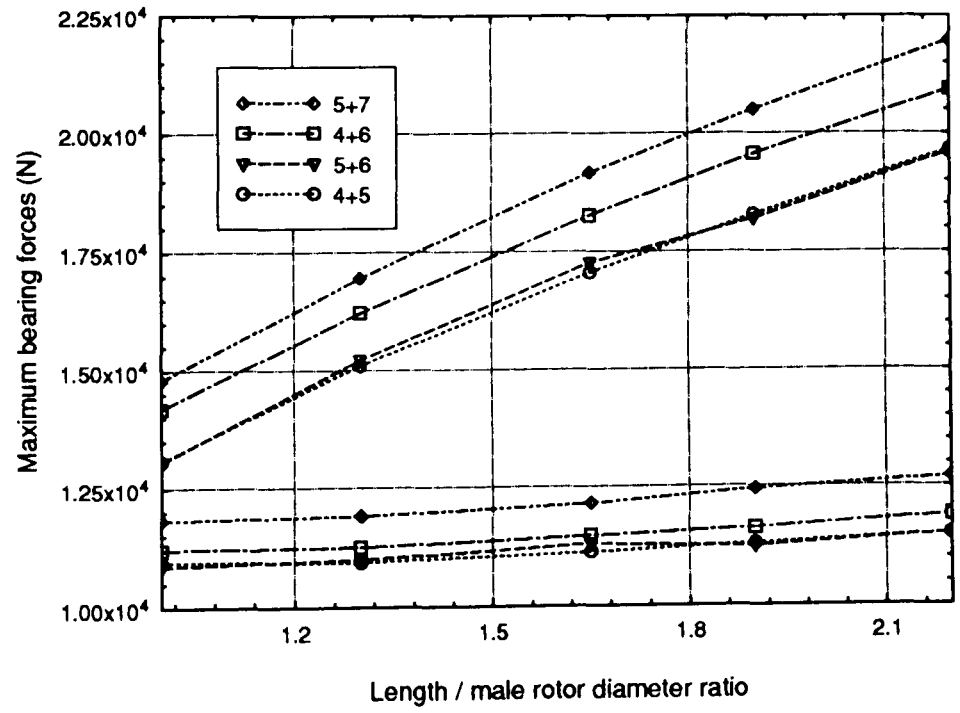

Fig. 5.9 Maximum bearing forces vs length / diameter ratio (female rotor)

is an increase of about 79-83 percent for the male rotor, and about 48-50 percent for the female rotor. On the other side, with the increase in length / diameter ratio from 1.0 to 2.2, the centre distance of the rotors is necessarily reduced, e.g. for the 5+6 combination from 186 mm to 143 mm, to maintain the same capacity. Consequently, the diameter of the bearings has to be reduced, which means that they may not be able to meet increased bearing

loads. Thus, short rotors give a situation which is preferable from the point of view of longer bearing life.

The computation results also reveal that the female rotor gas torque and the transmitted torque ratio remain almost unchanged with the increase in length / diameter ratio. Since the length of the power transmission section of the contact line increases somewhat with the increase in length / diameter ratio, the contact force per unit length is reduced slightly as shown in Fig. 5.10. Thus, from the point of view of obtaining longer rotor life, a higher length / diameter ratio is of advantage.

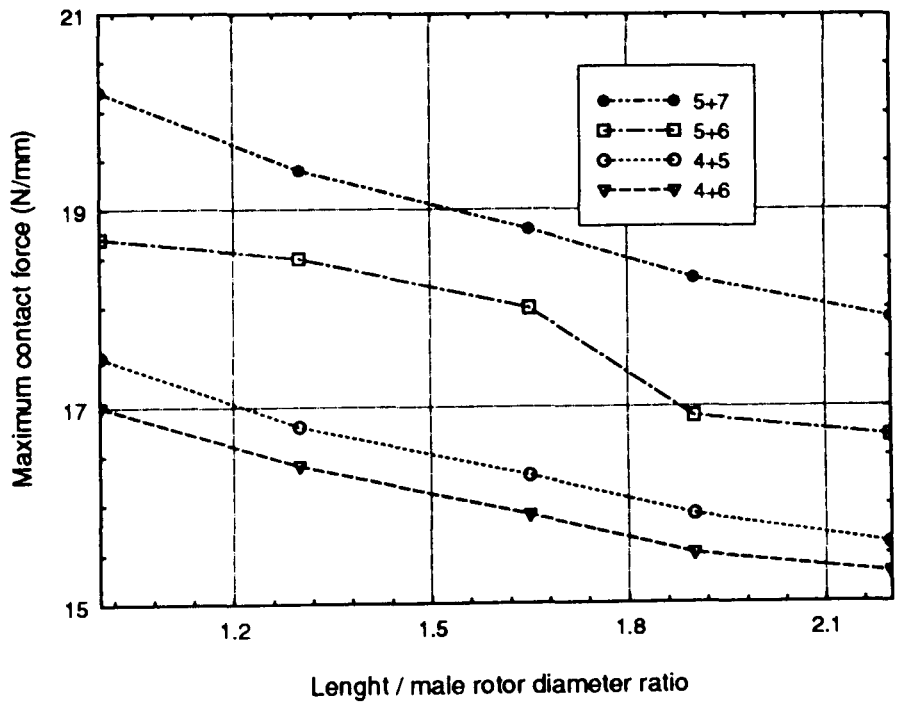

Fig. 5.10 Rotor contact force vs length / diameter ratio

5.4.3 Wrap Angle

Similarly, five different male rotor wrap angles ranging from 250 to 350 have been considered for the four lobe combinations with the following common parameters:

- Compressor real capacity: 275 kg/min
- length / male rotor diameter ratio: 1.65
- Volume ratios for radial and axial discharge: 2.6, 5.0

Since the displacement volume of the compressor is reduced with the increase in wrap angle, a necessary small change has been made in rotor dimension so as to maintain the same capacity. The results are presented in Figs. 5.11 - 5.15.

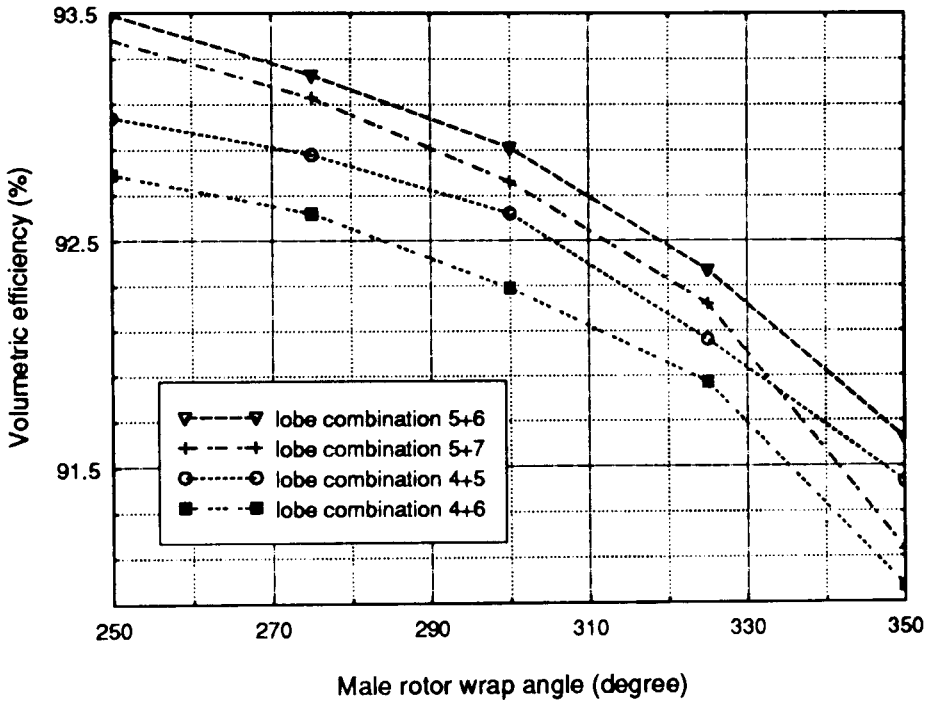

Fig. 5.11 Volumetric efficiency vs male rotor wrap angle

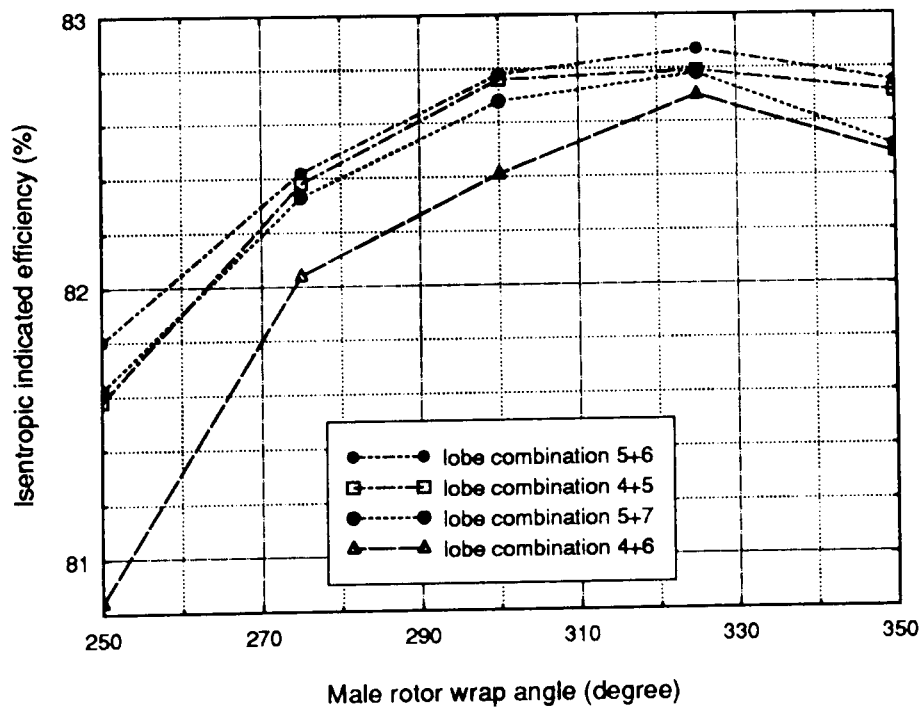

Fig. 5.12 Isentropic indicated efficiency vs male rotor wrap angle

Fig 5.11 shows that the volumetric efficiency decreases with increasing wrap angle as a result of an increasing sealing line length. However, as can be

seen from Fig. 5.12, the isentropic indicated efficiency of the compressor increases with increasing wrap angle up to about 325°. This is mainly a result of an increased discharge port area and hence reduced throttling effect. For higher wrap angles, since the discharge port is big enough, the increase in leakage has been dominant, resulting in a reduced indicated efficiency.

Again, this result is somewhat different from that reported by Pamlin (1992), in which there is a continuing increase in the adiabatic efficiency with increasing wrap angle. This implies that the variation of the indicated efficiency with wrap angle is related to compressor running conditions and should be optimized accordingly.

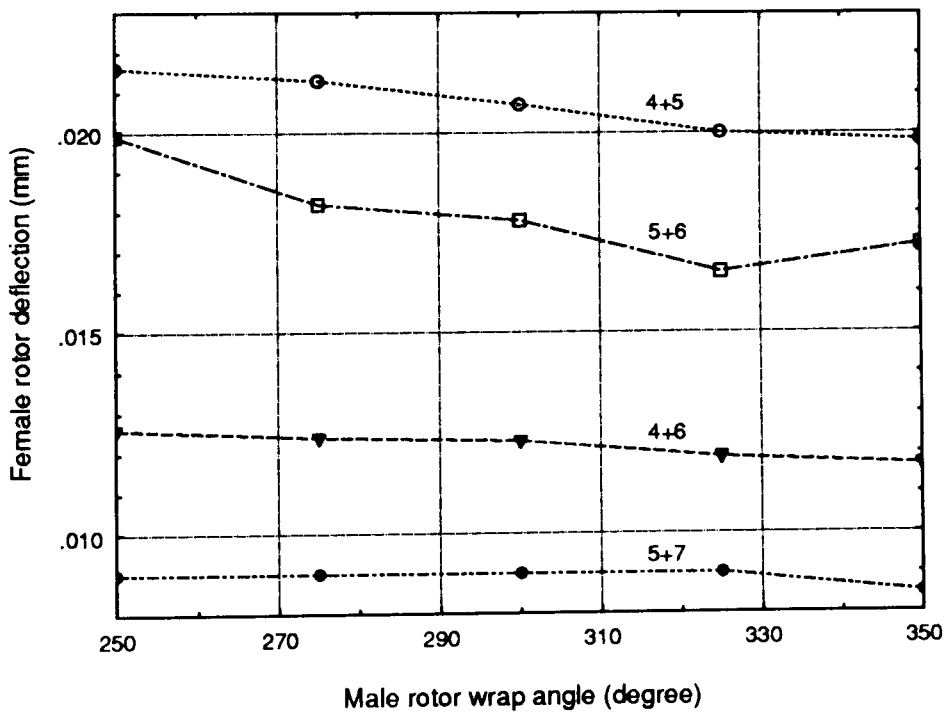

Fig. 5.13 Female rotor deflection vs male rotor wrap angle

The influence of the wrap angle on the female rotor deflection and on the contact forces and bearing forces (for the 5+6 combination) are shown in Figs. 5.13 - 5.15. It can be seen that the female rotor deflection, contact forces and bearing forces all decrease somewhat with increasing wrap angle. The extent of the effects is obviously very limited. This is also the case for other lobe combinations. Therefore, from the point of view of longer rotor and bearing life, a relatively high value of wrap angle is of help.

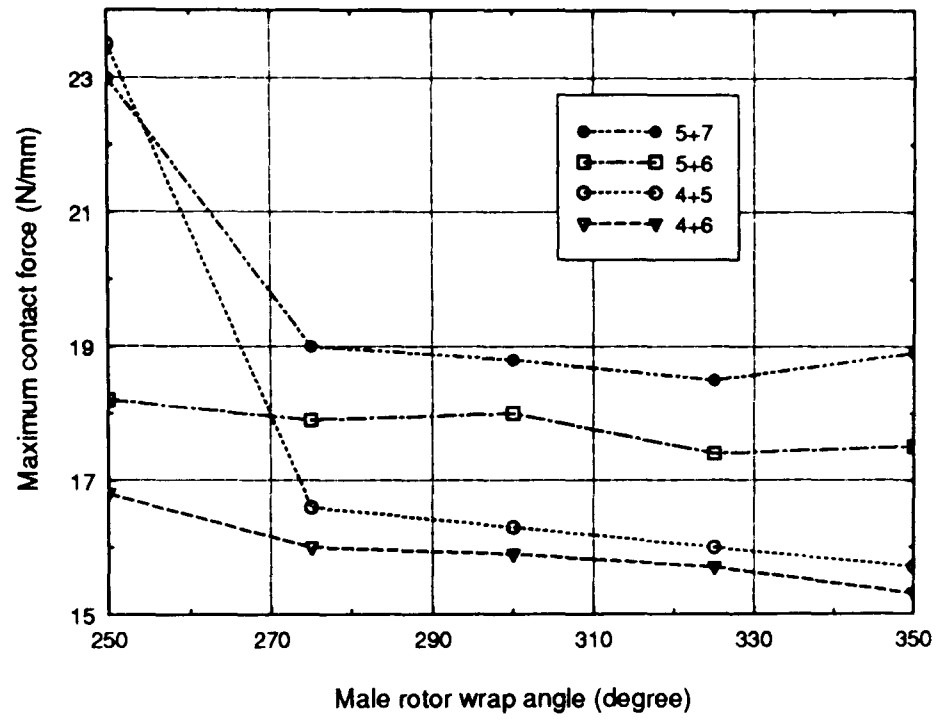

Fig. 5.14 Maximum contact forces vs male rotor wrap angle

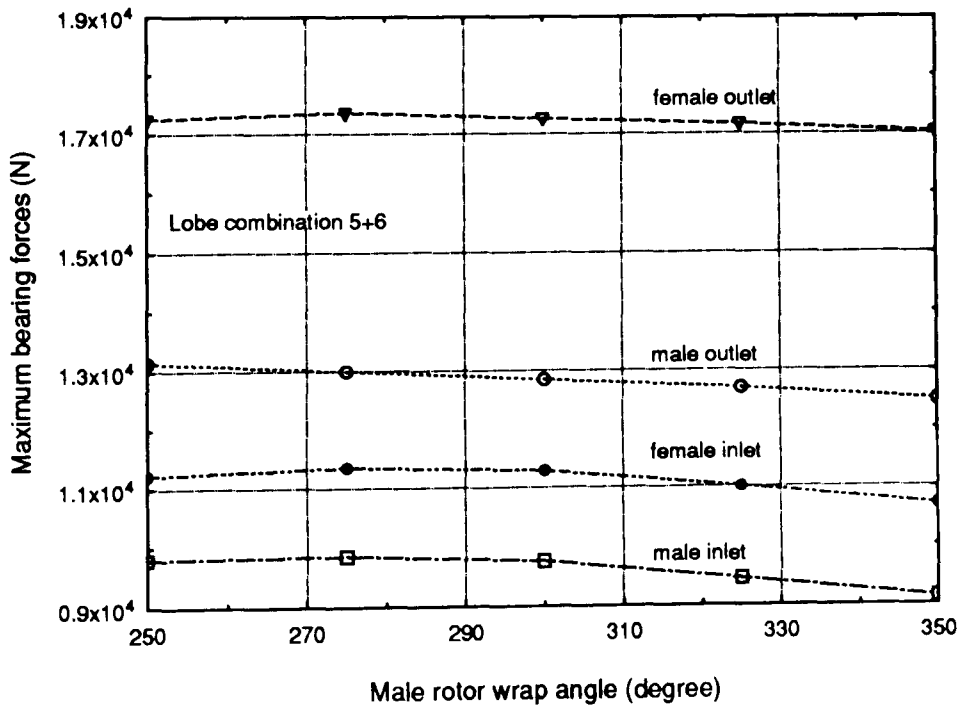

Fig. 5.15 Maximum bearing forces vs male rotor wrap angle

5.4.4 Conclusions

In addition to choosing an advanced modern rotor profile, the right choice of the rotor physical parameters, i.e. lobe combination, length / diameter ratio and wrap angle, is critical for designing high performance helical twin screw

compressors.

The compressor volumetric and isentropic indicated efficiencies are not the only criteria for choosing the rotor geometrical parameters. The factors which should also be taken into account include the female rotor deflection, the bearing forces and bearing life, the rotor contact forces and some other practical considerations, such as ease of manufacturing and assembly.

The 4+5 combination has the smallest dimension and weight and a relatively high isentropic indicated efficiency, but can only be used for small length / diameter ratios and low pressure level applications due to excessive female rotor deflection.

The 5+6 combination shows the best overall performance within the parameter ranges studied. However, the low stiffness of the female rotor may cause trouble if the pressure level is high. The 5+7 combination, which shows the next best performance and the lowest female rotor deflection, would then be the right choice for high length / diameter ratios and applications of high pressure levels.

The 4+6 combination can be used throughout the parameter ranges studied with a somewhat lower performance level. However, it is claimed that it can probably be produced at a somewhat lower cost (Pamlin, 1992).

It is not always true that the highest length / diameter ratio will lead to the highest indicated efficiency. In fact, for the 5+6 and 5+7 combinations the indicated efficiency starts to fall from $L / D_{o,1} = 1.65$ and 1.9 respectively for the conditions used. The high length / diameter ratio also causes an increase in female rotor deflection, an increase in bearing forces on the outlet side and a decrease in bearing diameters. Thus, an optimum length / diameter ratio needs to take all these factors into account.

It is also not true that the highest wrap angle always gives the highest indicated efficiency. As a matter of fact, the indicated efficiency starts to fall

from a wrap angle of 325° for all the lobe combinations at the conditions used. The volumetric efficiency also decreases with increasing wrap angle. However, an increased wrap angle does result in, although to a very limited extent, a decrease in rotor contact force and bearing forces. Additionally, short rotors with big wrap angle can cause problems with manufacturing. Accordingly, all these factors must be considered when choosing the optimum wrap angle.

5.5 Summary +

An effort has been made to achieve optimum lobe tip designs combined with the right choice of rotor geometrical parameter combinations for a certain applications.

The optimum lobe tip designs require considerations not only of the compressor volumetric and isentropic indicated efficiencies, but also the real capacity, the contact force between the rotors, and the viscous friction power loss at the lobe tips. Comparing the simulation results obtained in section 5.2 (considering viscous friction loss) and section 5.3 (considering efficiencies, capacity and contact force), it can be seen that, of all the tip design parameters, special attention must be drawn to the male rotor crest range angle β_3. From the point of view of obtaining high efficiencies, large capacity and low contact force, a relatively big β_3 is of advantages. However, this is not consistent with the requirement of reducing the viscous friction power loss at the lobe tips. Consequently, this parameter must be optimised for the minimum power consumption.

Similarly, for obtaining the optimum rotor physical parameter combination, not only the compressor efficiencies, but also the female rotor deflection, bearing forces and rotor contact force must be taken into account. The 4+5 and 5+6

combinations have in general high efficiencies, but less rigidity, and can thus only be applied to low or medium pressure level applications with short rotors. The 5+7 and 4+6 combinations show no problems with the female rotor deflection and can be used for any length / diameter ratio and applications of high pressure level. However, compared with other lobe combinations, the 4+6 combination displays relatively lower efficiencies, while the 5+7 combination shows a relatively higher contact force. The highest wrap angle and length / diameter ratio do NOT always lead to the highest compressor performance, which is in fact related to compressor running conditions. The bearing forces increase with increasing length / diameter ratio and therefore must be examined when deciding the length / diameter ratio.

Finally it is worth stressing that the discussions in this chapter are mainly from a performance point of view. Other demands like ease of manufacture (which can improve the quality and hence the performance) as well as economic considerations regarding tooling and standards, can change the picture. The demand for a design of the screw compressor which can handle any type of conditions, very often results in a solution which is not particularly good for anything.

+ The first part of this Chapter, *Optimum lobe tip designs with respect to oil viscous friction loss* has been presented in the European Conference - Developments in Industrial Compressors and their Systems, and has been published by the IMechE, London (Fleming, et al, 1994).

Chapter 6

Some Aspects of Refrigeration Screw Compressors and their Systems

6.1 Introduction

In this chapter the author further demonstrates how his bearing force and torque program is used in compressor design and in system development.

Helical twin screw compressors are increasingly used in the refrigeration industry. To achieve and maintain the desired refrigeration conditions, the design of the screw compressor and the other system components involves a number of important considerations which deserve special attention. In the design of a complete system, the characteristics of every component, i.e. the compressor, evaporator, condenser, drive, valves, oil separator and the control system must be determined if the system behaviour is to be determined. This chapter does not cover all the system components, since only the compressor is the subject of study. It concentrates on the following two topics, both drawn from actual practice which are directly related to the design of refrigeration screw compressors and the systems of which they are a part:

- Optimum design of the slide valve and slide stop (capacity control device)

and the choice of the related volume ratios for radial and axial discharge ports;

- Safe design of a non-reversing clutch used in preference to a non-return valve in the suction line of the system.

These two topics are independent of each other and are presented in sections 6.2 and 6.3, respectively. The chapter is summarized in section 6.4.

6.2 Optimum Slide Valve Design

In many applications of helical twin screw compressors to refrigeration duties, the load varies over a wide range. Capacity control is thus needed to enable the compressor to run at part load conditions. The most common method makes use of a slide valve which allows a measured quantity of the compressed cavity volume to "blow out" back to suction, as shown in Fig. 6.1. The slide valve has the advantage of being a geometrically simple device, but it exerts an important influence on compressor efficiency (Sjöholm, 1986; Shaw, 1988; Sauls, 1988, 1990).

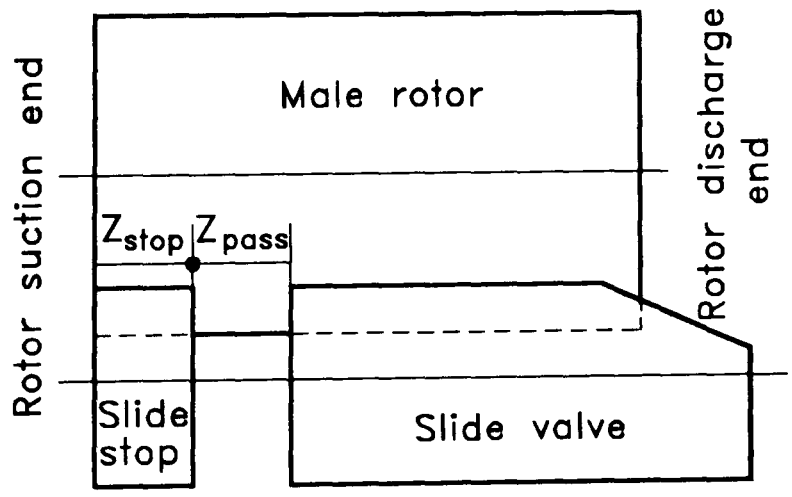

Fig. 6.1 Schematic view of a slide valve

The slide valve influences compressor full load performance. The addition of a slide valve mechanism to a compressor usually limits the width of the radial discharge port at full load to the width of the slide, due to space constraints.

The shaded area on Fig. 6.2 shows the area typically lost. The axial discharge port on the other hand controls the discharge process when the compressor runs at low load capacity. These changes in the construction of the discharge ports mean that the area of discharge flow in the machine with the slide valve at full load is less than that for the equivalent machine without a slide valve. The result is an increase in the gas flow resistance through the ports, over pressure in the cavity and a decrease in the indicted efficiency of the machine. In view of the huge number of helical twin screw compressors used for refrigeration duties, it is of interest to investigate the extent of this efficiency penalty and other important aspects of behaviour such as bearing reaction forces. This section describes the outcome of such an investigation, stimulated by the behaviour in the field of a real compressor and the need for the author to demonstrate the use of his program.

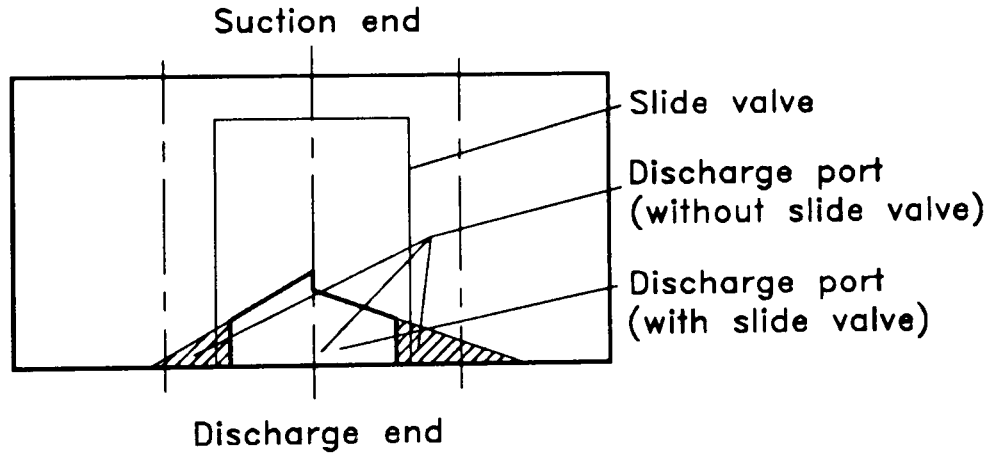

Fig. 6.2 Radial discharge port construction

The compressor part load performance depends to a great extent upon the design of the slide valve. As the slide-valve opens to allow bypass of gas back to suction, its far end moves towards the discharge end, partly covering the radial discharge port and resulting in a reduction of the area of flow. Although the volumetric capacity of the compressor is reducing as the compressor is unloaded, the reduction of the radial discharge port area will increase the discharge resistance and pressure drop, and cause a decrease in the indicated efficiency. Factors which influence the compressor

performance at part load condition include the compressor built in volume ratios for both radial and axial discharge ports and the slide valve design parameters (especially Z_{stop} as defined in Fig. 6.1). In order to provide a good performance in refrigeration systems these parameters should be optimized to suit the running conditions of the compressor.

Finally, overpressure in the cavity introduces the possibility of increased bearing forces. Indeed, a possibility exists that the bearing forces under certain part load conditions may be larger than those at the full load condition. To ensure the safe operation of the compressor the maximum bearing forces must be determined at the design stage for various possible running conditions.

Utilizing the University of Strathclyde's performance simulation program (Tang and Fleming, 1992) and the force analysis program described in Chapter 4, the influence of the slide valve on compressor efficiency and bearing forces is examined in this chapter. A design procedure for choosing optimal volume ratios for both the radial and axial discharge ports and for choosing Z_{stop} is presented. The circumstances under which bearing forces peak at part load condition are identified and discussed. The results should be of value to the designers and operators of twin screw compressors required to run under a range of operating conditions.

The specifications of the compressor used for the calculations are as follows:

- Rotor lobe profile: SRM D
- Lobe Combination: 4 / 6
- Wrap angle (male): 300°
- Rotor diameters: 204 mm
- Length / diameter: 1.65
- Driving rotor: male

The chosen running conditions:

- Refrigerant: *R* 22
- Evaporating temp.: -5°C
- Suction pressure: 4.21 bar
- Oil injected (40 °C): 150 kg/min
- Male rotor speed: 3000 rpm
- Condensing temperature: 25°C
- Discharge pressure: 10.44 bar
- Suction superheat: 30°C

6.2.1 The Influence of Slide Valve on Compressor Full Load Performance

The influence of the slide valve on compressor full load performance is shown in Fig. 6.3, in which the indicated efficiencies of the specified compressor with and without a slide valve are displayed as a function of the volume ratio for the radial discharge port. The volume ratio for the axial discharge port is 5.0 for the compressor with a slide valve, while for the compressor without a slide valve it is set to be the same as that for the radial discharge port.

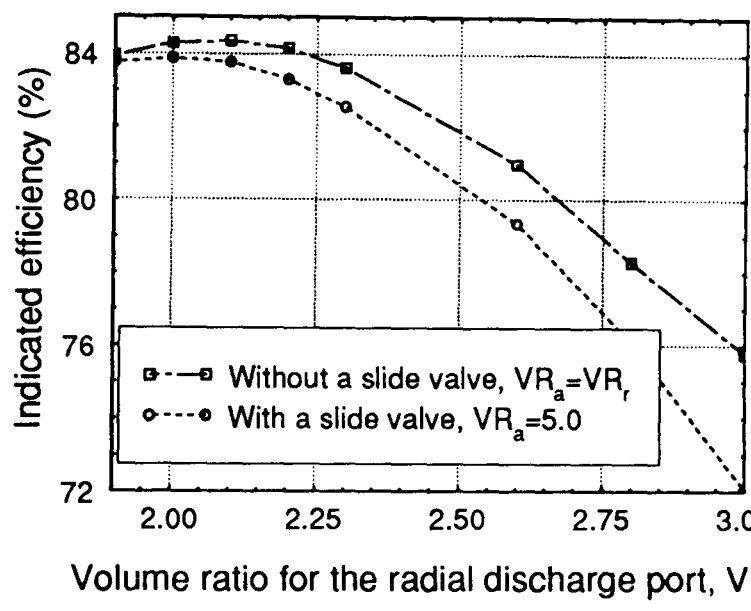

Fig. 6.3 Effect of slide valve on compressor full load performance

It can be seen that over a wide range of volume ratio for the radial discharge port, the indicated efficiency for the compressor without a slide valve is higher or much higher than that for the compressor with a slide valve. The curves peak at different volume ratios, with the highest indicated efficiency being 84.4 percent at a volume ratio of 2.1 for the compressor without a slide valve, and 83.9 percent at a volume ratio of 2.0 for the compressor with a slide valve. This means that, assuming the compressors in both cases were designed to achieve the highest efficiency, there is still a loss of indicated efficiency of about 0.5 percent due to the use of the slide valve at the full load condition. From Fig. 6.3 it is apparent that if a higher volume ratio is used for the radial discharge port in the compressor with a slide valve the loss of the indicated

efficiency at the full load condition will be much larger.

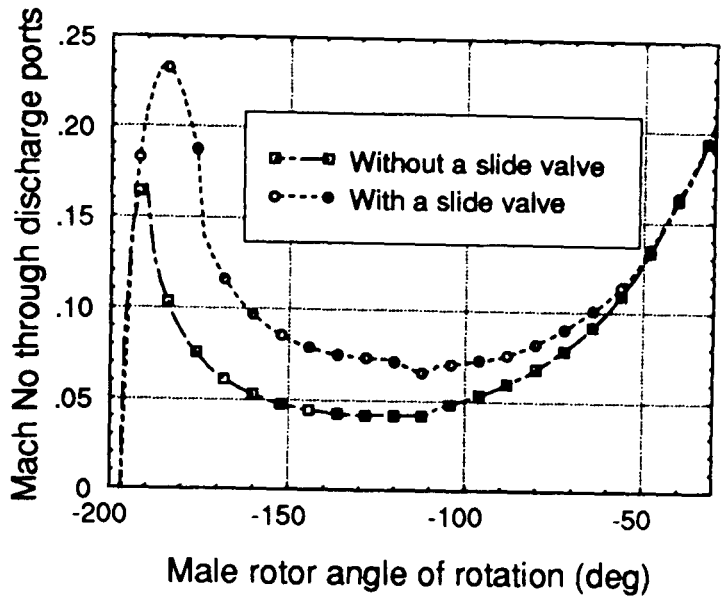

Fig. 6.4 Influence of slide valve on discharge Mach No

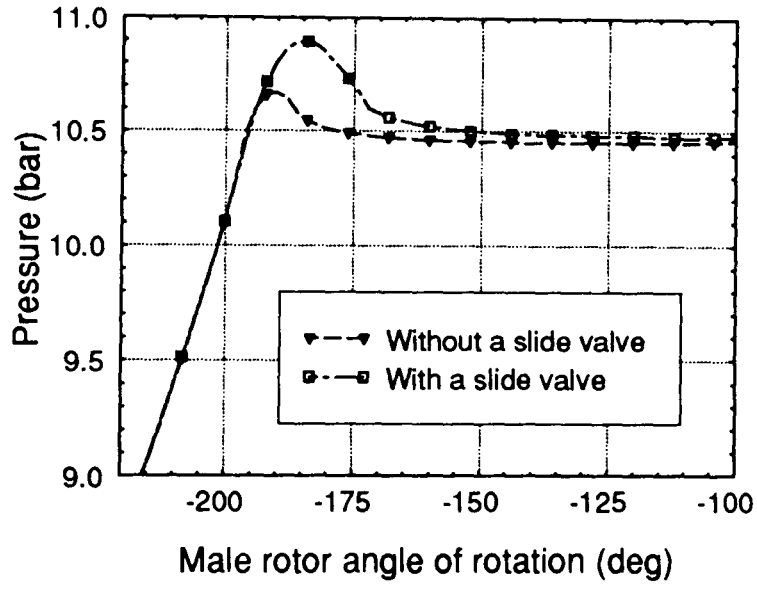

Fig. 6.5 Effect of slide valve on discharge pressure

The main reason for this loss in the indicated efficiency is, as mentioned before, the reduction of both the radial and axial discharge port areas due to the addition of the slide valve (see Fig. 6.2), which increases the resistance to gas flow through the discharge port, thus increasing the indicated power considerably. Fig. 6.4 shows the variation of the Mach number of the gas flow through the ports during the discharge process. The Mach number in the compressor with a slide valve is much higher than that in the machine without a slide valve. The larger the discharge Mach number, the larger the indicated

power and the lower the indicated efficiency. The waste of energy is obvious in Fig. 6.5 in which over-pressure occurs due to the reduction of the discharge port area caused by the presence of the slide valve.

Since the reduction of the discharge port area is inevitable due to the use of a slide valve (see Fig. 6.2), this loss of indicated efficiency is unavoidable in a compressor with a slide valve running at full load compared with the valveless compressor. However, it is quite common for two or more twin screw compressors to be employed in one refrigeration plant. In order to reduce the total energy consumption of the compressors, the author suggests that in such a situation some of the compressors should be without slide valves. They should have the same volume ratios for the radial and axial discharge ports, and always run under the full load condition. In view of the huge applications of twin screw compressors in the refrigeration industry, the potential for energy saving of such an arrangement is significant.

6.2.2 Optimisation of Volume Ratios for Discharge Ports

A typical twin screw compressor fitted with a slide valve has an axial discharge port which is smaller than the radial discharge port (at full load). It is possible to have a radial discharge port sized for a volume ratio of 2.6 combined with an axial port designed for an equivalent volume ratio of 5.0. These volume ratios which determine the design of the discharge ports are defined as the ratio of the maximum suction volume at full load over the trapped volume just before the discharge process through the individual port, i.e. $VR_a = V_{s,max} / V_{d,a}$ and $VR_r = V_{s,max} / V_{d,r}$. It is apparent that these volume ratios for the discharge ports are different from the actual volume ratios during slide valve unloading, which are defined as the effective suction volume over the V_d. Consequently, the effective volume ratios vary with the slide valve position. The operating volume ratio of the compressor is always the lower of the two deriving from axial or radial flow. In general, the radial port sets the volume

ratio at higher loads while the axial port dominates behaviour at low loads. In order to get the highest possible indicated efficiency over the entire operating range, the influence of these two volume ratios must be considered simultaneously in an optimisation procedure.

The Volume Ratio for the Axial Discharge Port VR_a

The volume ratio for the axial discharge port, VR_a, not only controls the discharge process at low load, but also sets the theoretical minimum volumetric load capacity at which the compressor can be run. This minimum volume, $V_{s,min}$ as shown in Fig. 6.6, is in fact the trapped volume in the rotors when the axial port is about to deliver, i.e. $V_{s,min} = V_{d,a}$. Thus, the minimum volumetric load cavity ratio, $VLCR_{min}$, can be expressed as $1/VR_a$ (i.e. $VLCR_{min} = V_{s,min} / V_{s,max} = V_{d,a} / V_{s,max} = 1 / VR_a$). The relationship between the VR_a and $VLCR_{min}$ is shown in Fig. 6.7. For the given minimum volumetric load capacity ratio a corresponding VR_a can then be determined.

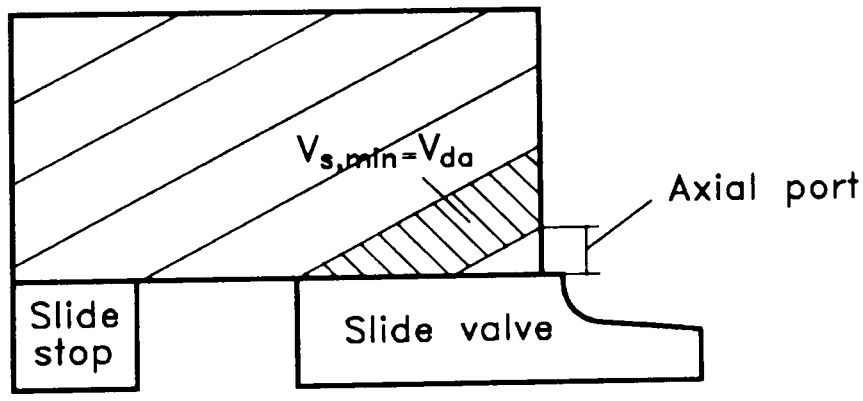

Fig. 6.6 Minimum load capacity of a slide valve

As far as the author is aware, many helical twin screw refrigeration compressors are at present designed with a volume ratio of about 5.0 for the axial discharge port. In practice, few run at such a low load as 20 percent of the full load capacity. The use of a higher VR_a implies a smaller discharge port and thus a decrease in the indicated efficiency. Fig. 6.8 reveals this effect of the VR_a for a minimum volumetric load capacity ratio of 0.4, for which VR_a should be larger than 2.5 according to Fig. 6.7.

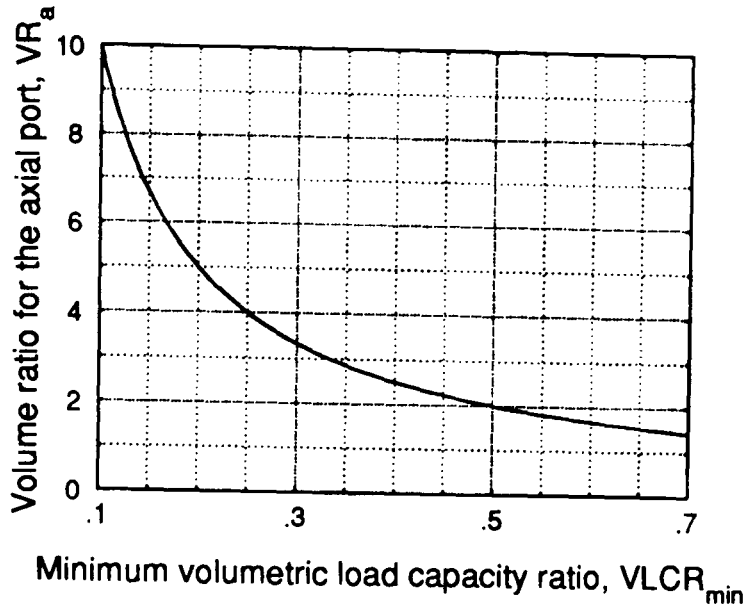

Fig. 6.7 Volume ratio for the axial discharge ports as a function of minimum load capacity ratio

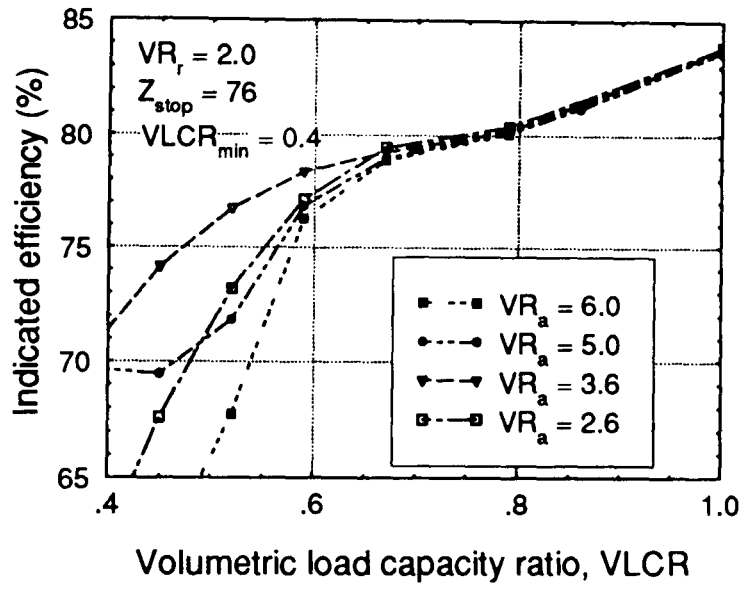

Fig. 6.8 Effect of the axial volume ratio on compressor part load performance

It can be seen that the use of the high volume ratios of 5.0 and 6.0 considerably reduce the indicated efficiency within the load range of 0.4 - 0.7; while the low volume ratio of 2.6 also did not produce the best performance. This is because the high volume ratio results in over-pressure while the low volume ratio causes under-pressure, both increasing energy consumption. For the operating conditions given, the best compressor performance over the entire load range was obtained with an intermediate axial volume ratio of 3.6.

In order to reduce the loss of the indicated efficiency caused by using a high volume ratio for the axial discharge port, it is suggested that the VR_a should be optimised for the most common running condition of the compressor.

The Volume Ratio for the Radial Discharge Port VR_r

In general, the volume ratio for the radial discharge port, VR_r, should be chosen according to the full load condition. From Fig. 6.3 it is known that the best VR_r equals 2.0 for the conditions specified, and, in fact, with this optimised VR_r the compressor provides a relatively good performance over the entire operating range, provided that the slide valve stop size is chosen wisely, as shown in Fig. 6.9.

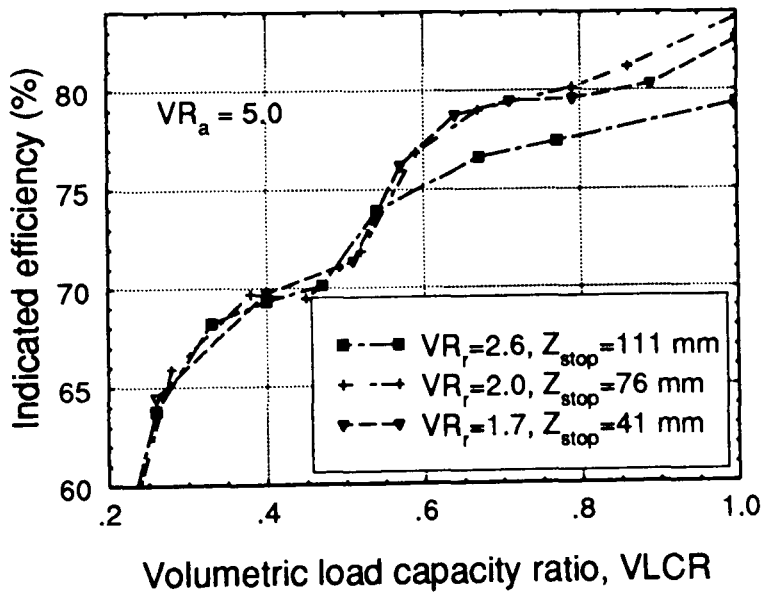

Fig. 6.9 Influence of the radial volume ratio on compressor part load performance

However, this optimised VR_r usually does not provide the best performance at all part load conditions. For instance, a smaller volume ratio of 1.7 could improve the compressor performance if the load capacity is lower than 50% for the specified condition, as shown in Fig. 6.10. This is because a bigger radial discharge port (i.e. smaller VR_r) reduces the over-pressure at the high load range. This suggests that VR_r may also be determined according to the compressor part load performance, provided that the machine operates

unloaded for a substantial part of its duty. However, it must be noted that this approach of improving the part load performance by changing VR_r will affect the fully loaded performance and other part load conditions, as shown in Fig. 6.10.

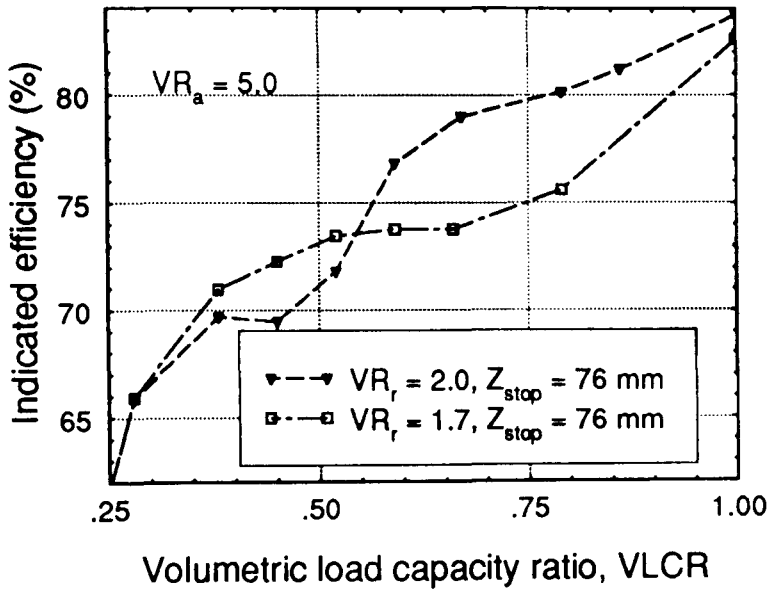

Fig. 6.10 Improving part load performance by changing VR_r

6.2.3 Optimal Slide Valve Design and Corresponding Bearing Loads

For the chosen volume ratios for both the axial and radial discharge ports, the slide valve parameters must be optimised for the given running condition. The most important one is the slide stop, which determines the compressor part load performance to a great extent.

Fig. 6.11 shows the effect of the slide stop on the indicated efficiency of the compressor during slide valve unloading. A small slide stop (e.g. 41 mm) tends to have a higher indicated efficiency at the high load range (0.8-1.0), while a big one tends to have a better performance at the low load range (<0.5). Thus, the best choice of the slide stop depends on the running conditions of the compressor.

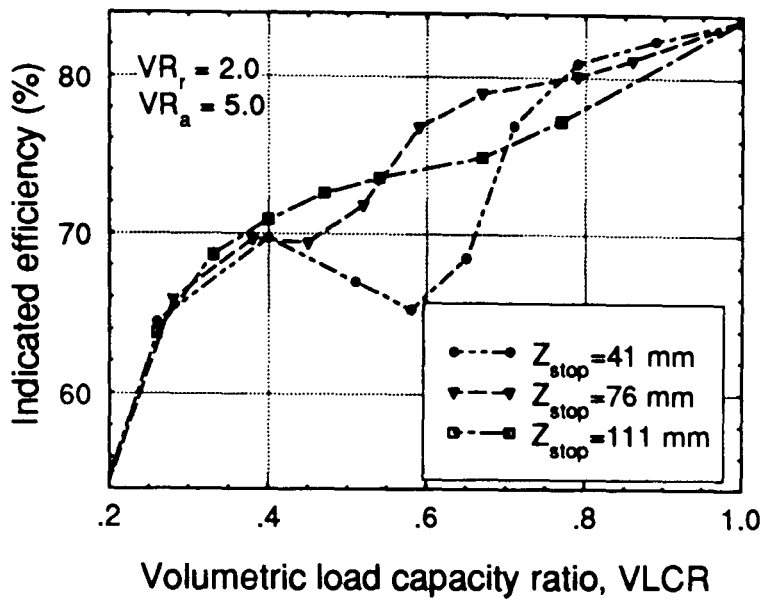

Fig. 6.11 Effect of slide stop on compressor part load performance

If a slide valve is designed in the way indicated here, there should be no severe over-pressure during slide valve unloading. The bearing loads calculated by the author's program corresponding to such an optimized slide valve design are shown in Fig. 6.12. It can be seen that the maximum values of all the components occur at the full load condition. This is also predicted for other running conditions and length / diameter ratios.

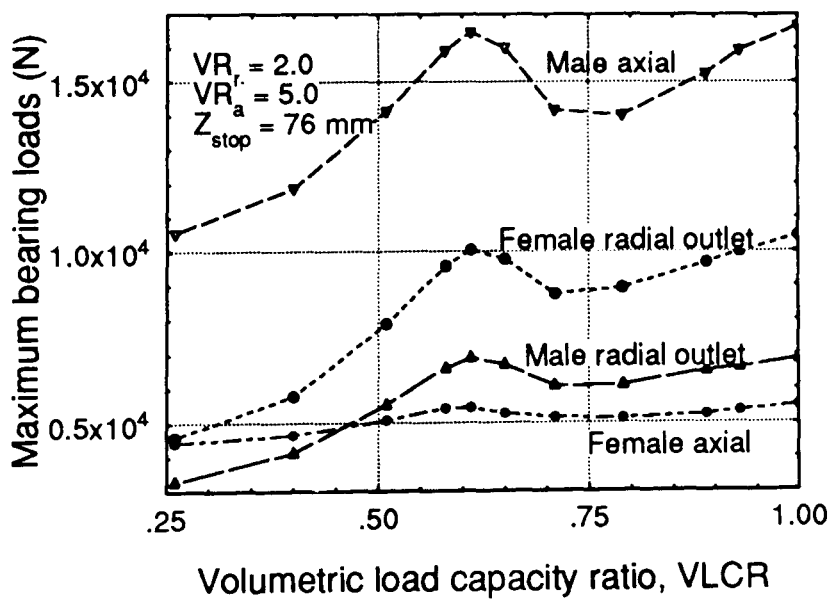

Fig. 6.12 Bearing loads for an optimized slide valve

However, if the machine is not run under its design condition or/and the slide stop or discharge ports are not the optimum for the given condition, severe

over-pressure may occur during slide valve unloading. Accordingly, the bearing loads at certain part load slide valve settings may be equal to or even higher than those at the full load condition, as shown in Fig. 6.13.

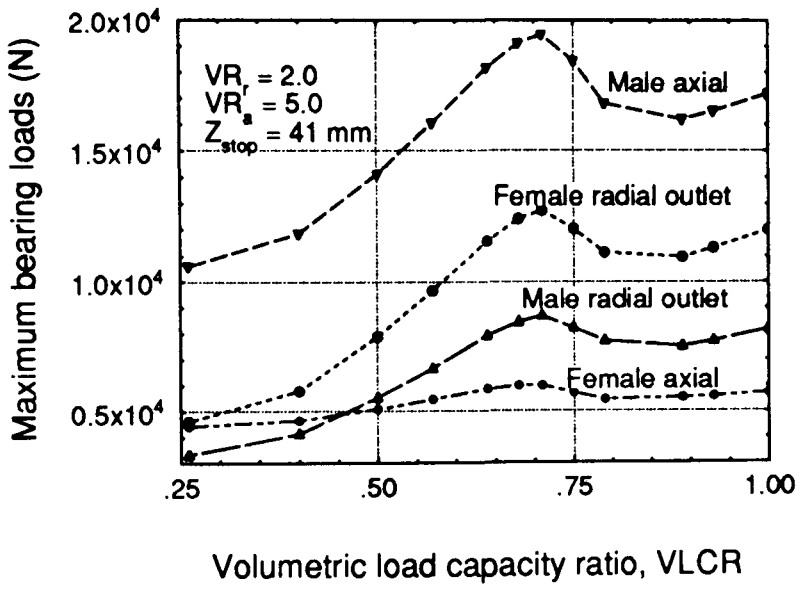

Fig. 6.13 Bearing forces for an improperly designed slide valve

When this situation occurs, the peak values of the maximum bearing loads usually appear in the load range of 0.55 - 0.75. This is explained as follows.

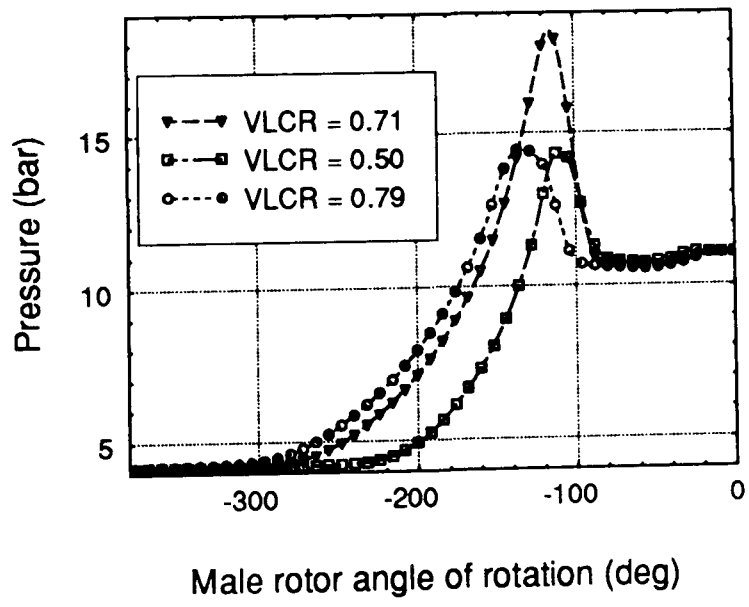

Fig. 6.14 Effect of load capacity ratio on discharge pressure

At the high load range (>0.75), the radial discharge port is still big enough for the gas to discharge without causing severe over-pressure. While at the low load range (<0.55), although there exists over-pressure in the compression

chamber due to the reduction of the radial port area, the rotor area exposed to the compressing gas is considerably reduced, as may be deduced from Fig. 6.14. This is the explanation of why high bearing forces appear at part load only for small slide stop values; i.e. over pressure is combined with a large cavity area. In summary, high bearing forces will only occur at part load in a compressor of a particular design (a small slide stop) running under particular conditions (about a volumetric capacity ratio of 0.65). In these circumstances, the female rotor radial bearing force at the discharge end and the male rotor axial force are both larger than their full load equivalents for the specified compressor and running condition.

6.2.4 Conclusions

- A slide valve ensures that the compressor obtains a relatively high indicated efficiency at part load condition, but reduces the compressor full load performance considerably. It is thus suggested that in the situation in which two or more twin screw compressors are used together, one or more should be without a slide valve and should always run under the full load condition with both the radial and axial discharge ports having the same volume ratios.

- The volume ratio for the axial discharge port not only controls the discharge process at low load, but also sets the theoretical minimum load capacity at which the compressor can be run. Using a high volume ratio for the axial discharge port, e.g. 5.0 for the minimum load capacity of 40 percent, may considerably decrease the indicated efficiency at the load range of interest. It is therefore suggested that the VR_a should be optimised for the most common running condition of the compressor.

- The volume ratio for the radial discharge port should be chosen according to the best full load performance. It can provide a relatively high indicated efficiency over the entire adjusting range of the slide valve. Additionally, the radial discharge volume ratio may also be used to improve compressor part

load performance, but to the detriment of the full load performance.

- A suitable slide stop should be determined to achieve a relatively high indicated efficiency over the load range within which the compressor is to be run.

- If the volume ratios and slide valve are designed to optimise the indicated efficiency, the maximum bearing forces appear at the full load condition. However, a change in running conditions combined with an unwise choice of slide stop may result in the occurrence of the maximum bearing forces at the part load condition of 0.6 - 0.7. To ensure safe operation, it is suggested that in addition to the performance prediction, a force analysis should also be carried out when changing the running condition or changing the slide valve design of a twin screw refrigeration compressor.

6.3 Removing the Non-Return Valve from the Refrigeration System

Refrigeration systems driven by twin screw compressors are normally fitted with a non-return valve in the suction line of the compressor to prevent the gas in the high pressure side from flowing backwards through the compressor into the suction chamber following system shutdown. This reverse flow would cause the compressor and prime mover to run in the reverse direction at a dangerously high speed. However, the use of non-return valves has the disadvantage of causing extra gas pressure drop, resulting in an increase in energy consumption and a decrease in the coefficient of performance (COP) of the refrigeration system. In view of the huge number of refrigeration applications worldwide, even a small gain in plant efficiency is of significance and this is achievable with the removal of the non-return valve, especially from systems which have long periods of continuous running and infrequent

shutdowns. Furthermore, malfunctions of non-return valves have been caused by contamination of the refrigerant. As a consequence, removing the valve results in an increase in system reliability. The purpose of the non-return valve in the high pressure side is to prevent the reverse flow of liquid refrigerant from the condenser into the oil separator following shutdown.

If the suction side non-return valve is removed, something must be done to prevent reverse rotation of the compressor and prime mover following shutdown. A practical approach is to fit a non-reversing clutch to the free end of the prime mover shaft. However, care must be taken with the design of the clutch since the shutdown torque caused by the high pressure gas filling the cavities of the compressor may reach a peak value considerably higher in value than the normal running torque.

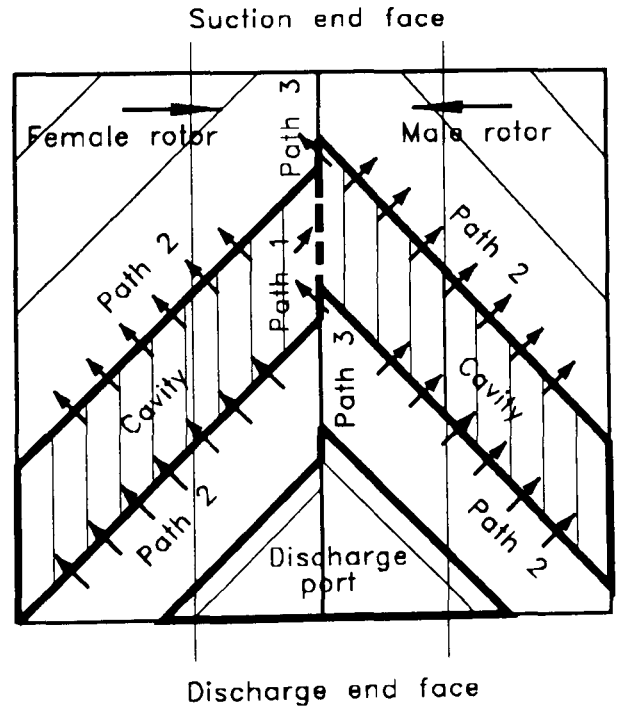

Fig. 6.15 Leakage paths for a cavity volume

Following the shutdown of a system without a suction non-return valve, gas will flow from the oil separator volume, which is of course at high pressure, backwards into the compressor and leak through various leakage paths to fill up the compressor cavities as shown in Fig. 6.15. A "quasi-steady-state" is reached when the mass flow rate into a cavity equals that out of the cavity.

At this stage the pressures developed in the cavities attain their peak values and will remain unchanged as long as the pressures in the discharge and suction chambers remain constant. The pressure pattern developed in the cavities following shut down is not the same as that for normal running. Consequently, the gas torques resulting from this pressure pattern may be rather different from those due to normal running conditions, and the difference between them may vary with the running conditions. For safe operation, the non-reversing clutch must be designed to transmit the maximum gas torque following shutdown. The determination of the shut down torque is therefore of importance to the designers of such systems.

The most economic and powerful technique available for the determination of the static gas torque is computer simulation. Utilizing the University of Strathclyde's performance simulation program (Tang and Fleming, 1992) the influence of the pressure drop across the non-return valve on the system COP and power consumption of a conventional single stage refrigeration system is examined.

For both normal running and shut down conditions the pressure distributions in the cavities of a real compressor are presented as an example, from which the normal running and shutdown torques are calculated by utilizing the force analysis program described in Chapter 4. The results obtained and the suggestions made may help the designers and operators to ensure the safe operation of a system with a non-reversing clutch used in preference to a non-return valve.

The specifications of the compressor used for the calculations are as follows:

- Rotor lobe profile: SRM D
- Lobe Combination: 4 / 6
- Wrap angle (male): 263.6°
- Rotors' diameter (mm): 204
- Length / diameter: 1.45
- Driving rotor: male

The chosen running conditions:

- Refrigerant: *R* 22
- Male rotor speed: 3000 rpm

- Evaporating temp.: 0 °C
- Condensing temperature: 35 °C
- Suction pressure: 4.98 bar
- Discharge pressure: 13.55 bar
- Oil injected (40 °C): 150 kg/min
- Suction superheat: 25 °C

6.3.1 Influence of Non-Return Valve on COP of the System

A single stage refrigeration system is assumed in this study as shown in Fig. 6.16. For a range of pressure drops due to the non-return valve in the suction line the power consumption and the COP of the system have been computed and are given in Figs. 6.17 and 6.18, respectively.

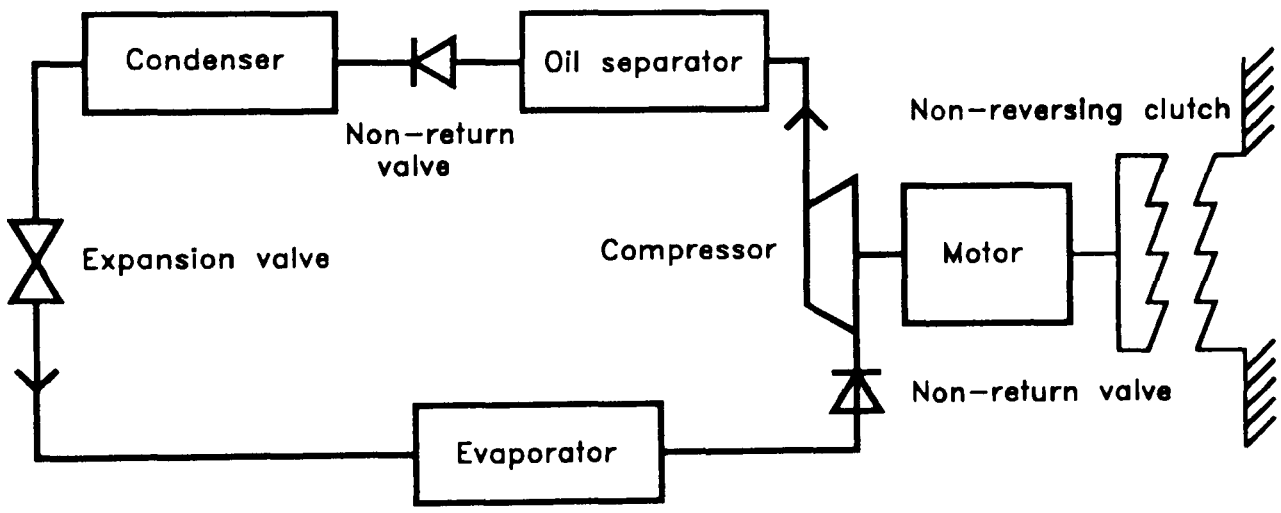

Fig. 6.16 A single stage refrigeration system

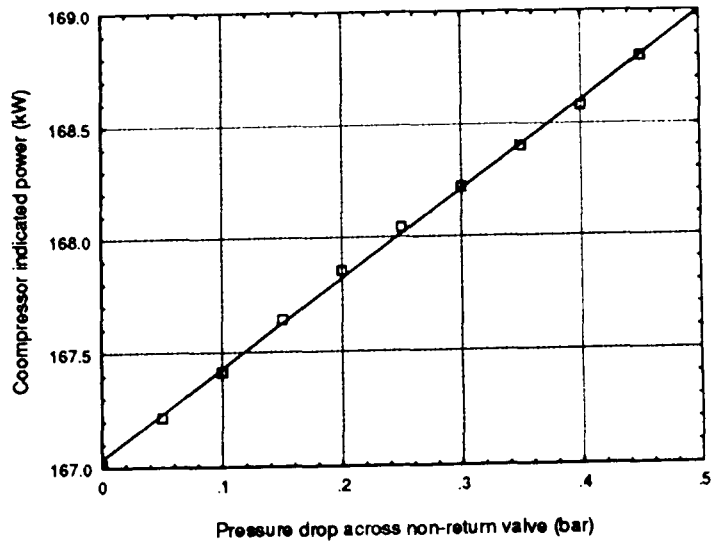

Fig. 6.17 The influence of the pressure drop across the non-return valve on the indicated power of the compressor

As shown in Fig. 6.17 the indicated power of the compressor increases linearly with the increase in the pressure drop across the non-return valve in the suction line. For a pressure drop of 0.20 bar, the indicated power increases by 0.84 kw, about 0.5 percent of that of the same system without the non-return valve.

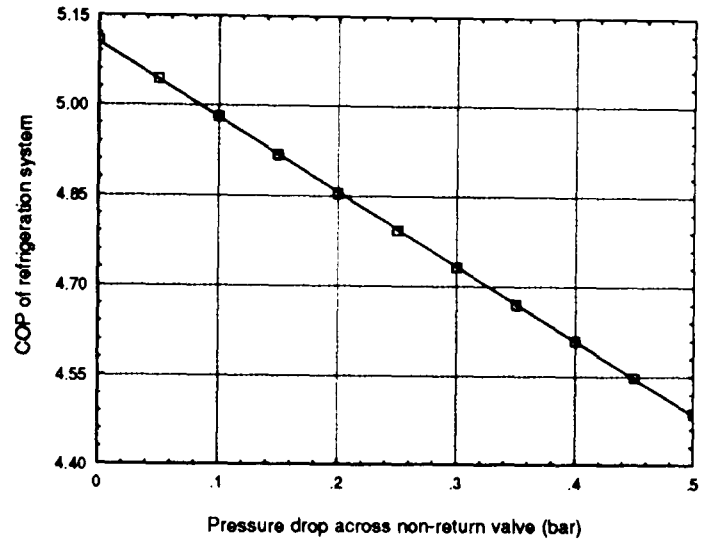

Fig. 6.18 The influence of the pressure drop across the non-return valve on the COP of the system

The detrimental effect of the non-return valve in the suction line is also apparent in Fig. 6.18, showing a linear decrease in the COP of the system with an increase in the pressure drop. Similarly, for a pressure drop of 0.20 bar, the COP of the system decreases by 5.0 percent compared with that of the same system after the removal of the non-return valve.

Thus, removing the non-return valve would be a clear advantage, but the consequences of this action must be assessable quantitatively by the designers.

6.3.2 Comparison between Normal Running Torques and Shutdown Torques

For the compressor and operating conditions specified, the gas pressures in the compression cavity are obtained from the thermodynamic performance

simulation program for both the normal running condition and the shut down situation. For the shut down case, a stationary rotor is approximately by a very slow speed of rotation. This permits all the leakages to occur for long enough to allow the maximum cavity pressure and thus torque to develop. The pressures in the cavity for both cases are shown in Fig. 6.19 as functions of male rotor angle of rotation. As expected, a big difference exists between these two pressure distribution patterns. Unlike the smooth pressure-volume curve due to normal running, the pressure distribution in the cavities at the quasi- steady-state following shut down exhibits a step curve pattern. It can be seen that for some angles the shut down cavity pressure is greater than that at normal running. The possibility thus exists that the maximum shutdown torque is larger than that due to normal running.

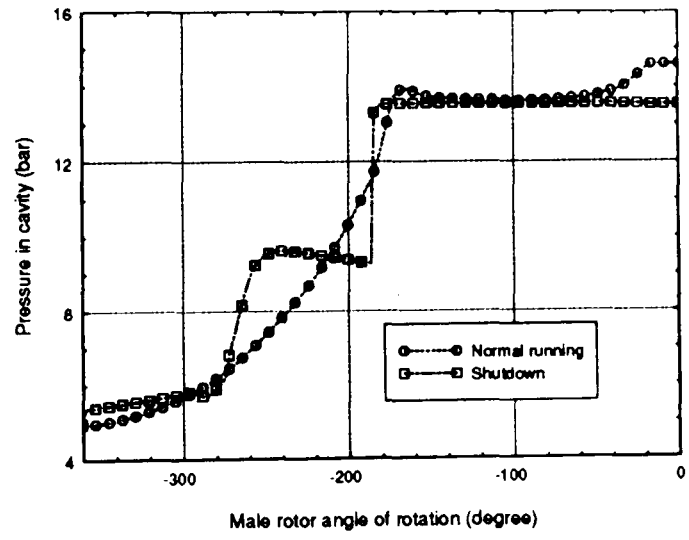

Fig. 6.19 Pressures in cavities vs male rotor angle of rotation

Fig. 6.20 reveals the difference between the torques at normal running and shut down. The friction torque of the compressor is not considered in this calculation, only the torque due to gas pressure. The zero-degree angle in the figure is the angle where the tip of the male rotor is located on the line connecting the male and female rotor centres in the discharge end plane. The torque curves vary with a period of 90°, that is 360° divided by the number of the male rotor lobes. For the conditions specified, the peak value of the shut down torque is 8.3 percent higher than the peak value of the normal running

torque, and 14.6 percent higher than the driving torque (taken as the average of the normal running torque here). The peak value of the shut down torque occurs at the male rotor rotational angle of -80°. Since the stop position of the rotors is absolutely random, a clutch chosen or designed according to the driving torque runs the risk of being broken.

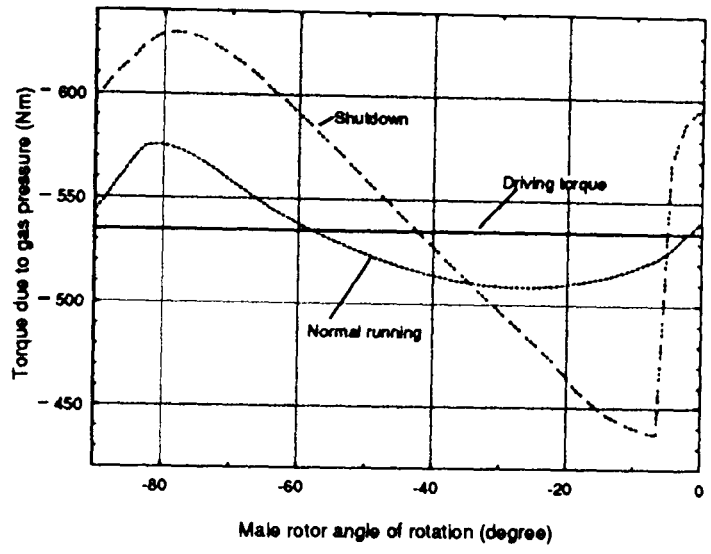

Fig. 6.20 Comparison between normal running torques and shutdown torques

Table 6.1 The influence of evaporating temperature on the maximum shutdown torque
(discharge pressure 13.55 bar / condensing temp. 35 °C)

Evaporating temperature (°C)	Suction pressure (bar)	Shutdown torque (N.m)	Driving torque (N.m)	Shutdown torque exceeds the driving torque (%)	Corresponding rotor position (deg)
0	4.98	650.61	567.90	14.56	-80
-5	4.21	718.58	580.65	23.75	-79
-10	3.54	780.32	591.81	31.85	-79
-15	2.94	835.04	600.51	39.06	-78
-20	2.45	883.32	607.50	45.40	-77
-25	2.01	922.1	616.6	49.6	-77
-30	1.64	959.4	622.3	54.2	-76
-35	1.32	991.5	634.5	56.3	-76
-40	1.05	1016.7	639.2	59.1	-75

It should be noted that the difference between the normal running torque and

the shut down torque will vary with the operating conditions. As an example, nine different evaporating conditions are used in this study and the results are tabulated in Table 6.1, in which only peak values of the torques and the corresponding rotor positions are given. It can be seen that the percentage by which the shut down torque exceeds the driving torque increases with the decrease in evaporating temperature (Fig. 6.21). Since the discharge pressures are same for all these cases, it can be concluded that the extent to which the maximum shut down torque exceeds the driving torque increases with the increase in the pressure ratio of the compressor. In contrast, the change in evaporating temperature has little influence on the angular position of the peak value of the shut down torque.

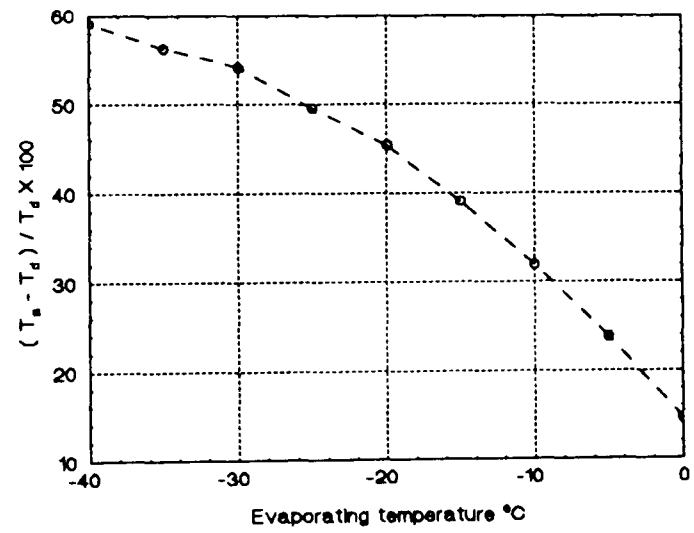

Fig. 6.21 The variation of torque difference with evaporating temperature

6.3.3 Suggestions for Shutting the System Down Safely

From the above discussion, it is clear that the non-reversing clutch in a refrigeration system should be chosen or designed according to the maximum shutdown torque, which guarantees a safe shut down of the system whether the shutdown is intentional or unintentional.

However, if the clutch is chosen or designed according to the driving torque due to the lack of the computing programs or measurement data, making use of the slide valve fitted in the compressor will help to achieve a safe shut down

of the system. Fully opening the slide valve alters the pressure pattern in the cavities of the compressor and results in a large reduction of shutdown gas torque. Fig. 6.22 shows the shutdown torque calculation results for the specified compressor under part load conditions, from which it can be seen that the shutdown torque under the part load condition is much lower than the driving torque under the full load condition. It is thus suggested that the slide valve should be fully opened prior to the shutdown of the system, which would greatly reduce the gas torque applied to the clutch following shut down. However, it must be pointed out that this approach does not relieve the risk of the clutch breaking following a sudden automatic shut down of a system for safety reasons if it is running at full load, at the instant at which it is shut down. However, a more sophisticated shut down procedure for the control system would solve this problem; i.e. slide valve unloading first followed by shut down.

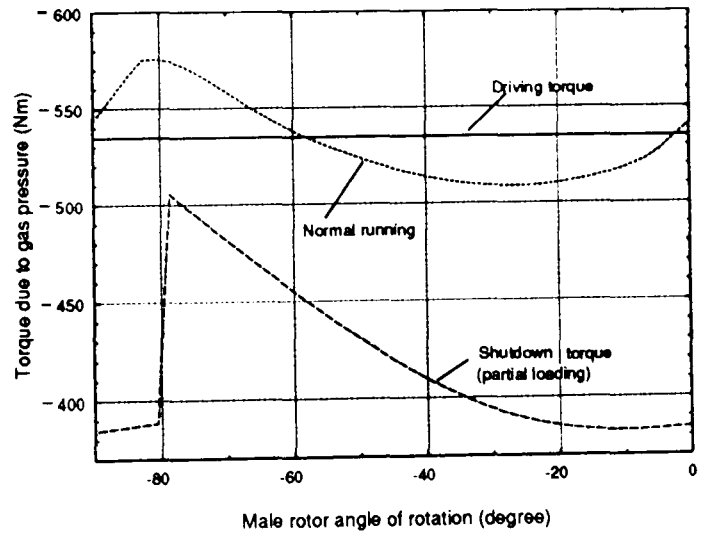

Fig. 6.22 Gas torques under partial load condition vs male rotor angle of rotation

6.3.4 Conclusions

The following conclusions can be drawn from this study:

- The COP of a refrigeration system with a twin screw compressor can be enhanced and the energy consumption of the compressor can be reduced by removing the non-return valve from the system. For the specified compressor

and running condition, a 5.0 % increase in COP and a 0.5 % decrease in indicated power can be achieved after the removal of a non-return valve in the suction line which causes a gas pressure drop of 0.20 bar.

- A non-reversing clutch can be used instead of a non-return valve to prevent the reverse rotation of the compressor and prime mover. Since the peak value of the shutdown torque may be considerably larger than the driving torque and the stop position of the rotors is absolutely random, the clutch must be chosen or designed according to the maximum shutdown torque, which varies with running conditions.

- In the case of clutches designed according to the driving torque due to the lack of appropriate facilities for calculating static and running torques, it is suggested that the compressor should be unloaded via its slide valve prior to the shutdown of the system. This will ensure that the maximum shutdown torque is smaller than that under the full load running condition.

6.4 Summary

Utilizing a suite of computer programs, a study on the optimum design of the slide valve and the non-reversing clutch, two important components in a screw refrigeration system, has been conducted.

The simulation shows that the slide valve has a great influence on compressor efficiency and bearing forces. The volume ratios for discharge ports and the slide stop (the most important design parameter of the slide valve) must be optimized for a given running condition, and a procedure for such a optimisation has been presented. The results suggest that the addition of a slide valve to a compressor results in a decrease in the indicated efficiency at the full load condition. For a particular minimum part load condition the volume ratio fixed by the axial discharge port should not be over high. If it is, a decrease in the indicated efficiency at the low load range will result.

However, the volume ratio for the radial discharge port should be chosen so as to obtain the highest indicated efficiency at full load. Compressor designers should be aware that the maximum bearing forces will occur at certain part load conditions for certain slide stop sizes.

The removal of the non-return valve from the refrigeration system with a twin screw compressor is realizable by fitting a non-reversing clutch to the prime mover to restrain the reverse rotation of the compressor following shut down. The results suggest that the use of the non-reversing clutch results in a decrease in energy consumption and an increase in system COP. The shut down torque may have a peak value considerably higher than the normal driving torque, thus care must be taken with the choice or design of the clutch.

+ The first part of this chapter, *Optimum Slide Valve Designs,* has been presented on the VDI-Tangung, Schraubenmaschinen '94, Dortmund, Germany, October 1994, and has been published by the VDI Verlag on VDI Berichte 1135, 1994 (Fleming, et al, 1994c).

The second part of this chapter, *Removing the Non-Return Valve from a Refrigeration System with a Twin Screw Compressor,* has been presented on the International Compressor Engineering Conference at Purdue, USA, July 1994 (You, et al, 1994b).

Chapter 7

Rotor Axial and Torsional Coupled Vibration Analysis

7.1 Introduction

In a wet screw compressor there are basically three different phenomena which are capable of exciting vibrations and noise:

Gas pulsations

In any positive displacement compressor gas pulsations are inevitable (i.e. due to periodic variation of the cavity gas pressure). The vibrations caused by this phenomenon can only be kept within acceptable limits by avoiding resonance and/or by adding damping. The gas pulsation problem has been studied by, among others, Lundin (1992) and Sångfors (1992). The gas pressure results in axial, radial and tangential components of force. As a consequence, it can excite axial, bending and torsional modes of vibration.

Vibrations from bearings

It has proved very important to be able to monitor the vibrations caused by the rolling element bearings. Changes in the vibration signatures of bearings give a very good warning of possible bearing failure (Lim, 1992).

Inter-rotor contact forces

The third phenomenon causing vibrations in the compressor is the rotor interaction. As with gas pressure forces, the inter-rotor contact force has axial, radial and tangential components, and so can excite axial, bending and torsional modes of vibration. In addition, manufacturing errors are capable of causing a different time history for the inter-rotor contact force from that which derives from the nominally perfect lobes.

Rotor interaction vibrations not only cause rotor noise, but may also damage the smooth contact of the rotors, resulting in an increased leakage loss and a shortened rotor service life. Fortunately, researches conducted in SRM (Öhman, 1992) have suggested that as long as there are oil films between the rotors and in the bearings the oil film will limit the damage to negligible levels. Even some manufacturing errors can be accommodated if the oil film is thick enough.

However, these periodically varying forces (and torques) are caused by different phenomena and appear in a wide range of frequencies. As a consequence, the possibility of one of the many harmonic components resonating with a natural frequency of the system of which the compressor is a part, has to be considered.

This requires that a frequency analysis of all the excitations be done and that the natural frequencies of the rotor - bearing system be calculated. To avoid any possible excitation of resonance, the frequencies of the forces and torques applied to the rotors must be different from the natural frequencies of the system.

The radial force applies bending moments which flex the rotors and, thus, can reduce performance by effectively increasing the clearances. Further, they can make the rotors rub against the housing bores. This is more likely to be a problem with longer rotors. Many present compressor designs make these

deflections small by the use of short stiff rotors. Accordingly, the natural frequency of the flexural vibration of such rotors is relatively high.

The axial load component and the torque vary with the rotation angle of the male rotor with a fundamental frequency equal to the male rotor lobe passing frequency, i.e. lobe number, multiplied by rotor rotating speed (rpm). These periodic loads cause the rotors to vibrate axially and torsionally. Furthermore, due to the helical lobes of the compressor rotors, these axial and torsional vibrations are coupled.

The general effect of the coupling on the natural frequency of a geared system is to replace the uncoupled frequencies by two new frequencies, the lowest coupled frequency being below the lowest uncoupled frequency and the highest coupled frequency being higher than the highest uncoupled frequency (Wilson, 1956).

A recent study of the axial and torsional vibration of screw compressor rotors (Honke and Yoshimura, 1992) gave a numerical example as follows:

Rotor geometry:

- SRM A-profile, rotor diameter 321.3 mm, length/diameter ratio 1.65

Eigen values (Hz):

- only torsional mode: 1.69, 234
- only axial mode: 192, 2027
- axial and torsional coupled mode: 1.86, 145, 193, 3092

It can be seen that the two uncoupled frequencies, i.e. the first mode of only axial vibration 192 Hz and the second mode of only torsional vibration 234 Hz, have been replaced by two coupled frequencies of *reduced* values of 145 Hz and 193 Hz respectively. This is why the coupling of axial and torsional vibration must be taken into account when analysing the rotor vibration of screw compressors. Assuming a 4+6 lobe combination which is quite common for SRM A-profile, it is obvious that a high amplitude vibration will occur if the

compressor rotating speed is 3000 rpm (corresponding to a frequency of 200 Hz). This example demonstrates the importance of determining the natural frequencies of the coupled axial and torsional vibration of the rotor - prime mover - bearing system at the compressor design stage.

However, the analysis made by Honke and Yoshimura (1992) did not consider the oil film presence between the rotors, which in general will have the effect of reducing the natural frequencies of the system.

In this study a model was created for the analysis of coupled axial and torsional vibration of oil-injected helical twin screw compressor rotors (see section 7.2). Due to the lack of reliable system parameters such as oil film stiffness coefficients, thrust bearing stiffness coefficients, etc., the model is not solved in this study, but is suggested as further work deriving from this study. However, since the model is linear, the solution can easily be conducted by using a standard procedure if all the parameters are available. Also presented in this chapter (section 7.3) is a FFT analysis of all the forces and torques applied to the rotors, the results of which, in addition to being used in a search for resonance, are also necessary if the response to the forced vibration is wanted. The chapter is summarized in section 7.4.

7.2 The Analytical Model

Most oil-injected helical screw compressors utilize male rotor drive, usually direct driven by an electric motor or engine through a coupling as shown in Fig. 7.1.

In the following treatment it is assumed

- that the compressor rotors and the prime mover rotor are rigid bodies compared with the coupling and power transmission shaft which (combined) have a torsional stiffness, k_3;

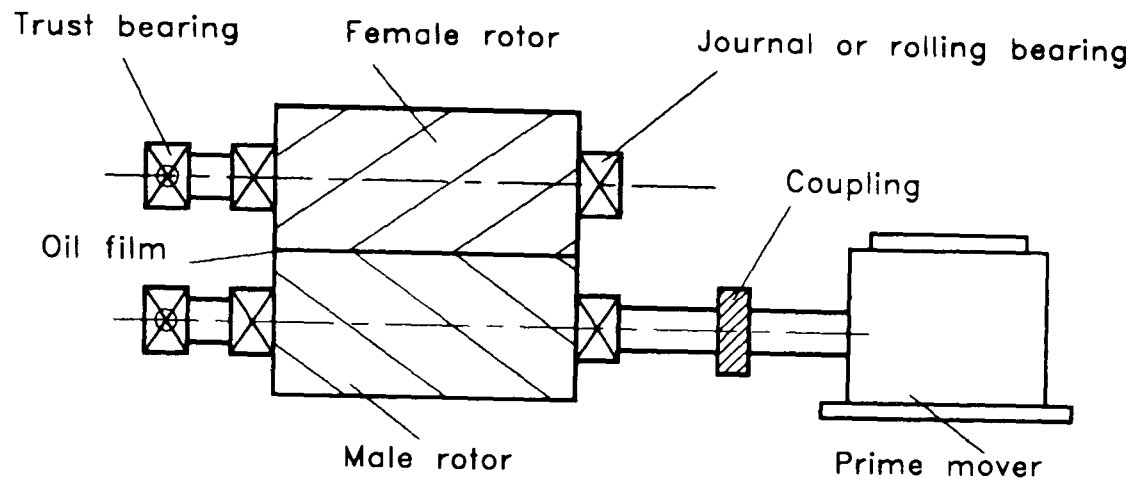

Fig. 7.1 Rotor - prime mover - bearing system

- that the thrust bearing supports have axial spring stiffness of k_1 and k_2;
- that the lobe interaction between helical screw rotors can be simplified to be the same as that in helical gears. Thus a common helix angle δ_p can be used in the analysis;
- that the oil film between the female rotor and male rotor provides radial, axial and circumferential stiffness coefficients, $k_{o,r}$, $k_{o,a}$ and $k_{o,t}$;
- that the influence of the transverse deflection of the shaft is negligible.
- that the amplitude of the vibratory torque on the rotors is less than the mean transmitted torque. This is true in most cases and accordingly, backlash in the rotor assembly does not affect the frequency calculations. That is, the phenomenon known as "chatter" is not considered here but is proposed as another suitable topic for further work.

Fig. 7.2 shows the idealised version of the system, where M, I, F, T, Z, and θ stand for mass, the 2nd moment of area, axial force, torque, axial and torsional variables respectively, while the subscripts $1,2,3$ are for the male rotor, female rotor and prime mover respectively.

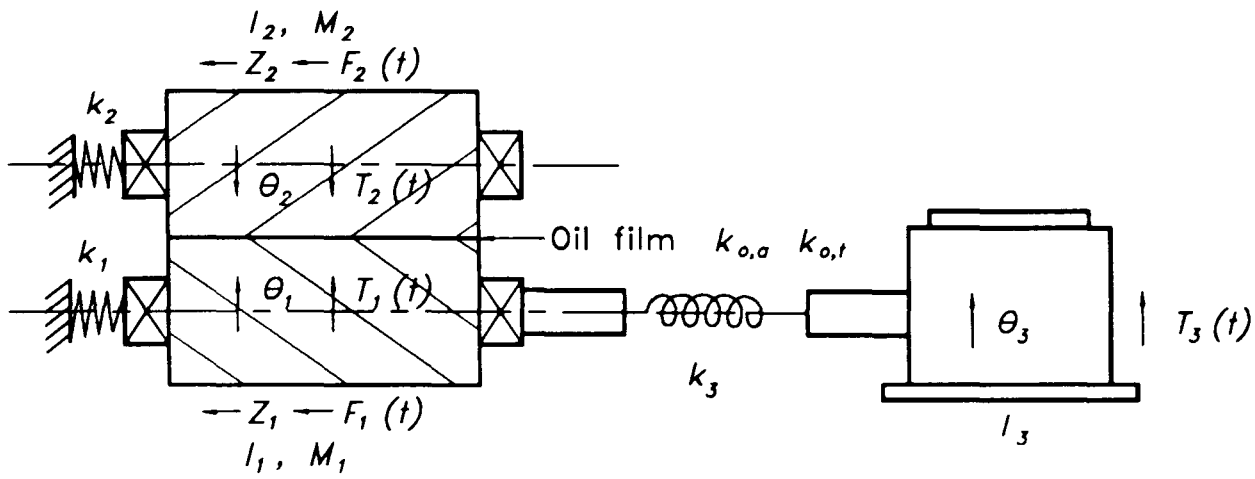

Fig. 7.2 Axial-torsional coupled vibration model

From the idealised system an axial and torsional coupled vibration analytical model is created as follows:

$$[M][\ddot{X}] + [K][X] = [F] \tag{7.1}$$

where

$$[M] = \begin{bmatrix} M_1 & 0 & 0 & 0 & 0 \\ 0 & M_2 & 0 & 0 & 0 \\ 0 & 0 & I_1 & 0 & 0 \\ 0 & 0 & 0 & I_2 & 0 \\ 0 & 0 & 0 & 0 & I_3 \end{bmatrix} \tag{7.2}$$

$$[X] = [Z_1 \; Z_2 \; \vartheta_1 \; \vartheta_2 \; \vartheta_3]^T \tag{7.3}$$

$$[F] = [F_1(t) \; F_2(t) \; T_1(t) \; T_2(t) \; T_3(t)]^T \tag{7.4}$$

$$[K] = \begin{bmatrix} k_1+k_{o,a} & -k_{o,a} & -r_{p,1}k_{o,t}\tan(\delta_p) & r_{p,2}k_t\tan(\delta_p) & 0 \\ -k_{o,a} & k_2+k_{o,a} & r_{p,1}k_{o,t}\tan(\delta_p) & -r_{p,2}k_{o,t}\tan(\delta_p) & 0 \\ -r_{p,1}k_{o,t}\tan(\delta_p) & r_{p,1}k_{o,t}\tan(\delta_p) & k_3+r_{p,1}^2k_{o,t} & -r_{p,1}r_{p,2}k_{o,t} & -k_3 \\ r_{p,2}k_{o,t}\tan(\delta_p) & -r_{p,2}k_{o,t}\tan(\delta_p) & -r_{p,1}r_{p,2}k_{o,t} & r_{p,2}^2k_{o,t} & 0 \\ 0 & 0 & -k_3 & 0 & k_3 \end{bmatrix} \tag{7.5}$$

For the eigen values of the system let the RHS of Eq. 7.1 equal zero. Assuming that the coordinate X performs harmonic motion with an undetermined frequency ω, viz.,

$$[X] = [\bar{X}] \sin(wt) \tag{7.6}$$

and substituting this in Eq. (7.1) leads to the following frequency determinant:

$$\left| -\omega^2 [M] + [K] \right| = 0 \tag{7.7}$$

For the response of forced vibration, since the excitations of forces and torques are not pure sinusoids, they have to be transferred to simple harmonic components by using a DFT (discrete Fourier transformation) method (Newland, 1989). The torque on the male rotor, for instance, will have a form of

$$T_1(wt) = \sum_{n=0}^{\infty} a_n \cos(n\omega t) + b_n \sin(n\omega t) \tag{7.8}$$

Assuming that each harmonic acts independently without interfering or interacting with other harmonics, the total response (from the principle of superposition) is obtained by the linear sum of the responses to all the individual harmonics.

7.3 Fourier Analysis of Forces and Torques

The forces and torques obtained from the force analysis program (Chapter 4) were analyzed by using an FFT technique, for which the MatLab commercial software was utilized in this study.

Figs. 7.3-7.10 show forces and torques of a numerical example in the time and frequency domains respectively. The compressor has a lobe combination of 4+6 and a running speed of 3000 rpm, giving a fundamental frequency of 200 Hz. The sampling frequency was set to be 9000 Hz and the sample

number was taken as 4096 so as to provide FFT results for the fundamental frequency.

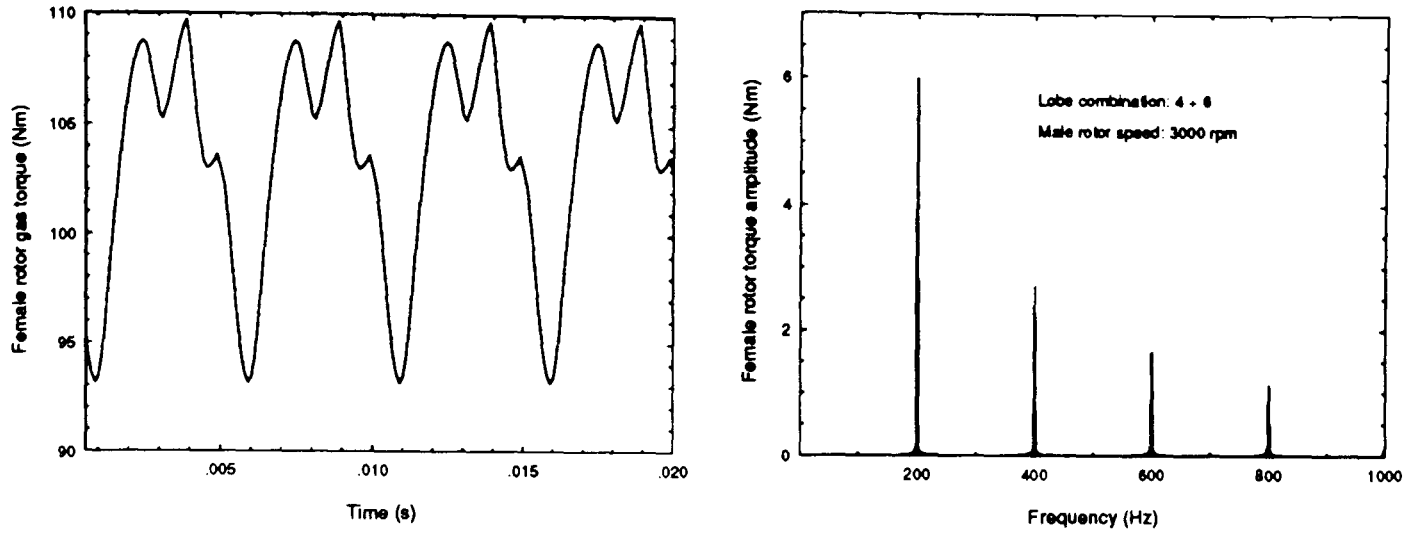

Fig. 7.3 Female rotor gas torque in the time and frequency domains

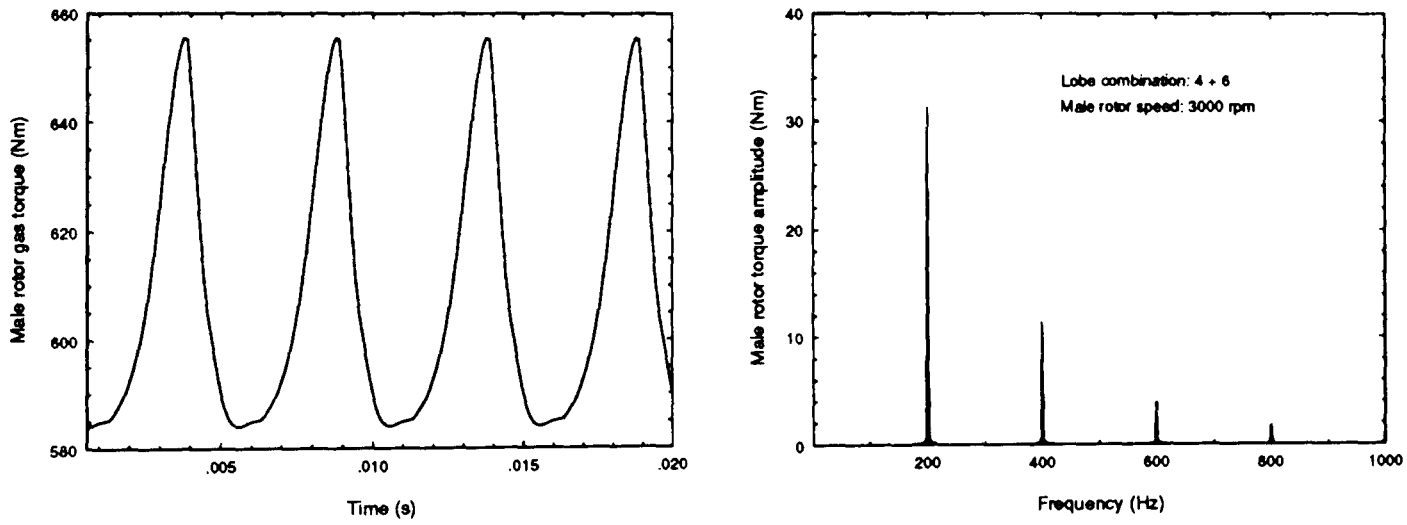

Fig. 7.4 Male rotor gas torque in the time and frequency domains

Figs. 7.3 and 7.4 show the gas torques on the female and male rotor respectively. As expected, the fundamental frequency appears at 200 Hz which is determined by the male rotor rotating speed and lobe number. While the fundamental mode dominates among all the frequency components, the second, third and even fourth harmonic excitations are apparently not negligible.

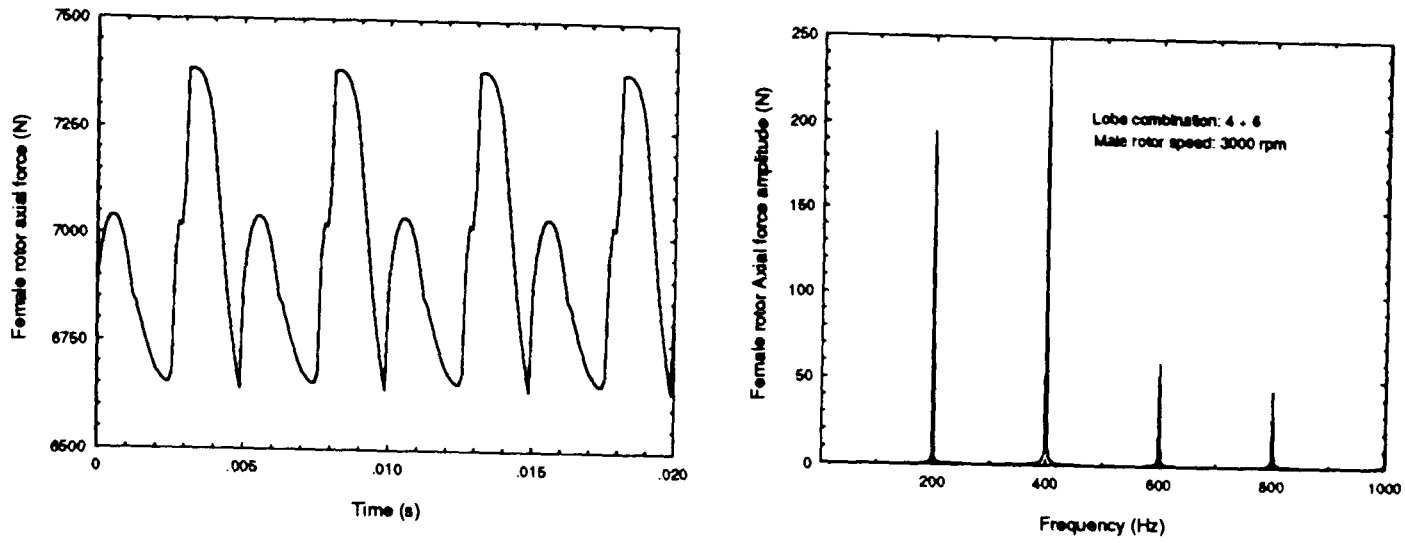

Fig. 7.5 Female rotor axial force in the time and frequency domains

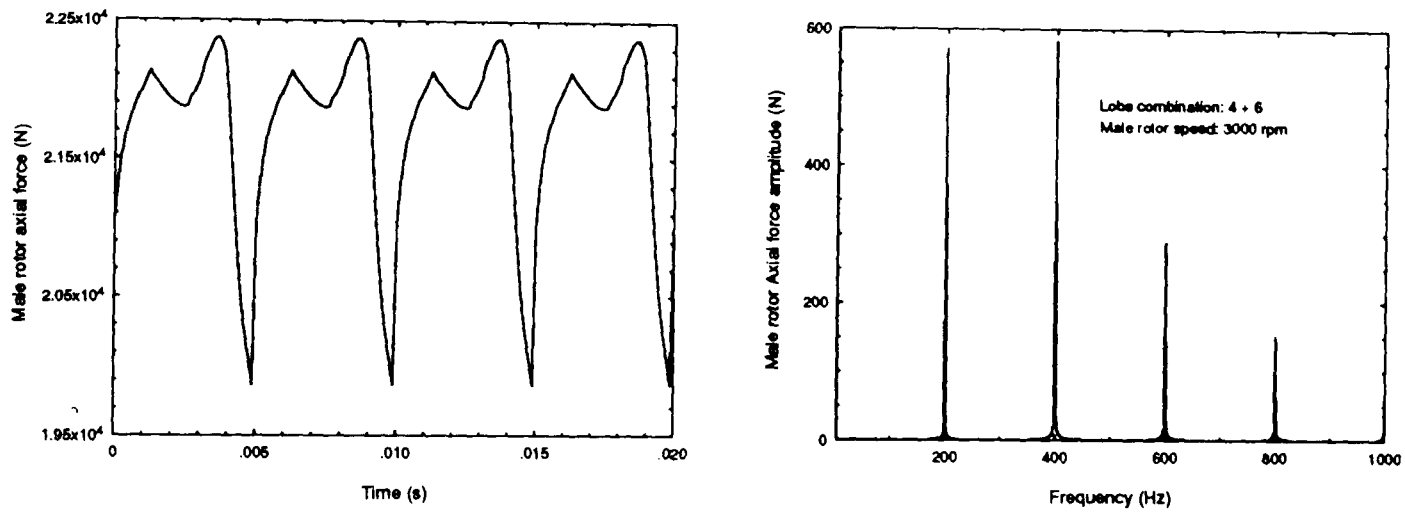

Fig. 7.6 Male rotor axial force in the time and frequency domains

In contrast to this, the frequency compositions of the axial forces on the male and female rotors have another picture (Figs. 7.5-7.6). The excitation of the second harmonic is slightly higher than the first harmonic, while the third and fourth harmonic remain at a low but not negligible level. There are no larger amplitude harmonics at higher frequencies.

Figs. 7.7-7.10 show the bearing radial forces in the time and frequency domains respectively. These forces are very much like the gas torques, with the fundamental harmonic being the largest of all the harmonics.

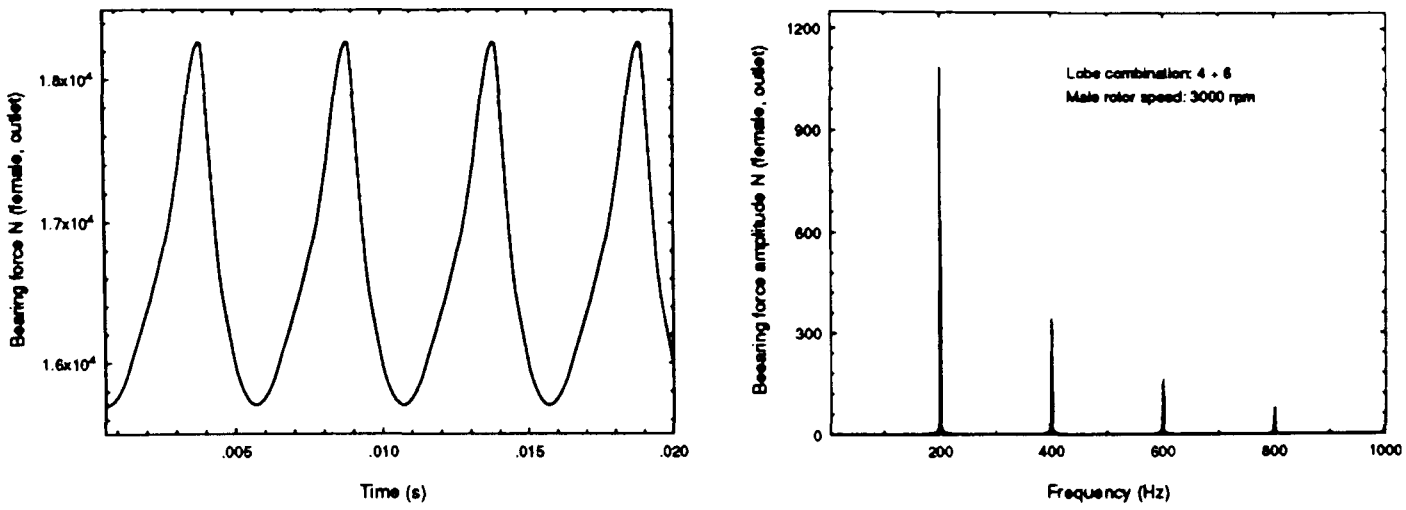

Fig. 7.7 Female rotor outlet side bearing radial force in the time and frequency domains respectively

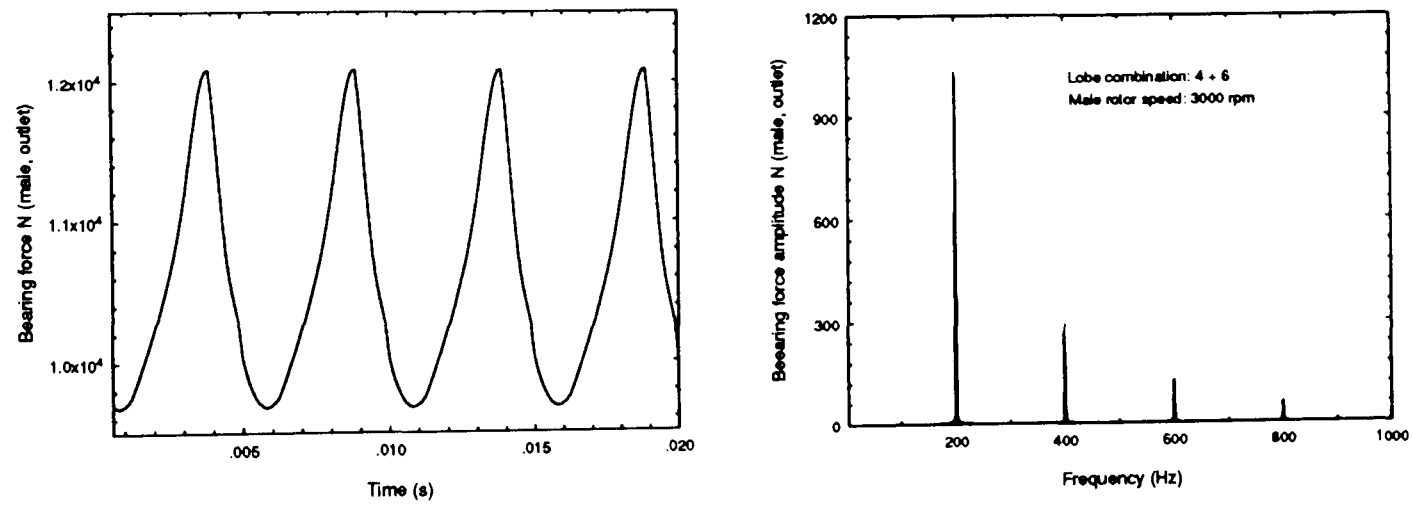

Fig. 7.8 Male rotor outlet side bearing radial force in the time and frequency domains respectively

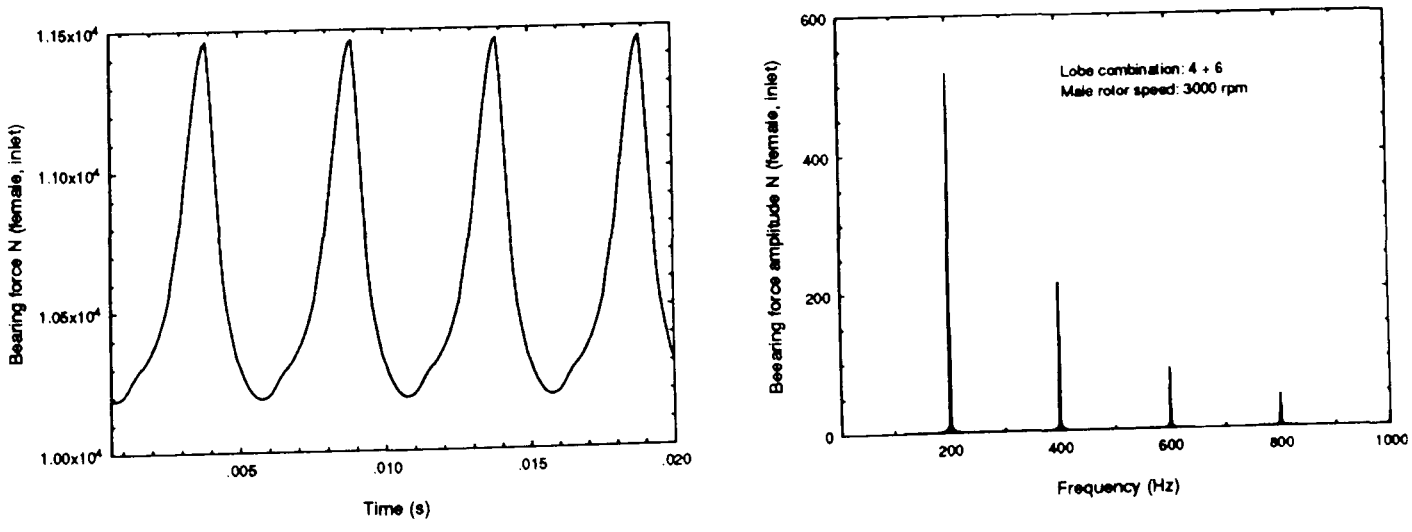

Fig. 7.9 Female rotor inlet side bearing radial force in the time and frequency domains respectively

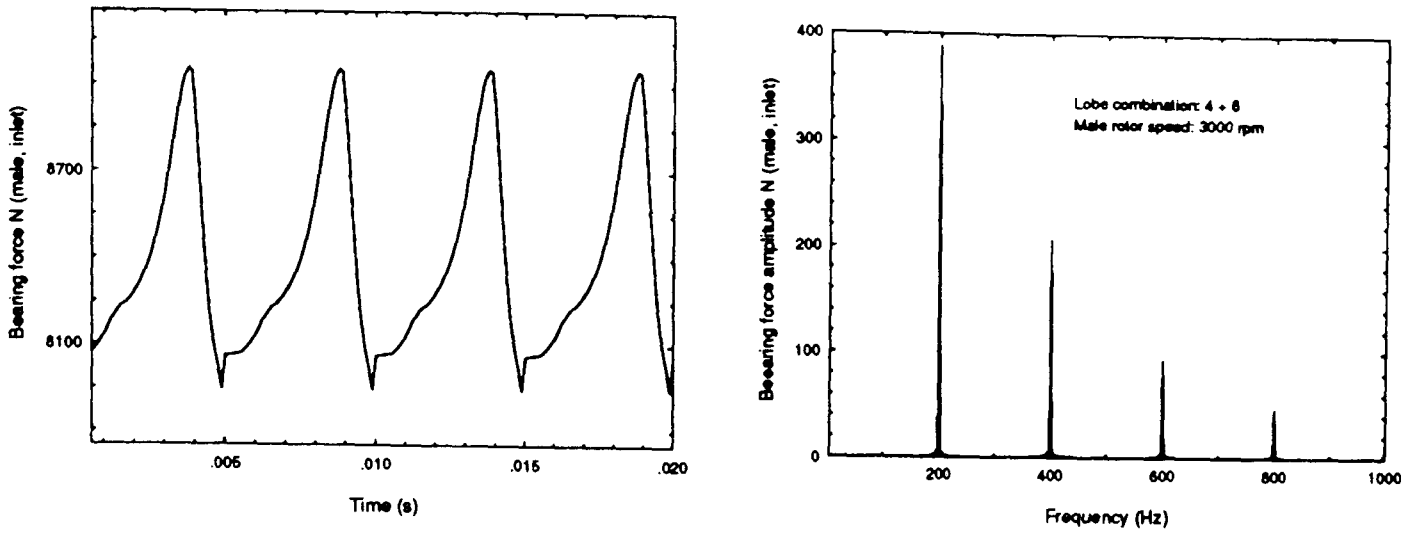

Fig. 7.10 Female rotor inlet side bearing radial force in the time and frequency domains respectively

7.4 Summary

Periodic loads exerted on rotors due to gas compression and lobe interaction cause coupled axial and torsional vibration in oil-injected helical twin screw compressors. The natural frequencies of such coupled vibration modes in a large machine may be relatively low and therefore require to be examined at the design stage. Utilizing assumptions which simplify the lobe interaction, an analytical model has been created, which provides a tool for compressor rotor vibration analysis if all system parameters are available.

Fourier analysis of all the forces and torques suggest that the fundamental harmonic, the frequency of which equals the male rotor speed multiplied by its lobe number, dominates among all the harmonic components. The axial forces are different, due to the second harmonic being slightly stronger than the first one.

Chapter 8

Discussions, Conclusions and Recommendations

8.1 Summary

This project deals with several aspects of refrigeration helical twin screw compressors and their systems. The work carried out may be grouped into the following two parts:

- The development of three computer programs for the generation of rotor profiles, the analysis of geometrical characteristics and the calculation of bearing forces and rotor torques;

- The investigation into several aspects of the refrigeration twin screw compressor and system designs, including (a) the optimisation of rotor lobe tip designs and rotor geometrical parameter combinations; (b) the effects of the slide valve and its optimisation; (c) the removal of the non-return valve from a refrigeration system driven by a twin screw compressor; and (d) the axial-torsional coupled vibration of a system comprising a twin screw compressor and its prime mover.

The first part of work reported here creates a foundation for the study of the

twin screw compressor, while the second part of the work demonstrates the capability of the programs developed for design and analytical purposes and gains an insight into aspects of the behaviour of refrigeration twin screw compressors and their systems.

8.1.1 The Development of the Computer Programs

The computer aided design technique demonstrated here has proven to be a fast, comprehensive and economic approach for the investigation of helical twin screw compressors. In this study, three computer programs have been developed, which are combined with the University of Strathclyde's performance simulation program and together form a powerful tool for optimising the design of twin screw compressors. Due to the complex geometry of the twin screw compressor rotors and the lack of detailed publications in the relevant areas, this work has been challenging and novel techniques have been used. All three programs developed were written in Turbo-Pascal and can be run in any IBM/DOS compatible personal computers.

Rotor Profile Generation Program

The analytical envelope method has been used in developing the program for the generation of twin screw compressor rotor profiles. The program is, to some extent, general because it is applicable to any profile types provided that the "known" segments of the profiles are circular arcs or straight lines or points. For SRM A and D profiles, the user just needs to specify some basic parameters (e.g. rotor outer diameter, lobe combination, centre distance, range angles for the lobe tip segment, etc), the program will calculate, according to the definition of the profile type, the parameters defining the position of all "known" segments, and then generate the conjugated parts according to the analytical envelope method. For other existing profiles or any new profile types (the "known" segments of which must be circular arcs or straight lines

or points), the user has to specify the position parameters of all "known" segments on line or by reading a pre-prepared data file.

The program is reasonably user friendly being menu driven. Basic input parameters are pre-saved as disk files and can be loaded and viewed and changed easily. Generated profiles can be viewed on screen. While viewing, it can be moved around and scaled up/down, so any part of the picture can be examined in great detail. The coordinates, the first derivative and pressure angle of generated rotor profiles are then saved to disk files for further use. The program developed has been used successfully for the generation of SRM A- and D- profiles.

Geometrical Characteristics Calculation Program

This program can be used for the calculation of the geometrical characteristics of the twin screw compressor, including the sealing line length between the male and female rotors and between the rotors and housing bores, the blow hole area, the inter-lobe area and the cavity volume. All these parameters as functions of the male rotor angle of rotation are given by the program.

The sealing line length between the rotors was calculated by assuming a linear connection between the two adjacent points on the contact line (see section 3.2), while the sealing line length between the rotors and housing bores was obtained through a curve integration along the lobe tip lines (see section 3.3). The blow hole area was calculated by using a modified three vertices method, while the inter-lobe area and cavity volume were determined utilizing the traditional slice method.

Similarly, the program is easy to use, being menu driven. It uses as input the data files output by the rotor profile generation program. The user has to specify rotor structure parameters, i.e. the length/diameter ratio and the wrap angle. The results of the calculation can be viewed on screen or saved as disk files for further use.

A good performance from the compressor requires that the sealing line length is as short as possible, the blow hole as small as possible, and the inter-lobe area and cavity volume as large as possible. The program can thus be, from the point of view of geometrical characteristics, instrumental in inventing entirely new profiles or modifying the existing profiles, and in optimizing rotor geometrical parameters such as lobe combination, wrap angle and length/diameter ratio.

The program has been applied successfully to SRM A- and D-profiles constructed to a wide range of geometrical parameters. It should be applicable to other types of rotor profiles, although some minor modifications may be needed if profile shapes differ significantly from the SRM-asymmetrical type.

Bearing Force and Rotor Torque Calculation Program

This program has been developed and integrated with a geometrical calculation program and a performance simulation program. The result is a calculation facility which is capable of computing the torques, bearing forces and female rotor deflections of a helical twin screw compressor for various settings of geometrical parameters and running conditions.

Compression gas forces applied to the helical surfaces of the rotors were calculated by using a modified slice method, in which the axial force can also be obtained. The forces applied to the rotor end faces due to both compression gas leakage and the exposure of the rotor ends to discharge and suction ports, were determined by transferring a area integration into the curve integration along the boundaries of the area to which compression gas is applied. The contact forces between the rotors were obtained by assuming a constant magnitude along the power transmission section of the contact line for a male rotor angle of rotation. The offset effects of axial forces on the radial bearing forces have been taken into account.

Again, the program is reasonably user friendly being menu driven. After loading the generated rotor end profile results and the cavity pressure simulation results, the user may specify the rotor structural parameters such as the position of bearings, length and diameters of rotor shafts, the pressures applied to the shaft ends, the position of discharge port, etc. The calculated results may be saved as disk files and/or viewed on screen.

The program has been verified by comparing its predictions with measured bearing radial forces. The capability of such an integrated program has been demonstrated by applying it to compressors for a range of slide valve settings, discharge and suction pressures, and geometrical parameter combinations and comparing the predictions with measured data.

8.1.2 Some Aspects of Refrigeration Helical Twin Screw Compressors and Their Systems

Utilizing the integrated computer programs described above, investigations have been carried out on several aspects of refrigeration helical twin screw compressors and their systems, from which some useful results are obtained and important conclusions are drawn.

Optimum Lobe Tip Designs

A comprehensive examination of rotor lobe tip designs has been conducted, taking into account not only the efficiencies of a compressor but also lobe tip oil viscous friction power loss, its volumetric capacity and inter-rotor contact force.

For the calculation of oil viscous friction power loss at lobe tips a simple calculation model was formulated. The predictions, though not yet verified by experiment, look encouraging. A parameter study shows that the introduction of a narrow sealing strip at lobe tips could greatly reduce the viscous friction

power loss, without at the same time causing a significant increase in blow hole leakage loss. A similar but not so significant effect can also be achieved for a lobe tip design without sealing strips by using a relatively small leading tip angle of the male rotor β_3 and a relatively big radius of the leading circular arc of the female rotor r_9 (Fig. 5.1)

However, the simulation analysis conducted by the author (see section 5.3) suggested that from the point of view of obtaining high efficiency, large capacity and low contact force, a relatively large β_3 would be an advantage. This is not consistent with the requirement of reducing the viscous friction power loss at the lobe tips. Consequently, this parameter must be optimised for the minimum power consumption.

It may be concluded that the influence of the lobe tip design parameters on compressor efficiencies, real capacity and rotor contact forces are significant, and must not be underestimated.

Optimum Rotor Parameter Combinations

A parameter study has been conducted using the four most common rotor lobe combinations, five different length / diameter ratios and five different wrap angles. Factors which have been taken into consideration include the efficiency of the compressor, female rotor deflection, inter-rotor contact force and bearing forces.

The 4+5 and 5+6 combinations have in general high efficiencies, but less rigidity, and can thus only be applied to low or medium pressure level applications with short rotors. The 5+7 and 4+6 combinations show no problems due to female rotor deflection and can be used for a range of length / diameter ratios and for high pressure ratios. However, compared with other lobe combinations, the 4+6 combination displays relatively lower efficiencies, while the 5+7 combination shows a relatively higher contact force. The highest

wrap angle and length / diameter ratio do NOT always lead to the highest compressor performance, which is in fact related to compressor running conditions. The bearing forces increase with increasing length / diameter ratio and therefore must be examined when deciding the length / diameter ratio.

In conclusion, the right choice of the rotor physical parameters, in addition to choosing an advanced modern rotor profile, is critical for designing high performance helical twin screw compressors, which can only be achieved for a relatively narrow range of running conditions.

Optimum Slide Valve Design

A slide valve is commonly used as a capacity control device in many applications of helical twin screw compressors to refrigeration duties. A comprehensive examination of its influence on compressor performance and bearing forces has been conducted, from which a procedure for determining optimum slide stop and volume ratios for both radial and axial discharge ports have been derived.

A slide valve ensures that the compressor obtains a relatively high indicated efficiency at part load condition, but reduces the compressor full load performance considerably. It is thus suggested that in the situation in which two or more twin screw compressors are used together, one or more should be without a slide valve and should always run under the full load condition with both the radial and axial discharge ports having the same volume ratios.

The volume ratio for the axial discharge port not only controls the discharge process at low load, but also sets the theoretical minimum load capacity at which the compressor can be run. The industry often uses a high volume ratio for the axial discharge port, usually a value of 5.0, which sets the minimum load capacity of 20 percent. However, the simulation has shown that using such a high volume ratio for the axial discharge port may considerably decrease the indicated efficiency at the load range of interest, which is usually

above 40 percent. It is therefore suggested that the volume ratio for the axial port should be optimised for the most common running condition of the compressor.

The volume ratio for the radial discharge port should be chosen according to the best full load performance. It can provide a relatively high indicated efficiency over the entire adjusting range of the slide valve. Additionally, the radial discharge volume ratio may also be used to improve compressor part load performance, but to the detriment of the full load performance.

A suitable slide stop should be determined to achieve a relatively high indicated efficiency over the load range within which the compressor is to be run.

If the volume ratios and slide valve are designed to optimise the indicated efficiency, the maximum bearing forces appear at the full load condition. However, a change in running conditions combined with an unwise choice of slide stop may result in the occurrence of the maximum bearing forces at the part load condition of 0.6 - 0.7. To ensure safe operation, it is suggested that in addition to the performance prediction, a force analysis should also be carried out when changing the running condition or changing the slide valve design of a twin screw refrigeration compressor.

Removing the Non-Return Valve from the Refrigeration Helical Twin Screw Compressor System

Refrigeration systems driven by twin screw compressors are normally fitted with a non-return valve in the suction line of the compressor to prevent the gas in the high pressure side from flowing backwards through the compressor into the suction chamber following system shutdown. The simulation has shown that the use of this non-return valve results in an increase in energy consumption and a decrease in system COP. The removal of such a non-

return valve from the system is realizable by fitting a non-reversing clutch to the prime mover to restrain the reverse rotation of the compressor following shut down.

Utilizing the integrated program, both the shut down torque and normal running torque were calculated and compared. It is shown that the shut down torque may have a peak value considerably higher than the normal driving torque. As a consequence, care must be taken with the choice or design of the clutch.

Rotor Axial-Torsional Coupled Vibration Analysis

In oil-injected helical twin screw compressors gas compression and lobe interaction exert periodic loads on the rotors, causing coupled axial and torsional vibration . The natural frequencies of such coupled vibration modes in some systems may resonate with harmonics of the gas force and torque. They therefore require to be examined at the design stage. Utilizing assumptions which simplify the lobe interaction, an analytical model has been created, which provides a tool for compressor rotor vibration analysis if all system parameters are available.

To avoid any possible excitation of resonance, the frequencies of the forces and torques applied to the rotors must be different from the natural frequencies of the system. A frequency analysis of all the excitations was conducted by using an FFT technique. The results suggest that the fundamental harmonic, the frequency of which equals the lobe passing frequency, dominates among all the harmonic components. The axial forces are different, due to the second harmonic being slightly stronger than the first one.

8.2 Recommendations for Further Research

The results of the present study suggest that further research should be carried out in order to further improve the performance of helical twin screw

compressors. Areas requiring investigation are given as follows:

Rotor Profile Generation Program

The rotor profile generation program developed by the author in this study is capable of generating any profile made up of straight lines, circular arcs and points. Although this is enough to accommodate many existing rotor profiles, including the powerful SRM D-profile, it is necessary to extend the types of curves which the program can generate. This work is of significance for developing new rotor profiles and analysing and modifying any existing profiles. It is suggested that polynomial-fit curve and data-fit curve, which could be any arbitrary curve in the form of discrete digitized points, may be added, so that the program is more powerful and can virtually generate any profile.

Oil Viscous Friction Loss at Rotor Flanks and Rotor Ends

In this study the torque due to oil viscous friction loss at the lobe tips was calculated. However, oil viscous friction loss also exists at the rotor flanks and ends. From this preliminary study, it is believed that the viscous friction power loss at these two parts are of the same order as that occurring at rotor lobe tips with sealing strips. Therefore, it is envisaged the total efficiency of the compressor could be improved if a better understanding of these power losses could be obtained.

Rotor Axial-Torsional Coupled Vibration Analysis

Due to the lack of reliable system parameters, like oil film stiffness coefficients, the rotor axial and torsional coupled vibration analysis model created in this study was not solved. Further research is thus recommended to determine these system parameters experimentally, so that the natural frequencies of the

system can be decided.

In order to gain an insight into the real rotor interaction, it is necessary to obtain the solution of the axial-torsional coupled vibration model. If the mean of the torque transmitted from the male rotor to the female rotor is less than its dynamic amplitude, the rotors may contact at the anti-drive side rather than driving side, causing a so called rotor "chatter" problem. The consequence of the rotor chatter is increased rotor noise and a possible damage to rotor flanks.

References

Adams, G. and **Soedel, W.** (1992) 'Remarks on Oscillating Bearing Loads in Twin Screw Compressors', Proceedings of International Compressor Engineering Conference at Purdue, USA, p.439-448.

Astberg, A. (1984), 'A Meshing-Screw Rotary Machine', UK Patent, No. 2092676B.

Bennewitz, C. (1992) 'Software Support for Screw Rotor Design, Manufacture and Quality Control', Proceedings of International Compressor Engineering Conference at Purdue, USA, p.431-438.

Cameron, A. (1983) 'Basic Lubrication Theory', 3rd edition, Ellis Horwood Limited, Chichester, UK.

Deng, D.G. and **Shu, P.C.**,'Rotary Compressors', Mechanical Industry Press, Beijing, China, 1988.

Edström, S. (1985) 'Rotor Technology', SRM Technical Screw Compressor Conference, Stockholm, Sweden.

Fleming J.S., **You C.X.** and **Tang Y.** (1994a), 'Rotor Tip Design in Oil Injected Helical Twin Screw Compressors with respect to Viscous Friction Loss', Proceedings of the Institution of Mechanical Engineers (London), European Conference on Developments in Industrial Compressors and their Systems, London, p.115-122.

Fleming, J.S., **Tang, Y.** and **Anderson, H.** (1994b) 'Optimisation Techniques Applied to the Design of a Refrigeration Twin Screw Compressor', Proceedings of International Compressor Engineering Conf. at Purdue, USA, p.641-646.

Fleming J.S., **You C.X.**,**Tang Y.** and **Anderson, H.** (1994c), 'The Influence of Slide Valve on the Thermodynamic Efficiency and Bearing Forces of a Refrigeration Helical Twin Screw Compressor', VDI-Bericht 1135, Verein Deutscher Ingenieure, VDI Verlag, p.63-74.

Hodge, J. (1970) 'Some Aspects of Screw Compressors', Proceedings of Institution of Mechanical Engineers, London, UK, **184**:153-158.

Honke, K. and **Yoshimura, S.** (1992) 'Axial and Torsional Coupled Vibration Analysis of Screw Compressor Rotor', SRM Technical Screw Compressor Conference, Stockholm, Sweden.

Howden Compressors Ltd. (1991a) '*R & D Report*', No. 291, Glasgow, UK.

Howden Compressors Ltd. (1991b) '*R & D Report*', No. 134, Glasgow, UK.

Kauder, K. and **Piatkowski, R.** (1987) 'Einfluß des Öls auf den mechanischen Wirkungsgrad Öleingespitzter Schraubenverdichter', VDI BERICHTE No. 640, p.11-30.

Li,Q.Y., Wang, N.C. and **Yi, D.Y.** (1981) 'Numerical Analysis', Hua Zhong University of Science and Technology Press, Wuhan, China, 1981.

Lim, K.P. (1992) 'Condition Monitoring - Detection of Machinery Malfunction', Ph.D thesis, University of Strathclyde, Glasgow, UK.

Lundin, S. (1992) 'Gas Pulsation noise in screw compressor outlet', SRM Technical Screw Compressor Conference, Stockholm, Sweden.

Lysholm, A.J.R. (1943) 'New Rotary Compressor', Proceedings of Institution of Mechanical Engineers, London, UK, **150**.

Newland, D.E. (1989) 'Mechanical Vibration Analysis and Computation', Longman Scientific & Technical, England.

Öhman, H. (1992) 'Low Noise Profile Development', SRM Technical Screw Compressor Conference, Stockholm, Sweden.

Pamlin, R. (1992) 'How to Make the Right Choice of Rotor Lobe Combination', SRM Technical Screw Compressor Conference, Stockholm, Sweden.

Peveling, F.J. (1987) 'Einfluß des Umschlingungswinkels auf das Betriebsverhalten von Schraubenmaschinen', VDI Bericht, No. 640, p.209-230.

Rinder, L. (1979) 'Schraubenverdichter', Wien, Springer-Verlag.

Sångfors, B. (1992) 'Computer Analysis of Gas-Flow Generated Resonance Effects in the Outlet of an Oil Injected Screw Compressor', SRM Technical Screw Compressor Conference, Stockholm, Sweden.

Sauls, J. (1988) 'Slide Valve Design Using a Screw Compressor Performance Simulation Model', SRM Technical Screw Compressor Conference, Stockholm, Sweden.

Sauls, J. (1990) 'The Design of Slide Valve Unloaders for Refrigeration Compressors in Air Conditioning Applications', VDI-Tagung Schraubenmaschinen, Dortmund, Germany, p33-44.

Schibbye, L.B. (1970), "Patent Specification", UK Patent, No. 1,197,432.

Shaw, D.N. (1988) 'Screw Compressors Control of V_i and Capacity, The Conflict', Proceedings of International Compressor Engineering Conference at Purdue, USA, p.236-243.

Shaw, D.N. (1990) 'Twin Screws of the Future for Air Conditioning and Refrigeration', Proceedings of International Compressor Engineering Conference at Purdue, USA, p.1-7.

Singh, P.J. and **Onushak, A.D.** (1984) 'A Comprehensive, Computerized Method for Twin-Screw Rotor Profile Generation and Analysis', Proceedings of International Compressor Engineering Conf. at Purdue, USA, p.519-527.

Singh, P.J. and **Patel, G.C.** (1984) 'A Generalized Performance Computer Program for Oil Flooded Twin-Screw Compressors', Proceedings of International Compressor Engineering Conference at Purdue, USA, p.544-553.

Singh, P.J. and **Bowman, J.L.** (1986) 'Effect of Design Parameters on Oil-Flooded Screw Compressor Performance', Proceedings of International Compressor Engineering Conference at Purdue, USA, p.71-88.

Singh, P.J. and **Bowman, J.L.** (1990) 'Calculation of Blow-Hole Area for Screw Compressors', International Compressor Engineering Conference at Purdue, USA, p.938-948.

Singh, P.J. and **Schwartz, J.R.** (1990), 'Exact Analytical Representation Of Screw Compressor Rotor Geometry', International Compressor Engineering Conference at Purdue, USA, p.925-937.

Sjöholm, L. (1986a) 'Different Operating Modes for Refrigeration Twin-Screw Compressors', Proceedings of International Compressor Engineering Conference at Purdue, USA, p.89-104.

Sjöholm, L. (1986b) 'Variable Volume-Ratio and Capacity Control in Twin-Screw Compressors', Proceedings of International Compressor Engineering Conference at Purdue, USA, p.494-508.

Stošić, N., **Kovačević, A.**, **Hanjalić, K.** and **Milutinović, Lj.** (1988) 'Mathematical modelling of the oil influence upon the working cycle of screw compressors', Proceedings of International Compressor Engineering Conference at Purdue, USA, p.354-360.

Stošić, N., **Milutinović, Lj.**, **Hanjalić, K.** and **Kovačević, A.** (1990) 'Experimental investigation of the influence of oil injection upon the screw compressor working process. Proc. of International Compressor Engineering Conference at Purdue, USA, p.34-43.

Svenningson, K. and **Sjölin, U.** (1992) 'The History of SRM Screw Compressor Development', Proceedings of SRM Compressor Technology Conference, Stockholm, Sweden.

Tang, Y. and **Fleming, J.S.** (1992a) 'Obtaining the Optimum Geometrical Parameters of a Refrigeration Helical Screw Compressor', Proceedings of International Compressor Engineering Conference at Purdue, USA, p.221-228.

Tang, Y. and **Fleming, J.S.** (1992b) 'Simulation of the Working Process of an Oil Flooded Helical Screw Compressor with Liquid Refrigerant Injection', Proc of International Compressor Engineering Conference at Purdue, USA, p.213-220.

Villadsen, V. and **Fleming, V.B.** (1980) 'Efficiency Measures in Ammonia Plants', Proceedings of International Institute of Ammonia Refrigeration Annual Meeting, Florida, USA.

Wilson, W.K. (1956) 'Practical Solution of Torsional Vibration Problems', Third Edition, Volume One, Frequency Calculations, Chapman and Hall Ltd, London.

Wu, B.Z. (1985) Refreigeration Screw Compressors, Mechanical Industry Press, Beijing, China.

Xing, Z.W., Deng, D.G. and **Shu, P.C.** (1992) 'A CAD System for Twin-Screw Compressors', Proceedings of International Compressor Engineering Conference at Purdue, USA, p.239-248.

You, C.X., Fleming, J.S. and **Tang, Y.** (1993) 'Computerised Analysis of the Rotor Forces and Torques due to Gas Compression in a Helical Screw Compressor', Proceedings of the International Compressor Engineering Conference, Xian, China, July 1993, p.390-399.

You C.X., Tang Y., Fleming J.S. and **Tramschek, A.B.** (1994a) 'A Generalized Computer Program for Determining the Bearing Loads in Helical Twin Screw Compressors', Proceedings of the International Compressor Engineering Conference at Purdue, USA, July 1994, p.653-658.

You C.X., Tang Y. and **Fleming J.S.** (1994b) 'Removing the Non-Return Valve from a Refrigeration System with a Twin Screw Compressor', Proceedings of the International Compressor Engineering Conference at Purdue, USA, July 1994, p.635-640.

Zhou, Z., Wang, D., Zhou, T. and **Mao, J.** (1990) 'Analysis of the Applied Forces in Twin-Screw Refrigerant Compressors', Proceedings of International Compressor Engineering Conference at Purdue, USA, p.8-17.

Appendix 1

SRM A- and D-Profile Geometry

This appendix presents a geometrical analysis of SRM A- and D-profile. The task of the geometrical analysis is, according to the definition of a profile, to determine position parameters which define all the "known" segments, provided that the basic parameters are given.

A1.1 SRM A-Profile Geometry

The basic parameters for SRM A-profile are:

- outer radius of the rotors, $r_{o,1}$, $r_{o,2}$;
- distance between the two rotor centres, C;
- the number of the male and female rotor lobes, $\bar{z}_1$, $\bar{z}_2$;
- the range angles of male rotor crest segment, β_1, β_2;

With reference to the coordinate system and symbols used in Fig. 2.3 (section 2.3 of Chapter 2) and Fig. A1.1 all "known" segments are defined as follows:

Segment $S_2\ Q_2$: Circular arc

Centre point coordinates: $x_{2c} = 0, \quad y_{2c} = 0$

Radius : $r = r_{o,2}$

Start and end angles : $t_s = 2\pi + \psi_6, \quad t_e = 2\pi + \psi_4$

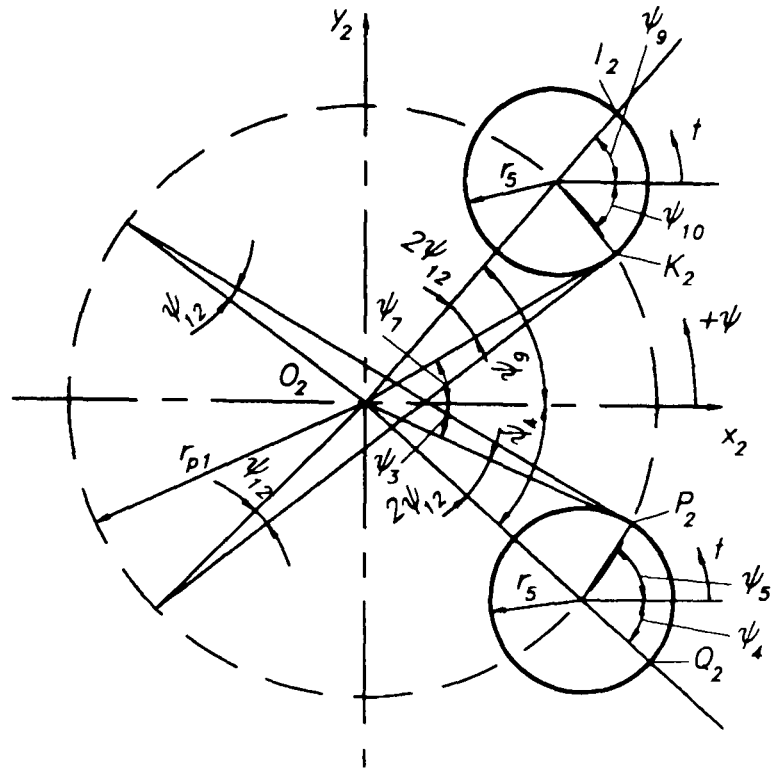

Fig. A1.1 Relationship between parameters of SRM A-profile

Segment $Q_2\ P_2$: Circular arc

Centre point coordinates : $x_{2c} = r_{p,2} \cdot \cos\psi_4$, $y_{2c} = r_{p,2} \cdot \sin\psi_4$

Radius : $r = r_5$

Start and end angles : $t_s = 2\pi + \psi_4$, $t_e = \psi_5$

Segment $N_2\ P_2$: Radial line

Start point coordinates : $x_{2,N}$, $y_{2,N}$

End point coordinates : $x_{2,P_2} = r_{p,2} \cdot \cos\psi_4 + r_5 \cdot \cos\psi_5$

$y_{2,P_2} = r_{p,2} \cdot \sin\psi_4 + r_{p,2} \cdot \sin\psi_5$

Point B_1 *for segment* $N_2\ B_2$: Point

Point B_1 coordinates : $x_{1,B} = r_{p,1} + r_3 \cdot \cos\beta_4$, $y_{1,B} = r_3 \cdot \sin\beta_4$

Start and end angles : $t_s = 0$, $t_e = \varphi_{1,N}$

Point N_2 *for segment* $N_1\ B_1$: Point

Point N_2 coordinates : $x_{2,N}$, $y_{2,N}$

Start and end angles : $t_s = \varphi_{1,N}$, $t_e = 0$

Segment $A_2\ B_2$: Circular arc

Centre point coordinates : $x_{2c} = r_{p,2}\ ,\quad y_{2c} = 0$

Radius : $r = r_3$

Start and end angles : $t_s = \pi - \beta_3\ ,\quad t_e = \pi - \beta_4$

Segment $A_2\ K_2$: Circular arc

Centre point coordinates : $x_{2c} = x_{2,M}\ ,\quad y_{2c} = y_{2,M}$

Radius : $r = r_4$

Start and end angles : $t_s = \pi - \psi_8\ ,\quad t_e = \pi - \beta_3$

Segment $K_2\ I_2$: Circular arc

Centre point coordinates : $x_{2c} = r_{p,2} \cdot \cos\psi_9\ ,\quad y_{2c} = r_{p,2} \cdot \sin\psi_9$

Radius : $r = r_5$

Start and end angles : $t_s = 2\pi + \psi_{10}\ ,\quad t_e = \psi_9$

Segment $I_2\ J_2$:

Centre point coordinates : $x_{2c} = 0\ ,\quad y_{2c} = 0$

Radius : $r = r_{o,2}$

Start and end angles : $t_s = \psi_9\ ,\quad t_e = \psi_{11}$

All unknown parameters in the above expressions are derived as follows.

The radii of the pitch circles of the two rotors are determined by using mesh condition:

$$r_{p,1} = \frac{\bar{z}_1 \cdot C}{\bar{z}_1 + \bar{z}_2} \qquad r_{p,2} = a - r_{p,1} = \frac{\bar{z}_2 \cdot C}{\bar{z}_1 + \bar{z}_2} \tag{A1.1}$$

Thus, the radius of the segment $Q_2\ P_2$ and $K_2\ I_2$ is

$$r_5 = r_{0,2} - r_{p,2} \tag{A1.2}$$

and the radius of the segment $A_2\ B_2$ is

$$r_3 = r_{o,1} - r_{p,1} \tag{A1.3}$$

The radius of the segment $A_2 K_2$ is

$$r_4 = r_3 + l_3 \tag{A1.5}$$

where $l_3 = \dfrac{r_3^2}{2(r_{p,2} \cdot \cos\beta_3 - r_3)}$ deduced from the following two equations:

In triangle $O_2 M K_2$: $\overline{O_2 M} = \sqrt{r_{p,2}^2 + r_4^2}$

In triangle $O_2 M T$: $\overline{O_2 M} = \sqrt{r_{p,2}^2 + l_3^2 - 2 \cdot r_{p,2} \cdot l_3 \cdot \cos(\pi - \beta_3)}$

Then, the coordinates of the centre point of the segment $A_2 K_2$ are:

$$x_{2,M} = r_{p,2} + l_3 \cdot \cos\beta_3 \quad y_{2,M} = - l_3 \cdot \sin\beta_3$$

The coordinates of the point N_2 are obtained by using Eq. (2.2):

$$\begin{aligned} x_{2,N} &= - x_{1,B}\cos(k\psi_{1,N}) + y_{1,B}\sin(k\psi_{1,N}) + C \cdot \cos(i \cdot \psi_{1,N}) \\ y_{2,N} &= + x_{1,B}\sin(k\psi_{1,N}) + y_{1,B}\cos(k\psi_{1,N}) - C \cdot \sin(i \cdot \psi_{1,N}) \end{aligned} \tag{A1.4}$$

where $\varphi_{1,N}$ is referred to as position parameter of the point N which can only be determined by a trial and error method. That is, a value of $\varphi_{1,N}$ is tried, from which $x_{2,N}$ and $y_{2,N}$ are calculated using Eq. (A1.4). The line $N_2 T$ is then checked to see if it is perpendicular to the radial line $O_2 N_2$ (this is required by the definition of the profile).

In addition, all relevant angles are obtained as follows:

$$\psi_4 = \psi_3 - 2 \cdot \psi_{12}$$

$$\psi_5 = \frac{\pi}{2} + \psi_{12} + \psi_4$$

$$\psi_8 = \arctan\left(\frac{r_{p,2}}{r_4}\right) - \arctan\left(\frac{y_{2,M}}{x_{2,M}}\right)$$

$$\psi_9 = \psi_7 + 2 \cdot \psi_{12}$$

$$\psi_{10} = \psi_9 - \frac{\pi}{2} - \psi_{12}$$

where

$$\psi_3 = \arctan\left(y_{2,N} / x_{2,N} \right)$$

$$\psi_{12} = \arcsin\left[r_5 / (2\, r_{p,2}) \right]$$

$$\psi_7 = \arctan\left(\frac{r_4}{r_{p,2}}\right) - \arctan\left(\frac{y_{2,M}}{x_{2,M}}\right)$$

Since the width of the segment $S_2\ Q_2$ is the same as that of the segment $I_2\ J_2$, and the lobes are identical, the following equations result:

$$\psi_{11} - \psi_9 = \psi_4 - \psi_6$$

$$\psi_{11} - \psi_6 = 2\pi / \bar{z}_2$$

which lead to

$$\psi_6 = (\psi_4 + \psi_9) / 2 - \pi / \bar{z}_2$$

$$\psi_{11} = (\psi_4 + \psi_9) / 2 + \pi / \bar{z}_2$$

A1.2 SRM D-Profile Geometry

The basic parameters for SRM D-profile are (see Fig. 2.4 and Fig. A1.2):

- outer radius of the rotors, $r_{o,1}$, $r_{o,2}$;
- distance between the two rotor centres, C;
- the number of the male and female rotor lobes, $\bar{z}_1$, $\bar{z}_2$;
- the range angles of male rotor crest segment, β_1, β_2;
- the radius and the range angle of the small circular arc close to the tip of the male rotor, r_6, β_6;
- the radius and the range angle of the small circular arc close to the tip of the female rotor, r_8, β_8;
- the pressure angles of the male rotor flank at the pitch circle, ε_3, ε_4;
- the radius of the small circular arcs close to the bottom of the male rotor flank, r_5, r_9;

Similar to the SRM A-profile, all "known" segments can be defined with reference to the coordinate system and symbols used in Fig. 2.4 (section 2.3 of Chapter 2) and Fig. A1.2:

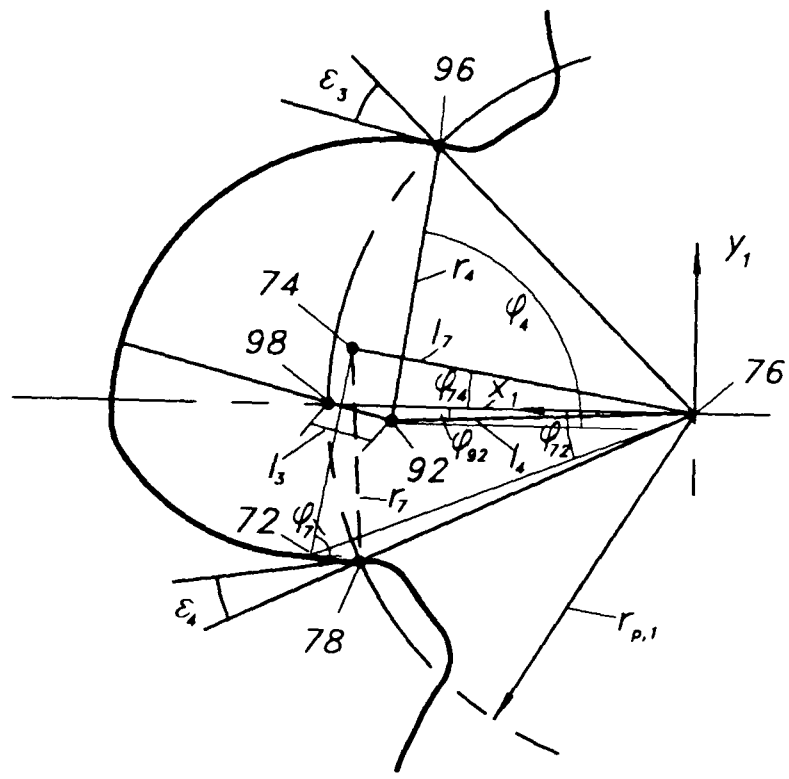

Fig. A1.2 Relationship between parameters of SRM D-profile

Segment 68-91 of the male rotor : Circular arc

Centre coordinates : $x_{1c} = r_{p,1}$, $y_{1,c} = 0$

Radius : $r = r_3 = r_{o,1} - r_{p,1}$

Start & end angles : $t_s = \pi - \beta_3$, $t_e = \pi - \beta_4$

Segment 91-94 of the male rotor : Circular arc

Centre coordinates : $x_{1c} = l_4 \cdot \cos\varphi_{92}$, $y_{1c} = l_4 \cdot \sin\varphi_{92}$

Radius: $r = r_4$

Start & end angles : $t_s = \varphi_4$, $t_e = \pi - \beta_3$

Segment 94-97 of the male rotor : Circular arc

Centre coordinates : $x_{1c} = (r_5 + C - r_{o,2}) \cdot \cos\varphi_{99}$, $y_{1c} = (r_5 + C - r_{o,2}) \cdot \sin\varphi_{99}$

Radius: $r = r_5$

Start & end angles : $t_s = \pi + \varphi_4$, $t_e = 2\pi - \varphi_{99}$

Segment 97-93 of the male rotor : Circular arc

Centre coordinates : $x_{1c} = 0$, $y_{1c} = 0$

Radius: $r = C - r_{o,2}$

Start & end angles : $t_s = \pi - \varphi_{93}$, $t_e = \pi - \varphi_{99}$

Segment 68-80 of the male rotor : Circular arc

Centre coordinates : $x_{1c} = (r_3 - r_6)\cdot\cos\beta_4 + r_{p,1}, \quad y_{1c} = (r_3 - r_6)\cdot\sin\beta_4$

Radius: $r = r_6$

Start & end angles : $t_s = \pi - \beta_4, \quad t_e = \pi - \beta_4 + \beta_6$

Segment 84-82 of the female rotor : Circular arc

Centre coordinates : $x_{1c} = x_{2,84} + r_8\cdot\cos\varphi_8, \quad y_{1c} = y_{2,84} + r_8\cdot\sin\varphi_8$

Radius: $r = r_8$

Start & end angles : $t_s = t_e - \beta_8, \quad t_e = \pi + \varphi_8$

Segment 72-70 of the male rotor : Circular arc

Centre coordinates : $x_{1c} = l_7\cdot\cos\varphi_{74}, \quad y_{1c} = l_7\cdot\sin\varphi_{74}$

Radius: $r = r_7$

Start & end angles : $t_s = \pi - \varphi_7, \quad t_e = t_s + \beta_7$

Segment 70-67 of the male rotor : Circular arc

Centre coordinates : $x_{1c} = (r_9 + C - r_{o,2})\cdot\cos\varphi_{69}, \quad y_{1c} = (r_9 + C - r_{o,2})\cdot\sin\varphi_{69}$

Radius: $r = r_9$

Start & end angles : $t_s = -\varphi_{69}, \quad t_e = -\varphi_7 + \beta_7$

Segment 67-63 of the male rotor : Circular arc

Centre coordinates : $x_{1c} = 0, \quad y_{1c} = 0$

Radius: $r = C - r_{o,2}$

Start & end angles : $t_s = \pi + \varphi_{69}, \quad t_e = \pi + \varphi_{63}$

Similarly, $r_{p,1}$, $r_{p,2}$ and r_3 can be determined using Eqs. (A1.1) and (A1.3). Other unknowns in the above expressions may be determined as follows:

Segments on the drive side, 91-94-97 :

In triangle 76-96-92 : $$l_4^2 = r_4^2 + r_{p,1}^2 - 2\, r_4\, r_{p,1} \cos\left(\frac{\pi}{2} - \varepsilon_3\right)$$

In triangle 76-98-92 : $l_4^2 = r_{p,1}^2 + l_3^2 - 2\, r_{p,1}\, l_3 \cos\beta_3$

and from geometry: $l_3 = r_4 - r_3$

thus,

$$r_4 = \frac{r_3^2 + 2\, r_{p,1}\, r_3 \cos\beta_3}{2\,(r_3 - r_{p,1}\sin\varepsilon_3 + r_{p,1}\cos\beta_3)} \quad , \qquad l_4 = \sqrt{r_4^2 + r_{p,1}^2 - 2\, r_4\, r_{p,1}\sin\varepsilon_3}$$

Also from triangle 76-98-92 : $l_3 = -l_4 \sin\varphi_{92} / \sin\beta_3$, thus

$$\varphi_{92} = -\arcsin\left(\frac{l_3}{l_4}\sin\beta_3\right)$$

In triangle 76-99-92 : $(r_5 + C - r_{o,2})^2 = (r_5 + r_4)^2 + l_4^2 - 2(r_5 + r_4)\, l_4 \cos(\varphi_4 + \varphi_{92})$

Thus, $$\varphi_4 = \arccos\left(\frac{(r_5 + r_4)^2 + l_4^2 - (r_5 + C - r_{o,2})^2}{2\,(r_5 + r_4)\, l_4}\right) - \varphi_{92}$$

Also from triangle 76-99-92 :

$$\varphi_{99} = \arccos\left(\frac{l_4^2 + (r_5 + C - r_{o,2})^2 + l_4^2 - (r_5 + C - r_{o,2})^2}{2\,(r_5 + r_4)\, l_4}\right) - \varphi_{92}$$

Segments on the anti-drive side, 68-80-72-70-67 :

Since the segment *68-84* of the female rotor is generated by the segment *68-80* of the male rotor, the coordinates and the first derivative of the flank at point *84* can be obtained using Eqs. (2.2), (2.17) and (2.19) (see Chapter 2) and are denoted here as

$$x_{2,84}\,,\ y_{2,84}\,,\ (dy_2 / dx_2)\big|_{84}$$

For circular arc *84-82* a common tangent is required at point *84*, this gives

$$\varphi_8 = \arctan\left(\frac{-1}{(dy_2 / dx_2)\big|_{84}}\right)$$

Similarly, the segment *80-72* of the male rotor is generated by the circular are *84-82* of the female rotor. Accordingly, the coordinates and the first

derivative of the flank at point *72* can be obtained using Eqs. (2.1), (2.13) and (2.15) (see Chapter 2) and are denoted here as

$$x_{1,72},\ y_{1,72},\ (dy_1 / dx_1)\big|_{72}$$

Thus,

$$\varphi_7 = \arctan\left(\frac{-1}{(dy_1 / dx_1)\big|_{72}}\right) \qquad \text{and} \qquad \varphi_{72} = \arctan\left(\frac{y_{1,72}}{x_{1,72}}\right)$$

In triangle 76-74-72: $l_7^2 = r_7^2 + (x_{1,72}^2 + y_{1,72}^2) - 2\, r_7 \sqrt{x_{1,72}^2 + y_{1,72}^2}\cos(\varphi_7 - \varphi_{72})$

In triangle 76-74-78: $l_7^2 = r_7^2 + r_{p,1}^2 - 2\, r_7\, r_{p,1}\cos(\pi/2 - \varepsilon_4)$

from which r_7 and l_7 can be obtained.

And in triangle 76-74-78 : $\varphi_{74} = \varphi_{72} + \arccos\left(\frac{l_7^2 + r_{p,1}^2 - r_7^2}{2\, l_7\, r_{p,1}}\right)$

In triangle 76-74-69 :

$$(r_7^2 + r_9^2) = l_7^2 + (r_9 + C - r_{o,2})^2 - 2\, l_7\, (r_9 + C - r_{0,2})\cos(\varphi_{74} - \varphi_{69})$$

from which φ_{69} can be obtained.

In addition, for segments *67-63* and *97-93* of the male rotor, the expressions for φ_{63} and φ_{93} are the same as those of SRM A-profiles:

$$\varphi_{63} = (\varphi_{69} + \varphi_{99}) / 2 - \pi / \bar{z}_1\ , \qquad \varphi_{93} = (\varphi_{69} + \varphi_{99}) / 2 + \pi / \bar{z}_1$$

Finally, it has to be noted that the above results apply only to the situation in which neither β_6 nor β_8 equals zero. If a point is used rather than a circular arc, an extra parameter is needed to be given as known parameter. In the case that $\beta_6 = 0$, it may be a good solution to let

$$l_8 = r_{p,2}\sqrt{\cos\varepsilon_4}\ ,$$

while in the case that $\beta_8 = 0$, then let

$$l_7 = 1.002\, r_{p,1}\cos(\varepsilon_4) \qquad \text{or} \qquad \sqrt{x_{1,72}^2 + y_{1,72}^2} = 1.1\, r_{p,1}.$$

These settings are within the definition of the profile.

Appendix 2

Instructions for the Use of the Programs Developed

A2.1 General Requirement and Feature

Three programs have been developed in this study: rotor profile generation program, geometrical characteristics calculation program and force analysis program. The general requirements and features of the programs are the same.

The programs are all based on the IBM compatible PC / MS-DOS system. Each of them plus relevant data files occupy about 500 kB disk space.

The programs are reasonably user friendly being menu driven. The user can simply follow the menu from input through calculation to output. The input parameters can be given on line or the user may choose a existing file. The data file loaded can be viewed on the screen and changed at will and saved with a file name chosen by the user. While viewing, the program facilitates zooming and scrolling, so that any part of the picture can be examined in great detail. The calculation results may be saved as disk files. The forenames of the files are identical and chosen by the user, while the extensions are different and chosen by the program.

A2.2 Rotor Profile Generation Program

This program can be used to generate rotor profiles, the known segments of which must be circular arcs or straight lines or points.

Input

SRM A- and D-Profiles: The user only need to input basic parameters for these profiles (see Appendix 1). The program can calculate the position parameters of all known segments.

Other Profiles: The user has to specify all position parameters either by input on-line or reading a existing data file. The segments must be numbered from the anti-drive side along the rotor flank to the drive side (e.g. for SRM A-profile (Fig. 2.3), the first segment is $S_2\ Q_2$, the second one is $Q_2\ P_2$, and the last one is $I_2\ J_2$). If choosing input on line, the user will be asked first to specify the type of the segment, then the program will prompt the user to input all position parameters. For a circular arc, for instance, the user has to input the coordinates of the arc centre, the radius and the start and end angles of the segment. If reading a existing data file, the user may just make some change, without taking the trouble to input all the segments parameters each time.

Output

The user can save the results of the generated profile as two disk files, the extensions of which are 'gen' and 'tan' respectively. The 'gen' file includes the coordinates of the male and female rotor flank points, and the corresponding male rotor angle for contacting, e.g. an angle of 30 degree means that the corresponding flank point will be in contact in the end plane when the male rotor rotates 30 degrees. It is to be noted that the results are associated with the coordinate systems used and the chosen zero-position. The 'tan' file contains the first derivative of the rotor flank points. This file is useful for the

calculation of inter-rotor contact forces and the design of rotor cutters.

A2.3 Geometrical Characteristics Program

This program can be used to calculate important geometrical characteristics of the twin screw compressor, i.e. sealing line length (between the rotors and between the rotors and housing bores), blow hole area and cavity volume.

Input

The user must choose a 'gen' file generated by the rotor profile generation program, and additionally, must specify the male rotor wrap angle and rotor length / diameter ratio. The user also has options of calculating all these geometrical characteristics or only some of them.

Output

The results of calculation may be saved as a 'geo' file, which includes all important geometrical characteristics calculated, such as sealing line length per lobe, blow hole area, maximum inter-lobe area and maximum cavity volume, etc. The variation of these parameters with male rotor angle of rotation may also be saved as disk files with different extension names ('lrr' for sealing line length between the rotors, 'lrb' for sealing line length between the rotors and housing bores, 'bla' for blow hole area, 'aav' for inter-lobe area and cavity volume).

A2.4 Force Analysis Program

This program can be used to calculate rotor torques, bearing radial and axial forces and female rotor deflection.

Input

The user has to choose (a) a 'gen' file produced by the rotor profile generation program, (b) a 'geo' file produced by the geometrical characteristics program, (c) a 'pre' file or 'SRM D New', and (d) a 'rgp' file. The 'pre' file is a two column data file, the first column is the male rotor angle of rotation, while the second one is the corresponding pressure in the cavity. This file may be obtained using a performance simulation program or by measurement. If 'SRM D New' is chosen, the program will read the results of the Strathclyde University's performance simulation program (Note that these results data files must be put in the same sub-directory as the bearing force program).

Output

Similarly, the important results of the force analysis program are saved as a disk file with extension 'res'. It includes maximum bearing radial and axial forces, maximum rotor torques, maximum female rotor deflection, etc. The variation of the forces and torques with male rotor angle of rotation are saved as disk files as well. The extension 'gtf' stands for rotor torques, 'gaf' for bearing axial forces, 'gbf' for bearing radial forces, 'def' for female rotor deflection.